Magnetically Interesting Coordination Complexes Based on Macrocyclic Ligands

Zineb Ras Ali, MSc

Department of Chemistry

Submitted in partial fulfillment

of the requirements for the degree of

Doctor of Philosophy

Faculty of Mathematics and Science, Brock University

St. Catharines, Ontario

Abstract

The synthesis and study of select *3d* and/or *4f* coordination complexes prepared from crown ether and Schiff-base dual compartmental macrocycles are described herein, working towards the discovery and study of new families of macrocyclic-based single molecule magnets (SMMs). *Chapter 1* introduces the general theory of magnetism, molecular magnetism and SMMs and provides the reader with a brief overview of the relevant coordination chemistry of the two families of macrocycles.

In Chapter 2, two 15-crown-5 complexes $[Ln(NO_3)_3(OH_2)_2(MeOH)]$, (where Ln(III) = Tb (**I**) and Dy (**II**)) have been prepared and characterized. X-ray diffraction studies reveal the two complexes crystallize as 1-D chains. Variable temperature ac magnetic susceptibility studies reveal that (**II**) is an SMM with two effective energy barriers, U_{eff} = 26 K (18 cm^{-1}); $\tau_0 = 4.10 \times 10^{-7}$ s and U_{eff} = 41 K (29 cm^{-1}); $\tau_0 = 1.35 \times 10^{-8}$ s, whereas *ab initio* studies suggest that the observation of slow relaxation of magnetization in the Tb complex (**I**) is hindered by the presence of rapid quantum tunneling mechanisms (QTM). Solid state photoluminescence measurements reveal the two complexes have well-resolved *f–f* transitions, where a Gaussian fit of the fine structure of the highest-energy emission band for the Dy(III) complex allows the Stark splitting of the ground state to be determined.

In Chapter 3, select Ln(III) complexes with benzo and dibenzo 15-crown-5 macrocycles were synthesized and characterized. Reaction of Dy(III) together with benzo 15-crown-5 afforded a unique $[Dy(OH_2)_8]^{3+}$ complex (**III**), where the hydrated Dy(III) cation is fully encapsulated within a supramolecular cage formed by three benzo 15-crown-5 macrocycles. Interestingly, the close to perfect square antiprismatic geometry of the *4f* ion enhances its axial anisotropy, which suppresses quantum tunnelling mechanisms (QTM) in the ground and first excited states, resulting

in the observation of SMM behavior in zero dc field. For this system the magnetic data were further supported by solid-state photoluminescence and *ab initio* studies, The introduction of a second benzene ring into the organic framework of the macrocycle increases its rigidity, where on coordination to Dy(III), affords the partially encapsulated complex (**IV**), which displays slow relaxation of magnetisation, consistent with SMM properties.

In Chapter 4, the coordination chemistry of a dual compartmental Schiff-base macrocycle **H_2L_3** containing O_3O_2 and N_3O_2 cavities was explored together with select *3d* and *4f* ions. In the first part of this chapter, the coordination chemistry of **H_2L_3** with *3d* metal ions is presented, where in the presence of NaOH, the Na(I) ions reside in the O_3O_2 cavity and the *3d* ions occupy the second N_3O_2 cavity. Three coordination complexes containing Cu(II), Zn(II), and Mn(II) ions were prepared and characterized. The Cu(II), and Zn(II) complexes are monomeric with molecular formulae $[CuNa(\mathbf{L_{3b}})ClCH_3OH]\cdot 6H_2O$ (**V**) and $[ZnNa(\mathbf{L_{3b}})(CH_3COO)(CH_3OH)]\cdot H_2O$ (**VI**) respectively, while the Mn(II) complex crystallizes as a trimer with stoichiometry $[Mn_3Na_2(\mathbf{L_3})_2(CH_3COO)_4]\cdot 5.75CH_3OH\cdot 0.5H_2O$ (**VII**). For complexes (**V**) and (**VI**), nucleophilic addition of the NH of the N_3O_2 cavity to the carbon atom of the adjacent imine results in a contraction of the N_3O_2 cavity and the formation of a five-membered imidazoline ring to afford the modified ligand **L_{3b}**.The magnetic properties of (**V**) and (**VII**) are also reported. In the second part of this chapter, coordination of the macrocycle to select *4f* ions in the absence of any base afforded the mononuclear complexes $[Dy(\mathbf{H_2L_3})(H_2O)_2(CH_3OH)_2]Cl_3\cdot CH_3OH$, (**VIII**), and $[Ln(\mathbf{H_2L_3})(H_2O)_3(CH_3OH)]Cl_3$, where Ln(III) = Tb (**IX**), Er (**X**), and Gd (**XI**), in which the Ln(III) ion is coordinated in the O_3O_2 cavity. Magneto-structural studies on these complexes reveal that the Dy complex has a slightly different structure than the other three complexes, however all four

4f ions crystallize with square antiprismatic geometries, where only the Dy(III) complex (**VIII**) displays SMM properties.

Acknowledgements

First and foremost, I would like to thank my supervisor, Prof. Melanie Pilkington. I am so grateful to you allowing me to join your group, for providing me with great advice, often through difficult times and for your support, patience, and encouragement which has enabled me to become an independent researcher. I am also appreciative of your confidence in me to supervise the less experienced students in the lab, for providing me with opportunities to present my work at conferences, and for the great time you personally spend with us all to just to talk and laugh. I would not be where I am today without you, you have been the best supervisor.

In addition, I would like to thank my committee members: Professors Georgii Nikonov and Feng Li. Their valuable comments, suggestions, and advice throughout my graduate studies at Brock are greatly appreciated.

A special thanks goes also to Prof. Jeremy Rawson (U. Windsor) who has helped me the most to learn and understand the fundamentals of magnetism.

I would also like to thank Dr. Dimitris Alexandropoulus (U. Oxford) for collecting magnetic susceptibility data on several of my complexes, and to Dr. Rute Ferreira (U. Aveiro) for collecting and modelling all the solid-state photoluminescence data.

I would like to thank the Ministry of Education of the Libyan government for the financial support throughout my graduate studies, as well as the Canadian Bureau for International Education (CBIE) for their guidance, advice and help to manage my finances throughout my studies in Canada.

I would also like to thank my group members, both past and present, Dr. Emma Stares, Jeffrey Regier, Majeda Al Hareri, Amy Pham, Parisa Abbasi, Anne Worrell, and Gabriele Delle Monache. For their help, advice and the great time we all spent together.

Finally, I would also like to thank from the bottom of my heart my parents, and my husband for their huge love and support throughout my life. Finally, I must extend this thank you to my kids for giving me the energy and determination to study and work hard to achieve my dream.

Table of Contents

Abstract ii

Acknowledgements v

Table of Contents vii

List of Tables ix

List of Figures xii

List of Schemes xxiv

List of abbreviations xxv

1 Introduction 1

1.1 Molecular magnetism 1

1.1.1 Origin of magnetism 1

1.1.2 Molecule-based magnets 10

1.1.3 Single molecule magnets (SMMs) 11

1.2 Luminescence in Ln(III) complexes 30

1.2.1 Luminescent *4f* SMMs 35

1.3 Crown ethers 40

1.3.1 Historical overview 40

1.3.2 Luminescent crown ether complexes 42

1.3.3 Crown ether based single molecule magnets 43

1.4 Schiff-base ligands 53

2 Dual-Property Supramolecular H-Bonded 15-Crown-5 Ln(III) Chains: Joint Magneto-Luminescence and *Ab Initio* Studies 65

2.1 Introduction 65

2.2 Experimental section 68

2.2.1 Synthesis of 15-crown-5 complexes 68

2.2.2 Physical measurements 69

2.3 Results and discussion 73

2.3.1 Synthesis and structural studies 73

2.3.2 Magnetic studies 78

2.3.3 *Ab initio* studies 86

2.3.4 Photoluminescence studies 89

2.4 Conclusions and future work 93
3 Ln(III) Complexes of Bz and diBz15C5 Macrocycles: Syntheses, Magneto-Structural, Optical and Theoretical Studies 95
3.1 Introduction 95
3.2 Experimental 98
3.2.1 Synthesis of Ln(III) Bz and diBz15C5 complexes 98
3.2.2 Physical measurements 100
3.3 Results and discussion 106
3.3.1 Ln(III) complexes of Bz15C5 106
3.3.2 Ln(III) complexes of diBz15C5 129
4 3*d*-Heterodinuclear and 4*f*-Mononuclear Complexes of a Schiff-Base Compartmental Macrocycle 146
4.1 Introduction 146
4.2 Experimental 149
4.2.1 Physical measurements 154
4.3 Results and discussion 158
4.3.1 Synthesis and structural studies of select *3d* complexes of **H_2L_3** 158
4.3.2 Magnetic and EPR studies 169
4.3.3 Synthesis and structural studies of Ln(III) complexes of **H_2L_3** 174
4.3.4 Magnetic studies 180
4.4 3*d*-4*f* Heterodinuclear complexes of a dual compartmental macrocycle 187
4.5 Conclusions and future work 188
5 Appendices 190
5.1 Crystallographic data 190
5.2 Computational details 200
6 References 215

List of Tables

Table 2-1 Summary of select crystallographic data for complexes **2.5** and **2.6**. 70

Table 2-2 Continuous shape measures (CSMs) of the 9-coordinate Dy(III) coordination polyhedron in the Dy complex **2.5**..... 75

Table 2-3 Continuous shape measures (CSMs) of the 9-coordinate Tb(III) coordination polyhedron in **2.6** 77

Table 2-4 Calculated relative energies, g-tensors, and angles (θ) of the ground- and first-excited-state pseudo doublets for the Tb1 ion in complex **2.6** 88

Table 3-1 Selected crystallographic parameters for **3.3** to **3.6.**..... 102

Table 3-2 Continuous shape measures (CSMs) of the 8-coordinate Dy(III) polyhedron in **3.1**. 108

Table 3-3 Continuous shape measures (CSMs) of the 9-coordinate Ln(III) coordination polyhedron in complexes Tb15C5 (**3.4**) and Gd15C5 (**3.5**) 111

Table 3-4 Energy peak position (E, ± 3.0 cm^{-1}) and full-width-at-half maximum (fwhm, ± 5.0 cm–1) of the $^4F_{9/2} \rightarrow {}^6H_{15/2}$ Stark components determined from the experimental emission spectrum 128

Table 3-5 Continuous shape measures (CSMs) of the 9-coordinate Dy(III) coordination polyhedron in complex **3.6**. 131

Table 4-1 Selected crystallographic parameters for complexes **4.2** – **4.4**..... 156

Table 4-2 Selected crystallographic parameters for complexes **4.5 - 4.8**. 157

Table 4-3 Continuous shape measures (CSMs) for the 5-coordinate Cu(II) ion in **4.2**..... 161

Table 4-4 Continuous shape measures (CSMs) for the 5-coordinate Zn(II) coordination polyhedron in complex **4.3**. 167

Table 4-6 Continuous shape measures (CSMs) of the 9-coordinate Ln(III) coordination polyhedra in complexes **4.5**-**4.8** 177

Table 4-7 Summary of the coordination geometries and SMM properties of complexes **4.1** and **4.5**..... 187

Table 5-1 Selected bond lengths (Å) and angles (°) for Dy15C5 complex (**2.5**)..... 190

Table 5-2 Selected bond lengths (Å) and angles (°) for Tb15C5 complex (**2.6**). 191

Table 5-3 Selected bond lengths and angles for DyBz15C5 complex (**3.3**). 192

Table 5-4 Selected bond lengths and angles for TbBz15C5 complex (**3.4**)..... 192

Table 5-5 Selected bond lengths and angles for the GdBz15C5 complex (**3.5**). 193

Table 5-6 Selected bond lengths and angles for the DydiBz15C5 complex (**3.6**). 194

Table 5-7 Selected bond lengths and angles for the Cu complex (**4.2**)..... 195

Table 5-8 Selected bond lengths and angles for the Zn complex (**4.3**)..... 195

Table 5-9 Selected bond lengths and angles for the Mn_3 complex (**4.4**). 195

Table 5-10 Selected bond lengths and angles for the Dy complex (**4.5**). 197

Table 5-11 Selected bond lengths and angles for the Tb complex (**4.6**)..... 198

Table 5-12 Selected bond lengths and angles for the Er complex (**4.7**)..... 199

Table 5-13 Selected bond lengths and angles for the Gd complex (**4.8**). 199

Table 5-14 Long (B_1) and short (B_2) basis sets used for the calculations of the Dy and Tb complexes **2.5** and **2.6**..... 200

Table 5-15 Energies of the eight Kramers doublets within the $^6H_{15/2}$ multiplet for the two Dy(III) ions in complex (**2.5**). 201

Table 5-16 Energies of the 13 singlet states within the $^7F_6$ multiplet for the Tb(III) ion of complex (**2.6**)..... 201

Table 5-17 g-Tensors for the eight Kramers doublets within the $^{6}H1_{5/2}$ multiplet for the two Dy(III) ions of complex (**2.5**). 202

Table 5-18 Energies of the Eight Kramers Doublets (KDs) in the $^{6}H_{15/2}$ Multiplet for the Dy1 and Dy2 Ions in (**2.5**). 203

Table 5-19 Crystal field parameters for the Dy1 ion of complex (**2.5**) using the CASSCF/RASSI wavefunctions. 206

Table 5-20 Crystal field parameters for the Dy2 ion of complex (**2.5**) using the CASSCF/RASSI wavefunctions. 207

Table 5-21 Crystal field parameters for the Tb(III) ion of complex (**2.6**) using the CASSCF/RASSI wavefunctions. 208

Table 5-22 (left) long basis sets and (right) short basis sets used for each structural model for the DyBz15C5 complex (**3.3**). 209

Table 5-23 Energies of the eight Kramers doublets (KD) in the $^{6}H_{15/2}$ multiplet for the DyBz15C5 complex (**3.3**). 209

Table 5-24 Difference between the main magnetic axes of the eight Kramers doublets in the $^{6}H_{15/2}$ multiplet for the DyBz15C5 complex (**3.3**). 209

Table 5-25 g-tensors of the eight Kramers doublets (KD) of the $^{6}H_{15/2}$ multiplet for the DyBz15C5 complex (**3.3**). 210

Table 5-26 Computed crystal field parameters for the four models of the complex using the CASSCF/RASSI wavefunctions for the DyBz15C5 complex (**3.3**). 212

Table 5-27 *Ab Initio* computed eight low-lying Kramers doublet energies (cm^{-1}) and g-tensors of each Kramers doublets in DydiBz15C5 complex (**3.6**). 213

Table 5-28 SINGLE_ANISO computed crystal field parameters for DydiBz complex (**3.6**) ... 214

List of Figures

Figure 1.1 Different types of magnetic interactions: a) paramagnetic, b) antiferromagnetic, c) ferromagnetic and d) ferrimagnetic. 3

Figure 1.2 Plot of M *vs.* H for a paramagnetic material..... 5

Figure 1.3 Example of a typical hysteresis loop where the saturation magnetization (Ms), coercive field (Hc), and remnant magnetization (Mr) are shown. 7

F**igure 1.4** χ_M *vs* T for paramagnetic, ferromagnetic, and antiferromagnetic responses. 7

Figure 1.5 A plot of $\chi_M T$ *vs* T for paramagnetic, ferromagnetic, and antiferromagnetic responses. 8

Figure 1.6 A plot of χ_M^{-1} *vs* T for paramagnetic, ferromagnetic, and antiferromagnetic responses 9

Figure 1.7 Left, the molecular structure of Mn_{12} (**1.1**) 15

Figure 1.8 Representation of the perturbations that split the degeneracy of the 4*f* configurations of a Dy(III) ion..... 17

Figure 1.9 Molecular structure of $[Bu_4N]$ $[Pc_2Tb]$ (**1.2**) where Pc^{2-} = phthalocyanine. 19

Figure 1.10 The shape of the electron density distribution of Ln(III) ions: oblate (as Ce(III); Pr(III); Nd(III); Tb(III); Dy(III); and Ho(III)), prolate (Pm(III); Sm(III); Er(III); Tm(III); and Yb(III)), spherical as Gd(III) 20

Figure 1.11 Top: The oblate-prolate model: characterization of low- and high-energy configurations of oblate electron density distribution in an axial ligand field (left), and (right) a prolate electron density distribution in an equatorial ligand field.. 21

Figure 1.12 Left, the molecular structure of [Dy(bbpen)Br] (1.4), where the equatorial plane of pentagonal. bipyramidal coordination sphere is highlighted.[32] Right, the crystal structure of the $[Dy(O^tBu)_2(py)_5][BPh_4]$ complex (**1.5**).....22

Figure 1.13 Crystal structure of $[Dy(Cp^{ttt})_2][B(C_6F_5)_4]$ (**1.7**). Hydrogen atoms and $[B(C_6F_5)_4]^-$ counter anion are omitted for clarity.....23

Figure 1.14 Crystal structure of $[(Cp^{iPr5})Dy(Cp^*)]^+$ (**1.8**).....24

Figure 1.15 A typical χ'' *vs* T plot for an SMM showing the frequency-dependence of the magnetization.....25

Figure 1.16 A plot of the natural logarithm of the relaxation time, $\ln(\tau_c)$, *vs* 1/T, where the energy barrier can be determined.....27

Figure 1.17 M *vs* H of plot for Mn_{12} showing steps in the hysteresis loops due to QTM 29

Figure 1.18 Top: luminescence spectra of select Ln(III) ions in the visible (left) and near-infrared (right); bottom: splitting of the electronic energy levels of the lanthanides.....31

Figure 1.19 Jablonski diagram showing the absorption-energy transfer-emission mechanism from an organic ligand sensitizer to a *4f* ion.....32

Figure 1.20 Forster and Dexter energy transfer mechanisms 33

Figure 1.21 Luminescence spectrum of $Na[Dy(DOTA)(H_2O)]\cdot 4H_2O$ (**1.10**) at room temperature irradiated at 365 nm. Inset: magnification of the $^4F_{9/2} \rightarrow {}^6H_{15/2}$ transitions.....37

Figure 1.22 Top: magnification of $^4F_{9/2} \rightarrow {}^6H_{11/2}$ transition at 14 K. Multi-Gaussian function fit components that resulting from the first (cyan shadow) and second (pink shadow) $^4F_{9/2}$ Stark sublevel to the $^6H_{15/2}$ multiplet. 38

Figure 1.23 Molecular structures of 12C4,15C5, and 18C6. 41

Figure 1.24 Eu(II) complex with 12-crown-4 (left), with 15-crown-5 (middle), and with 18-crown-6 (right) 43

Figure 1.25 Molecular structure of $[Co(12C4)_2](I_3)2(12C4)$ (**1.12**) 44

Figure 1.26 Two half sandwich Dy(III) complexes with 12-crown-4 (**1.13**) (left) and 15-crown-5 (**1.14**) (right) macrocycles 44

Figure 1.27 $[Ln(18C6)(NCS)_3]$ (**1.15**) complexes (Ln(III) = Eu, Tb) 46

Figure 1.28 Left, the half-sandwich complex $Dy(12C4)(NO_3)_3$ (**1.16**); center, the double-decker complex $Dy(12C4)_2(CH_3CN)(ClO_4)_3$ (**1.17**); right, the dinuclear complex, $Dy_2(12C4)_2(ClO_4)_4(OH)_2(H_2O)_2$ (**1.18**) 47

Figure 1.29 The two crystallographically independent molecules in the unit cell of the double-decker complex $[Dy(12C4)(15C5)(CH_3CN)][Dy\ (12C4)(15C5)]_2(CH_3CN)_2(ClO_4)$ (**1.19**). 48

Figure 1.30 Molecular structure of Dy(III) complexes with 18-crown-6. $[Dy(18C6)(NO_3)_2]ClO_4$ (**1.20**, left) and $[Dy(18C6)(NO_3)_2]BPh_4$ (**1.21**, right), that differ in the dihedral angles of their apical bidentate nitrate groups 48

Figure 1.31 Molecular structure of $[Ln(NO_3)_3(18C6)]$ (**1.22**) with 18-crown-6 (left) and $[Ln(NO_3)_3(1,10\text{-diaza}18C6)]$ (**1.23**) with 1,10-diaza-18-crown-6 (right) where Ln(III) = Ce(III); Pr(III); and Nd(III)) 49

Figure 1.32 $[Ln(18C6)(Cl_4Cat)(NO_3)]$ (**1.24**) (Ln=La, Ce, Nd, Gd, Tb, Dy (left) and $[La(18C6)(Br_4Cat)(NO_3)]$ complex (right) 50

Figure 1.33 Ln(III) complexes $[Ln(H_2O)_3(18C6)](ClO_4)_3$ (**1.25**) 51

Figure 1.34 Three classes of a) diformyl- or b) diketo- and c) diamine precursors 56

Figure 1.35 Molecular structures of mono- and heterodinuclear complexes (**1.26** to **1.28**) prepared from [1 + 1] asymmetric compartmental Schiff-base ligands. 56

Figure 1.36 Molecular structure of the heterodinuclear Eu-Na complex (**1.29**), comprising of the asymmetric [1 + 1] compartmental Schiff-base ligand. 57

Figure 1.37 Structure of the N1, N3-bis(3-methoxysalicylidene)diethylenetriamine (H_2valdien) ligand 58

Figure 1.38 Molecular structures of [Dy_2] complexes with dichloroacetate (Cl_2CHCOO^-) and hexafluoroacac ($CF_3COCHCOCF_3^-$) terminal ligands 60

Figure 1.39 Molecular structures of theN_3O_2, N_5 and db-N_3O_3 macrocycles 61

Figure 1.40 Molecular structure of the dual compartmental Schiff-base macrocycle **H_2L_3** 62

Figure 1.41 Crystal structure of $[Ln_2Na_2(L_3)_2(Cl)_4(MeOH)]\cdot xH_2O$, (**1.31**-**1.33**). 62

Figure 2.1 Molecular structures of the sandwich complexes $[Sm(15C5)_2]^{3+}$ (**2.1**, left)[102] and $[Ln(P_c)_2]^-$ (**2.2**, right) 66

Figure 2.2 Half- and pseudo sandwich topologies of Dy(III) complexes of 12C4 (**2.3**), and 15C5 (**2.4**) 67

Figure 2.3 Molecular structure of the asymmetric unit of $\{[Dy(NO_3)_3(H_2O)_2(CH_3OH)]\cdot(15C5)\}_n$ (**2.5**) with appropriate atomic numbering scheme 74

Figure 2.4 Coordination geometry of the Dy1 and Dy2 cations superimposed on an idealized capped square antiprism for Dy1 and Dy2 in complex **2.5** 75

Figure 2.5 Crystal packing of **2.5** 76

Figure 2.6 Molecular structure of $\{[Tb(NO_3)_3(H_2O)_2(CH_3OH)]\cdot(15C5)\}_n$ (**2.6**) with appropriate atomic numbering scheme 76

Figure 2.7 Coordination geometry of Tb(III) cation superimposed on an idealized capped square antiprism for **2.6** 77

Figure 2.8 (a), Crystal packing of **2.6** showing the 1-D chains that are connected via inter-chain H-bonds to afford 2D-sheets in the *bc* plane; b) view down the *b*-axis of the unit cell showing the large channels between the 2-D layers.....78

Figure 2.9 Plots of $\chi_M T$ *vs*. T for **2.5** (left) and **2.6** (right) in a 0.1 T field, from 5-300 K 79

Figure 2.10 Plots of $1/\chi$ *vs*. T for **2.5** (left) and **2.6** (right) from 5-300 K. The black line is a best-fit to the Curie-Weiss law, giving Weiss constants θ of -3.95 K and -1.86 K.....79

Figure 2.11 Plot of χ'' *vs* field for **2.5** at 2 K, displaying selected data from experimental frequencies measured between 30 and 1000 Hz 80

Figure 2.12 Out-of-phase χ''_M *vs* T plot for **2.5** in a 2000 Oe applied field from 3-10 K 81

Figure 2.13 Out-of-phase χ''_M *vs* frequency plot for **2.5** in a 2000 Oe applied field: (a) from 9.8 to 4.3 K and (b) from 4.3 to 2.2 K 81

Figure 2.14 (a to d) out-of-phase χ''_M *vs* T plots for 2.5 in 300, 800, 1000 and 2000 Oe applied fields from 3-10 K, showing the resolution of two maxima as QTMs are supressed.....82

Figure 2.15 Modeled out-of-phase χ'' vs in-phase χ' in a 2000 Oe applied field with kinks in the Cole−Cole semicircles clearly visible below 5 K (the lines represent the fit to the Cole−Cole equations) (left). Fit of the data to the Arrhenius model (right) 83

Figure 2.16 Plot of χ'' *vs* T for **2.6** in zero dc field below 15 K, showing no frequency dependence in χ'', consistent with rapid relaxation of the magnetization.....86

Figure 2.17 Crystallographic models used for the *ab initio* calculations of **2.5** and **2.6** comprising of a $[Ln(III)(NO_3)_3(OH_2)_2(MeOH)]$ core for the small model (Model 2) and the additional two hydrogen bonded benzo-15C5 molecules for the larger model (Model 1).....86

Figure 2.18 (a, b) Plots of KD1± and KD2± for Dy1 and Dy2 in **2.5** showing the average matrix elements of the transition moments between states (numbers next to arrows) for Model 1, long

basis set. Red arrows are used for thermally activated transitions, blue arrows for ground and excited QTM, and green arrows for Orbach spin−lattice relaxation. (c, d) Crystal structures of Dy1 and Dy2 coordination spheres showing the H-bonded crown ethers and the main magnetic axes of the ground (green) and first-excited (purple) KDs 87

Figure 2.19 (a, b) Emission spectra excited at 365 nm for complexes **2.6** (a) and **2.5** (b). Excitation spectra associated with the 480 nm emission (**2.6**, c) and the 573 nm emission (**2.5**, d) 89

Figure 2.20 (a) High-resolution emission spectrum (15 K) excited at 365 nm for 2.5. (b) Multi-Gaussian function envelope fit..... 92

Figure 3.1 Molecular structure of $[Eu(Bz15C5)_2](ClO_4)_2$ (**3.1**)..... 97

Figure 3.2 Molecular structure of $\{[Eu(CH_3OH)_6(H_2O)_2][PMo_{12}O_{40}]\}\cdot(Bz15C5)_2\cdot(CH_3CN)_2\cdot(CH_3OH)_2$ (**3.2**)..... 97

Figure 3.3 (a) Molecular structure of $[Dy(OH)_8]^{3+}$(benzo-15C5)$_3$ (3.3) showing H-bonding interactions as blue dashed lines; (b) space filling model highlighting the encapsulation of the Dy(III) ion inside the molecular cavity formed by the benzo-15C5 macrocycles..... 107

Figure 3.4 Coordination geometry of the Dy(III) cation superimposed on an idealized square antiprism (dark green) in **3.3**..... 108

Figure 3.5 Molecular structure of $[Dy(OH_2)_8](Bz15C5)_3\cdot(ClO_4)_3$ (**3.3**) showing H-bonding interactions to the perchlorate anions as blue dashed lines..... 109

Figure 3.6 Molecular structures of **3.4** and **3.5** with the appropriate atomic labelling schemes. 110

Figure 3.7 Coordination geometry of the Tb(III) ion in **3.4** (left) and the Gd(III) ion in **3.5** (right) superimposed on an idealized muffin polyhedron (dark green). 112

Figure 3.8 View of the crystal packing of **3.4** showing H-bonding interactions to the perchlorate anions as blue dashed lines. 113

Figure 3.9 Plots of $\chi_M T$ *vs*. T shown as red, black, and green circles for complexes **3.3-3.5** respectively in a field of 0.1 T from 2 - 300 K. 114

Figure 3.10 Plot of χ''_M *vs* temperature for **3.3** in zero dc field below 8 K, showing the frequency dependence to the susceptibility and lack of resolved maxima 115

Figure 3.11 Plot of χ''_M *vs* T for **3.3** in applied dc fields of 300, 800 and 1500 Oe, below 15 K. 116

Figure 3.12 (a and b) χ'_M and χ''_M *vs*. temperature in 800 Oe applied dc field, below 10 K; (c) out-of-phase χ'' *vs*. frequency in 800 Oe applied field from 3–10 K; (d) modelled out-of-phase χ'' versus in-phase χ' plot in 800 Oe applied field with kinks in the Cole–Cole semicircles visible above 3.5 K 117

Figure 3.13 Temperature dependence of the relaxation time for **3.3** at "high" (6.0 - 4.5 K) temperature, blue circles – domain A and "low" (4.0 – 2.9 K) temperatures, red and green circles – domains B and C respectively, under a static field of 800 Oe 120

Figure 3.14 Model 1 with three hydrogen bound benzo-15C5 molecules and three perchlorate counter anions; (b) Model 2 including only the coordinating water molecules.[106] 121

Figure 3.15 (a) View down the non-crystallographic 4-fold axis of the $[Dy(OH_2)_8]^{2+}$ cation of 3.3 showing the anisotropy axes for the three lowest Kramers doublets, the ground state (KD1), the ±1 excited state (KD2) and ±2 excited state (KD3) for Model 1 (long basis set); (b) lowest three Kramers doublets and the *ab initio* computed relaxation mechanism for Model 1 (long basis set) of DyBz(3.3). 122

Figure 3.16 Excitation spectrum acquired at 14 K for **3.3** monitored at 440 nm. 124

Figure 3.17 (a and b) Magnification of the $^4F_{9/2}$ - $^6H_{15/2}$ transition at 12 K and excited at 365 nm. Multi-Gaussian functions envelope fit (circles) and the components arising from the (orange shadow) first and (purple shadow) second $^4F_{9/2}$ Stark sublevels to the $^6H_{15/2}$ multiplet; (c) fit regular residual plot; (d) schematic diagram of the radiative transitions between the Stark sublevels of the $^4F_{9/2}$ and $^6H_{15/2}$ multiplets of the Dy(III) ion.....124

Figure 3.18 (a) Emission and (b) excitation spectra for **3.3** acquired at 300 K (blue lines) and at 14 K (black lines) for 3.3 excited at 365 nm and monitored at 574 nm respectively.....125

Figure 3.19 Emission decay curve (300 K) for **3.3** monitored at 577 nm and excited at 390 nm. 126

Figure 3.20 Molecular structure of **3.6** with the appropriate atomic numbering scheme. H-bonds are shown as blue dashed lines (top). Molecular structure of **3.6** highlighting intermolecular H-bonds as blue dashed lines (bottom). 130

Figure 3.21 Coordination geometry of the Dy(III) cation superimposed on an idealized muffin polyhedron (grey).....132

Figure 3.22 Spacefill representation of the crystal packing of **3.6** showing two the two enclosed $[Dy(H_2O)_9]^{3+}$ cations and the hydrocarbon fence around them.....133

Figure 3.23 Temperature dependence of the $\chi_M T$ product for **3.6**. Solid red lines are the calculated $\chi_M T$ product from the *ab initio* studies. 134

Figure 3.24 Field dependence of Magnetization (M) for **3.6** at different temperatures (left) and plot of reduced magnetization ($M/N\mu_B$) *vs.* HT^{-1} for **3.6** at applied fields of 1–7 T and in the 2–5 K temperature range (right). 135

Figure 3.25 Temperature dependence of the in-phase $\chi'T$ product (top) and out-of-phase χ'' (bottom) ac susceptibility signals of DydiBz15C5 (**3.6**) in a 2 Oe field oscillating at the indicated frequencies 136

Figure 3.26 Out-of-phase susceptibility *vs* frequency plots for **3.6** in various applied dc fields at 5 K. 137

Figure 3.27 Out-phase (χ'') component of the magnetic susceptibility *vs* frequency, under 1000 Oe applied dc field (left). Cole-Cole plot for **3.6** obtained using the ac susceptibility data under 1000 Oe applied dc field (right).. 137

Figure 3.28 Field dependence of magnetic relaxation time τ^{-1} at 5 K (left) and temperature dependence of τ^{-1} under 1000 Oe applied filed (right) 138

Figure 3.29 Magnetization blocking barrier for the Dy site in **3.6** 141

Figure 3.30 (top) Emission spectra of 3.6 acquired at 297 K and 15 K for excitation at 284 nm. (bottom) Excitation spectra of 3.6 acquired at 297 K and 15 K and monitored at (green line) 411/432 nm (orange line) and 573 nm. Self-absorptions between the $^6H_{15/2}$ level and the (1) $^4D_{7/2}$, (2) $^6P_{7/2}$, $^4M_{15/2}$ and (3) $^6P_{5/2}$ excited states. 142

Figure 3.31 (top) Time-resolved emission spectra (starting delay = 5×10^{-5} s) excited at 284 nm and acquired at 15 K and 300 K. (bottom) Emission decay curves excited at 280 nm, monitored at 440 nm and acquired at distinct temperature values 144

Figure 4.1 Crystal structure of $[Dy_2Na_2(L_3)_2(Cl)_4(MeOH)]\cdot 2H_2O$ (**4.1**).. 149

Figure 4.2 Molecular structure of $[CuNa(L_{3b})ClCH_3OH]H_2O$ (**4.2**). 159

Figure 4.3 Coordination geometry of the Cu(II) cation superimposed on an idealized spherical square pyramidal polyhedron (purple) in **4.2** (left) and coordination geometry of Na(I) cation superimposed on an idealized pentagonal pyramidal polyhedron (purple) (right). 161

Figure 4.4 Crystal packing of **4.2**.....162

Figure 4.5 Molecular structure of [ZnNa(L_{3b})(CH_3COO)(CH_3OH)] (**4.3**).....163

Figure 4.6 Coordination geometry of the Zn(II) cation superimposed on an idealized spherical square pyramidal polyhedron shown in grey for **4.3** (left) and coordination geometry of Na^+ cation superimposed on an idealized capped trigonal prism polyhedron shown in purple for **4.3** (right). 164

Figure 4.7 Crystal packing of **4.3**. View down the *b*-axis of the unit cell 165

Figure 4.8 Molecular structure of [$Mn_3Na_2(L_3)_2(CH_3COO)_4$]·4$CH_3OH$·$H_2O$ (**4.4**).....166

Figure 4.9 Coordination geometry of the Mn1, Mn2, and Mn3 cations in complex **4.4**, superimposed on an idealized octahedron. 168

Figure 4.10 Coordination geometry of Na(I) cation superimposed on an idealized pentagonal pyramid polyhedron shown in gray for **4.4**.....168

Figure 4.11 The crystal packing of the Mn_3 trimers in complex **4.4** showing H-bonding interactions as blue dashed lines. H-atoms are omitted for clarity; (left) view down the *a*-axis of the unit cell highlighting the butterfly shaped topology; (right) view down the *b*-axis of the unit cell showing the ribbons with the solvent molecules in the void space in between the ribbons.169

Figure 4.12 Left, plot of $1/\chi$ *vs* T for **4.2**; the blue line is the best fit to the Curie Weiss plot for *S* = ½ and g = 2.0); right, plot of χ_MT *vs* T for **4.2** at 0.1 T from 2 – 300 K.....170

Figure 4.13 Plot of M *vs* H for **4.2** at 2, 5 and 7 K (left). The dashed lines represent a fit to the Brillouin function for g = 2 and *S* = ½. Plot of the reduced magnetization *vs* H for **4.2** (right), with a fit to the Brillouin function (dashed lines) for g = 2 and *S* = 1/2. 171

Figure 4.14 X-band EPR spectrum of complex **4.2** at room temperature.....171

Figure 4.15 Plot of χ_MT *vs*. T for the Mn_3 trimer, 4.4 in a field of 0.1 T from 2 - 300 K.....172

Figure 4.16 The 1*J* model used to fit the experimental dc magnetic data in PHI. 173

Figure 4.17 Molecular structure of the Mn_3 trimer **4.9**. 173

Figure 4.18 Plot of M *vs* H for complex **4.4** at 2K. 174

Figure 4.19 Molecular structures of complexes **4.5** and **4.6** with selected labelling 175

Figure 4.20 Molecular structure of Ce(III) complex (**4.10**) of the methyl analogue 176

Figure 4.21 Coordination geometry of Dy(III) (top left), Tb(III) (top right), Er(III) (bottom left), and Gd(III) (bottom right) ions superimposed on an idealized spherical capped square antiprismatic polyhedra (shown in grey) for complexes **4.5**-**4.8**. 178

Figure 4.22 View of the crystal packing of 4.5 down the *b*-axis of the unit cell showing hydrogen bonding interactions and the shortest intermolecular Dy···Dy distances as blue (top) and green dashed lines (bottom) respectively. 179

Figure 4.23 Crystal packing of **4.6**. View down the *b*-axis of the unit cell showing the H-bonds as blue dashed lines. 180

Figure 4.24 Plots of $\chi_M T$ *vs*. T shown as red, black, grey and green circles for complexes **4.5** - **4.8** respectively in a field of 0.1 T from 2 - 300 K. 181

Figure 4.25 Field dependence of the magnetization, i.e. plots of M *vs* T for complexes (**4.5**, left) and (**4.6**, right). 182

Figure 4.26 Temperature dependence of the in-phase $\chi'T$ (left) and out-of-phase χ'' (right) component of the ac susceptibility for the Dy(III) complex **4.5** in a 2 Oe field, oscillating at the indicated frequencies. 183

Figure 4.27 Out-of-phase susceptibility for complex **4.5** in various applied dc fields at 2 K ... 183

Figure 4.28 In phase χ' (left) and out-phase (χ'') (right) components of the magnetic susceptibility *vs*. frequency for complex **4.5** under a 400 Oe applied dc field 184

Figure 4.29 Cole-Cole plot for complex **4.5** obtained from the ac susceptibility data collected under a 400 Oe applied dc field 185

Figure 4.30 Arrhenius plot for the Dy(III) complex **4.5** under a 400 Oe applied dc field. 185

Figure 4.31 χ' *vs*. T (left) and χ'' *vs*. T (right) plots for the Tb(III) complex **4.6** in zero dc field. 186

Figure 5.1 Plots of the stationary states within the $^{6}H_{15/2}$ multiplet of Dy1 in (**2.5**) using the different structural models and basis sets 203

Figure 5.2 Plots of the stationary states within the $^{6}H_{15/2}$ multiplet of Dy2 in (**2.5**) using the different structural models and basis sets 204

Figure 5.3 Plots of the stationary states within the $^{7}F_{6}$ multiplet of Tb(III) in (**2.6**) using the different structural models and basis sets 205

Figure 5.4 Main magnetic axes and relaxation pathways for Model 1 (short basis set) for DyBz complex (**3.3**). 211

Figure 5.5 Main magnetic axes and relaxation pathways for Model 1 (long basis set) for DyBz complex (**3.3**). 211

Figure 5.6 Main magnetic axes and relaxation pathways for Model 2 (short basis set) for the DyBz15C5 complex (**3.3**). 211

Figure 5.7 Main magnetic axes and relaxation pathways for Model 2 (long basis set) for the DyBz15C5 complex (**3.3**). 212

List of Schemes

Scheme 1.1 Synthesis of the bis[2-(*o*-hydroxyphenoxy)ethyl]ether and dibenzo-18-crown-6....40

Scheme 4.1 Preparation of the $\mathbf{L_3}'$ 149

Scheme 4.2 Preparation of $\mathbf{H_2L_3}$ 150

List of abbreviations

Å	Angstrom
AC	Alternating current
C	Curie constant
°C	Degrees Celsius
$CDCl_3$	Deuterated chloroform
CH_3CN	Acetonitrile
CSM	Continuous shape measurement
cm^{-1}	Wavenumbers
DCM	Dichloromethane
DC	Direct current
D	Zero-Field splitting parameter
DMSO	Dimethyl sulfoxide
EnT	Energy transfer
EPR	Electron paramagnetic resonance
ESI-MS	Electrospray Ionization Mass Spectrometry
F	Fluorescence emission
g	Lande g-factor (proportionality constant)
g	Grams
H	Applied magnetic field
hr	Hour(s)
$\hat{H}$	Spin hamiltonian

H_c	Coercive magnetic field
Hz	Hertz
IR	Infrared
ISC	Intersystem crossing
J	Total angular momentum
k	Boltzmann constant (1.380×10^{-23} J K^{-1})
K	Kelvin
KDs	Kramers doublets
L	Ligand
L	Total orbital angular momentum
Ln	Lanthanide
M	Magnetization
M	Metal
MeOH	Methanol
m/z	Mass/Charge Ratio
M_S	Spin quantum number
M_r	Remnant magnetization
min	Minutes
mL	Milliliters
mmol	Millimole
M_S	Magnetic saturation (emu G mol^{-1})

N	Avogadro's number (6.022×10^{23} mol^{-1})
NaOH	Sodium hydroxide
NMR	Nuclear magnetic resonance
nm	Nanometer
P	Phosphorescence emission
P_c	Phthalocyanine
QTM	Quantum tunnelling of the magnetization
r.t.	Room temperature
S	Total spin angular momentum
s	Spin angular momentum
S_0	Ground singlet state
S_1	Excited singlet state
SQUID	Superconducting quantum interference device
SOC	Spin-orbit coupling
SMM	Single molecule magnet
str	Stretch
T	Temperature
T	Tesla
T_1	Excited triplet state
TA-QTM	Thermally assisted quantum tunneling of magnetization
T_C	Curie temperature

T_N	Neel temperature
U_{eff}	Effective energy barrier
UV	Ultraviolet
χ	Magnetic susceptibility
χ'	Real, or in phase susceptibility
χ''	Imaginary, or out of phase susceptibility
χ_M	Molar magnetic susceptibility
ZFS	Zero-field splitting
μ_β	Bohr magneton
λ	Wavelength
Λ	Spin–orbit coupling constant
Δ	Crystal field splitting

1 Introduction

1.1 Molecular magnetism

Magnetism is a physical phenomenon whose origins and applications can be traced to ancient times when magnets and their properties were described and recorded in Greece, China, and India, as far back as 2500 years ago. For many decades, technological advancements and the evolution of much scientific knowledge has been linked closely to magnets and their uses. However, despite the broad ranging applications of classical magnets to-date, they do suffer from some drawbacks that include chemical reactivity and/or high energy consumption. These disadvantages may be overcome by studying and developing new families of magnetic materials and in this respect, alongside the traditional area of bulk magnets, the field of molecular magnetism is now emerging as one of the most fascinating and rapidly growing interdisciplinary areas of modern day research.[1] However, in order to develop and study new classes of molecule-based magnets, it is important to first grasp a solid understanding of the basic fundamentals of classical magnetism.

1.1.1 Origin of magnetism

The magnetic properties of an atom or molecule arise from the movement of electrons in an orbit around the nucleus and the spin of electrons around their axes, defined as orbital angular momentum *L*, and spin angular momentum *S*, respectively. Furthermore, the observed magnetic behavior of an atom or molecule arises from its total magnetic moment which is defined as the sum of the individual magnetic moments of its constituent electrons. The magnetic properties of a material are classified by two types of behaviour: (i) Diamagnetism, which refers to the presence of paired electrons oriented antiparallel, resulting in a net magnetic moment of zero result diamagnetic materials are not attracted

towards an applied magnetic field, and (ii) Paramagnetism, which refers to the presence of unpaired electrons, resulting in a non-zero magnetic moment. Such materials are attracted towards an applied magnetic field and their magnetic behavior is temperature dependant.[2–4] The magnetic properties of any material (diamagnetic or paramagnetic) can be determined by measuring the magnetic susceptibility χ, which is defined as the magnetic response of a compound towards an applied magnetic field as described by (Eqn. 1.1):

$$\chi = \partial \mathrm{M} / \partial \mathrm{H} \qquad \textbf{Eqn. 1.1}$$

Where M is the magnetization and H is the magnetic field strength.

As long as the applied magnetic field is small, the change of the magnetization as a function of the field is constant and thus χ can be defined by (Eqn. 1.2):

$$\chi = M/H \qquad \textbf{Eqn. 1.2}$$

From the above relationship the units of χ are dimensionless however, χ is most commonly converted to, or expressed as molar susceptibility designated as χ_M (or often just χ) which has units of $cm^3 \cdot mol^{-1}$.[5,6] The total molar susceptibility of a material is the sum of the diamagnetic and paramagnetic susceptibilities χ_D and χ_P, (Eqn. 1.3):

$$\chi_\mathrm{M} = \chi_D + \chi_P \qquad \textbf{Eqn. 1.3}$$

The value of χ_P is always positive, while the value of χ_D is negative. When χ_P dominates, the material is paramagnetic, while if χ_D dominates the material will be diamagnetic.[5,7]

1.1.1.1 Classes of magnetic materials

It is important to mention that the interactions between the spins of substances can lead to different classes of magnetic interactions that are defined as paramagnetic, ferromagnetic, antiferromagnetic, and ferrimagnetic, (Figure 1.1).[4]

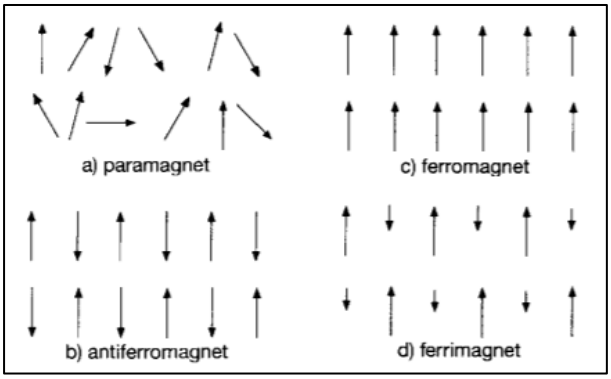

Figure 1.1 Different types of magnetic interactions: a) paramagnetic, b) antiferromagnetic, c) ferromagnetic and d) ferrimagnetic.[8] Reproduced with permission from reference 8.

Paramagnetic behavior - In a paramagnetic material, the spin of each electron is randomly oriented and is not affected by its surrounding neighbor's spins. When an external magnetic field is applied, random thermal motion can be overcome, and the spins of the unpaired electrons align parallel or antiparallel to the applied field. However, once this field is removed, the paramagnetic material loses any magnetization as the spins randomize once again due to thermal motion. The molar susceptibility of a paramagnetic material is both field and temperature dependent.[2–4] The temperature dependence of the molar susceptibility of a paramagnetic material is described by the Curie law, (Eqn. 1.4):

$$\chi_M = \frac{Ng^2\mu_B^2}{3kT} S(S+1) \qquad \textbf{Eqn. 1.4}$$

Where *N* is Avogadro's number (6.022×10^{23} mol^{-1}), g is the Lande g-factor, or proportionality constant, μ_β is the Bohr magneton (9.274×10^{-24} J T^{-1}), k is the Boltzmann constant (1.380×10^{-23} J K^{-1}), T is the temperature, *S* is the spin quantum number and C is the Curie constant (emu·K mol^{-1}), which is defined in (Eqn.1.5):

$$C = \frac{Ng^2\mu_B^2}{3K}S(S+1) \qquad \textbf{Eqn. 1.5}$$

So, by replacing $\frac{Ng^2\mu_B^2}{3K}S(S+1)$ with C**,** Eqn. 1.5 simplifies to:

$$\chi_M = \frac{C}{T} \qquad \textbf{Eqn. 1.6}$$

Eqn 1.6 is typically referred to as Curie law, where it is apparent that for a paramagnetic material, the molar susceptibility χ_M, changes inversely with temperature T. As mentioned previously, the molar susceptibility of a paramagnetic material is also field dependent, so at low magnetic fields the magnetization increases with increasing magnetic field H, resulting in a linear relationship between M and H, (Eqn 1.7) (Figure 1.2):

$$M = \chi H \qquad \textbf{Eqn. 1.7}$$

However, at higher magnetic fields, the magnetization M increases and reaches a saturation value M_S, as the strength of magnetic field increases when T is constant, (Eqn. 1.8):

$$M_s = \mu_B N_A S g \qquad \textbf{Eqn. 1.8}$$

where M_S is the magnetic saturation (emu·G·mol^{-1}) that depends on the value of S.

$$\frac{M_s}{N_A\mu_B} = Sg = 2\ n/2 = n \qquad \textbf{Eqn. 1.9}$$

Where $Ms/N_A\mu_\beta$ is the reduced magnetization and n is the number of unpaired electrons in the system.[4,7]

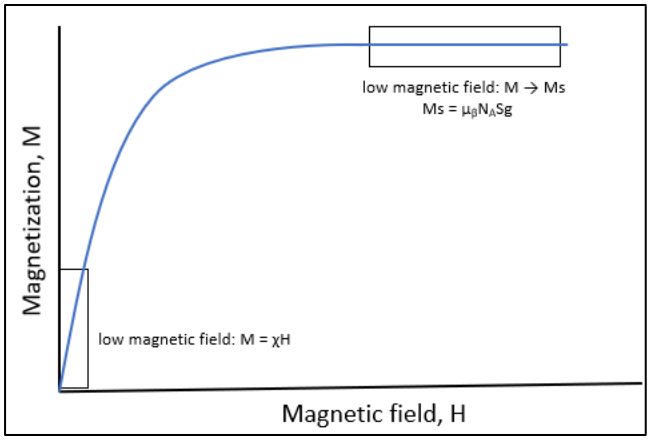

Figure 1.2 Plot of M *vs.* H for a paramagnetic material. Redrawn from reference 7.

Ferromagnets, antiferromagnets and ferrimagnets - These properties are commonly exhibited by bulk materials and can be attributed to long-range ordering of magnetic spins. Ferromagnets, antiferromagnets, and ferrimagnets tend to behave like paramagnets and lose their long-range ordering above a specific temperature referred to as the Néel temperature, T_N for antiferromagnets, and the Curie temperature, T_C for ferromagnets and ferrimagnets, since above these temperatures, the thermal energy is sufficient to overcome any magnetic ordering.[5] Ferromagnetic interactions occur when adjacent spins are aligned parallel with respect to each other. Generally, the interactions within a ferromagnet are divided into domains and each domain has a net magnetization in the absence of a magnetic field. However, the magnetic moments of all the domains are randomly oriented giving a net magnetization of zero. Below the ordering temperature, when a magnetic field is applied, it stimulates the displacement of the domain walls. This leads to the formation of a new domain structure and the magnetic moments of the domains start aligning along the direction of the magnetic field. When the applied field is subsequently removed, the ferromagnet remains magnetized.[3] For antiferromagnets, below the Neel temperature T_N,

the unpaired spins are aligned in an antiparallel arrangement, cancelling each other out when a magnetic field is applied. Finally, ferrimagnets like antiferromagnets have adjacent spins which are aligned antiparallel, however, in contrast, their have different magnitudes and thus do not completely cancel each other out, resulting in a net magnetic moment. The molecular interactions in ferrimagnets like ferromagnets are divided into domains, which give rise to zero magnetization in the absence of a magnetic field, but below their ordering temperature they can be magnetized in the presence of an applied magnetic field.

One of the classical features of magnets is that they exhibit hysteresis, which is a phenomenon that is always associated with the spontaneous magnetization of ferromagnetic or ferrimagnetic materials after application and subsequent removal of a magnetic field. A typical hysteresis loop is generated by measuring the magnetization of the sample as a function of an applied magnetic field. When such a magnetic field is applied, the magnetization of the sample reaches saturation M_S, then when the magnetic field is turned off, the magnetization does not reduce to zero but remains as the remnant magnetization M_r. So, the sample remains magnetised in zero magnetic field. For these compounds, a second applied magnetic field known as the coercive field H_c is required to switch the magnetization in the opposite direction and reduce it to zero (Figure 1.3).[9] Depending on the nature of their hysteresis loops, two types of magnets can be classified: (i) hard magnets (H_c >100 Oe) with broad loops, which can be magnetized sufficiently to saturation by applying a magnetic field and that remain magnetized when the magnetic field is removed and (ii) soft magnets (H_c < 10 Oe) with narrow loops, that can be temporarily magnetized, but lose their magnetization once the magnetic field is removed.[5,8,9] The parameters H_c, M_s, and M_r are used to determine the potential

applications of a magnet. For example, hard magnets are used for magnetic data storage, while soft magnets are used for alternating current motors.[8]

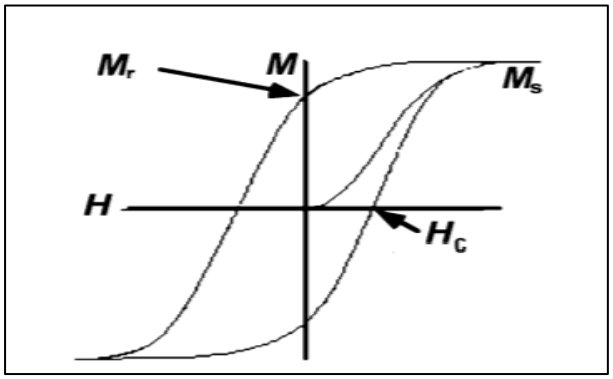

Figure 1.3 Example of a typical hysteresis loop where the saturation magnetization (Ms), coercive field (Hc), and remnant magnetization (Mr) are shown. Reproduced with permission from reference 8.

It is difficult to determine the type of magnetic interactions (paramagnetic, ferromagnetic, or antiferromagnetic) in a sample by plotting the molar susceptibility (χ_M) *vs* temperature, because for both ferro- and antiferromagnetic interactions, the molar susceptibility increases as the temperature decreases (Figure 1.4).

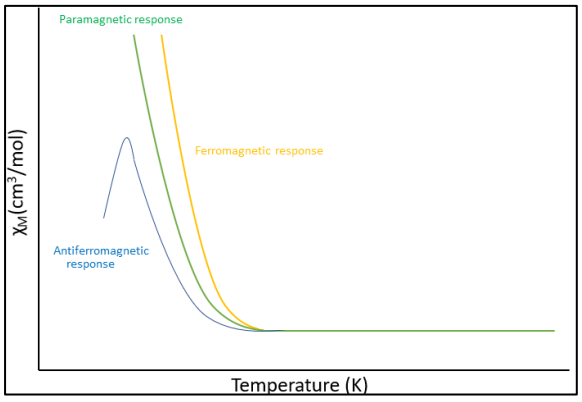

Figure 1.4 χ_M *vs* T for paramagnetic, ferromagnetic, and antiferromagnetic responses. Redrawn from reference 10.

A plot of the susceptibility temperature product, $\chi_M T$ ($cm^3\ mol^{-1}\ K$), *vs* temperature, T (K), is therefore more commonly used to characterize magnetic interactions, where the responses for the different types of magnetic interactions are shown in (Figure 1.5).

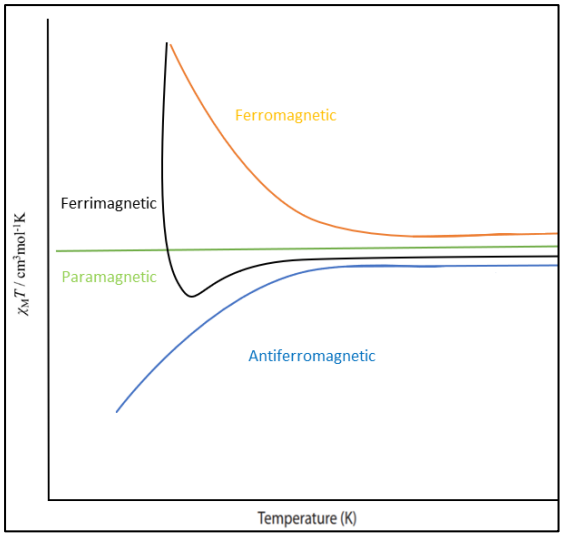

Figure 1.5 A plot of $\chi_M T$ *vs* T for paramagnetic, ferromagnetic, and antiferromagnetic responses. Redrawn from reference 10.

Examining this plot, we can see that for a true paramagnetic material, $\chi_M T$ is independent of T, as defined by the Curie law however, changes in $\chi_M T$ *vs* T are observed for ferromagnetic, antiferromagnetic, and ferrimagnetic materials. In the case of a ferromagnetic material, $\chi_M T$ increases as the temperature decreases. Conversely, for an antiferromagnetic compound, $\chi_M T$ decreases as the temperature decreases and for a ferrimagnetic material, as the temperature is lowered, a decrease in $\chi_M T$ is first observed due to the presence of short range antiferromagnetic interactions between adjacent spins, followed by an increase in $\chi_M T$ due to the presence of longer range interactions.[10,11] For many paramagnets the presence of weak, short range ferro- or antiferromagnetic

interactions lead to deviations from classical Curie behaviour and as such, these systems are better described by the Curie-Weiss law (Eqn. 1.10):

$$\chi_M = \frac{C}{T - \theta} \qquad \textbf{Eqn. 1.10}$$

Where θ is the Weiss constant.

By plotting inverse molar susceptibility (χ_M^{-1}) *vs* temperature, a true paramagnetic material displays a linear relationship as described by the Curie law, where C is equal to the slope of the line and θ is zero. However, the presence of weakly ferromagnetic and antiferromagnetic interactions in such materials results in a significant deviation from this linear relationship at low temperature. In this context, a downward shift and positive Weiss constant is indicative of dominant ferromagnetic interactions and an upward deviation, accompanied by a negative Weiss constant is characteristic of antiferromagnetic interactions, (Figure 1.6).

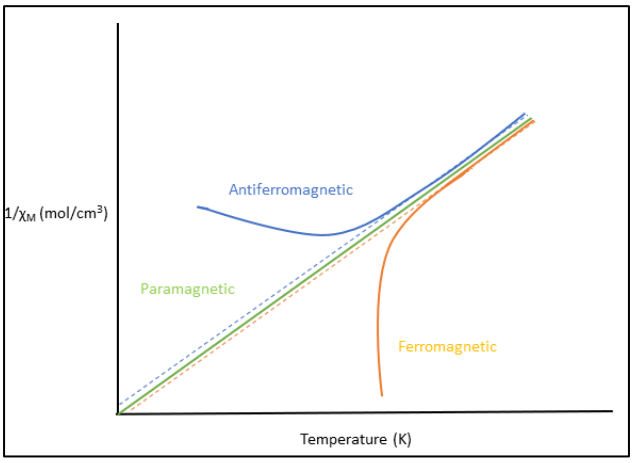

Figure 1.6 A plot of χ_M^{-1} *vs* T for paramagnetic, ferromagnetic, and antiferromagnetic responses. Redrawn from reference 10.

As apparent from (Figure 1.6), at high temperatures all three systems display a linear relationship because the thermal energy is large enough to overcome the energy of

the weak magnetic interactions. It should also be noted that these systems differ from true ferromagnets or antiferromagnets since the magnetic exchange interactions in these systems are short range and only occur in the presence of an applied magnetic field, that in contrast to the bulk systems are not retained when the applied magnetic field is removed.

1.1.2 Molecule-based magnets

For thousands of years magnets comprising of metals (e.g. Fe, Co, Ni, Gd), or their oxides (e.g. CrO_2, Fe_3O_4) have been known, where the magnetic properties arise due to interactions between their unpaired electrons which reside in *d*- or *f*-orbitals. The formation of these materials typically requires high temperature metallurgical methods. Over the past three decades, a new field in magnetism has emerged where magnets built from molecular precursors that have unpaired electron(s) residing in *d*-, *f*- and/or *p*-orbitals have been developed. Molecule-based magnets have a diverse range of molecular structures and show many of the same properties as the metal or atom-based magnets which include remnant magnetization and hysteresis with saturation. In addition, molecule-based magnets typically have high solubilities in organic solvents, they can be formed by low temperature synthetic chemistry methodologies and can be structurally modified to posses a combination of physical properties allowing novel, dual property systems to be prepared and studied such as magnetic conductors. The first molecular compound recognized to display magnetic properties was $[Fe(C_5Me_5)_2]^{\cdot+}[TCNE]^{\cdot-}$ (TCNE = tetracyanoethylene), which is an ionic salt that exhibits ferromagnetic ordering below its Curie temperature T_c = 4.8 K.[12–14] Interestingly, it has a H_c of 1.3 kOe at 2 K, which is greater than the values required for magnetic data storage, demonstrating that molecule-based compounds could potentially lend themselves to magnetic data storage applications.[12–14]

Since this initial discovery, several families of molecule-based magnets have been developed and studied over the past 30 years which include Prussian blue analogues which have afforded the first room temperature molecule-based magnets,[1] 2- and 3-D oxalate bridged complexes,[8] spin crossover complexes,[14] organic radical based systems,[8] as well as single molecule and single chain magnets.[14] Given that this thesis concerns the discovery of new single molecule magnets (SMMs), the second half of this review is focused on the fundamental concepts behind the development and study of SMMs.

1.1.3 Single molecule magnets (SMMs)

SMMs are typically coordination complexes of paramagnetic metal ions that can be magnetized when a magnetic field is applied and then when the magnetic field is switched off, they stay magnetized for a period of time below a specific temperature known as their blocking temperature, T_B.[15] Above this temperature SMMs typically behave as paramagnets without any retention of their magnetization.[16] SMMs are different from the previously described classical magnets in that their magnetic properties are attributed to individual molecules that are isolated magnetically from each other and hence there is typically no interaction between them.[15] Indeed, the presence of no significant intermolecular interactions is a pre-requisite for the observation of SMM properties.[17] Interestingly, SMMs display many similar physical properties to classical magnets that include retention of their magnetization and the observation of hysteresis loops, as well as new phenomena such as quantum tunnelling of magnetization (QTM).[15]

1.1.3.1 Transition metal or 3*d*-SMMs

For a molecule to behave as a SMM it must display slow relaxation of magnetization blow its blocking temperature. This property arises due to a combination of a large spin ground state (S) and a significant negative magnetic anisotropy (D),[17] which enables the molecule to be more easily magnetized in one direction, often referred to as the easy axis of magnetization.[18] This combination affords an energy barrier U to reversal of the magnetisation where the height of the energy barrier is equal to $S^2\,|D|$, or $(S^2\ 1/4)|D|$ for integer and half-integer spins respectively.[17] The presence of the energy barrier slows down the relaxation of the magnetization at low temperature, when the magnetic field is removed, so that the magnetization of the molecule does not reduce to zero immediately and a hysteresis loop is often observed, which is similar to the behavior displayed by bulk ferro- and ferri-magnets.[7] For 3*d*-based SMMs, the presence of significant magnetic anisotropy splits the M_S microstates of the molecules with a total S spin ground state in zero magnetic field.[19] This splitting is termed "zero-field splitting" (ZFS) and the size of this splitting is determined by D or the ZFS parameter, which defines the magnetic anisotropy. D can be positive or negative and this determines which M_S state will be the lowest in energy in zero magnetic field.[7] For example, for a complex with S =10, with a positive D, the M_S = 0 state will be the lowest in energy so it will cost no energy to lose the direction of the spin in going from M_S = +10 to M_S = 0 and hence no magnetization will be achieved. In contrast however, when D is negative, the two $M_S = \pm 10$ states will lie lowest in energy and the system will possess a bistable ground state necessary for SMM behaviour.[20] When such a complex is cooled to low temperature in zero magnetic field, then the $M_S = \pm 10$ states will be populated equally and no magnetization will be observed.

However, when the complex is cooled in the presence of an applied magnetic field, then depending on the direction of the applied field, the $M_S = \pm 10$ states will not be populated equally, and a net magnetization will be observed. Moreover, if the magnetic field is then turned off, for the population of the $M_S = \pm 10$ states to become equal via classical magnetic relaxation, then the electrons must have sufficient thermal energy to overcome the energy barrier (U).

Relaxation of the magnetization in SMMs typically occurs via two relaxation processes. The first process collectively known as the Orbach process is the classical relaxation process where the spins relax back thermally over the energy barrier which typically dominates at higher temperatures. At low temperature however, a second class of relaxation processes known as quantum tunneling mechanisms (QTM) are dominant since at low temperatures most of the electrons do not have sufficient thermal energy to overcome the energy barrier.[7] When both thermal relaxation and QTM contribute to the magnetic relaxation, the process is referred to as the quantum-assisted thermal regime, while when the magnetization is relaxing entirely by QTM below a certain temperature then this is referred to as the quantum regime.[15] The two relaxation processes follow first-order kinetics as described in (Eqn. 1.11):

$$\tau_c = \tau_0 \exp(\Delta E \,/\, KT) \qquad \textbf{Eqn. 1.11}$$

Where τ_c is the temperature dependent relaxation time. For thermal relaxation where $\Delta E = U$, the pre-exponential factor or relaxation rate τ_0 is temperature dependent, while for quantum tunneling mechanisms, τ_0 is temperature independent.

For quantum tunneling processes, instead of climbing over the energy barrier, electrons in degenerate M_S states transfer from one side of the barrier to the other by

tunnelling directly through it, leading to a rapid decrease in the magnetization of the sample that results in the observation of steps in the experimental hysteresis loops.[7,21] To reduce this process, a small magnetic field is typically applied in the ac measurements to remove the degeneracy of the *M*s states and suppress QTMs. In recent years it has become apparent that many observations of Ln-SMMs are inconsistent with solely Orbach and/or QTM and that other processes such as two-phonon Raman relaxation and ground state (pseudo-) doublet direct relaxation can also be operational. Hence the study of such alternative relaxation process is a matter of active discussion that is currently ongoing in the field of SMMs.

The first SMM reported is commonly referred to as Mn_{12} and is a mixed valence cluster of stoichiometry $[Mn_{12}O_{12}(OAc)_{16}(H_2O)_4]$ (**1.1**) (Figure 1.7).[22] Mn_{12} is comprised of 12 manganese ions, the four internal Mn(IV) ions are surrounded by an external crown of eight Mn(III) ions, and all are bridged by acetate linkers. Mn_{12} has spin ground state, $S = 10$ that arises from the spins of the eight Mn(III) ions ($S = 2$) all aligned antiparallel to the spins of the four Mn(IV) ions ($S = 3/2$). The zero-field splitting parameter D of Mn_{12} was found to be - 0.5 cm^{-1}, that splits the degeneracy of the M_S states of the ground state S, as shown in (Figure 1.7), which are then in turn separated by the energy barrier, U. For this system, the energy barrier U to spin reversal = $S^2|D| = 10^2 |-0.5\ cm^{-1}| = 50\ cm^{-1}$. Mn_{12} thus displays slow relaxation of magnetization below its blocking temperature of 10 K.[20]

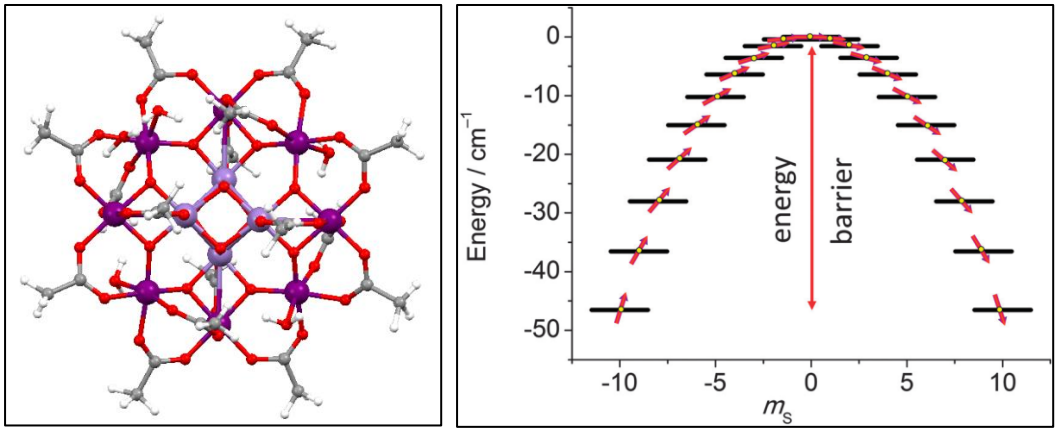

Figure 1.7 Left, the molecular structure of Mn_{12} (**1.1**).[23] Colour code: red = O, dark purple = Mn(III), light purple = Mn(IV), gray = C, white = H. Right, the energy level diagram for $[Mn_{12}O_{12}(OAc)_{16}(H_2O)_4]$ with S = 10 and D = -0.5 cm^{-1}. In the absence of an applied magnetic field, the ground state splits into 21 M_S microstates, (2S + 1 = 2(10) + 1= 21), with M_S values ranging from -10 to +10. Reproduced with permission from reference 18.

After the initial discovery of Mn_{12}, research in this field focused on designing large transition metal clusters in order to increase the energy barrier and blocking temperatures of SMMs for practical applications. However, in most cases small or no energy barriers were observed since although many of these clusters had high spin ground states, they often lacked significant magnetic anisotropy. Over the past decade research attention has shifted to the employment of lanthanide ions for the assembly of SMMs, since *4f* ions such as Dy(III) and Tb(III) have both a large number of unpaired electrons and a large intrinsic magnetic anisotropy due to spin orbit coupling.[24]

1.1.3.2 Lanthanide-based SMMs

4f ions such as Dy(III) are suitable candidates for the design of SMMs due to their large strong spin-orbit coupling and large magnetic moments which can in turn be further enhanced by crystal field effects.[25] In *4f*-based SMMs the energy barrier originates from

the splitting of M_J microstates by the crystal field.[7] The electronic structures of Ln(III) ions are quite different from the aforementioned *3d* metals. For Ln(III) ions, the degeneracy of the 4*f* configuration is lifted by several factors including inter-electronic repulsive interactions, spin–orbit coupling and the crystal-field (Zeeman effects). Inter-electronic repulsions whose origin is the electrostatic interactions between the *4f* electrons splits the degeneracy of the 4*f* configurations into $(2S + 1)L$ terms with a separation of 104 cm^{-1}. Each term is then split further into *J*-levels with a separation of 103 cm^{-1} via spin-orbit coupling, which is the interaction between the electron spin and the magnetic field generated by the movement of the electrons around the nucleus. These *J*-levels are the free ion levels that are described by the term symbols $^{(2S+1)}L_J$ where *L* is the total orbital angular momentum, [*S (L= 0), P (L= 1), D (L= 2), F (L= 3), G (L= 4), H (L= 5), I (L= 6)]; J* is the total angular momentum of the *f* electrons ($J = |L+S|, \ldots, |L - S|$); *S* is the total spin orbital angular momentum and (2*S*+1) is the total spin multiplicity. Then, when a *4f* ion is coordinated to a ligand in a complex, each *J*-level ($^{(2S+1)}L_J$) is split further by crystal field effects due to interactions between the electrons of the ligand and the *4f* electrons, affording sub-levels or microstates also known as Stark levels, where $m_J = +J, \ldots, -J$, with a separation of 102 cm^{-1} (Figure 1.8).[7,26,27]

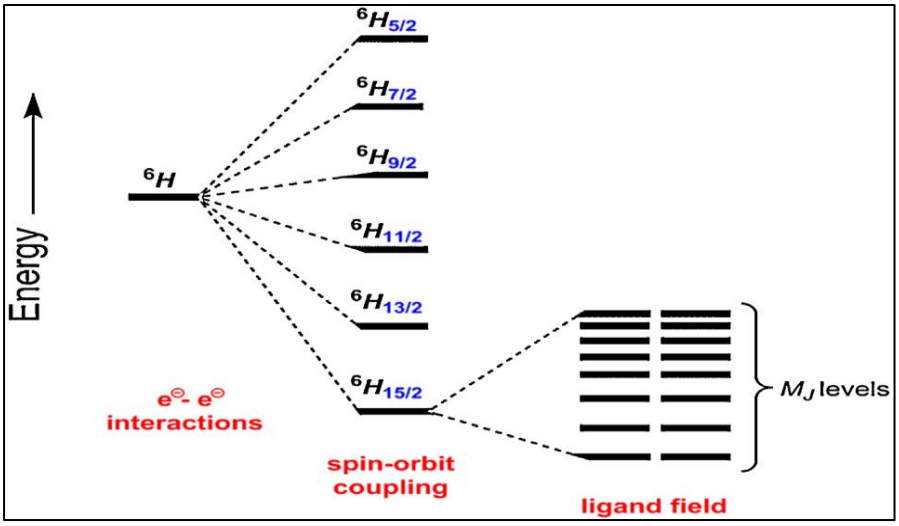

Figure 1.8 Representation of the perturbations that split the degeneracy of the 4*f* configurations of a Dy(III) ion. Reproduced with permission from reference 15.

It should be noted that at high temperature, the spin–orbit coupling constant, ʎ, is greater than the crystal field splitting Δ, thus the crystal field splitting is neglected and then the magnetic properties of lanthanide complexes are like those of the free ion.

For Ln(III) ions, Hund's rules of maximum multiplicity are used to determine the *S*, *L*, and *J* values for the free ion. For example, a Dy(III) ion with a $4f^9$ configuration has $S = 5/2$, $L = 5$, $J = |L+S|, \ldots, |L - S|$, thus $J = 15/2$, 13/2, 11/2, 9/2, 7/2, and 5/2. As a consequence, for Dy(III), its term symbols are $^6H_{5/2}$, $^6H_{7/2}$, $^6H_{9/2}$, $^6H_{11/2}$, $^6H_{13/2}$, and $^6H_{15/2}$ (Figure 1.8).

Depending on Hund's rules for more than a half-filled shell, the largest *J* term is the ground state, thus for Dy(III), $^6H_{15/2}$ is the ground term and the rest are excited states (^6H_J), so the $^6H_{13/2}$ is the first excited term and these terms will be separated by $ʎJ(J+1)$. For Dy(III) this will be $15ʎ/2$ and then the separation between $^6H_{15/2}$ and $^6H_{13/2}$ will be 13,640 cm^{-1}, thus even at room temperature, the excited terms will not be thermally

populated. In contrast, for Eu(III) the ground term is $^7F_0$ and the spin and orbital moments are equal and opposite. Despite this there are six unpaired electrons, the magnetic moment is zero because in this case the separation between the $^7F_0$ ground term and the first exited term $^7F_1$ is 236 cm^{-1}, thus the magnetism of Eu(III) complexes results from both the ground and low-lying excited states.

At temperatures < 50 K, the crystal field effect (Δ) becomes non-negligible and splits the degeneracy of the M_J microstates of the $^{(2S+1)}L_J$ ground term into Kramers doublets (KDs), each corresponding to $\pm M_J$, where the separation of these microstates depends on the coordination geometry of the complex. As a consequence, like bistable transition metal clusters, Ln(III) complexes with an odd number of *f*-electrons such as Dy(III) will provide non-integer *J* Kramers doublets (KDs) which are also bistable, regardless of their ligand field symmetry and often behave as mononuclear single molecule magnets. In contrast, Ln(III) ions with integer *J* values e.g.Tb(III) will have M_J microstates from $-J$ to $+J$ including $M_J = 0$, and if $M_J = 0$ is the ground or the low-lying excited state, then rapid relaxation will occur and no SMM properties are observed.

The most commonly employed *4f* ions for the design of SMMs are the late Ln(III) ions with a $4f^n$ electronic configuration, where n >7. These ions include Dy(III), Tb(III), Ho(III), Er(III), and Yb(III), since they all have larger *J* values, when compared to the early Ln(III) ions.[7,28] Dy and Tb ions are the most commonly used because as previously mentioned, Dy(III) is a Kramers ion, it has significant magnetic anisotropy and a large energy gap between its ground and first excited M_J state. In contrast, Tb(III) is more anisotropic and has a larger energy gap between its first and excited M_J compared to Dy(III), but it has an odd number of electrons and is therefore not a non-Kramers ion,

which means that its microstates can be singlets or doublets. Hence for Tb(III) ions, its microstates will be bistable only if the ligand field has sufficient axial symmetry. Er(III), and Yb(III) are both Kramers ions, while like Tb(III), Ho(III) is also a non-Kramers ion.[15,28]

In 2003 *4f* ions entered the field of SMMs with the report of slow relaxation of magnetization in double-decker phthalocyanine (Pc) complexes $[Bu_4N]$ $[Pc_2Ln]$ (**1.2**), where Ln(III) = Dy and Tb (Figure 1.9).[29] In these systems, the Ln(III) ion is sandwiched between two $[Pc]^{2-}$ ligands, where it coordinated to four nitrogen atoms from each ligand in an eight-coordinate, square antiprismatic geometry.[28] Since this discovery, a considerable number of Ln-SMMs have been reported as homometallic 4*f* or heterometallic 3*d*-4*f* complexes from a broad range of ligands.[15]

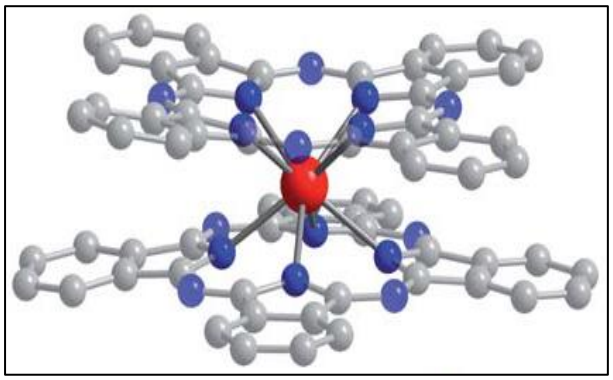

Figure 1.9 Molecular structure of $[Bu_4N]$ $[Pc_2Tb]$ (**1.2**) where Pc^{2-} = phthalocyanine. Hydrogen atoms are omitted for clarity. Colour code: red = Tb(III), blue = N, gray = C. Reproduced with permission from reference 30.

After this discovery it became apparent that the ligand field plays an important role in enhancing the anisotropy of *4f*-based SMMs. In 2011, Long *et al.,* proposed an electrostatic model describing the relationship between the electrostatic effects of the

ligand field and the distribution of the electron density of Ln(III) ions. He proposed that this relationship should play a crucial role in determining the orientation of the anisotropy axes in Ln-SMMs.[15,31] In this respect, the distribution of the electron density of a Ln(III) ion can be oblate (equatorially expanded), prolate (axially elongated), or isotropic (spherical) as shown in Figure 1.10.

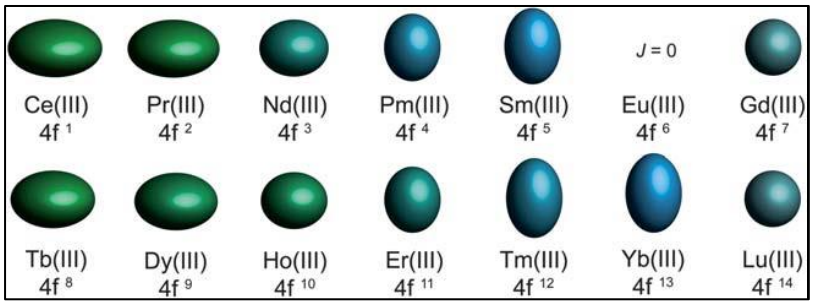

Figure 1.10 The shape of the electron density distribution of Ln(III) ions: oblate (as Ce(III); Pr(III); Nd(III); Tb(III); Dy(III); and Ho(III)), prolate (Pm(III); Sm(III); Er(III); Tm(III); and Yb(III)), spherical as Gd(III). Reproduced with permission from reference 30.

Based on the shape of the electron density of a particular *4f* ion, the ligand field can be optimised by carefully choosing organic ligands that maximize the magnetic anisotropy. For ions with oblate electron density, this can be enhanced by employing axial field ligands. For example, in a sandwich type D_{4d} geometry, the electron density is concentrated above and below the *xy* plane that leads to the orientations of the M_J microstates parallel and antiparallel to the molecular axis, which reduces repulsive interactions between their lone pairs and the electron density of the *4f* ion. In contrast, the magnetic anisotropy of prolate ions can be enhanced be employing equatorially-coordinating ligand fields that serve to minimize charge contact between the electron density of the *4f* ion and the ligand field (Figure 1.11).[30]

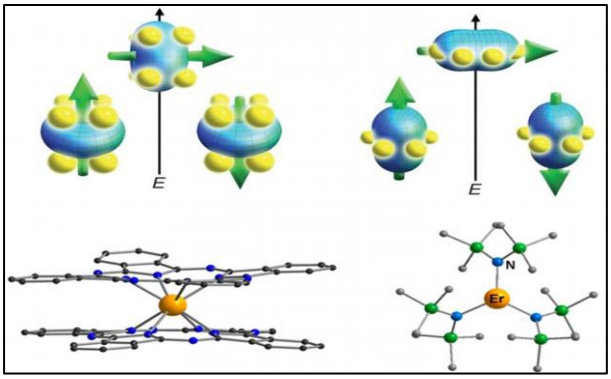

Figure 1.11 Top: The oblate-prolate model: characterization of low- and high-energy configurations of oblate electron density distribution in an axial ligand field (left), and (right) a prolate electron density distribution in an equatorial ligand field. With two examples (bottom) the $[Bu_4N]$ $[Pc_2Ln]$ complex (**1.2**) (left) and $Er[N(\text{-}SiMe_3)_2]_3$ (**1.3**), (right). Reproduced with permission from reference 31.

In addition to the local D_{4d} square antiprismatic symmetry that is found in sandwich type complexes,[31] pentagonal bipyramidal geometry that confers local D_{5h} symmetry on *4f* ions has also been shown to also significantly enhance axial anisotropy of Dy(III) complexes, giving rise to large energy barriers and higher blocking temperatures.[32,33] The Pilkington group were one of the first to report and study the magnetic properties of Dy(III) complexes with pentagonal bipyramidal geometry. Since then other coordination complexes with Dy(III) ions in D_{5h} geometries have been reported with very high energy barriers. For example, the [Dy(bbpen)Br] complex (**1.4**), (where bbpen = N,N′-bis(2-hydroxybenzyl)-N,N′-bis(2-methylpyridyl)ethylenediamine) was reported by Tong *et al.* to have a high effective energy barrier of over 1000 K,[31] and a second complex $[Dy(O^tBu)_2(py)_5][BPh_4]$ (**1.5**), prepared by Zhang *et al.* has a U_{eff} = 1815K (Figure 1.12).[32,33] In these complexes the high energy barriers are attributed to the presence of two negatively charged ligands on the single axis of the coordination sphere which serves to

significantly enhance the axial anisotropy of the oblate shaped *4f* ion. The energy barriers in both of these complexes are accompanied by hysteresis loops of up to 14 K.[32,33]

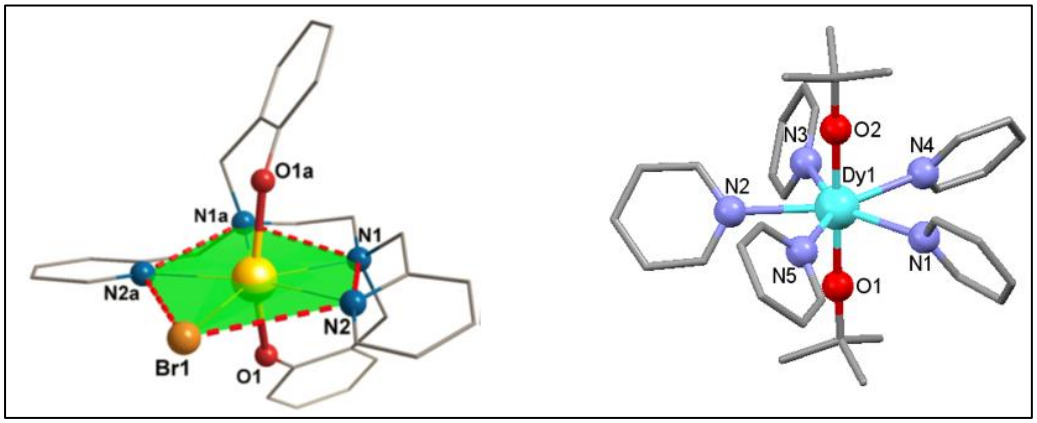

Figure 1.12 Left, the molecular structure of [Dy(bbpen)Br] (**1.4**), where the equatorial plane of bipyramidal coordination sphere is highlighted.[32] Reproduced with permission from Right pentagonal reference 32. Right, the crystal structure of the $[Dy(O^tBu)_2(py)_5][BPh_4]$ complex (**1.5**). Hydrogen atoms and counter anion are omitted for clarity.[33] Colour code: gray = C, blue = N, red = O, yellow (left) or aqua blue (right) = Dy(III) and orange = Br.

Since the initial discovery of SMMs, the major challenge has been always to increase the temperature at which these molecules display slow relaxation of their magnetization, for practical applications. The highest blocking temperature reported to-date for a *3d* cluster based SMM is 4.5 K with a U_{eff} of 86.4 K for $[Mn^{III}_6O_2(Et\text{-}sao)_6(O_2CPh(Me)_2)_2(EtOH)_6]$ (**1.6**) ($Et\text{-}saoH_2$ = 2-hydroxyphenylpropanone oxime), which has stood for over a decade.[34] In sharp contrast, for the *4f*-based systems, blocking temperatures above the liquid-helium regime have now been achieved,[29,35–37] the best of which are for $[Dy(Cp^{ttt})_2][B(C_6F_5)_4]$ (**1.7**), (where Cp^{ttt} = 1,2,4-tri(tertbutyl)cyclopentadienide), which has an effective energy barrier of 1837 K and a blocking temperature of 60 K, that is very close to liquid nitrogen.[38,39] In this complex, the

4f metal is coordinated between two aromatic π-ligands and is close to linear geometry, which is theoretically reported to be the best for enhancing the axial anisotropy of oblate Dy(III) ions. However, *4f* complexes with this geometry are not easy to realize synthetically given that 4*f* ions typically prefer much higher coordination geometries.[38,39]

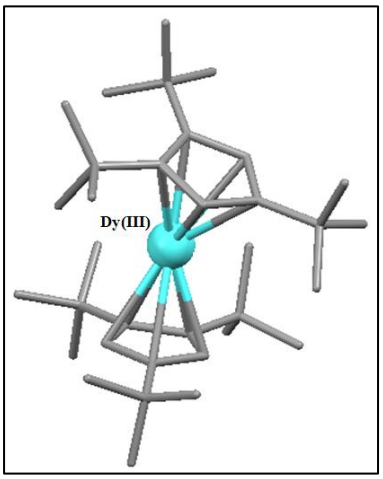

Figure 1.13 Crystal structure of $[Dy(Cp^{ttt})_2]$ $[B(C_6F_5)_4]$ (**1.7**). Hydrogen atoms and $[B(C_6F_5)_4]^-$ counter anion are omitted for clarity.[38] Colour code: light gray = C, aqua blue = Dy(III).

More recently, Layfield *et al.*, improved on this result by reporting a Dy metallocene cation $[(Cp^{iPr5})Dy(Cp^*)]^+$(**1.8**), (where Cp^{iPr5} = penta-iso-propylcyclopentadienyl, Cp* = pentamethylcyclopentadienyl) (Figure 1.14), that displays magnetic hysteresis above liquid-nitrogen temperatures with an effective energy barrier (U_{eff}) of 1541cm^{-1}.[40] In this study the electrostatic model was used to stabilize the oblate Dy(III) ion density so the dysprosium metallocene cation was prepared with sufficiently bulky cyclopentadienyl substituents to prevent coordination of equatorial ligands and obtain a complex with a wide Cp-Dy-Cp angle and short Dy-Cp bond distances, that served to further increase the axiality of the crystal field. Analysis of the X-ray crystal structure of this complex revealed that the Dy-Cp* and Dy-Cp^{iPr5} distances are 2.296(1) and 2.284(1) Å respectively, i.e.

shorter than those of the analogous $[Dy(Cp^{ttt})_2]^+$ complex (**1.7**). Hence, the crystal field in the latter complex $[(Cp^{iPr5})Dy(Cp^*)]^+$ (**1.8**) is more axial than in the $[Dy(Cp^{ttt})_2]^+$ (**1.7**) which affords an SMM with magnetic hysteresis up to 80 K, representing a major advance in the field of *4f*-SMMs.

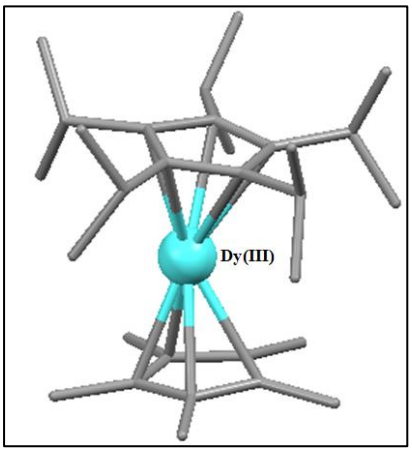

Figure 1.14 Crystal structure of $[(Cp^{iPr5})Dy(Cp^*)]^+$ (**1.8**). Hydrogen atoms and $[B(C_6F_5)_4]^-$ counter anion are omitted for clarity.[40] Colour code: carbon = gray, aqua blue = Dy(III).

1.1.3.3 The detection of SMM behaviour

SMM behavior is typically characterized by carrying out a series of direct current (dc) and alternating current (ac) magnetic susceptibility measurements using a SQUID magnetometer (Superconducting Quantum Interference Device), or a PPMS (Physical Property Magnetic System).[15] Ac magnetic measurements are performed at liquid-helium temperatures in order to measure the magnetic susceptibility or magnetic response (χ) of a compound to an ac magnetic field.[15] The ac measurement is often carried out in both in zero and in the presence of a small applied static dc magnetic field.[7] Ac measurements provide information about the magnetization dynamics of the sample and in this case, the susceptibility χ from this measurement is split into the in-phase real component χ', and the

out-of-phase, imaginary component χ″. In a typical ac measurement, a small oscillating ac field of ca. 2-5 Oe is applied to the sample at a specific frequency ω, and the in-phase χ′, and out-of-phase χ″ components of the ac susceptibility are measured relative to the ac field. At high temperature SMMs behave as paramagnets and follow perfectly the oscillating magnetic field giving rise to in-phase susceptibility, χ′, where the value of χ′ is similar to the sample susceptibility χ. In contrast, at low temperature when the sample relaxes slowly, the spin cannot follow perfectly the oscillating magnetic field (due to the presence of the energy barrier) and an out-of-phase χ″ signal is observed, indicating the onset of slow magnetic relaxation, characteristic of an SMM. At low temperature (below the T_B), the maximum in χ″ is frequency dependent since only at low ac frequencies does the spin have enough time to follow the oscillating field, while at higher frequencies the spin is not able to relax back fast enough (due to the energy barrier) to keep in phase with the ac field and hence χ″ is non-zero (Figure 1.15).[7]

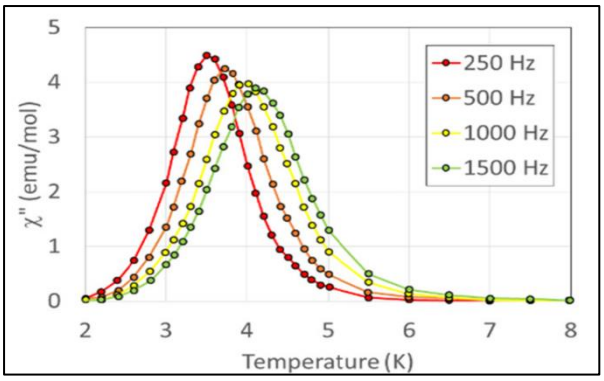

Figure 1.15 A typical χ″ *vs* T plot for an SMM showing the frequency-dependence of the magnetization. Reproduced with permission from reference 7.

The relaxation of the magnetization can be quantified from the ac data. The blocking temperature can also be determined for a specific ac frequency directly from a

plot of χ'' *vs* T as the temperature at which χ'' reaches its maximum value. From ac susceptibility measurements the energy barrier U and the relaxation rate, or pre-exponential factor τ_0 can be determined.[41] Firstly, the temperature dependent relaxation parameter τ_c is determined from a plot of χ'' *vs* frequency, where $\tau_c = 1/2\pi\,\upsilon$ and υ is the frequency corresponding to the maxima of the χ'' signal. Then, the energy barrier, U (K) and the relaxation rate τ_0, can subsequently be determined by plotting first the values of τ_c *vs* T and then fitting the resulting experimental data to the Arrhenius equation (Eqn. 1.12):[15]

$$\tau_c = \tau_o \exp^{\frac{U_{eff}}{kT}} \qquad \textbf{Eqn. 1.12}$$

By finding the natural logarithm of Arrhenius equation (Eqn. 1.13):

$$ln(\tau_c) = \frac{U_{eff}}{K} \cdot \frac{1}{T} + ln\,(\tau_0) \qquad \textbf{Eqn. 1.13}$$

Then, plotting ln(τc) *vs* 1/T for multiple frequencies, the energy barrier U (K) is determined from the slope of the line and the y-intercept gives the value of ln τ_0, from which the relaxation rate, also referred to as the pre-exponential factor τ_0, can be determined, (Figure 1.16).[7]

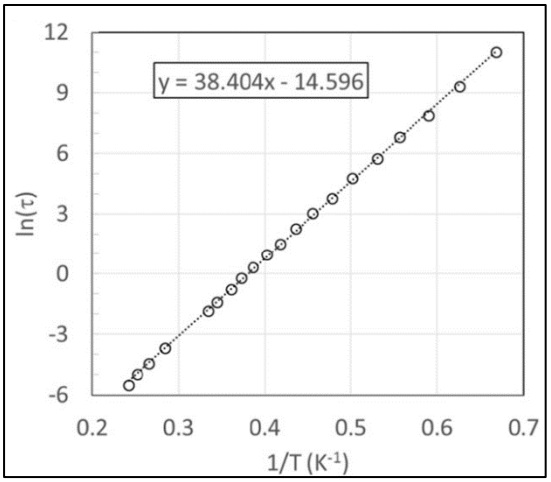

Figure 1.16 A plot of the natural logarithm of the relaxation time, ln(τ_c), *vs* 1/T, where the energy barrier can be determined (the lines are the fitting data and the circles are the experimental). Reproduced with permission from reference 7.

In some cases, well resolved maxima in χ'' cannot be observed in the zero-field ac data because of the existence of quantum tunneling processes which reduce the effective energy barrier to relaxation. In these cases, the maximum in χ'' is often resolved by applying a small static dc magnetic field to reduce the quantum tunneling by removing the degeneracy of the M_S or M_J microstates where the tunneling occurs, so that the energies of the microstates are shifted slightly which helps to minimize the difference between the true energy barrier U that occurs in zero field and the effective energy barrier U_{eff} calculated in a non-zero static field.

In systems where no maximum in χ'' is observed because there are several relaxation processes, or in other cases where there is overlap between relaxation processes that makes identification of the maxima in χ'' difficult,[7] the dynamics of the magnetization (energy barrier, relaxation time) can be investigated through Cole–Cole plots.[39] In this respect χ'' is plotted against χ' for a series of different frequencies, and χ'' *vs* frequency for a fixed temperature. For

a single relaxation process the χ'' and χ' susceptibilities follow the Cole-Cole equations **1.14** and **1.15**:

$$\chi' = \chi_s + \frac{(\chi_T - \chi_s)}{2}\ 1 - \frac{\sin h\ [(1-\alpha)\ln(\omega\tau_C)]}{\cosh(1-\alpha)\ \ln(\omega\tau_C)] + \cos[1/2(1-\alpha)\pi]} \qquad \textbf{Eqn. 1.14}$$

$$\chi'' = \frac{(\chi_T - \chi_s)}{2}\ 1 - \frac{\sin\ [(1/2(1-\alpha)\pi]}{\cosh(1-\alpha)\ \ln(\omega\tau_C)] + \cos[1/2(1-\alpha)\pi]} \qquad \textbf{Eqn. 1.15}$$

The χ'' *vs* χ' plot can then be modelled at a specific temperature using these equations, where χ_S is the adiabatic susceptibility, χ_T is the isothermal susceptibility, and α is a measure of the dispersivity of relaxation times known also as the Cole-Cole parameter that takes values of 0 to 1, where a value of zero indicates a single relaxation pathway with one relaxation time and a value closer to 1 corresponds to an infinite number of relaxation pathways, characterized by an infinite number of relaxation times.[11] Then as previously described, the values of τ_c can be used to determine the τ_0 and the energy barrier by plotting $\ln(\tau_c)$ *vs* 1/T. When multiple relaxation processes are active, a two-component equation, (Eqn. 1.14 and Eqn. 1.15) is typically used with two sets of different parameters τ_{c1} and τ_{c2} and α_1 and α_2, etc.[7]

Beside ac susceptibility measurements, the magnetic properties of SMMs can also be studied by dc susceptibility measurements, where the field dependence of the magnetization is measured. In this case at very low temperature, typically below 5 K, a dc field is increased from 0 to +H (high field typically 7 T) in order to saturate the magnetisation and then the field is cycled from +H to −H and back to +H to check for hysteresis. If a hysteresis loop is observed in the M *vs* H plot, then this indicates the

retention of magnetisation when the field is removed (M ≠ 0) and thus confirms the presence of an energy barrier towards magnetic relaxation.[15] The highest temperature at which a hysteresis loop opens up in plots of *M* versus *H* is typically defined as the magnetic blocking temperature (T_B). It is also noteworthy to mention that the value of T_B depends on the sweep rate of the magnetic field and thus comparing the blocking temperatures of various SMMs should be done with some caution.[28] As explained previously, bulk magnets also exhibit hysteresis loops however, the hysteresis loops for SMMs arise from an energy barrier towards reorientation of their magnetization and typically exhibit steps that arise from quantum tunneling (Figure 1.17), all of which are properties attributed a single molecule and not a bulk material.[7]

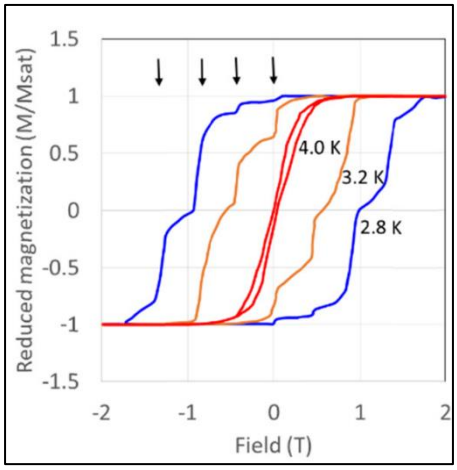

Figure 1.17 M *vs* H of plot for Mn_{12} showing steps in the hysteresis loops due to QTM. Reproduced with permission from reference 7.

Despite the broad applications of classical magnets, new families of molecule-based magnets have been discovered over recent years that have expanded the future promise and potential technological applications of magnetic materials. For researchers in this field, the goal is not to replace classical magnets, but to use molecular chemistry to

design complementary systems that display new properties that present new opportunities for applications. SMMs are currently being pursued as qubits for quantum computers, where their low operating temperatures are not so problematic. However, for more conventional data storage, their operating temperatures still need to be increased and their magnetic properties must be physically addressable and interfaced with real world devices. Two important challenges currently at the forefront of this field are: (i) to employ suitable ligand systems to optimise the crystal field of Ln-based SMMs to realize compounds with higher blocking temperatures that are more suitable for practical applications and (ii) to develop dual property SMMs whose magnetic properties can ultimately be addressed via the application of a second physical property such as light or a redox switch. Both of these challenges are currently being addressed by current research efforts in the Pilkington group.

1.2 Luminescence in Ln(III) complexes

In general, luminescence is a process that involves absorption of energy followed by the subsequent emission of light.[42,43] Ln(III) complexes are known for their unique luminescence properties that make them attractive for a wide variety of applications.[44] These properties result from shielding of the 4*f* orbitals by the fully occupied $5s^2 5p^6$ sub-shells. The absorption and emission spectra of Ln(III) ions consists of sharp, narrow bands mostly in the visible and near-IR regions of the EM spectrum with long lifetimes (10^{-6}–10^{-3} s) in solution and the solid state that arise from *f*–*f* transitions, characteristic to a specific metal ion, (Figure 1.18).[45]

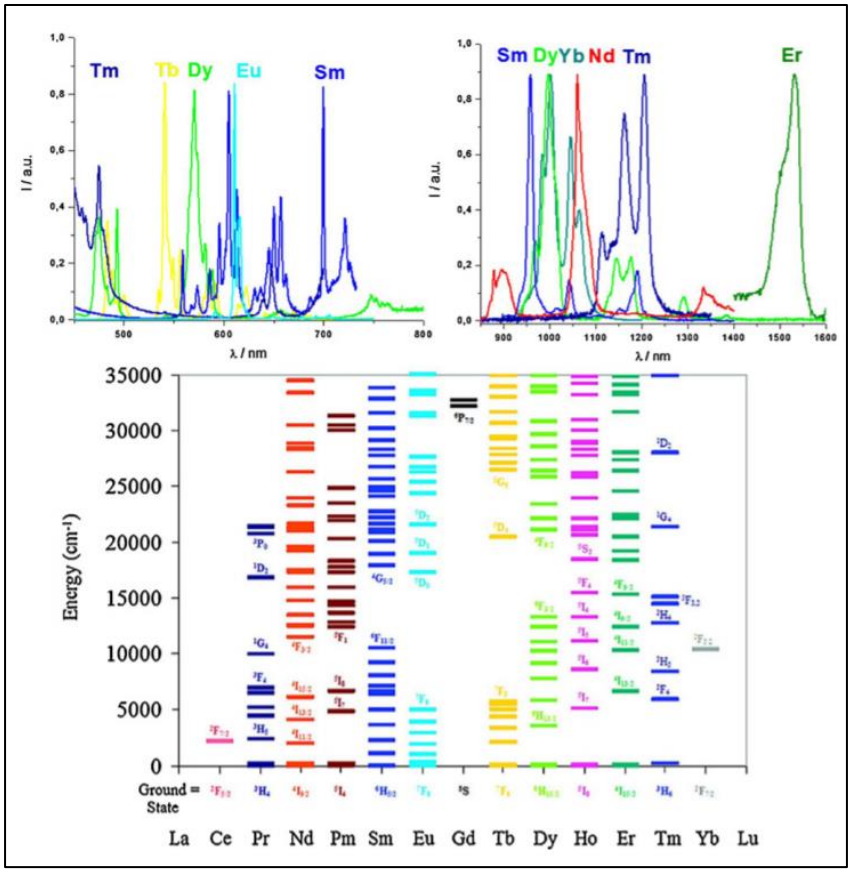

Figure 1.18 Top: luminescence spectra of select Ln(III) ions in the visible (left) and near-infrared (right); bottom: splitting of the electronic energy levels of the lanthanides. Reproduced with permission from reference 45.

These intra configurational *f–f* transitions are Laporte forbidden and hence afford weak absorption and emission intensities with very low molar absorption coefficients (< 3 M^{-1} cm^{-1}).[27] Basically, the direct excitation of Ln(III) ions rarely produces highly luminescent materials however, this can be overcome by indirect excitation via luminescence sensitization or the antenna effect by coordinating or attaching the *4f* ion to a strongly absorbing framework or chromophore that can participate in the energy transfer process.[27]

In the luminescence process, the absorption of a UV photon excites one electron of the organic ligand from the singlet ground state (S_0) to the first excited singlet state (S_1). Then the electron may return from (S_1) to (S_0) by radiative emission which results in the observation of fluorescence, where the spin orientation of the electron does not change. On the other hand, the ligand may undergo intersystem crossing (ISC), where the electron passes from the excited singlet state (S_1) to an excited triplet state (T_1), resulting in a change of the spin orientation. The electron may then relax back from the excited triplet state (T_1) to the original ground singlet state (S_0) by a radiative emission known as phosphorescence. The third scenario is that the complex may undergo intramolecular energy transfer (EnT) from the triplet state of the ligand to the *4f* level of the lanthanide ion and then the ligand relaxes back to its ground state.[27]

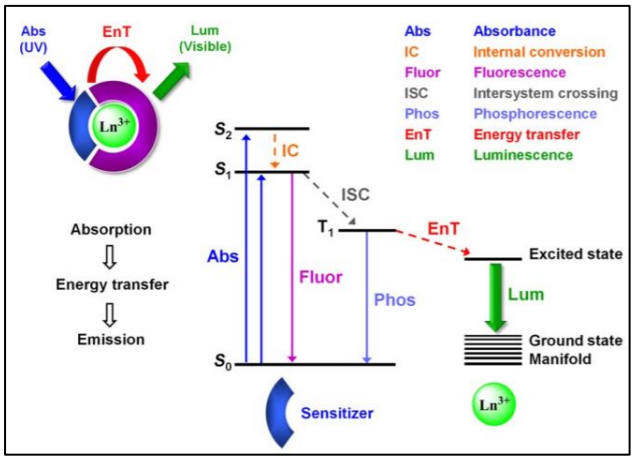

Figure 1.19 Jablonski diagram showing the absorption-energy transfer-emission mechanism from an organic ligand sensitizer to a *4f* ion. Reproduced with permission from reference 46.

In the latter case, energy transfer takes place via non-radiative processes i.e. no emission and re-absorption of light occurs, and the energy transfer is facilitated by two

non-radiative processes known as the Forster and Dexter mechanisms. The Forster dipole–dipole mechanism occurs through space,[47,48] while the Dexter mechanism involves through bond or electron-exchange and requires physical overlap between the orbitals of the ligand and the *4f* ion and is therefore distance dependent. In this case for efficient electron transfer, the triplet state should be located at least 1500 cm^{-1}, but more preferably 2000 to 3500 cm^{-1} above the emission level of the lanthanide ion.[27] Although the physical origins of both mechanisms are fundamentally different, they produce the same products i.e. a ground-state donor and an excited-state acceptor, (Figure 1.20).[48]

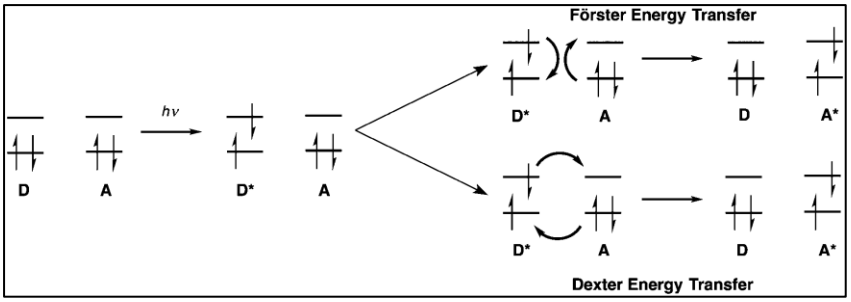

Figure 1.20 Forster and Dexter energy transfer mechanisms. Reproduced with permission from reference 48.

These transfer processes influence the luminescence quantum yields (φ) of Ln(III) complexes, which is the emission efficiency of the complexes and is defined as the ratio between the number of photons emitted by the system *vs* the number of photons absorbed (Eqn. 1.16).[48]

$$\varphi = \frac{\neq \text{ photons emitted}}{\neq \text{ photons absorbed}} = \frac{I_{em}}{I_{abs}} \qquad \textbf{Eqn. 1.16}$$

So, when the energy transfer process is efficient the quantum yields are large. Also, the luminescence quantum yield of *4f* complexes depends on the energy separation between the highest sub-level of the ground multiplet and the lowest lying excited state of the metal ion. The smaller this separation, the easier it can be accessed by non-radiative deactivation processes, for example through vibrations of bound ligands like O–H. Furthermore, high energy vibrations e.g. from O-H groups in the inner or outer coordination spheres of the metal cations can also quench their luminescence properties. With regards to the energy gap, Eu(III), Gd(III), and Tb(III) ions have high energy separations where, ΔE = 12 300 ($^5D_0 \rightarrow {}^7F_6$); 32 200 ($^6P_{7/2} \rightarrow {}^8S_{7/2}$); and 14 800 ($^5D_4 \rightarrow {}^7F_0$) cm^{-1} respectively and as a result they should be the best luminescent ions. However, Gd(III) ion is not very useful since it emits in the UV and as a result, its *4f* emission tends to interfere with the absorption or emission processes of organic ligands.[49] Basically, the local environment surrounding the *4f* ion needs to be comprised of ligands with sufficient chromophoric groups to absorb light and populate the 4*f* excited states through energy transfer, while at the same time provide a rigid and protective coordination shell to minimize non-radiative de-activation processes.[49]

Employing Ln(III) complexes as luminescent agents has attracted significant interest in several areas of chemistry. To-date, Eu(III) and Tb(III) ions have received the most attention due to their high energy separation as mentioned earlier, as well for their distinct, sharp pure red and green emissions in the visible region which are often accompanied by long luminescence lifetimes.[50]

1.2.1 Luminescent *4f* SMMs

Besides the broad applications of Ln(III)-based luminescent materials, their optical properties also provide remarkable opportunities for the design of bifunctional emissive SMMs. Furthermore, luminescence spectroscopy is a useful technique that can provide a detailed picture of the crystal field splitting of the ground state of *4f* ions, subsequently permitting the energy separation between the ground and the first excited M_J states i.e. the Orbach barrier to be determined, that can be correlated with magnetic measurements to help understand relaxation dynamics that can ultimately be employed to optimize the physical properties of these systems.[51]

In this respect, the *4f* ion should have high magnetic anisotropy and a large magnetic moment and simultaneously the resulting complexes should display well resolved emission spectra with long lifetimes. In addition, the choice of a suitable ligand or ligands should provide an optimal coordination geometry for the class of *4f* ion employed to facilitate slow relaxation of magnetization, while at the same time act as sensitizer to enhance the luminescence efficiency of the complex. Dy(III) is the most exploited *4f* ion to-date for the design of luminescent SMMs since as previously discussed from the magnetism perspective, it is Kramers ion with a large *J* value ($J = 15/2$), and oblate shaped electronic density that can be easily stabilized with traditional ligands that can further synthetically modified further to optimize the crystal field in order to afford complexes with higher blocking temperatures. In addition, Dy(III) ions also display emissive properties in the visible region of the electromagnetic spectrum, affording useful optical properties that can be further exploited.[51]

The first example of a luminescent *4f*-SMM was reported in 2009 by Gao *et al.*, with the formula $[Dy_4(PTC_4A)_2(\mu_4\text{-}OH)Cl_3(CH_3OH)_2(H_2O)_3]$ (**1.9**) (PTC_4A= *p*-phenylthiacalix[4]arene), and comprises of a tetranuclear Dy(III) complex coordinated by a calixarene ligand.[52] Magnetic studies show slow magnetic relaxation consistent with SMM properties, while the optical properties at room temperature are dominated by ligand emission with very weak *4f* transitions that suggest a moderate efficiency for the sensitization of the Ln(III) ion by the calixarene ligand.[52] After this work, many mono- or polynuclear Dy(III) complexes with different ligands that include beta-diketonates, carboxylic acids and Schiff-bases have been reported. However, in these studies no interplay between their SMM and luminescence properties have been observed.[51] In fact, the correlation between the two properties was first reported in 2012 by Sessoli *et al.*, for $Na[Dy(DOTA)(H_2O)]\cdot 4H_2O$ (**1.10**) which exhibits slow magnetic relaxation with a U_{eff} value of 42 cm^{-1}.[51,53] The solid-state emission studies were performed at room temperature on a polycrystalline sample of this complex, which after being excited at 365 nm displays well resolved peaks at 20800, 17500, and 15200 cm^{-1}, corresponding to the $^4F_{9/2}\rightarrow{}^6H_{15/2}$, $^4F_{9/2}\rightarrow{}^6H_{13/2}$, and $^4F_{9/2}\rightarrow{}^6H_{11/2}$ transitions, respectively, (Figure 1.21). In addition to these eight transitions that correspond to the eight $\pm m_J$ doublets of the splitting of the $^6H_{15/2}$ ground state, 'hot bands" including excited doublets from the $^4F_{9/2}$ state were also observed in the room temperature data.[51,53]

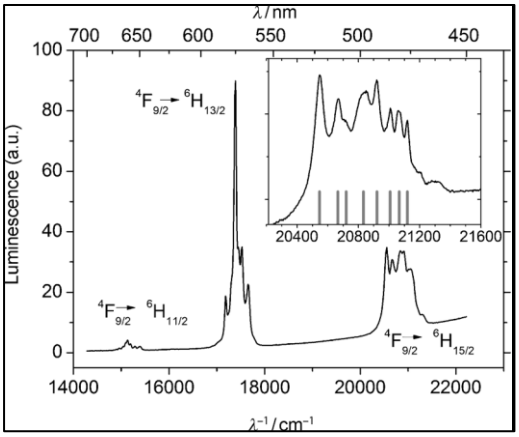

Figure 1.21 Luminescence spectrum of Na[Dy(DOTA)(H_2O)]·4H_2O (**1.10**) at room temperature irradiated at 365 nm. Inset: magnification of the $^4F_{9/2} \rightarrow {}^6H_{15/2}$ transitions. The gray bars are attributed to the emission transitions extracted from the simulation of the spectrum. Reproduced with permission from reference 53.

Analysis of the high-energy region using Gaussian functions permitted the separation between the two lowest sublevels of the ground to be determined affording a value of 53 cm^{-1}, which is slightly higher than the effective energy barrier determined from ac susceptibility experiments.[51,53] Shortly afterwards in 2012, Long *et al.*, reported a Zn(II)/Dy(II) Schiff-base complex with the formula [Zn(NO_3)(L)Dy(NO_3)$_2$(H_2O)] (**1.11**), where H_2L = N,N´-bis(3-methoxysalicylidene)-1,2-diaminoethane). The Schiff-base ligand is incorporated as an antenna with the Dy(III) ion in order to enhance the luminescence properties of the complex through the aforementioned energy transfer process. The complex displays field induced slow magnetic relaxation with effective energy barrier U_{eff} of 27.38 cm^{-1}. The solid-state emission at 14 K shows well resolved peaks between 20500 and 21300 cm^{-1} that are assigned to the $^4F_{9/2} \rightarrow {}^6H_{15/2}$ transition. The high emission spectrum shows eight well resolved transitions that are expected from the

Stark splitting of the $^6H_{15/2}$ ground state and four additional ‘‘hot bands” arising from excited state.[51,54]

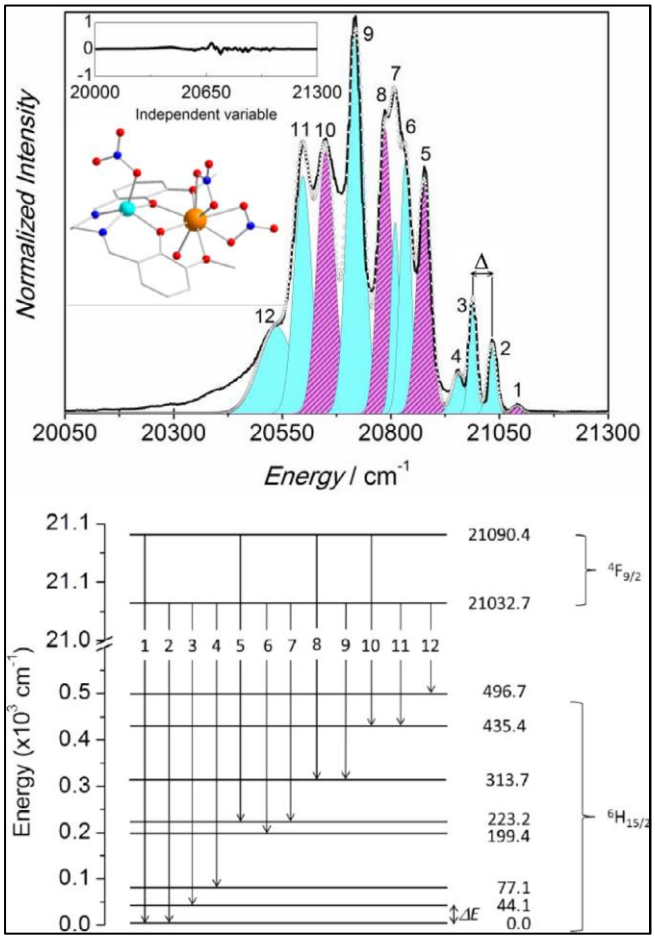

Figure 1.22 Top: magnification of $^4F_{9/2} \rightarrow {}^6H_{11/2}$ transition at 14 K. Multi-Gaussian function fit components that resulting from the first (cyan shadow) and second (pink shadow) $^4F_{9/2}$ Stark sublevel to the $^6H_{15/2}$ multiplet. The inset shows the fit regular residual plot. Bottom: schematic diagram of the radiative transitions between the Stark sublevels of the $^4F_{9/2}$ to the $^6H_{15/2}$ states of the Dy(III) ion. Reproduced with permission from reference 51.

Deconvolution of the peaks using Gaussian functions permit the energy separation between the two lowest sublevels of the $^6H_{15/2}$ ground multiplet to be determined, affording a value of 44.1 ±3.0 cm^{-1}. The difference between the magnetic energy barrier (U_{eff} = 27.38

cm^{-1}) and the energy barrier U obtained from luminescence spectroscopy, the Orbach barrier = 48 cm^{-1} is attributed to the presence of quantum tunneling mechanisms between degenerate Kramers doublets or dipolar interactions, neither of which the luminescence measurements can account for.[49,52, 53]

It is also worth mentioning that, sometimes theoretical *ab initio* calculations are also employed together with luminescence studies to understand the magnetic relaxation or to confirm the picture of the crystal field splitting in cases where the *4f* emission is too weak or too broad, or the complexes coordinate more than one lanthanide ion, as well as in cases where hot bands arising from ligand excited states and/or vibrionic transitions prevent analysis of luminescence data.[51] In this respect, the correlation between the magnetic and luminescence data is only carried on mononuclear SMMs because the crystal field analysis is too complex in the presence of more than one crystallographically inequivalent lanthanide site. Additionally, the Orbach barrier obtained from luminescence measurements is typically higher than the effective energy barrier (U_{eff}) obtained from magnetic measurements indicating that other relaxation processes such as QTM, Raman, or direct relaxation process are likely at play.[51]

In contrast to Dy, there are fewer reported examples of luminescent Tb(III) SMMs since although it is an oblate ion, as a non-Kramers ion it requires high symmetry to observe slow magnetic relaxation. However, Tb(III) ions are generally easier to sensitize by conventional ligands and resolved emission bands can be found even at room temperature when compared with the Dy(III) systems that require low-temperature measurements to obtain sufficient resolution. For the other Ln(III) ions, to the best of our knowledge no luminescent SMMs have been reported to-date for these systems.[51]

1.3 Crown ethers

1.3.1 Historical overview

In 1967, crown ether macrocycles were discovered accidentally by Pederson while studying the effects of bi- and multidentate phenolic ligands on the catalytic properties VO. In this respect, Pederson attempted to synthesize the multidentate ligand *bis*[2-(o-hydroxyphenoxy)ethyl] ether from the reaction between *bis*(2-chloroethyl)ether and mono tetrahydropyranyl protected catechol that was contaminated with about 10% of unreacted catechol. The reaction was carried out in n-butanol under basic conditions and afforded a mixture of the desired compound together with a trace amount (ca. 0.4%) of unknown white silky, fibrous crystals which Pederson subsequently characterized as dibenzo-18-crown-6, (Scheme 1.1).[55]

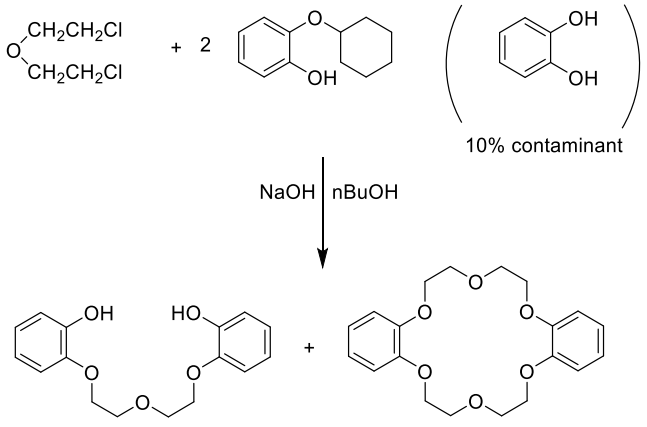

Scheme 1.1 Synthesis of the bis[2-(*o*-hydroxyphenoxy)ethyl]ether and dibenzo-18-crown-6.

Pederson named these polyethers, crown ethers where the number before the crown refers to the total number of atoms in the ring and the number after the crown indicates the

number of oxygen atoms in the macrocyclic ring.[56] The molecular structures of three of the most well-known crown ethers are shown in (Figure 1.23).

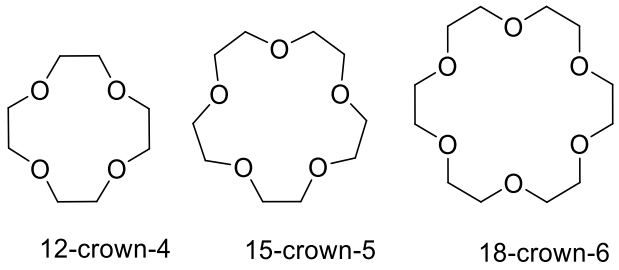

Figure 1.23 Molecular structures of 12C4,15C5, and 18C6.

In later studies these compounds were reported to form complexes with alkaline earth metals, ammonium ions, and select transition metal ions.[55] The saturated crown ethers are typically better ligands than their aromatic benzo and dibenzo counterparts due to the reduced electron density of the donor oxygens as a consequence of the electron-withdrawing benzene rings in the latter.[57] Their coordination complexes are formed by the electrostatic attraction between the positive charge of the cation and the negative dipolar charge on the oxygen atoms that are arranged around the cation in the crown ether. Pederson also investigated the stability of these complexes and he found that their stability is dependent upon the relationship between the ionic diameter of the cation and the cavity size of the polyether. If the size of the cation is comparable with the size of the macrocyclic cavity then the cation lies within the plane of the macrocycle however, complexes with sandwich type topologies can be isolated if the radius of the cation is larger than the cavity of the crown ether. Saturated crown ethers produce coordination complexes with low melting points that are soluble in most organic solvents, while complexes prepared from the aromatic crowns have higher melting points and are not so soluble in aprotic solvents

[55] Pedersen by reporting the binding ability of crown ethers, discovered the first artificial molecules to undergo host-guest interactions, for which he was awarded the Nobel Prize in chemistry in 1987.[56] Following this discovery, the ability of crown ethers to coordinate cations have played an important role in mimicking biological systems where the crown ethers function as ion carriers in membrane transport systems,[58] or as enzymes for bond forming reactions.[59] In addition, crown ethers have also been employed as phase transfer catalysts,[60] as well as for the design of solar cells.[61]

1.3.2 Luminescent crown ether complexes

Although crown ethers are not good antenna ligands due to the lack of a suitable chromophore to transfer efficient energy to the *4f* ions, they have been used to prepare luminescence materials since they are able to form stable complexes due to the macrocycle effect and at the same time encapsulate a Ln(III) ion and/or saturate its coordination sphere that serves to reduce the number of oscillating moieties such as the OH group of solvent molecules, preventing quenching effects, therefore affording complexes more efficient luminescence properties.[44,62–64] Basically, the advantage of these complexes lies in the interplay between the emissive properties of the *4f i*ons and the encapsulation abilities of the crown ether ligands.[44]

Many examples of Ln(III) crown ether complexes have subsequently studied that include the 15C5 Eu(II) complex that has a sandwich type structure (Figure 1.24, middle). This topology serves to efficiently shield the molecule from its external environment resulting in a luminescence maximum λ of 433 nm at room temperature and 417 nm at 77 K. In contrast, in the 12-crown-4 complex, the Eu(II) ion is bonded to four oxygens of the crown ether and three water molecules and one chloride anion and shows a luminescence

maximum at λ = 429 nm in the room temperature spectrum and at 410 nm at 77 K (Figure 1.24, left). In the 18-crown-6 system, the Eu(II) ion is coordinated to two perchlorate anions on one side and an 18-crown-6 macrocycle on the opposite side, and the complex shows a weak maximum, where λ = 411.5 nm at 77 K (Figure 1.24, right).[65]

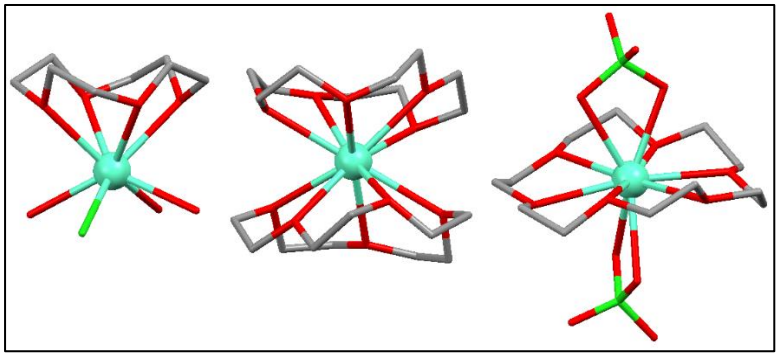

Figure 1.24 Eu(II) complex with 12-crown-4 (left), with 15-crown-5 (middle), and with 18-crown-6 (right). Hydrogen atoms and counter anion are omitted for clarity. Colour code: light green = Eu(II), dark green = Cl, red = O, and gray = C.[65]

1.3.3 Crown ether based single molecule magnets

Prior to beginning this research in the Pilkington group in 2015, there were no examples of crown ether based SMMs reported in the chemical literature. However in recent years crown ether macrocycles have started to attract attention as suitable ligands for the discovery of SMMs due to their ability to bind to a range of *3d* and *4f* metal ions, together with the fact that their cavity size, type and number of donor atoms can be easily modified in a systematic way.[66] With respect to the design of SMMs, several *3d* and *4f* crown ether complexes have now been reported. The first reported example was the Co(II) complex, $[Co(12C4)_2](I_3)2(12C4)$ (**1.12**) (Figure 1.25), where the 3*d* ion is coordinated to the four oxygen atoms of two 12-crown-4 ligands in a distorted square antiprism geometry. Magnetic susceptibility measurements reveal the Co(II) complex is a field induced SMM

with an energy barrier of U_{eff} = 17.0 cm^{-1}. Although its energy barrier is not high, this complex is considered to be the first example of mononuclear transition-metal complex with a high coordination number exhibiting SMM properties.[67]

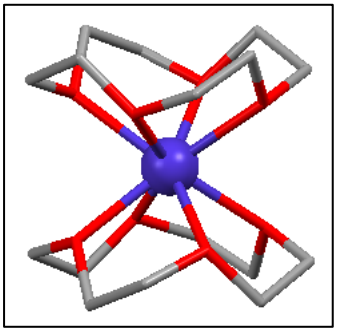

Figure 1.25 Molecular structure of $[Co(12C4)_2](I_3)2(12C4)$ (**1.12**). Colour code: dark purple = Co (II), gray = C, red = O. Hydrogen atoms, counter anion and non-coordinating molecules are omitted for clarity.[67]

Shortly after this work Pilkington *et al.*, were the first to report Ln-SMMs based on crown ether macrocycles. In this respect, two half sandwich Dy(III) complexes with 12-crown-4 and 15-crown-5 macrocycles, $[Dy(12C4)(H_2O)_5](ClO_4)_3 \cdot H_2O$ (**1.13**) and $[Dy(15\text{-}C\text{-}5)(H_2O)_4](ClO_4)_3 \cdot (15C5) \cdot H_2O$ (**1.14**) were structurally and magnetically characterized, (Figure 1.26).[66]

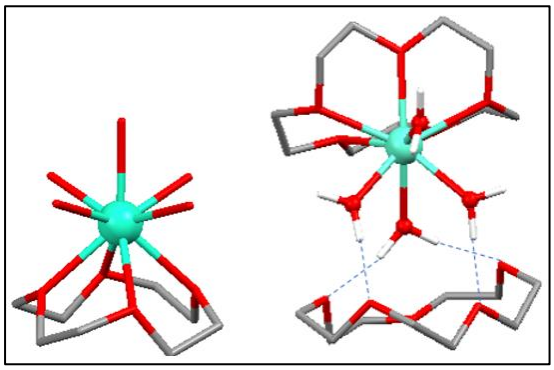

Figure 1.26 Two half sandwich Dy(III) complexes with 12-crown-4 (**1.13**) (left) and 15-crown-5 (**1.14**) (right) macrocycles. Colour code: green = Dy, gray = C, red = O. H-bonds

are shown as blue dashed lines. H atoms, ClO_4^- counter ions and H_2O solvent are omitted for clarity.[66]

The physical properties of the two complexes were studied by magnetic susceptibility, solid state photoluminescence spectroscopy and further probed by *ab initio* calculations. In both complexes the Dy(III) ion is 9-coordinate with capped square antiprismatic geometry, but the different structural topologies result in diverse magnetic properties. The 15C5 complex displays slow magnetic relaxation in zero dc field with an energy barrier U_{eff} = 58 cm^{-1}, while rapid quantum tunnelling of magnetization in the 12C4 complex affords no SMM behaviour. *Ab initio* studies of the two complexes support the experimental measurements, affording a well isolated ground state for **1.14**, supporting the observation of SMM properties in zero dc field, while for **1.13**, the small energy gap between the ground state and the first excited state results in fast relaxation and no SMM behaviour. Photoluminescence studies reveal the two complexes have well-resolved *f–f* transitions that allowed the Stark splitting of the ground state to be determined, providing values of the ground and first excited states that were in excellent agreement with those calculated from the theoretical studies. This work reveals that modifying the organic framework of the crown ether ligands can significantly change the local symmetry of the *4f* ions that in turn has a major affect on their dynamic magnetic properties.[66]

In 2015 Novotortsev and co-workers reported anhydrous Ln(III) complexes, $[Ln(18C6)(NCS)_3]$ (**1.15**) (Figure 1.27) that were synthesized by replacing the H_2O molecules in $[Ln(H_2O)_5(NCS)_3]\ H_2O$ (Ln(III) = Eu, Tb) complexes by the 18-crown-6 ligand. One of the aims of this study were to investigate the effect of coordination of the

18-crown-6 macrocycle on the magnetic and luminescent properties of the resulting complexes.[68]

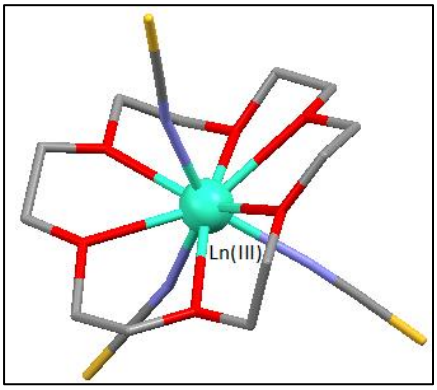

Figure 1.27 [Ln(18C6)$(NCS)_3$] (**1.15**) complexes (Ln(III) = Eu, Tb). H atoms are omitted for clarity. Colour code: gray = C, red = O, blue =N, yellow = S, green = Ln(III).[68]

This replacement of the water ligands by the macrocycle increased the coordination number of the Ln(III) center from 8 to 9. Magnetic susceptibility measurements show the absence of frequency-dependent out-of-phase signals for the Tb(III) complexes. Furthermore. photoluminescence studies reveal that the luminescent properties of the *4f* ions are completely quenched on coordination to the 18-crown-6.[68]

Ding and co-workers reported a series of Dy(III)-crown-ether complexes with different coordination environments for Dy(III) ions. In this study 12-crown-4, 15-crown-5, and 18-crown-6 ethers were used. Firstly, two different Dy(III) complexes were prepared from 12-crown-4. With $Dy(NO_3)_3$ a half-sandwich complex $Dy(12C4)(NO_3)_3$ (**1.16**) was obtained and by employing $Dy(ClO_4)_3$, a double-decker-like complex $Dy(12C4)_2(CH_3CN)(ClO_4)_3$ (**1.17**) was first obtained after which modifying the reaction conditions the dinuclear complex, $Dy_2(12C4)_2(ClO_4)_4(OH)_2(H_2O)_2$ (**1.17**) was isolated (Figure 1.28).[69]

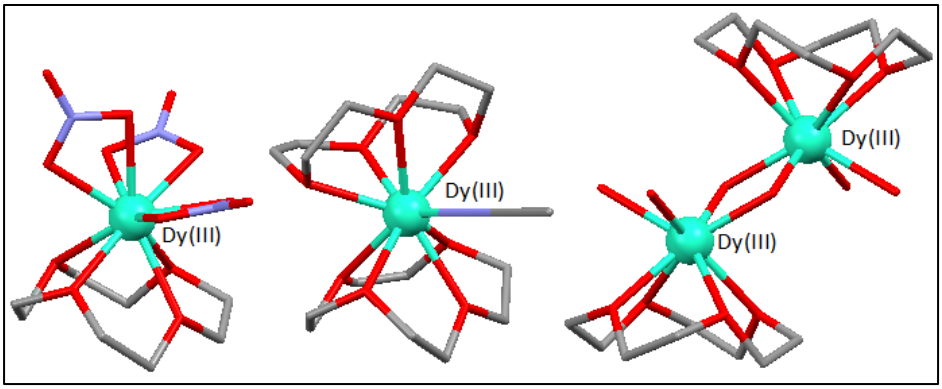

Figure 1.28 Left, the half-sandwich complex Dy(12C4)$(NO_3)_3$ (**1.16**); center, the double-decker complex Dy(12C4)$_2(CH_3CN)(ClO_4)_3$ (**1.17**); right, the dinuclear complex, Dy_2(12C4)$_2(ClO_4)_4(OH)_2(H_2O)_2$ (**1.18**). Colour code: gray = C, red = O, blue = N, green = Dy(III). H atoms and ClO_4^- counter ions are omitted for clarity.[69]

On further using both 15-crown-5 ether and 12-crown-4 macrocycles the double-decker complex, [Dy(12C4)(15C5)(CH_3CN)][Dy (12C4)(15C5)]$_2(CH_3CN)_2(ClO_4)$ (**1.19**) was obtained. Interestingly, the crystal structure of this complex contains two crystallographically independent molecules. The first comprises of a 9-coordinate Dy(III) ion sandwiched between two crown ether macrocycles (Figure 1.29, left), and the second molecule contains a 10-coordinate Dy(III) ion that in addition to the two crown ether macrocycles, is axially coordinated to a CH_3CN ligand, (Figure 1.29, right).[69]

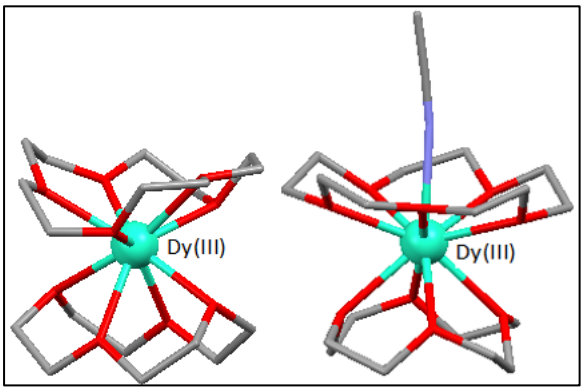

Figure 1.29 The two crystallographically independent molecules in the unit cell of the double-decker complex [Dy(12C4)(15C5)(CH_3CN)][Dy (12C4)(15C5)]$_2$(CH_3CN)$_2$(ClO_4) (**1.19**). Colour code: gray = C, red = O, blue = N, green = Dy(III). H atoms, CH_3CN solvent, and ClO_4^- counter ions are omitted for clarity.[69]

Using 18-crown-6 together with both $Dy(NO_3)_3$ and $Dy(ClO_4)_3$ resulted in the isolation of [Dy(18C6)(NO_3)$_2$]ClO_4 (**1.20**), whereas reaction of the above complex further with $NaBPh_4$ afforded [Dy(18C6)(NO_3)$_2$]BPh_4 (**1.21**), where the perchlorate ions are exchanged for more bulkier tetraphenylborate counterions. In these two complexes the Dy(III) are coordinated in the macrocyclic cavity of the 18-crown-6 and are bonded to two bidentate nitrate groups, where the dihedral angles of the two NO_3 groups are different, i.e. at 90° and 68° respectively, which has an impact on the magnetic relaxation of the two complexes (Figure 1.30).

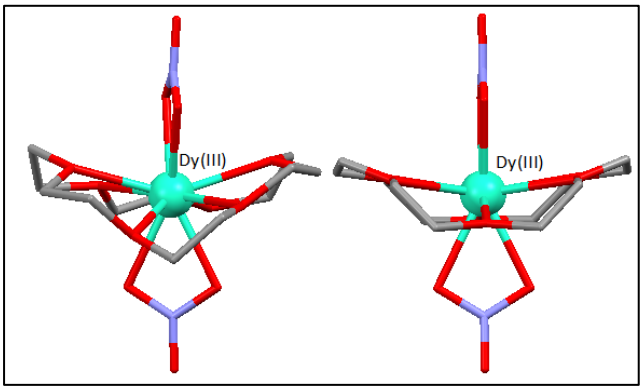

Figure 1.30 Molecular structure of Dy(III) complexes with 18-crown-6. [Dy(18C6)(NO_3)$_2$]ClO_4 (**1.20,** left) and [Dy(18C6)(NO_3)$_2$]BPh_4 (**1.21,** right), that differ in the dihedral angles of their apical bidentate nitrate groups. Colour code: gray = C, red = O, blue = N, green = Dy(III).[69]

In this respect, in the presence of a small applied dc field, for complex **1.20** where the ONO angle is 90°, the U_{eff} = 63 K, whereas for complex **1.21**, where the ONO angle is significantly less than 90°, the U_{eff} = 43 K. Ac magnetic studies for the two complexes reveal no SMM behavior in zero dc field, most likely due to the presence of QTM.[69]

In 2017 Kajiwara and co-workers reported the syntheses and magnetic properties of two isostructural families of crown ether complexes containing the oblate *4f* ions, Ce(III); Pr(III); and Nd(III), with 18-crown-6 and 1,10-diaza-18-crown-6 macrocycles. The two complexes have the structural formulae $[Ln(NO_3)_3(18C6)]$ (**1.22**). and $[Ln(NO_3)_3(1,10\text{-diaza}18C6)]$ (**1.23**), (Figure 1.31). The objectives of this study were to confer an appropriate anisotropic crystal field using neutral donor sets from macrocyclic ligands in the equatorial positions of oblate-type Ln(III) ions and then introduce anionic ligands into the axial positions to stabilize the electronic density and maximize the axial anisotropy of oblate *4f* ions. Slow magnetic relaxation was observed for those complexes containing the Kramers ions Ce(III) and Nd(III), which are field induced SMMs. Interestingly, the aza-18-crown-6 complexes have higher energy barriers and shorter relaxation times when compared to the 18-crown-6 complexes.[70]

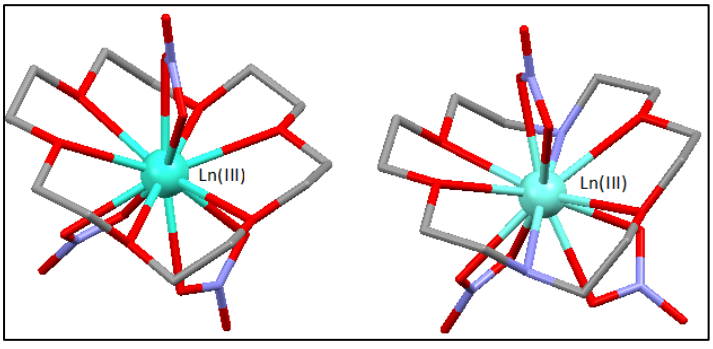

Figure 1.31 Molecular structure of $[Ln(NO_3)_3(18C6)]$ (**1.22**) with 18-crown-6 (left) and $[Ln(NO_3)_3(1,10\text{-diaza}18C6)]$ (**1.23**) with 1,10-diaza-18-crown-6 (right) where Ln(III) =

Ce(III); Pr(III); and Nd(III)). Colour code: gray = C, red = O, blue = N, green = Ln(III). H-atoms and anions are omitted for clarity.[70]

Structural studies reveal that the donor atoms of the aza-18-crown-6 showed a larger deviation from the ideal equatorial plane than the 18-crown-6 derivative which results in a weak repulsion between the aza-18-crown-6 and the electronic distribution of the ground sublevels, leading to a larger gap between the ground and first excited states and subsequently a higher energy barrier.[70]

In 2018 Boskovic and co-workers also used an18-crown-6 macrocycle and reported two series of lanthanide complexes with the general formula [Ln(18C6)(X_4Cat)(NO_3)] (**1.24**) (Ln(III) = La, Ce, Nd, Gd, Tb, Dy), by reacting of Ln(III) nitrate salts together with 18-crown-6 and deprotonated tetrahalocatechol (X_2Cat^{2-} where X=Cl, Br) (Figure 1.32).[71]

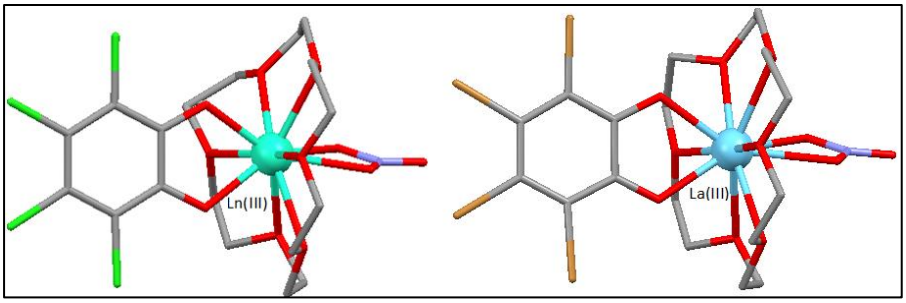

Figure 1.32 [Ln(18C6)(Cl_4Cat)(NO_3)] (**1.24**) (Ln=La, Ce, Nd, Gd, Tb, Dy (left) and [La(18C6)(Br_4Cat)(NO_3)] complex (right). Colour code: gray = C, red = O, blue = N, light green = Cl, brown = Br, blue = La(III), green = Ln(III). H-atoms are omitted for clarity.[71]

The yield of the Ln(III) complexes decreased from left to right across the period due to the increasingly weaker interaction between the *4f* ions and the 18-crown-6 macrocycle. Interestingly, the smaller Ln(III) ions, Ho(III), Er(III), and Yb(III) afforded only crystals of 18-crown-6 and [Ln(NO_3)$_3$(H_2O)$_3$]. In all complexes, the six oxygen atoms

of the crown ether ligand occupy the equatorial positions around the *4f* ions, and the axial positions are occupied by the four oxygen atoms of the nitrate and the catecholate ligands. Magnetic studies of the two series reveal that the Ce, Nd, Tb, and Dy complexes are all field induced SMMs. No slow relaxation of the magnetisation was observed in zero dc field due to QTM promoted via dipolar interactions. Basically, the intermolecular separation between Ln(III) centers is small which facilities intermolecular dipolar interactions that affects the dynamic magnetic properties of the complexes. In the case of the Dy(III) system, dilution of this complex into a diamagnetic La(III) host suppresses the dipolar interactions and subsequently switches on its SMM properties in zero dc field.[71]

Ruiz and co-workers in 2018 reported the syntheses and magnetic properties of 18-crown-6 complexes with both oblate and prolate Tb(III), Dy(III), Er(III), and Yb(III) ions. In this case a family of Ln(III) complexes with general formula $[Ln(H_2O)_3(18C6)](ClO_4)_3$ (**1.25**) were prepared (Figure 1.33).[72]

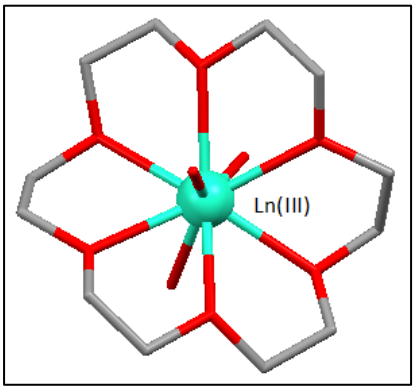

Figure 1.33 Ln(III) complexes $[Ln(H_2O)_3(18C6)](ClO_4)_3$ (**1.25**) (where Ln(III) = Tb, Dy, Er, and Yb. Colour code: gray = C, red = O, green = Ln(III). H-atoms and ClO_4^- counterions are omitted for clarity.[72]

In this work the authors tried to take the advantage of the relationship between the electrostatic effects of the ligand field and the shape of the electron density of the *4f* ions (prolate or oblate) for the design of Ln(III)-SMMs. So, the neutral 18-crown-6 ligand was used in order to reduce the electrostatic repulsion in equatorial plane of the oblate ion and the electron density was once again maximized in the axial positions by the employment of anionic ligands. Magnetic studies reveal that the Dy(III) and Yb(III) complexes show relaxation of magnetization in the presence of an applied dc field, while the Tb(III) and Er(III) complexes are not SMMs due to the presence of very efficient quantum tunneling mechanisms in the ground state. In the case of the Dy(III) complex, analysis of the shape of the electron density and the calculated electrostatic potentials produced by the ligands indicated that the similarity of the donor character between the oxygen atoms of the 18-crown-6 in the equatorial positions and the water molecules in the axial positions afforded an isotropic electronic density distribution around the *4f* ion instead of the desired anisotropic distribution to maximize the axial anisotropy of the oblate ion. In addition, during this study the distortion of crown ethers by the Ln(III) ions was analyzed by comparing the structure of the macrocycle in four Ln(III) complexes, where Ln(III) = Tb; Dy; Er; and Yb, containing a symmetrical crown ether that has a regular hexagonal disposition of its oxygen atoms. This study revealed that for the heavier Ln(III) complexes, there is a large distortion of the 18-crown-6 ether macrocycle due to the lanthanide contraction. Moreover, analysis of the Ln−O bond distances for the complexes revealed that the Dy(III) ion has the most suitable size to fit into the 18-crown-6 cavity to keep the highest symmetry.[72]

1.4 Schiff-base ligands

In 1864 the Italian chemist Hugo Schiff discovered Schiff-bases with the general formula (-R_2C=N-R; where R = an alkyl or aryl group). The synthesis of Schiff-bases takes place via a reversible reaction involving the condensation between a primary amine and an aldehyde or a ketone, where the active carbonyl is replaced by an imine or an azomethine group.[73,74] Schiff-bases are formed more readily from aldehydes rather than ketones, and Schiff-bases of aromatic aldehydes with effective conjugated systems are generally more stable than those formed from aliphatic aldehydes, which are relatively unstable and easily polymerizable.[75] The mechanism of Schiff-base formation involves nucleophilic addition of the nitrogen of the amine which attacks the carbonyl of the aldehyde or ketone forming a carbinolamine intermediate, that is subsequently dehydrated affording the Schiff-base, (Scheme 1.2).[73] Schiff-base preparation generally takes place in alcohols, under acid or base catalysis, either with or without refluxing conditions.[75] Normally the synthesis of Schiff-bases is carried out at mildly acidic pHs because at higher acid concentrations the amine is protonated becoming non-nucleophilic, and thus the equilibrium is displaced to the left, disfavouring the formation of the carbinolamine.[73] The driving force for the Schiff-base reaction is typically the removal of water from the system by carrying out the reaction in the presence of a Dean Stark or via addition of activated molecular sieves to the reaction mixture. In some cases, precipitation of the Schiff-base out of the reaction mixture also drives the reaction from left to right.

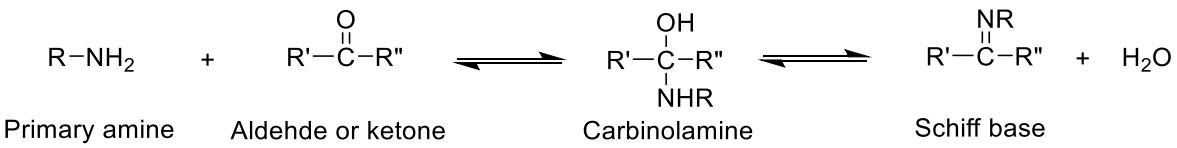

Scheme 1.2 Formation of a Schiff-base via a carbinolamine intermediate.

Since their discovery, Schiff-bases have been widely used as ligands and play a pivotal role in the development of coordination chemistry due to their facile synthesis, remarkable versatility and ability to form a wide range of *3d/4f* complexes of chemical, biological and industrial importance.[76,77] Most Schiff-base ligands are comprised of N and O donor atoms, or contain mixed donor atoms such as P and S, including mono-, di-, tri-, tetra- and multidentate systems.[78] Furthermore, reaction between a carbonyl group and a primary amine gives rise to a broad range of both acyclic and macrocyclic Schiff-bases that are able to encapsulate, or to bind to two or more metal ions.[79,80] Acyclic and macrocyclic Schiff-base ligands, including dinuclear and/or compartmental systems, have received much attention in recent years for a diverse range of applications in biochemistry, materials science, catalysis, and molecular magnetism. These ligands are typically synthesized via self-condensation reactions between suitable formyl- or keto- and primary amine-precursors or template reactions, where the complexes form directly in the presence of a metal ion with a suitable ionic radius.[79,81] Furthermore, the latter class of complexes can undergo transmetallation reactions which permits the preparation of complexes that are otherwise synthetically inaccessible. It is also worth mentioning that both the template and transmetallation reactions generally produce complexes in excellent yields with high purities. Macrocyclic systems can be formed with different ring sizes, depending on the size of the formyl- and amine precursors as well as the metal ion employed in the case of template reactions. Based on the number and ratio of the dicarbonyl and diamine precursors, [1 + 1], [2 + 2] [3 + 3] and [4 + 4] macrocycles have all been reported (Scheme 1.3).[79,82]

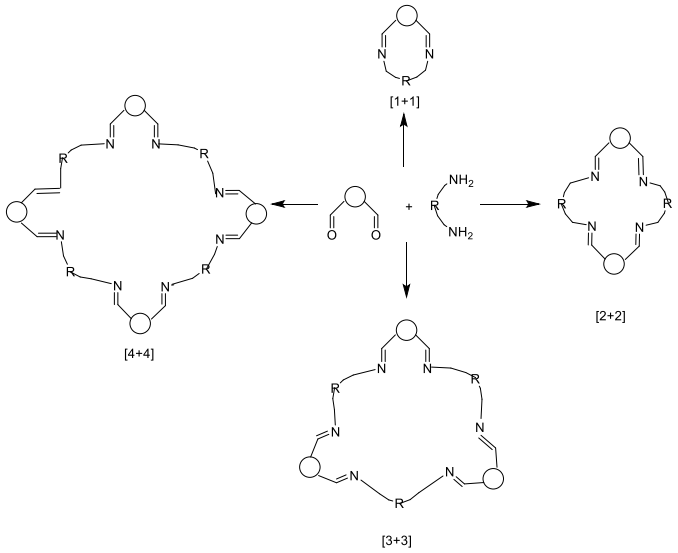

Scheme 1.3 Synthetic pathway to [1 + 1], [2 + 2], [3 + 3] and [4 + 4] Schiff-base macrocycles.

In addition, the diformyl or diketo precursors may also contain bridging or spacer groups between their formyl substituents, while the amine precursors can bear additional donor groups in their side chains, (Figure 1.34).[82]

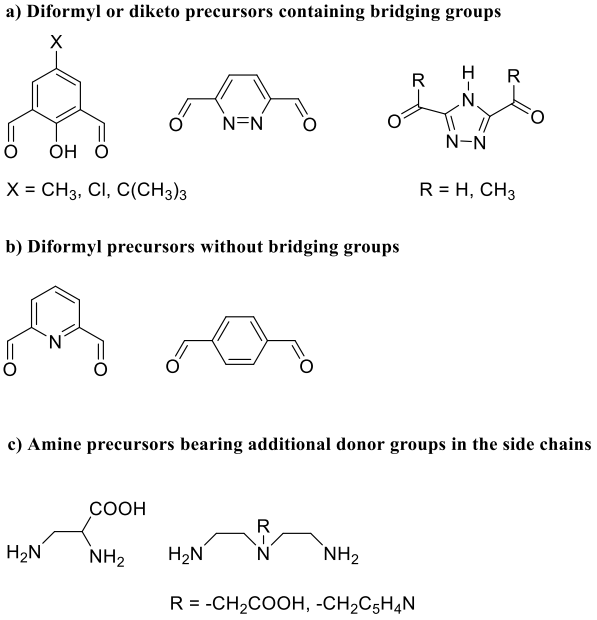

Figure 1.34 Three classes of a) diformyl- or b) diketo- and c) diamine precursors.

Acyclic and macrocyclic compartmental Schiff-bases with identical or different compartments separated by spacers have been all been employed to form homo- and hetero-dinuclear or polynuclear complexes.[79,80,82] Asymmetric compartmental ligands have received much attention during last decade as they contain two cavities of different size and donor type, that can selectively accommodate two different metal ions, affording heterodinuclear complexes with significantly different chemical and physical properties coming from the two metal ions.[83] One family of such systems are the asymmetric [1 + 1] Schiff-base ligands that contain two different coordination sites, the first an O_2O_3, O_2O_4, O_2O_5 or O_2O_6 'crown like' site and a second N_2O_2 or N_3O_2 Schiff-base site that is formed via the condensation of an appropriate diformyl and polyamine precursor, or via a template reaction in the presence of a suitable metal ion.[84] These systems have been employed for the synthesis of mononuclear 4*f*,[84] heterodincuclear 3*d*-4*f*,[83] and homonuclear 4*f*-4*f*complexes.[85] In the *3d/4f* systems, the Schiff-base site is typically occupied by a 3*d*-metal ion, while the 4*f* ions prefer the harder, crown-like cavity, (Figure 1.35).[83,84,86]

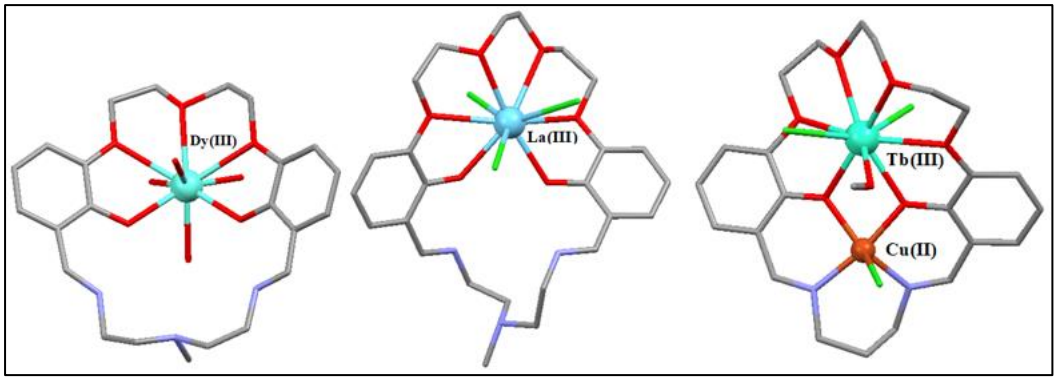

Figure 1.35 Molecular structures of mono- and heterodinuclear complexes (**1.26** to **1.28**) prepared from [1 + 1] asymmetric compartmental Schiff-base ligands. Colour code: gray

= C, red = O, blue = N, dark green = Cl. H-atoms and counterions are omitted for clarity.[83,84,86]

In recent years, the [1 + 1] asymmetric compartmental macrocyclic ligand H_2L_3, containing both N_3O_2 Schiff-base and O_3O_2 crown-ether-like cavities was used to prepare heterodinuclear complexes containing *4f* and Na^+ ions for applications as Ln-shift reagents in NMR spectroscopy.[87] In these complexes, the Ln(III) ions occupy the N_3O_2 site, and the Na^+ ions are coordinated in the O_3O_2 cavity. Although both ions prefer the O_2O_3 cavity, NaOH is employed first as a base to deprotonate the Schiff-base macrocyle prior to its coordination, which results in the Na^+ ions preferentially occupying the crown ether like cavity, leaving the N_3O_2 cavities free for the *4f* ions (Figure 1.36).[87]

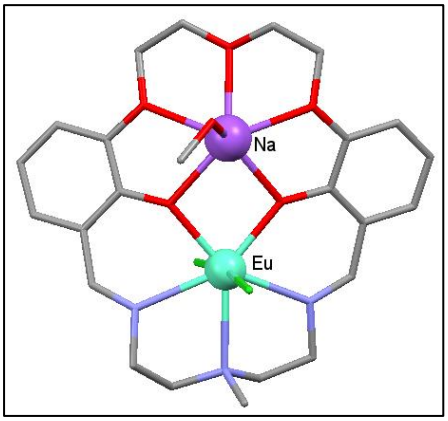

Figure 1.36 Molecular structure of the heterodinuclear Eu-Na complex (1.29), comprising of the asymmetric [1 + 1] compartmental Schiff-base ligand. Colour code: gray = C, red = O, blue = N, dark green = Cl, green = Eu(III). H-atoms and counter ions are omitted for clarity.[87]

Different types of acyclic and macrocyclic Schiff-bases have been widely employed for the design of 3*d*, 4*f*, and 3*d*/4*f* SMMs due to their ability to provide binding sites of different sizes and donor types that can selectively encapsulate metal ions, as well

as provide stability, solubility and bulky groups that can alter the stereochemistry of the metal ions.[88,89]

In 2015 Andruh *et al.* published a review article about the coordination chemistry of Schiff-base ligands obtained from *o*-vanillin, or 2-hydroxy-3-methoxybenzaldehyde. This family of ligands are well known to form a variety of complexes with interesting physical properties that include magnetism, luminescence, chirality, catalysis, cytotoxicity, and ferroelectricity.[89] Also, Schiff-base ligands based on the *o*-vanillin system have proven to be particularly effective for the synthesis of 4*f* and 3*d*/4*f* SMMs since they can provide several coordination sites and act as chelating bridging ligands.[90–92] Murugesu *et al.*, have recently explored the coordination chemistry of an acyclic compartmental Schiff-base ligand based on this *o*-vanillin motif namely ,N1,N3-bis(3-methoxysalicylidene)diethylenetriamine (H_2valdien) (Figure 1.37), that contains an inner set of N_3O_2 and an outer set O_4 donors.

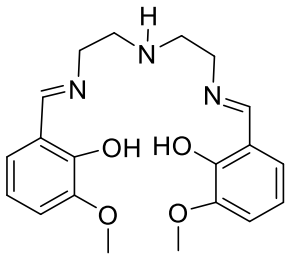

Figure 1.37 Structure of the N1, N3-bis(3-methoxysalicylidene)diethylenetriamine (H_2valdien) ligand.

In this approach, a family of dinuclear lanthanide complexes were prepared with the formula $[Ln_2(valdien)_2(NO_3)_2]$ (**1.26**), where Ln(III)=Eu, Gd, Tb, Dy and Ho). For all complexes, an antiferromagnetic interaction between the two lanthanide ions was

observed. Only the [Dy_2] complex displayed slow magnetic relaxation, but weak exchange coupling between the lanthanide ions affected the QTM. In addition, *ab initio* calculations indicated that the exchange interaction increases when the Ln(III)-O3-Ln(III) angle in the bridge increases and the intramolecular Ln(III)-Ln(III) distance decreases.[93] Dilution studies on the [Dy_2] complex were also performed using the Y(III) analogue to determine the origin of the observed slow relaxation of the magnetization. Dilution studies indicated that the slow relaxation arises from the single ion relaxation of the Dy(III) ions that is entangled with the relaxation of the neighboring Dy(III) ion within the complex through weak intramolecular exchange-biased interactions which affect the quantum tunneling of the magnetization in the [Dy_2] complex at zero field.[94]

Additionally, the [Dy_2] complex was used by Murugesu's group to study the effect of electron-withdrawing ligands on the energy barriers of SMMs. In this study the coordination geometry of the Dy(III) centers was maintained while the nitrate terminal ligands on the axial position of the Dy(III) ions were replaced by monoanionic, bidentate ligands with highly electron withdrawing atoms. The reaction of the Schiff-base ligand with Dy(III) salts afforded six dinuclear Dy(III) complexes with the general formula [Dy_2(valdien)$_2$(L)$_2$]·solvent (**1.30**), where the ligand L = NO_3^-, CH_3COO^-, $ClCH_2COO^-$, Cl_2CHCOO^-, $CH_3COCHCOCH_3^-$, $CF_3COCHCOCF_3^-$. It was found that introducing highly electron withdrawing atoms on the terminal ligands enhances the energy barrier U_{eff} of the complexes significantly with the most drastic increase observed for the dichloroactate (U_{eff} = 60 K, 2-fold increase in U_{eff}) and hexafluoroacac ligands (U_{eff} = 110 K, 7-fold increase in U_{eff}), (Figure 1.38).[95]

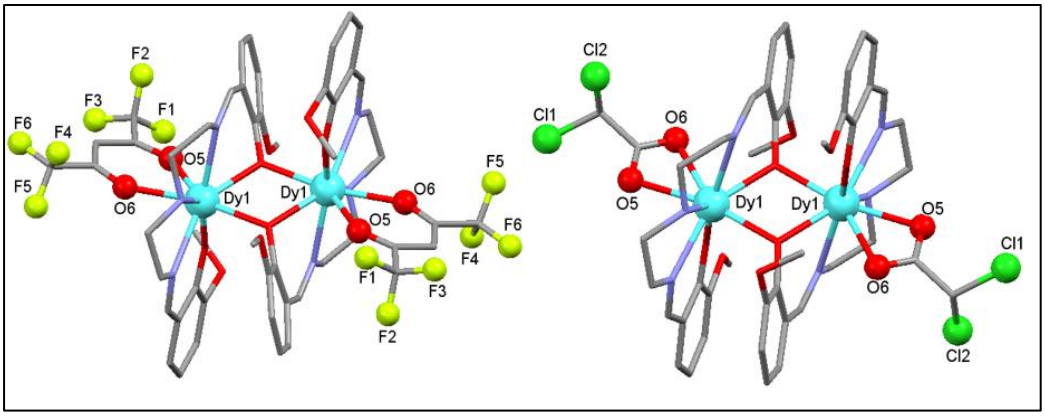

Figure 1.38 Molecular structures of [Dy_2] complexes with dichloroacetate (Cl_2CHCOO^-) and hexafluoroacac ($CF_3COCHCOCF_3^-$) terminal ligands. Colour code: gray = C, red = O, blue = N, aqua blue = Dy(III). H-atoms are omitted for clarity.[95]

In recent years, the Pilkington group has employed Schiff-base macrocycles including the Schiff-base N_3O_2 ligand to prepare chiral Fe(II) complexes with spin crossover properties,[96] as well as N_3X_2 (X = NH, O) and N_3O_3 ligands to form Mn(II) and Gd(III) complexes as potential contrast agents for magnetic resonance imaging (MRI).[97] In addition, N_5, N_3O_2 and db-N_3O_3 Schiff-base macrocycles have been employed to study the magnetic properties of Dy(III) complexes with pentagonal bipyramidal geometries, (Figure 1.39).[98] The only difference between the N_5 and N_3O_2 macrocycles is the nature of their donor atoms and the db-N_3O_3 macrocycle was used to investigate the effect of a large cavity size and additional steric bulk on the properties of the *4f* coordination complexes. Although the structural studies of transition metal complexes with these macrocycles were first studied by Nelson *et al.*, in the 1970s,[99] the structural and magnetic studies of *4f* complexes with these macrocycles were not previously reported. Hence, these pentadentate macrocycles were employed to bind in an equatorial fashion to Dy(III) ions

that together with two axial ligands confer pentagonal bipyramidal geometry of the *4f* ion, in order to enhance the axial anisotropy of the oblate ion and suppresses QTMs.

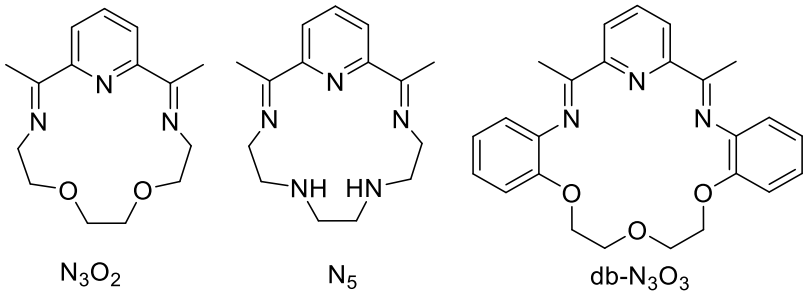

Figure 1.39 Molecular structures of theN_3O_2, N_5 and db-N_3O_3 macrocycles.[98]

Magnetic studies reveal that Dy (III) complexes of the N_5, N_3O_2 macrocycles display slow relaxation of magnetisation in zero field. Unfortunately, these complexes were all amorphous and so no single crystals could be grown which made it impossible to perform magneto-structural studies to rationalise the observed differences in their magnetic properties.[98]

Further work in Pilkington group, preparing Ln(III) based SMMs with pentagonal bipyramidal geometry led to the employment of a close derivative of the asymmetric [1 + 1] compartmental Schiff-base ligand H_2L_3, (Figure 1.40) that comprises of two asymmetric N_3O_2 and O_3O_2 cavities, that as previously mentioned was first prepared in 1990s as a Ln-shift reagent.[87]

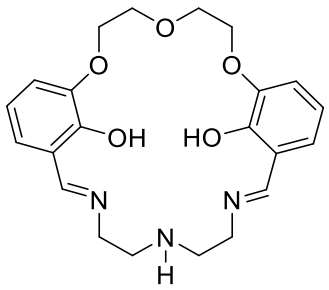

Figure 1.40 Molecular structure of the dual compartmental Schiff-base macrocycle **H_2L_3**.

Although Ln(III) ions prefer to coordinate to the O_2O_3 crown like cavity, in the initial synthetic procedure NaOH is used first to deprotonate the macrocycle and the Na^+ ions therefore occupy the O_3O_2 crown like cavity, making the N_3O_2 Schiff-base cavity available for coordination to the *4f* ions. In the first study, three Ln(III) complexes of stoichiometry $[Ln_2Na_2(L_3)_2(Cl)_4(MeOH)]\cdot xH_2O$, (**1.31-1.33**) were prepared, where Ln(III) = Tb (**1.31**), Dy (**1.32**) and Er (**1.33**). Tb(III) was chosen because it has oblate electronic density which could further be stabilized by an optimal pentagonal bipyramidal crystal field.[100] Dy (III) was chosen due to the fact that as a Kramers ion its ground state is always doubly degenerate regardless of the crystal field, it has a high *J* value (*J* = 15/2), is oblate in character and hence its axial anisotropy could be enhanced by the application of a pentagonal bipyramidal crystal field. In contrast, the Er(III) ion is a Kramers ion but is a prolate ion and thus was employed to investigate the effects of a pentagonal bipyramidal crystal field on a prolate *4f* ion. Single crystal X-ray diffraction of the three complexes reveal they were isostructural and crystallized as dimers.[100]

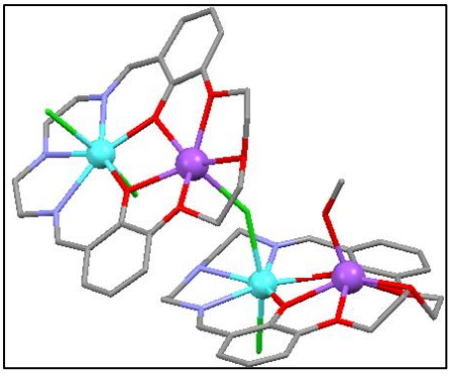

Figure 1.41 Crystal structure of $[Ln_2Na_2(L_3)_2(Cl)_4(MeOH)]\cdot xH_2O$, (**1.31-1.33**). Colour code: gray = C, red = O, blue = N, green = Cl, purple = Na, aqua blue = Ln(III) (Dy, Tb, or Er) . H-atoms are omitted for clarity.[100]

A Na^+ ion occupies the O_3O_2 crown like cavity with trigonal prismatic coordination geometry. The *4f* ions occupy the N_3O_2 cavity with pentagonal bipyramidal geometry, where the *4f* ion is equatorially coordinated by the N_3O_2 cavity with two chloride ligands in the axial positions. A bridging chloride links the Ln(III) ion of one monomer with the Na(I) ion of the other monomer (Figure 1.41). Magnetic studies reveal that Dy(III) complex displays slow magnetic relaxation under a small static applied dc field ,with an effective energy barrier U_{eff} of 12.6 cm^{-1} and fast QTM in zero dc field. Unfortunately, for the Tb(III) and Er(III) complexes, ac susceptibility studies revealed no SMM behaviour in either zero or the presence of a small static dc field due to the significant deviation from ideal D_{5h} geometry that permits rapid QTM. *Ab initio* calculations were performed on all three complexes revealing that for the Dy(III) system, the first Dy(III) relaxes via a spin-lattice relaxation mechanism, consistent with field induced SMM behaviour, while with the second Dy(III) ion undergoes fast magnetic relaxation due to the presence of rapid quantum tunnelling in the ground state. For the Tb(III) complex, the absence of a doubly degenerate ground state resulted in no SMM behaviour, whereas the Er(III) is a Kramers ion which afforded a doubly degenerate ground state, however the ground state contains a large transverse anisotropy that facilitates fast quantum tunnelling processes in the ground state and thus no SMM behaviour observed which further supports the ac susceptibility data.[100] Given the recent breakthrough in the field of *4f*-based SMMs, where it has now been established that the optimization of the crystal field of *4f* ions can afford Ln SMMs with large energy barriers and high blocking temperatures, we set out to investigate further the coordination chemistry of crown ether and dual compartmental Schiff-base macrocycles together with paramagnetic *3d* and/or *4f* ions to investigate; (i) how subtle

changes to their molecular structures and/or the metal ions employed affects their magneto-structural properties and (ii) to gain a better understanding of the dynamic magnetic properties in such systems.

2 Dual-Property Supramolecular H-Bonded 15-Crown-5 Ln(III) Chains: Joint Magneto-Luminescence and *Ab Initio* Studies

The results of these studies have been published in the following full paper: M. Al Hareri, Z. Ras Ali, J. Regier, E.L. Gavey, L.D. Carlos, R.A.S. Ferreira and M. Pilkington, *Inorg. Chem.,* 2017, **56**, 7344.

Zineb Ras Ali and Majeda Al Hareri are joint first authors of this work and as such, their names are listed alphabetically. Ras Ali and Al Hareri prepared and grew suitable single crystals of the complexes for characterization by X-ray crystallography. Ras Ali fully characterized the complexes and prepared single crystals for magnetic susceptibility and photoluminescence studies. Gavey collected the magnetic susceptibility data in house at Brock and assisted Ras Ali in modelling the ac susceptibility data. Regier carried out the *ab initio* studies and international collaborators Dr. L.D. Carlos and Dr. R.A.S Ferreira (U of Aveiro, Portugal) carried out solid-state photoluminescence measurements.

2.1 Introduction

As previously mentioned, crown ethers first discovered by Pederson in the 1960s are a commercially available class of macrocyclic ligands in which both the cavity size and number of donor atoms can be structurally tuned to accommodate a broad range of metal cations.[55,101] In addition to elucidating the relationship between the cavity diameter and the atomic radius of the cation, Pederson also established that crown ethers with smaller cavities such as 15C5 and 12C4 accommodate larger metal cations by forming sandwich-type topologies, (Figure 2.1, left, **2.1**), where the cation is displaced out of the plane of the

macrocycle, reminiscent of the double-decker $[LnPc_2]^-$ complex **2.2** shown in Figure 2.1 (left).

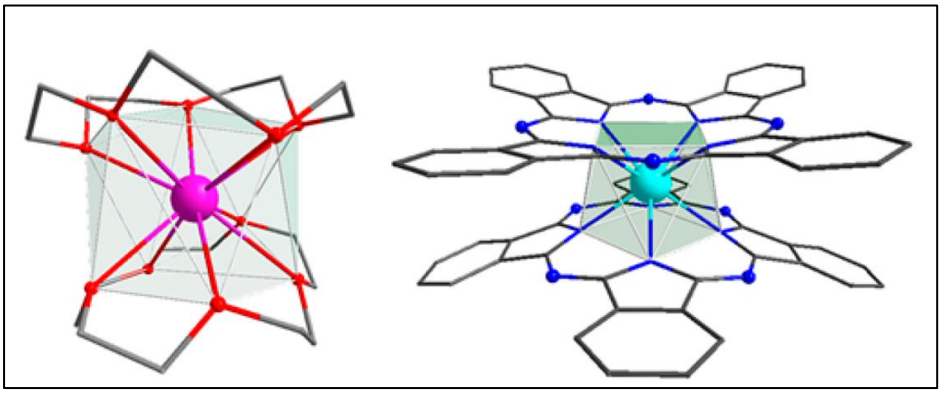

Figure 2.1 Molecular structures of the sandwich complexes $[Sm(15C5)_2]^{3+}$ (**2.1**, left) and $[Ln(P_c)_2]^-$ (**2.2**, right).[113]

In addition to their applications in supramolecular host–guest chemistry, the photoluminescence properties of Ln(III) crown ether complexes have also been exploited for the development of luminescent probes.[44] It occurred to us therefore that the emission spectra of *4f* crown ether complexes might also provide important information regarding the Stark splitting of the ground-state $^{2S+1}L_J$ multiplet of the 4*f*-ion into its component m_J microstates or sub-levels.[53,54] In theory, the energies of the aforementioned microstates can be gleaned spectroscopically via a Gaussian fit of the fine structure of the highest-energy emission band; however, in practice this can be quite challenging, and only a handful of Ln(III) complexes with well-resolved emissive bands have been successfully fit to date.[53,54,66,104–106] Given the abilities of the smaller crown ether ligands to coordinate metal cations in sandwich-type topologies, we proposed that the range of available crown ether macrocycles might afford Ln-SMMs, through which the effects of structural variation on

magnetic properties could be studied in a systematic manner. The Pilkington group therefore set out to investigate their coordination chemistry with select *4f* ions and to investigate the structural and magneto-optical properties of the resulting complexes. In the first study, 15C5 and 12C4 macrocycles were employed together with $Dy(ClO_4)_3$ for the preparation of two mononuclear complexes namely, the half- and pseudo-sandwich complexes **2.3** and **2.4**, respectively (Figure 2.2).[66]

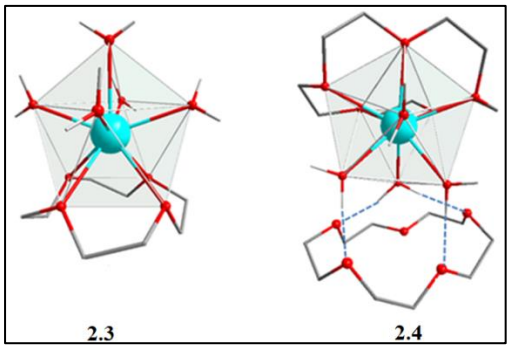

Figure 2.2 Half- and pseudo sandwich topologies of Dy(III) complexes of 12C4 (**2.3**), and 15C5 (**2.4**).[113]

For these two complexes, magneto-optical and theoretical studies revealed that, despite their comparable O9 coordination spheres, they display remarkably different magnetic properties with only the 15C5 Dy(III) complex displaying SMM behavior in zero field.[66] Given these differences and in order to shed more light as to how the structures of the coordination complexes affect the magnetization dynamics, in this project we set out to investigate further the coordination chemistry of 15C5 macrocycles with select *4f* ions. In order to accomplish this, we first set about changing the lanthanide salt from perchlorate to nitrate since we anticipated that in addition to balancing the charge, the nitrate counterions might also act as coordinating and/or bridging counterions, affording diverse structural topologies with interesting magnetic properties.

2.2 Experimental section

2.2.1 Synthesis of 15-crown-5 complexes

All reagents were supplied by Sigma-Aldrich and used without further purification, unless otherwise stated.

Preparation of $\{[Dy(NO_3)_3(H_2O)_2(CH_3OH)]\cdot(15C5)\}_n\cdot 0.5H_2O$ (2.5):

15-crown-5 (205 μL, 1.04 mmol) was added in one portion to a solution of $Dy(NO_3)_3\cdot 5H_2O$ (655 mg, 1.04 mmol) in MeOH/MeCN (1:3, 6 mL). The solution was heated to 55 °C and vigorously stirred for 3 h. After cooling to room temperature, the solution was filtered through a plug of cotton wool and left to slowly evaporate at room temperature. After 3 weeks, single crystals of **2.5** were isolated as colorless plates. Yield = 13%. IR (cm^{-1}): 3215 (br), 2921 (w), 2883 (w), 1655 (w), 1453 (m), 1295 (s), 1268 (s), 1088 (s), 943 (m), 840 (w), 814 (w), 741 (m), 656 (w). UV−vis (MeOH, nm): λ_{max} = 270 (ε = 1080 L mol^{-1} cm^{-1}). FAB-MS: *m/z* = 598 $[M-3H_2O]^+$. Anal. Calcd for $C_{11}H_{29}O_{17.5}N_3Dy$: C, 20.46; H, 4.30; N, 6.51%. Found: C, 20.19; H, 4.30; N, 6.51%.

Preparation of $\{[Tb(NO_3)_3(H_2O)_2(CH_3OH)]\cdot(15C5)\}_n\cdot 2H_2O$ (2.6):

$Tb(NO_3)_3\cdot 5H_2O$ (469 mg, 1.08 mmol) and 15-crown-5 (214 μL, 1.08 mmol) were vigorously stirred in CH_3OH/CH_3CN (1:3, 6 mL) at 55 °C for 3 h. After cooling to room temperature, the reaction mixture was filtered through a plug of cotton wool and the solvent was evaporated to yield a viscous yellow solid. The solid was re-dissolved in a 1:3 mixture of $MeOH/CH_3CN$ (6 mL) and left to crystallize via slow evaporation to yield, after 3 weeks, light brown single crystals of **2.6** suitable for X-ray diffraction. Yield = 44%. IR (cm^{-1}): 3209 (br), 2921 (w), 2883 (w), 1656 (w), 1458 (m), 1295 (s), 1267 (s), 1090 (s), 1022 (m), 943 (s), 840 (w), 813 (w), 741 (m), 649 (w). UV−vis (MeOH, nm): λ_{max} = 208

(ε = 7050 L mol^{-1} cm^{-1}). FAB-MS: *m/z* = 508 $[M-2H_2O-CH_3OH-NO_3^-]^+$. Anal. Calcd for $C_{11}H_{28}N_3O_{17}Tb$: C, 19.48; H, 4.90; N, 6.19%. Found: C, 19.47; H, 4.55; N, 6.27%.

2.2.2 Physical measurements

Infrared spectroscopy: Infrared (IR) spectra were measured on a Bruker Alpha FT-IR spectrometer.

UV−visible studies: UV−visible studies (UV-vis) data were collected on a Beckman Coulter DU 720 General-Purpose UV− visible spectrophotometer.

Mass spectrometry: Data were measured on a Carlo Erba/Kratos GC/MS acquisition system and processed using a SPARC workstation.

Elemental analysis: Elemental analysis (C, H, and N) data were collected by Atlantic Microlab.

X-ray Crystallography measurements: Suitable single crystals were mounted on a cryoloop with paratone oil and measured on a Bruker APEX-II, Kappa CCD X-ray diffractometer equipped with an Oxford Cryoflex device. X-ray data were collected at 150(2) K with Mo Kα radiation (λ = 0.710 73 Å) using the Bruker APEX II software.[107,108] SAINT was used for cell refinement and data-reduction. A multiscan absorption correction was applied to the data using the SADABS program.[109] The structures of the complexes were solved by direct methods (SHELXS-97)[110] and refined using SHELXL-2014 in the Bruker SHELXTL suite.[110] Hydrogen atoms were added at calculated positions and refined with a riding model. Disordered solvent was removed using the SQUEEZE procedure in PLATON.[111] A Summary of crystallographic data for complexes **2.5** and **2.6** is presented in Table 2.1.

Complex	Dy (2.5)	Tb (2.6)
Chemical formula	$CH_8DyN_3O_{12}·C_{10}H_{20}O_5$	$C_{11}H_{28}N_3O_{17}Tb$
M_r	636.86	633.28
Crystal system, space group	Monoclinic, $P2_1/c$	Monoclinic, $P2_1/c$
Temperature (K)	150(2)	150(2)
a, (Å)	16.6173 (13)	17.1899 (8)
b, (Å)	16.0429 (13)	16.5885 (8)
c, (Å)	16.6959 (13)	16.1637 (8)
β (°)	89.978 (4)	100.467 (2)
V (Å^3)	4451.0 (6)	4532.5 (4)
Z	8	4
Radiation type	Mo *K*α	Mo *K*α
μ (mm^{-1})	3.44	1.60
Crystal size (mm)	0.31 × 0.30 × 0.28	0.3 × 0.3 × 0.3
T_{min}, T_{max}	0.523, 0.757	0.549, 0.754
No. of measured, independent and observed [$I > 2\sigma(I)$] reflections	92922, 16831, 15785	27230, 7454, 7325
R_{int}	0.046	0.053
$(\sin\theta/\lambda)_{max}$ (Å^{-1})	0.796	0.595
$R[F^2 > 2\sigma(F^2)]$, $wR(F^2)$, *S*	0.045, 0.089, 1.16	0.119, 0.274, 1.13
No. of reflections	16831	7454
No. of parameters	593	242
No. of restraints	12	7
$\Delta\rho_{max}$, $\Delta\rho_{min}$ (e Å^{-3})	2.75, −2.50	2.95, −6.65

Table 2-1 Summary of select crystallographic data for complexes **2.5** and **2.6**.

Magnetic measurements: Variable-temperature magnetic measurements were carried out in house by Dr. Emma Gavey on freshly prepared crushed single crystals of the two complexes. Both samples were encapsulated in a diamagnetic gelatin sample holder. Pascal's constants were used to estimate the diamagnetic corrections, which were subtracted from the experimental susceptibilities to afford the molar paramagnetic susceptibility (χ_M). Direct current susceptibility data were collected on a Quantum Design

SQUID MPMS magnetometer in an applied field of 0.1 T, from 5 to 300 K. Alternating current measurements were made using a Quantum Design PPMS magnetometer. The first set of ac measurements were collected at 2 K, with frequencies in the range 10−1000 Hz and static fields from 0 to 5000 Oe with a 5 Oe oscillating field. A second set of ac measurements were collected with 13 frequencies between 50 and 10000 Hz below 10 K and 7 frequencies between 10−15 K, with static applied fields between 0 and 0.2 T and a 3.5 Oe oscillating field.

Photoluminescence Spectroscopy: Photoluminescence studies were carried out in collaboration with Dr. Maria Rute Ferriera, University of Aveiro, Portugal. Photoluminescence data for **2.5** and **2.6**, were measured at 300 and 14 K, on a modular double-grating excitation spectrofluorimeter equipped with a TRIAX 320 emission monochromator (Fluorolog-3, Horiba Scientific), coupled to an R928 Hamamatsu photomultiplier, using a front-face acquisition mode. A 450 W Xe arc lamp was used as the excitation source. The excitation spectra were corrected for the spectral distribution of the lamp intensity with a photodiode reference detector, and the emission spectra were corrected for the detection and optical spectral response of the spectrofluorimeter. The emission decay curves for **2.5** at 300 K were measured using a pulsed Xe−Hg lamp (6 ms pulse at half width and 20−30 × 10^{-6} s tail). Furthermore, for **2.5** the decays were acquired on a Fluorolog TCSPC spectrofluorometer (Horiba Scientific) coupled to a TBX-04 photomultiplier tube module (950 V), with 200 ns time-to-amplitude converter and 70 ns delay; the excitation source was a Horiba Jobin Yvon pulsed diode (NanoLED-390, peak at 390 nm, 1.2 ns pulse duration, 1 MHz repetition rate, and 150 ns synchronization delay). The absolute emission quantum yields were measured at 300 K using a Hamamatsu

(C9920-02) quantum yield measurement system equipped with a 150 W xenon lamp coupled to a monochromator for wavelength discrimination, an integrating sphere as the sample chamber, and a multichannel analyzer for signal detection. Data was collected for each sample in triplicate, and the average value is reported to an accuracy of within 10%.

***Ab initio* calculations:** *Ab initio* calculations of the CASSCF + RASSI/SINGLE_ANISO type were performed on **2.5** and **2.6** by Jeffrey Regier using the MOLCAS quantum chemistry package.[112] The calculations were performed using coordinates determined from single-crystal X-ray diffraction without any further geometry optimization. For both complexes, the structural model that best describes the coordination sphere of the Ln(III) ions comprises a [Ln(III)$(NO_3)_3(OH_2)$(MeOH)] core plus the two H-bonded uncoordinated 15C5 macrocycles. For **2.5**, because of the inversion symmetry, one Dy(III) center was calculated while the other magnetic center was replaced with a diamagnetic Lu(III) ion. The complete active space approach was used, where the active space was chosen to include the nine electrons of the seven 4*f* orbitals. Relativistic basis sets from the ANO-RCC library were used exclusively for all calculations. For a determination of whether the choice of basis sets influences the calculations, two types of basis sets (long and short) were used as summarized in Table 5-14 in the Appendix section of the thesis. Strong, spin-orbit coupling was included in the CASSI procedure which uses the spin-free eigenstates of the CASSCF procedure as the elements in the state interaction determinant. In the CASSCF procedure, 21 roots were used for the sextets, and 224 roots were used for the quartets. The doublet configurations were omitted because of limited computer resources. In the state interaction procedure, strong spin−orbit coupling was introduced into the calculation in the RASSI module, where 21 sextet and 128 quartet spin-free states were

mixed. The doublet states were omitted because of limited computer resources. Local magnetic properties were calculated in the SINGLE_ANISO module which uses the resulting spin−orbit multiplets from the RASSI procedure. The g-tensors of each of the Kramers doublets (KDs) were calculated using the $S = 1/2$ pseudospin formalism.

2.3 Results and discussion

2.3.1 Synthesis and structural studies

As previously mentioned, following initial studies on *4f* complexes of crown ether macrocycles,[65] We set out to further investigate the coordination chemistry of 15C5 macrocycles with *f*-block ions, by first changing the counter ion of the metal salt from perchlorate to nitrate. In this context, reaction of one equivalent of 15C5 and $Ln(NO_3)_3$ in a 1:3 mixture of methanol and acetonitrile afforded single crystals of H-bonded chains of formula $\{[Ln(NO_3)_3(H_2O)_2(CH_3OH)]\cdot(15C5)\}_n$, where Ln-(III) = Dy (**2.5**) and Tb (**2.6**). Selected bond lengths and angles for the two complexes are presented in Table 5-1 and Table 5-2 of the Appendix section of this thesis.

Both complexes crystallize in the monoclinic space group $P2_1/c$, with similar unit cells, but are not isostructural (Table 2.1). The asymmetric unit of **2.5** is comprised of two independent, 9-cooordinate $[Dy(NO_3)_3(H_2O)(CH_3OH)]$ units that are H-bonded to the oxygen atoms of two crystallographically independent 15C5 macrocycles affording a 1-D chain topology, (Figure 2.3). For the Dy1 ion, intermolecular H-bonding interactions between the O10 coordinated water molecule and O25 and O29 of a 15C5 macrocycle are 1.855 and 1.838 Å, and those between the O11 coordinated water molecule and O32 and O34 of a second 15C5 macrocycle are 1.858 and 1.845 Å. For the second Dy2 ion, the water O22 is H-bonded to O25 and O28 (1.903 and 1.797 Å) of one crown, and O23 is H-

bonded to O30 and O33 of the second crown (1.830 and 1.833 Å). In addition, the H atoms of two coordinated methanol ligands are also H-bonded to an oxygen atom of a neighboring 15C5 macrocycle in the chain such that O12−H12···O26 = 2.356 Å and O24−H24···O31 = 2.190 Å. The Dy−O bond in the complex distances are 2.329(4)−2.480(4) Å for Dy1 and 2.343(4)−2.453(4) Å for Dy2.

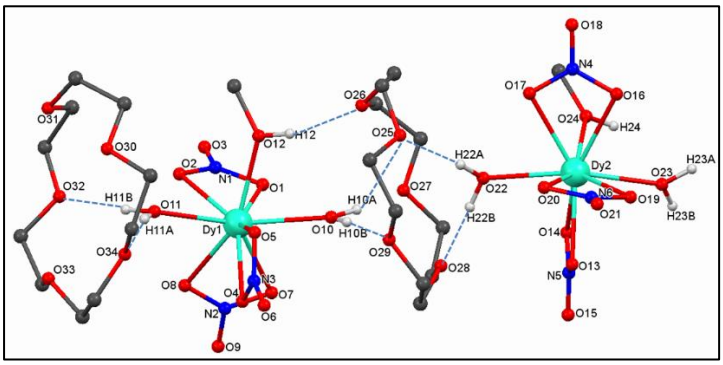

Figure 2.3 Molecular structure of the asymmetric unit of $\{[Dy(NO_3)_3(H_2O)_2(CH_3OH)]\cdot(15C5)\}_n$ (**2.5**) with appropriate atomic numbering scheme. H-bonds are shown as blue dashed lines. Only selected H-atoms are shown.[113]

Shape analyses[114] of the two Dy(III) centers reveal that they are closest to 9-coordinate, spherical capped square antiprismatic geometry, with continuous shape measures (CSMs) of 1.81 and 1.96 for Dy1 and Dy2, respectively (Table 2-2), which confirms their deviation from idealized capped square antiprismatic polyhedra (Figure 2.4).

Polyhedron	Symmetry	CSM Dy1	CSM Dy2
EP-9	D_{9h}	34.89	34.13
OPY-9	C_{8v}	22.74	22.17
HBPY-9	D_{7h}	18.32	17.08
JTC-9	C_{3v}	13.63	13.22
JCCU-9	C_{4v}	9.91	9.77
CCU-9	C_{4v}	8.52	8.39
JCSAPR-9	C_{4v}	2.96	3.00

CSAPR-9	C_{4v}	1.81	1.96
JTCTPR-9	D_{3h}	3.33	3.09

Table 2-2 Continuous shape measures (CSMs) of the 9-coordinate Dy(III) coordination polyhedron in the Dy complex **2.5**. The value in red indicates the closest polyhedron according to the CSMs. Abbreviations: EP-9, Enneagon; OPY-9, Octagonal pyramid; HBPY-9, Heptagonal bipyramid; JTC-9, Johnson triangular cupola J3; JCCU-9, Capped cube J8; CCU-9, Spherical-relaxed capped cube; JCSAPR-9, Capped square antiprism-Johnson; CSAPR-9, Spherical capped square antiprism ; JTCTPR-9, Tricapped trigonal prism J51.[113]

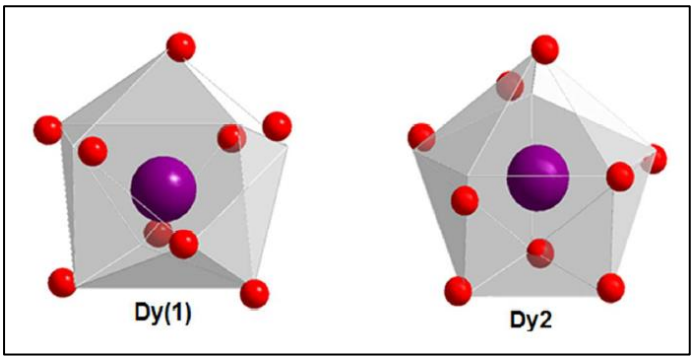

Figure 2.4 Coordination geometry of the Dy1 and Dy2 cations superimposed on an idealized capped square antiprism for Dy1 and Dy2 in complex **2.5**.[113]

Detailed analysis of the crystal packing of **2.5** reveals that the chains pack along the *c*-axis of the unit cell, stabilized by interchain H-bonding interactions from a nitra to oxygen atom of one chain to the CH proton from an uncoordinated 15C5 macrocycle of a neighboring chain, such that O20···H7−C7 = 2.506(2) Å (Figure 2.5). The intrachain Dy···Dy distances are 8.809(8) and 8.806(8) Å, and the shortest interchain distances are 8.854(7) Å, which are slightly shorter than the Dy···Dy distances of 8.880(8) and 8.875(5) Å, previously reported for the half- and pseudo-sandwich complexes, respectively.[66]

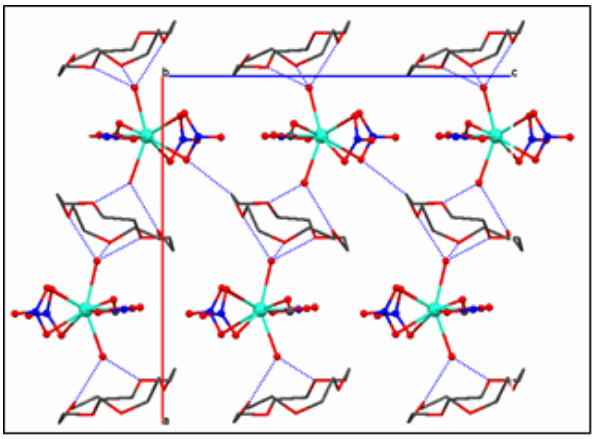

Figure 2.5 Crystal packing of **2.5**. H-atoms are removed for clarity. View down the *b*-axis of the unit cell. H-bonding interactions are shown as blue dashed lines.[113]

The Tb complex, **2.6** crystallizes with one $[Tb(NO_3)_3(OH_2)(MeOH)]$ unit H-bonded via its two ligated water molecules to 15C5 macrocycles, such that O11−H11A···O15 = 1.76, O11−H11B···O15 = 1.77 Å, O10−H10A···O16 = 1.87 and O10−H10B···O14 = 1.71 Å, (Figure 2.6). The Tb−O bond distances are in the range 2.318(9) – 2.5261(12) Å. Continuous shape analysis[114] of the *4f* ion reveals that, like the Dy(III) ions in **2.5**, it adopts a 9-coordinate geometry that is closest to spherical capped square antiprismatic, (Figure 2.7) with a CSM of 2.29, (Table. 2.5).

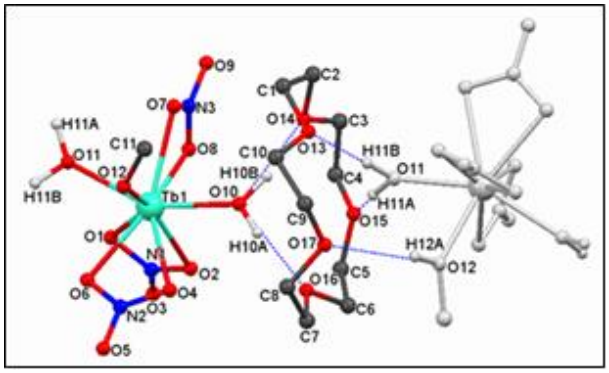

Figure 2.6 Molecular structure of $\{[Tb(NO_3)_3(H_2O)_2\ (CH_3OH)]\cdot(15C5)\}_n$ (**2.6**) with appropriate atomic numbering scheme. Interchain H-bonding interactions are shown as

blue dashed lines. The crystallographically unique atoms in the asymmetric unit are shown in colour.[113]

Polyhedron	Symmetry	Tb(III) CSM
EP-9	D_{9h}	34.01
OPY-9	C_{8v}	22.10
HBPY-9	D_{7h}	18.20
JTC-9	C_{3v}	13.96
JCCU-9	C_{4v}	10.31
CCU-9	C_{4v}	9.05
JCSAPR-9	C_{4v}	3.22
CSAPR-9	**C_{4v}**	**2.29**
JTCTPR-9	D_{3h}	3.26

Table 2-3 Continuous shape measures (CSMs) of the 9-coordinate Tb(III) coordination polyhedron in **2.6**. The value in red indicates the closest polyhedron according to the CSMs. Abbreviations: EP-9, Enneagon; OPY-9, Octagonal pyramid; HBPY-9, Heptagonal bipyramid; JTC-9, Johnson triangular cupola J3; JCCU-9, Capped cube J8; CCU-9, Spherical-relaxed capped cube; JCSAPR-9, Capped square antiprism-Johnson; CSAPR-9, Spherical capped square antiprism ; JTCTPR-9, Tricapped trigonal prism J51.[113]

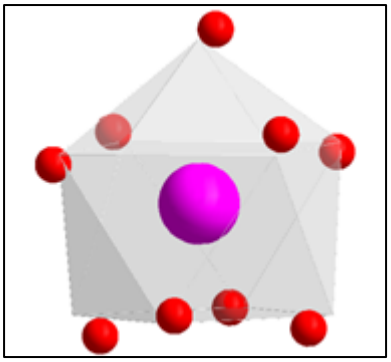

Figure 2.7 Coordination geometry of Tb(III) cation superimposed on an idealized capped square antiprism for **2.6**.[113]

Further analysis of the crystal structure of **2.6** reveals that the molecules pack as H-bonded chains that are aligned co-parallel along the *b*-axis of the unit cell, with interchain H-bonding interactions between nearest neighbors giving rise to 2-D sheets (Figure 2.8a). Interestingly, perpendicular to these sheets there are very large channels that accommodate disordered solvent molecules which were removed from the crystallographic model, but serve to magnetically isolate the Tb(III) ions in the chains along the *a*-direction (Figure 2.8b).

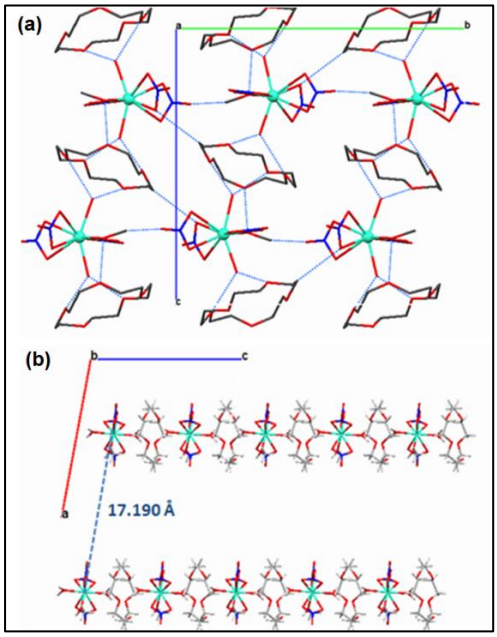

Figure 2.8 (a), Crystal packing of **2.6** showing the 1-D chains that are connected via inter-chain H-bonds to afford 2D-sheets in the *bc* plane; b) view down the *b*-axis of the unit cell showing the large channels between the 2-D layers. The Tb···Tb distance between the sheets is shown as a blue dashed line. H-atoms are omitted for clarity.[113]

2.3.2 Magnetic studies

Direct current susceptibility measurements (dc) were carried out on freshly prepared crystalline samples of **2.5** and **2.6** in an applied static field of 0.1 T between 5

and 300 K (Figure 2.9 and Figure 2.10). Above 15 K, both complexes display Curie Weiss behavior with Curie constants of 13.86 and 12.02 $cm^3\ mol^{-1}\ K$, in excellent agreement with the theoretical values of 14.17 and 11.82 $cm^3\ mol^{-1}\ K$ for non-interacting Dy(III) ($^6H_{15/2}$, S = 5/2, g = 4/3) and Tb(III) ($^7F_6$, S = 3, g = 3/2) ions, respectively. For both complexes, the decrease in $\chi_M T$ below 50 K is likely due to the thermal depopulation of excited Stark sub-levels within the ground multiplet of the respective *4f* ion.[66]

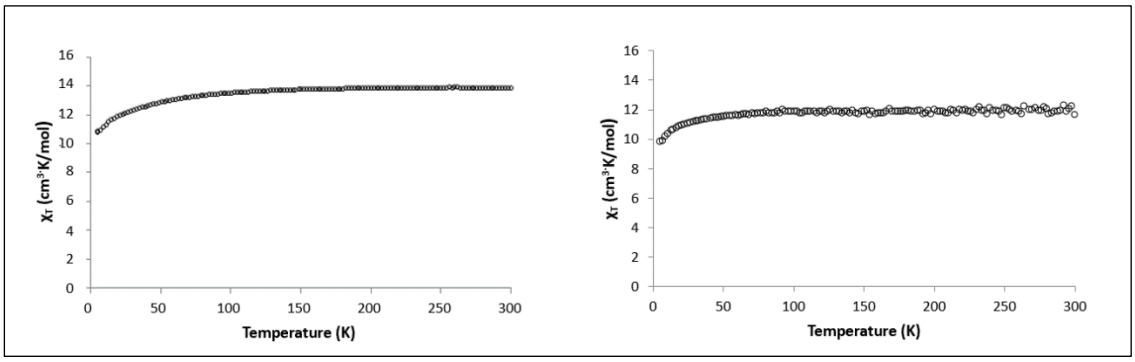

Figure 2.9 Plots of $\chi_M T$ *vs*. T for **2.5** (left) and **2.6** (right) in a 0.1 T field, from 5-300 K.[113]

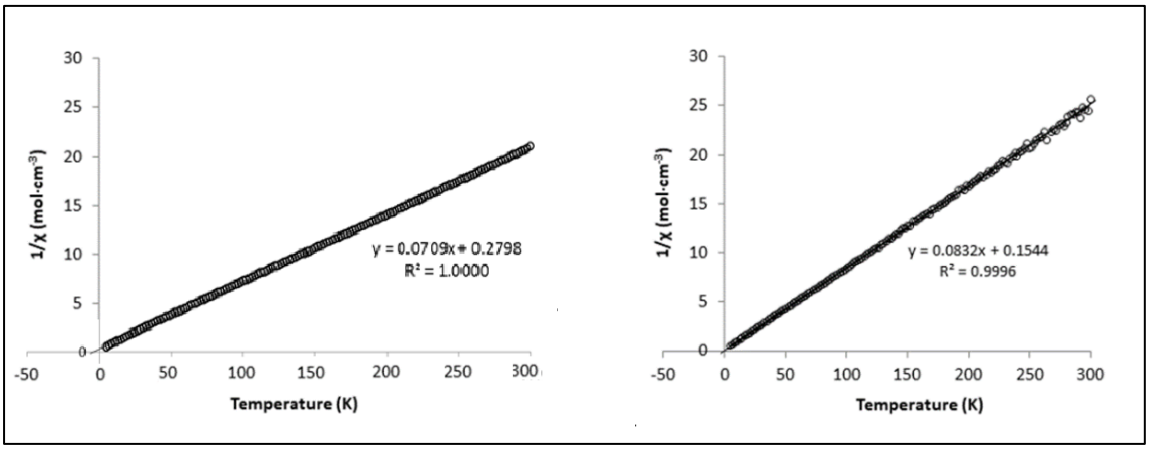

Figure 2.10 Plots of $1/\chi$ *vs*. T for **2.5** (left) and **2.6** (right) from 5-300 K. The black line is a best-fit to the Curie-Weiss law, giving Weiss constants θ of -3.95 K and -1.86 K.[113]

Alternating current susceptibility measurements (ac) were carried out on both complexes in an oscillating field of 3.5 Oe in zero and non-zero static fields, between 2

and 15 K, using frequencies between 50 and 10000 Hz. Additional field-dependent measurements at 2 K were recorded in fields up to 5000 Oe, with frequencies ranging from 30 to 1000 Hz. The Dy complex **2.5** displays no frequency-dependent signals in zero field, most likely because of fast quantum tunnelling mechanisms. However, when a series of static fields between 300 and 2000 Oe were applied to suppress QTM, the out-of-phase χ'' components of the susceptibility show a clear frequency dependence, consistent with SMM behavior, (Figure 2.11).

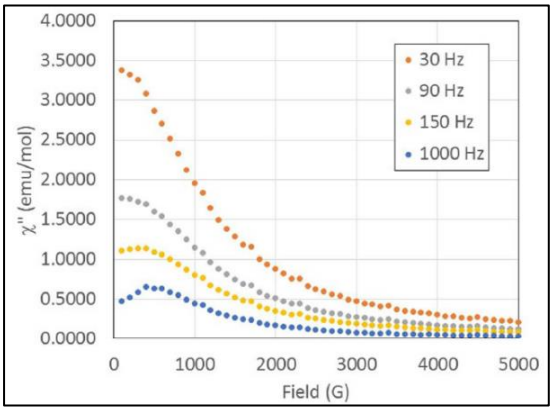

Figure 2.11 Plot of χ'' *vs* field for **2.5** at 2 K, displaying selected data from experimental frequencies measured between 30 and 1000 Hz.[113]

Plots of χ'' versus temperature in an applied field of 2000 Oe (Figure 2.12) reveal that, at higher ac frequencies, well-resolved maxima in χ'' can be observed below 5 K with partial resolution of the maxima into two components observed at the upper limit of our hardware setup (10000 Hz), indicating the presence of two relaxation pathways.

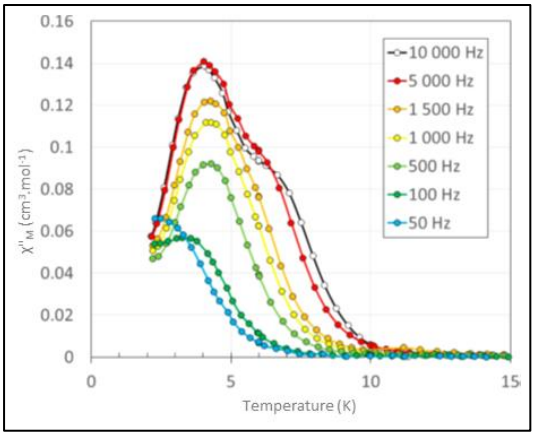

Figure 2.12 Out-of-phase χ''_M *vs* T plot for **2.5** in a 2000 Oe applied field from 3-10 K.[113]

When these data are replotted in the form of χ'' versus frequency at different temperatures (Figure 2.13a), we again see the diagnostic frequency-dependence of the out-of-phase susceptibility expected for SMM behavior, with well-resolved maxima emerging below 6.4 K. Upon further cooling below 4 K (Figure 2.13b), a significant change in the temperature-dependence of χ'' is observed in which the maximum in χ'' around 6000 Hz decreases in intensity and a low-frequency "tail" begins to emerge, although no low frequency maximum could be observed down to 2 K.

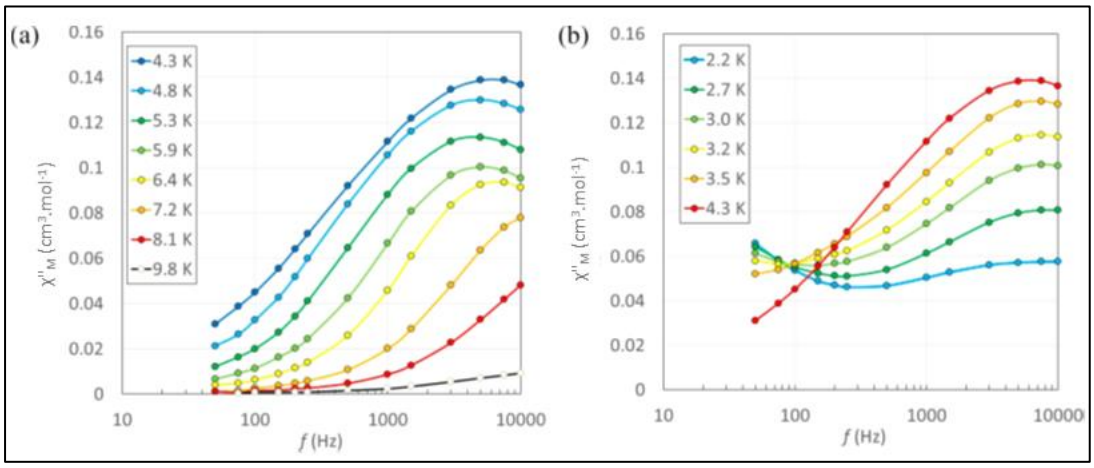

Figure 2.13 Out-of-phase χ''_M *vs* frequency plot for **2.5** in a 2000 Oe applied field: (a) from 9.8 to 4.3 K and (b) from 4.3 to 2.2 K (the lines are a guide for the eye).[113]

The evolution of the temperature-dependence behaviour reflects a change in the dominant relaxation processes occurring in this system upon cooling. Ac measurements in other static fields are shown in Figure 2.14.

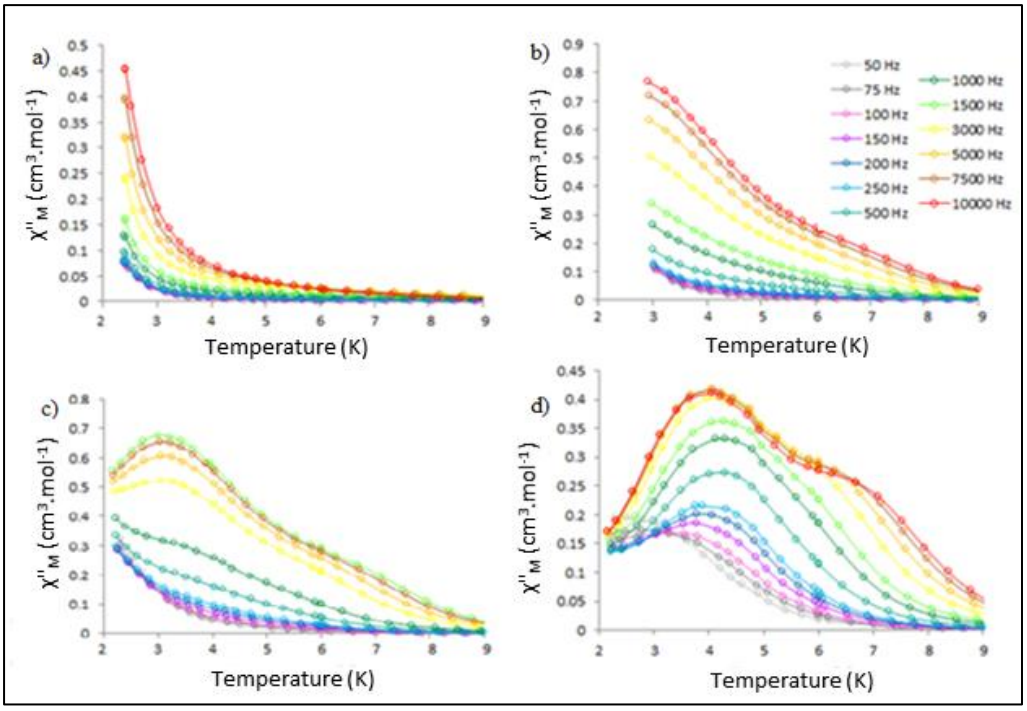

Figure 2.14 (a to d) out-of-phase χ''_M *vs* T plots for **2.5** in 300, 800, 1000 and 2000 Oe applied fields from 3-10 K, showing the resolution of two maxima as QTMs are supressed.[113]

For an investigation into these relaxation pathways, further Cole−Cole plots were examined at different temperatures (Figure 2.15, left).

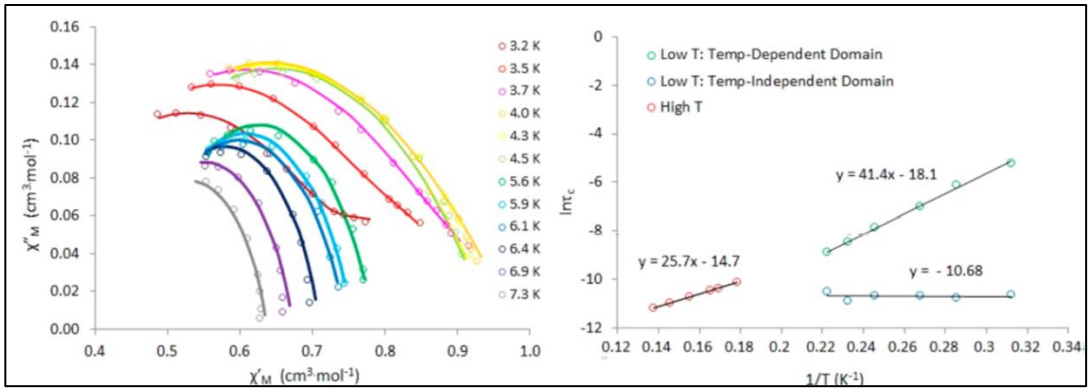

Figure 2.15 Modeled out-of-phase χ″ vs in-phase χ′ in a 2000 Oe applied field with kinks in the Cole−Cole semicircles clearly visible below 5 K (the lines represent the fit to the Cole−Cole equations) (left). Fit of the data to the Arrhenius model (right).[113]

In the low-temperature region below 5 K, several of the χ′ versus χ″ semicircles are visibly kinked, indicative of two partially merged arcs, each corresponding to a distinct relaxation domain. This behavior is reminiscent of the previously studied 15C5 sandwich-type complex and was therefore modeled using two combined modified Debye functions.[66,106] In this respect, the Arrhenius plot for the relaxation comprises two regions: at high temperature, the Cole−Cole data were best fit as a single relaxation process whereas at low temperature, a two- component Debye term was used.

The Cole-Cole model describes the ac susceptibility as:

$$\boldsymbol{\chi(\omega) = \chi_S + \frac{\chi_T - \chi_S}{1 + (i\omega\tau_c)^{1-\alpha}}} \qquad \textbf{Eqn. 2.1}$$

Where $\omega = 2\pi f$, χ_T is the isothermal susceptibility, χ_S is the adiabatic susceptibility, τ_c is the temperature-dependent relaxation time, and α is a measure of the dispersivity of relaxation times, with $\alpha = 0$ reflecting a single Debye-like relaxation time and $\alpha = 1$ reflecting an infinitely wide dispersion of τ_c values.

Dividing Eqn. 2.1 into its in-phase and out-of-phase components gives:

$$\chi'(\omega) = \chi_S + \frac{(\chi_T - \chi_S)}{2}\left\{-\frac{\sinh[(1-\alpha)\ln(\omega\tau_c)]}{\cosh[(1-\alpha)\ln(\omega\tau_c)] + \cos\left[\frac{1}{2}(1-\alpha)\pi\right]}\right\} \quad \textbf{Eqn. 2.2}$$

$$\chi''(\omega) = \frac{(\chi_T - \chi_S)}{2}\left\{-\frac{\sin\left[\frac{1}{2}(1-\alpha)\pi\right]}{\cosh[(1-\alpha)\ln(\omega\tau_c)] + \cos\left[\frac{1}{2}(1-\alpha)\pi\right]}\right\} \quad \textbf{Eqn. 2.3}$$

In the case of complex **2.5**, the susceptibility behavior below 5 K is due to contributions from two distinct relaxation pathways. The relaxation in this temperature region can thus be described by the sum of two combined, modified Debye functions shown below:

$$\chi(\omega) = \chi_{S1} + \frac{\chi_{T1} - \chi_{S1}}{1 + (i\omega\tau_{c1})^{1-\alpha 1}} + \chi_{S2} + \frac{\chi_{T2} - \chi_{S1}}{1 + (i\omega\tau_{c2})^{1-\alpha 2}} \quad \textbf{Eqn. 2.4}$$

Dividing Eqn. 2.4 into its in-phase and out-of-phase components gives:

$$\chi'(\omega) = \chi_S + (\chi_{T1} - \chi_S)\left\{\frac{1 + (\omega\tau_{c1})^{1-\alpha_1}\sin(\pi\alpha_1/2)}{1 + (\omega\tau_{c1})^{1-\alpha_1}\sin(\pi\alpha_1/2) + (\omega\tau_{c1})^{2-2\alpha_1}}\right\} + (\chi_{T2} - \chi_S)\left\{\frac{1 + (\omega\tau_{c2})^{1-\alpha_2}\sin(\pi\alpha_2/2)}{1 + (\omega\tau_{c2})^{1-\alpha_2}\sin(\pi\alpha_2/2) + (\omega\tau_{c2})^{2-2\alpha_2}}\right\} \quad \textbf{Eqn. 2.5}$$

where $\chi_S = \chi_{S1} + \chi_{S2}$

The Arrhenius equation, relating relaxation time τ_c to temperature T, is given by:

$$\tau_c = \tau_0 e^{U_{eff}/k_B T} \quad \textbf{Eqn. 2.6}$$

where τ_0 is the tunneling rate and U_{eff} is the effective energy barrier. The temperature-dependence of the relaxation can be written in terms of different relaxation mechanisms:

$$\tau^{-1} = \tau_0^{-1} exp\left(-\frac{U_{eff}}{k_B T}\right) + AB^m T + CT^n + D \quad \textbf{Eqn. 2.7}$$

Here, the first term refers to the thermally activated Orbach type relaxation with the latter terms reflecting direct, Raman, and quantum tunnelling processes, respectively, where m = 2 and n = 5 for Kramers ions such as Dy(III).[115] Above 5 K, the data were fitted to a single thermally activated process [U_{eff} = 26 K (18 cm^{-1}), $\tau_0 = 4.10 \times 10^{-7}$ s], consistent

with an Orbach mechanism. In the low-temperature region, the separation of the relaxation processes reflects the persistence of an Orbach process [U_{eff} = 41 K (29 cm^{-1}), $\tau_0 = 1.35 \times 10^{-8}$ s] coupled with a temperature-independent term consistent with a quantum tunnelling mechanism ($\tau_0 = 2.30 \times 10^{-5}$ s) arising from tunnelling between $\pm m_J$ levels of the ground state. We emphasize here that the poor deconvolution of the two relaxation processes gives rise to considerable uncertainty in the fitting of the Cole−Cole data. Nevertheless, the features in the χ'' *vs* T data (Figure 2.12) and the marked temperature dependence of the χ'' *vs* frequency data (Figure 2.13) are all consistent with two relaxation processes in the low-temperature regime. Furthermore, the α parameters of 0.28−0.45 for domain A and 0.39−0.44 for domain B suggest that multiple relaxation processes are at play. In sharp contrast, ac susceptibility studies on the corresponding Tb(III) analogue **2.6** in both zero and applied static dc fields showed no frequency-dependence, (Figure 2.16) and thus, we conclude that this complex displays no SMM behavior. As previously explained, Tb(III) ions require an appropriate axial crystal field in order to display slow relaxation of the magnetization and *ab initio* studies were therefore carried out in order to shed more light on this observation, (*vide infra).*

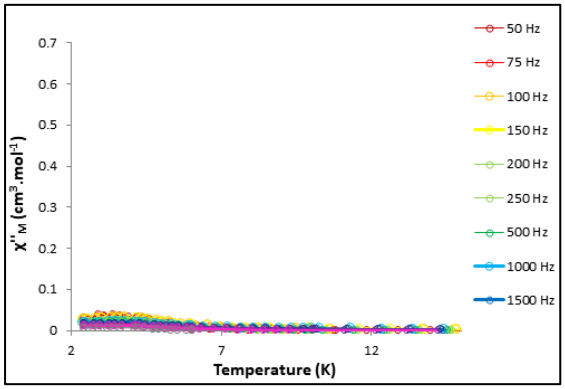

Figure 2.16 Plot of χ'' *vs* T for **2.6** in zero dc field below 15 K, showing no frequency dependence in χ'', consistent with rapid relaxation of the magnetization.[113]

2.3.3 *Ab initio* studies

To help us understand further the dynamic magnetic properties of these two complexes, *ab initio* calculations were carried out using the MOLCAS 8 quantum chemistry package.[112] For both complexes, the structural model that best describes the coordination sphere of the Ln(III) ions comprises a [Ln(III)$(NO_3)_3(OH_2)$-(MeOH)] core plus the two H-bonded uncoordinated 15C5 macrocycles (Model 1, Figure 2.17).

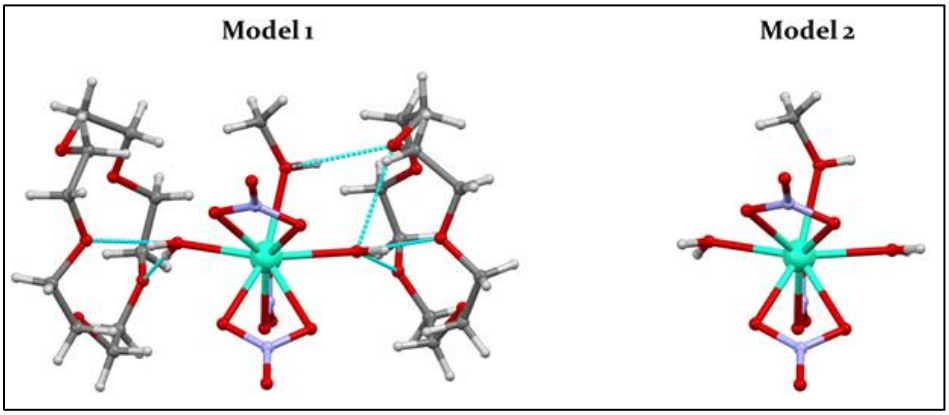

Figure 2.17 Crystallographic models used for the *ab initio* calculations of **2.5** and **2.6** comprising of a [Ln(III)$(NO_3)_3(OH_2)_2$(MeOH)] core for the small model (Model 2) and the additional two hydrogen bonded benzo-15C5 molecules for the larger model (Model 1). H-bonds are shown as blue dashed lines.[113]

For **2.1**, the relative energies and the directionality of the main anisotropy axes of the KD in the $^6H1_{5/2}$ ground state of the Dy(III) ion were evaluated. The main magnetic axes of the ground- and first-excited-state KDs are summarized in Table 5-18 in the Appendix section of the thesis and projected onto the symmetry axis of the molecule in Figure 2.18.

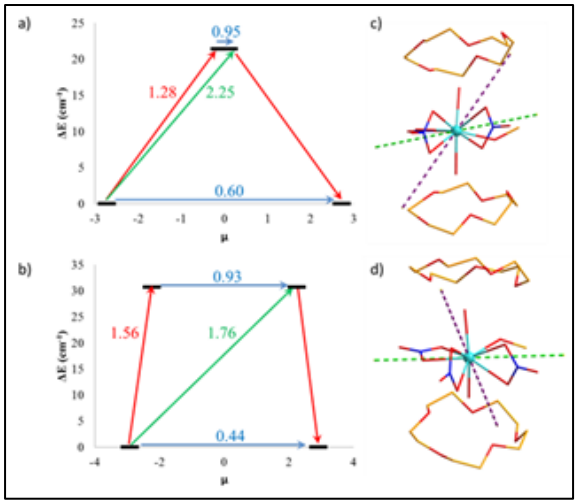

Figure 2.18 (a, b) Plots of KD1± and KD2± for Dy1 and Dy2 in **2.5** showing the average matrix elements of the transition moments between states (numbers next to arrows) for Model 1, long basis set. Red arrows are used for thermally activated transitions, blue arrows for ground and excited QTM, and green arrows for Orbach spin−lattice relaxation. (c, d) Crystal structures of Dy1 and Dy2 coordination spheres showing the H-bonded crown ethers and the main magnetic axes of the ground (green) and first-excited (purple) KDs.[113]

The calculations reveal that both the ground- and first-excited-state Kramers doublets (KD1± and KD2±, respectively) contain a significant contribution from the transverse g_{xy} parameters, deviating significantly from Ising with g_z values of 16.360 and 13.183, respectively, for Dy1 and 17.474 and 12.391 for Dy2. For both crystallographically unique Dy(III) ions, the ground wave functions consist of mainly $m_J = \pm 15/2$, whereas the first excited state includes a large contribution from all m_J states. Examination of the magnitude of the matrix elements between the KD1± and KD2± spin states (0.60 for Dy1 and 0.44 for Dy2) reveals that QTM involving the ground-state doublets of both ions is accessible in a zero-dc field. In addition, the large matrix element connecting the ground and first excited state of opposite spin for both ions also supports the presence of a second,

thermally assisted relaxation process (Figure 2.18). In the presence of a small applied dc field, QTM involving the ground state of the two Dy(III) ions is suppressed. In this case, the calculations support the presence of a dominant Orbach relaxation process which is consistent with the experimental data. The calculated energy gap between the ground (1±) and the first (2±) excited state in **2.5** is 21 cm^{-1} for Dy1 and 31 cm^{-1} for Dy2. Furthermore, the lack of well-isolated first excited states and the large deviation from Ising character for both ions also supports the presence of rapid QTM, consistent with the absence of zero-field SMM behavior. Theoretical studies were also carried out on the Tb(III) analogue **2.6** to shed more light on its dynamic magnetic properties. The g-tensors and the relative energies and angles of the principle anisotropy axes of the ground and first excited states are summarized in Table 2-4.

Ground Multiplet	
g_x	0
g_y	0
g_z	17.436
Energy (cm^{-1})	0.00 and 0.49
First- Excited state Multiplet	
g_x	0
g_y	0
g_z	14.301
Energy (cm^{-1})	37.32 and 39.21
Angle (^{0})	7.848

Table 2-4 Calculated relative energies, g-tensors, and angles (θ) of the ground- and first-excited-state pseudo doublets for the Tb1 ion in complex **2.6**.[113]

As expected for the non-Kramers Tb(III) ion, all of the pseudo doublets in the model are of the pure Ising-type. The ground-state pseudo doublet possesses a g_z value of

17.40, approaching that expected for a pure $m_J = \pm 6$ state where $g_z = 18$.[116] Interestingly, a significant tunnel splitting is observed within the ground multiplet for this complex (Δ_{tun} = 0.30 cm^{-1}), suggesting that the states are interacting with each other through QTM, supporting our experimental observations of rapid relaxation of the magnetization, consistent with no-single ion behavior.

2.3.4 Photoluminescence studies

Complexes **2.5** and **2.6** both display emissions at room temperature, as illustrated in Figure 2.19 for an excitation wavelength of 365 nm.

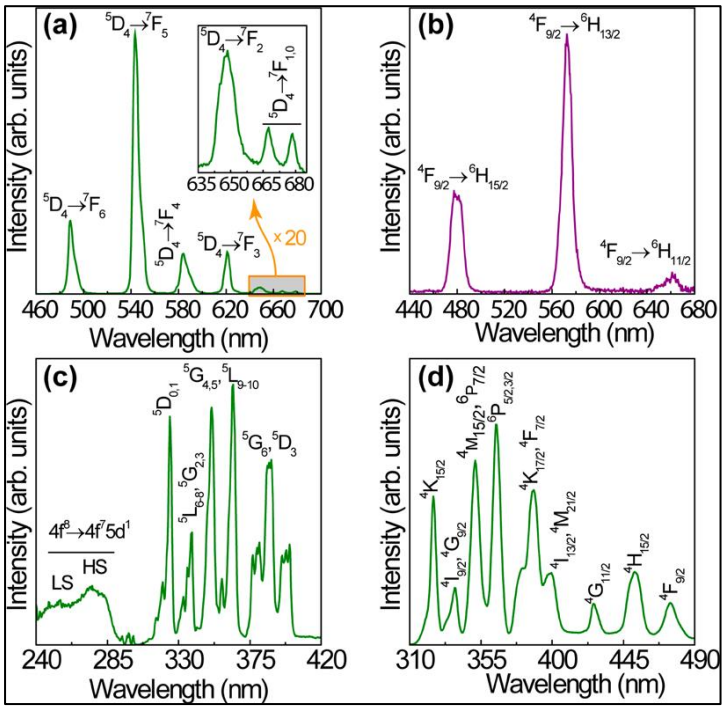

Figure 2.19 (a, b) Emission spectra excited at 365 nm for complexes **2.6** (a) and **2.5** (b). Excitation spectra associated with the 480 nm emission (**2.6**, c) and the 573 nm emission (**2.5**, d); for clarity, the $^7F_6$ and the $^6H_{11/2}$ ground states were omitted for **2.6** and **2.5**, respectively. All data were acquired at 300 K.[113]

The emission spectra reveal the characteristic luminescence of Dy(III) ions in **2.5** and Tb(III) ions in **2.6**, ascribed to $^4F_{9/2} \rightarrow {}^6H_{15/2-11/2}$ and $^5D_4 \rightarrow {}^7F_{6-0}$ transitions, respectively. On cooling from 300 to 14 K, a decrease in the full width at half-maximum (fwhm) is observed, as well as the Stark splitting of the intra-4*f* lines, as described below for complex **2.5**. The excitation spectra were monitored within the more intense $^4F_{9/2} \rightarrow {}^6H_{13/2}$ (**2.5**) and $^5D_4 \rightarrow {}^7F_5$ (**2.6**) transitions. For complex **2.5**, the spectrum reveals a series of intra-4f^9 straight lines attributed to transitions between the $^4K_{15/2,17/2}$, $^4I_{9/2,13/2}$, $^4G_{9/2,11/2}$, $^4M_{15/2-21/2}$, $^6P_{3/2-7/2}$, $^4F_{7/2-9/2}$, and $^4H_{15/2}$ excited levels and the $^6H_{11/2}$ ground multiplet. For complex **2.6**, the spectrum shows a series of sharp lines, assigned to the transitions between the $^7F_6$ and $^5G_{4-6}$, $^5L_{9,10}$, and $^5D_{2-4}$ levels of the Tb(III) ion, and a broad band between 240 and 290 nm, assigned to the contribution of the spin-allowed (low-spin, LS) and spin-forbidden (high-spin, HS) interconfigurational Tb-(III) *f-d* transitions.[117] Similar to what is found for the emission spectra, apart from a decrease of the fwhm for the intra-4*f* lines, the excitation spectrum observed at 14 K resembles that measured at 300 K (not shown). The lifetime values of the excited levels for **2.5** ($^4F_{9/2}$) and **2.6** ($^5D_4$) were evaluated at 300 K. Whereas, for the former complex, the decay lies below the detection limits of the experimental setup (10−9 s), the emission decay curve for **2.6** reveals a single exponential behavior, yielding a lifetime value of $(0.742 \pm 0.002) \times 10^{-6}$ s.

The emission features of both complexes were further quantified by measuring their absolute emission quantum yields. Whereas for complex **2.5**, very low values were found (< 0.01) for **2.6**, the maximum value is 0.42 ± 0.04 for excitation values between 360 and 380 nm. The high quantum yield found for the **2.6** is surprising given that the absence of chromophores in crown ether ligands generally renders them poor antenna

ligands.[44] These findings do, however, agree with related studies on similar systems carried out by Belian *et al*., who concluded that, despite the lack of quantum yield values for Tb15C5 and Eu12C4 complexes, the absence of coordinated water molecules known to quench Tb(III) and Eu(III) luminescence, coupled together with the macrocyclic effect served to minimize the non-radiative relaxation rate in the two systems.[44] In addition, it is also noted that the Tb(III) complexes tend to have the highest emission intensity, probably due to the fact that these compounds tend to have less affinity for water molecules, i.e., are less hygroscopic in nature.[117] We therefore conclude that the coordination of two nitrato and a methanol ligand to the 4*f*-ions in **2.5** and **2.6** prevents their coordination spheres from becoming fully hydrated, with each complex containing just two coordinated water molecules. Furthermore, the incomplete hydration sphere in **2.6** together with the slightly larger atomic radii of the Tb(III) vs the Dy(III) ion may therefore, at least in part, account for its higher-than-expected quantum yield. Given the recently demonstrated importance of photoluminescence studies for elucidating the magnetic anisotropy of Dy(III) ions,[53,54,66,104–106,118–125] in particular to gain additional insight into the synergy between SMM properties and luminescence,[118] the $^4F_{9/2} \rightarrow {}^6H_{15/2}$ transition of complex **2.5** was acquired at low temperature with high resolution (Figure 2.20).

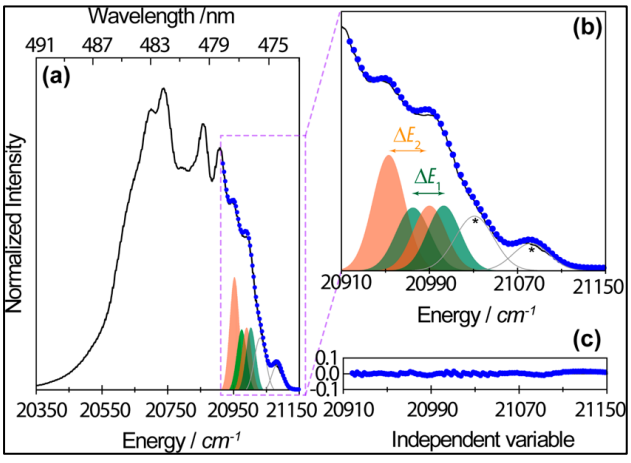

Figure 2.20 (a) High-resolution emission spectrum (15 K) excited at 365 nm for **2.5**. (b) Multi-Gaussian function envelope fit (●) and the components from the first $^4F_{9/2}$ Stark sublevels to the $^6H_{15/2}$ multiplet in the range 20910−21150 cm^{-1}. The asterisks denote hot bands arising from transitions from the first $^4F_{9/2}$ Stark sublevel to the ground level of the $^6H_{15/2}$ multiplet. (c) Residual plot ($R^2 > 0.98$) for a judgment of the fit quality.[113]

The Dy(III) ions in **2.5** occupy a low-symmetry group, and thus the splitting of the electronic levels ($^4F_{9/2}$ and $^6H_{15/2}$) into the maximum number of allowed components to (2J + 1)/2 KDs is expected, leading to 5 and 8 components for $^4F_{9/2}$ and $^6H_{15/2}$, respectively. The presence of the two distinct Dy(III) local coordination sites (Dy1 and Dy2) in **2.5** makes it extremely difficult to unambiguously fit the $^4F_{9/2} \rightarrow {}^6H_{15/2}$ transition (with, at least, 16 Stark levels, assuming that only the $^4F_{9/2}$ low-energy component is populated). Therefore, following the previously reported analysis of related systems,[54] only the high-energy region (20900−21100 cm^{-1}) was analyzed and used to estimate the energy difference between the ground and the first $^6H_{15/2}$ Stark component for the two distinct local sites, namely, ΔE_1 and ΔE_2 for Dy1 and Dy2, respectively. Following this methodology, the high-resolution emission spectrum of **2.5** was fit with 6 components using Gaussian functions, whose energy was constrained to the peak position by careful analysis of the spectrum, taking into account the experimental error (±5 cm^{-1}); the fwhm and the relative intensity were free to vary. The two high-energy components are hot bands (marked with an asterisk in Figure 2.20) arising from transitions from the first $^4F_{9/2}$ Stark sub-level.[54] From the best fit of the emission spectra, two average energy barriers, ΔE_1 = 28 ± 5 cm^{-1} and ΔE_2 = 37 ± 5 cm^{-1}, were estimated, which are in excellent agreement with the calculated values for ΔE_1 from the *ab* initio studies.

2.4 Conclusions and future work

To conclude, the structural and magnetic properties of two H-bonded 15C5 Ln(III) chains have been prepared and characterized. Although both complexes crystallize in similar unit cells, they are not isostructural, with complex **2.5** containing two crystallographically independent Dy(III) ions and the Tb(III) analogue **2.6** comprising just a single crystallographically unique 4*f*-ion. Magneto-luminescence studies reveal that **2.5** is a dual-property emissive SMM, whereas the presence of a fast quantum tunneling mechanisms in **2.6** thwarts the observation of slow relaxation of magnetization. Magnetic susceptibility studies of **2.5** reveal the presence of two effective energy barriers (29 and 0 cm^{-1}) below 5 K and a third U_{eff} of 18 cm^{-1} between 5 and 7 K. At 14 K, the well-resolved solid state emission spectrum of the Dy(III) complex permitted a Gaussian fit of the fine structure of the highest-energy emission band, affording an energy separation between the ground- and first-excited-state KD of 28 ± 5 and 37 ± 5 cm^{-1} for the Dy1 and Dy2 ions, respectively. *Ab initio* studies shed additional light on the magnetization dynamics of the two complexes; the energy gap ΔE_1 between the ground-and the first-excited-state KD in complex **2.5** was calculated to be 21 cm^{-1} for Dy1 and 31 cm^{-1} for Dy2, in excellent agreement with the luminescence data. Furthermore, in the presence of a small applied dc field to suppress quantum tunnelling processes, theoretical studies support the presence of a dominant Orbach relaxation process, consistent with the experimental ac susceptibility data. For the Tb(III) derivative **2.6**, the calculations reveal a significant tunnel splitting (Δ_{tun} = 0.30 cm^{-1}) within the ground multiplet suggesting that the m_J states are interacting with each other through QTM, supporting experimental observations of no-SMM behavior. This study serves to further highlight the versatility of crown ether ligands to afford dual-property Ln(III) coordination complexes whose magnetic and optical

properties can be exploited in conjunction with *ab initio* studies to shed important light on the anisotropy barriers and magnetization dynamics in Ln-based SMMs.

Future work could involve the preparation of redox active Ln-SMMs by chemically modifying the crown ether framework. In this respect, using a redox active group such as ferrocene would give us the opportunity to introduce switchable functionality which may enable us to address SMM properties chemically via one-oxidation and reduction processes.

3 Ln(III) Complexes of Bz and diBz15C5 Macrocycles: Syntheses, Magneto-Structural, Optical and Theoretical Studies

The DyBz15C5 system has been published as a front cover in: M. Al Hareri, E. L. Gavey, J. Regier, Z. Ras Ali, L. D. Carlos, R. A. S. Ferreira and M. Pilkington, *Chem. Commun*., 2016, 52, 11335. Al Hareri, Gavey, Regier and Ras Ali all contributed equally to this work. Ras Ali prepared and structurally characterized the complexes. Al Hareri and Gavey collected the magnetic susceptibility data in house at Brock and assisted Ras Ali in modeling the ac magnetic susceptibility data. Regier carried out the *ab initio* calculations on the Dy(III) system. The Gd(III) and Tb(III) complexes were prepared and fully characterized by Z. Ras Ali and are unpublished to-date. Dr. L.D. Carlos and Dr. R.A.S Ferriera carried out the solid-state photoluminescence measurements on the complexes. For the diBz15C5 system, the Dy(III) complex was prepared and characterized by Ras Ali. Magnetic data was collected by Dr. D. Alexandropolous and modelled by Alexandopolous and Ras Ali. *Ab initio studies* were carried out in collaboration with Dr. K.R. Vignesh and photoluminescence measurements were carried out in collaboration with Dr. L.D. Carlos and Dr. R.A.S. Ferreira.

3.1 Introduction

In the last decade there has been an exponential increase in the publication of *f*-element complexes that possess slow relaxation of their magnetization due to the substantial orbital angular momentum and spin–orbit coupling effects associated with Ln(III) ions.[18] The application of a crystal field splits the degeneracy of the m_J microstates of the $^{2S+1}L_J$ ground term of the lanthanide ion. For Dy(III) ion with a non-integer value of *J*, this results in a Kramers doublet ground state i.e. a degenerate pair of $\pm m_J$ microstates

which offer a bistable magnetic moment ($+m_J$ or $-m_J$) that can be used to store information at a molecular level. Since the anisotropy of the m_J ground state and the energy barrier to excited m_J states is sensitive to the nature of the crystal field,[18,28,126] the long term challenge is to control the local symmetry of the Ln(III) ions in these complexes via rational design.[18] In this respect, high symmetry coordination environments can be achieved in certain point groups, *e.g.* S_8, D_{4d} and D_{5h}, that have been theoretically shown to allow for the control of fast quantum tunnelling of the magnetization (QTM) by the disappearance of certain terms in the crystal field Hamiltonian.[32,127,98,103,128–136] Based on the coordination properties of the smaller crown ether macrocycles such as 15C5, that as previously discussed tend to form sandwich-type complexes with Ln(III) ions, in this project we focused our efforts on keeping the cavity size and donor atom type of the crown constant, but making subtle modifications to the organic framework of the macrocycle. In this project therefore introduced benzo substituents into the organic framework of 15C5 to primarily increase the rigidity of the macrocycle to investigate how this alters the coordination chemistry of the crown. In this respect we anticipated that benzo and dibenzo substituted 15C5 macrocycles may not so easily afford sandwich type systems.[137] We therefore set out to investigate the coordination chemistry and physical properties of benzo- and dibenzo 15C5 macrocycles with select *4f* ions.

Prior to this study, several Ln complexes have been reported with *4f* ions in different oxidation states. In 2002, Starynowic *al et*. reported the Eu(II) complex, $[Eu(Bz15C5)_2](ClO_4)_2$ (**3.1**) (Figure 3.1), which crystallizes in a sandwich structure where the Eu(II) ion is sandwiched between two benzo-15-crown-5 macrocycles in a distorted pentagonal antiprismatic coordination geometry.[138]

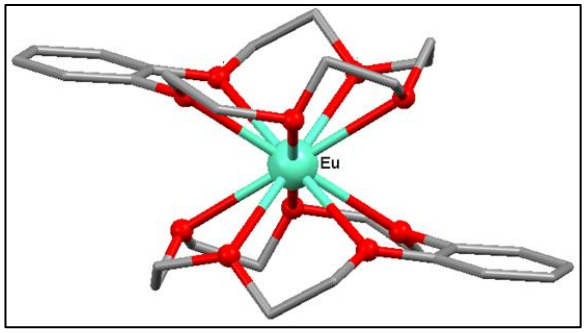

Figure 3.1 Molecular structure of $[Eu(Bz15C5)_2](ClO_4)_2$ (**3.1**). H-atoms and counter anions are omitted for clarity. Colour code: red = O, gray = C and blue/green Eu(II).[138]

In contrast, the Eu(III) complex with Bz15C5 has quite a different molecular structure in which the Eu(III) ion is coordinated to six CH_3OH and two H_2O molecules that are hydrogen-bonded to two benzo-15-crown-5 macrocycles affording a partially enclosed $[Eu(CH_3OH)_6(H_2O)_2]^{3+}$ cation in which the Eu(III) has a distorted triangulated dodecahedral geometry (Figure 3.2).[139]

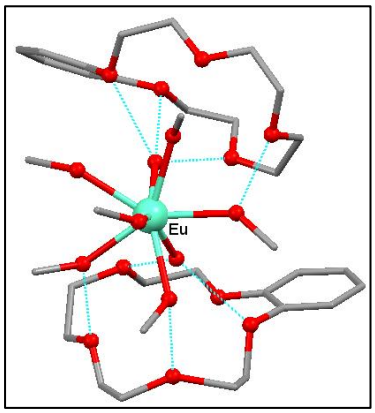

Figure 3.2 Molecular structure of $\{[Eu(CH_3OH)_6(H_2O)_2][PMo_{12}O_{40}]\}\cdot(Bz15C5)_2\cdot(CH_3CN)_2\cdot(CH_3OH)_2$ (**3.2**), showing H-bonding interactions as blue dashed lines. Hydrogen atoms, $[PMo_{12}O_{40}]$, and solvent molecules are omitted for clarity. Colour code: red = O, gray = C and blue/green Eu(III).[139]

For this particular study we employed the oblate Dy(III) and Tb(III) ions with large *J* values, as well as the spherical Gd(III) ion. We also selected both Kramers and non-Kramers ions. It is worth mentioning that although Gd(III) is an isotropic ion and thus from an SMM perspective it is not interesting, it is however very useful to probe the preliminary coordination chemistry of ligands with *4f* ions and its complexes are useful to assess the strength of magnetic exchange interactions that are often masked by the magnetic anisotropy of other *4f* ions. In this project perchlorate salts were employed since they are quite large in size which we proposed should likely afford isolated 0-D complexes (a prerequisite for SMM behaviour) that are nicely crystalline and thus suitable for subsequent magneto-structural and optical studies. In the first part of this study we prepared and characterized three benzo 15C5 complexes with Gd, Dy and Tb ions. In the second part of the study with dibenzo 15C5 we focused our attention solely on the preparation of the Dy(III) complex, since this was the most likely to afford a complex with SMM properties.

3.2 Experimental

3.2.1 Synthesis of Ln(III) Bz and diBz15C5 complexes

All reagents and solvents were purchased from Sigma-Aldrich and used without further purification.

Preparation of $[Dy(H_2O)_8(Bz15C5)_3](ClO_4)_3$ (3.3)

Bz15C5 (1 eq., 31.8 mg, 1.20 mmol) was added in one portion to a solution of $Dy(ClO_4)_3$(aq) (40% w/w, 1 eq., 0.924 mL, 1.20 mmol) in MeOH/MeCN (1:3, 30 mL). The solution was heated to 55°C and vigorously stirred for 3 h. After cooling to r.t., the solution was filtered through cotton wool and left to crystallize by slow evaporation. After

2 weeks, complex **3.3** was isolated as orange single crystals suitable for X-ray diffraction. Yield 22 %. IR (cm^{-1}): 3520 (br), 3241 (b), 2926 (w), 2870 (w), 1659 (w), 1595 (m), 1250 (m), 1124 (s), 934 (s), 758 (s). UV-vis (MeOH, nm): λ_{max} = 224 (ε = 4700 L mol^{-1} cm^{-1}). ESI-MS: *m/z* = 1275 $[(Dy(OH_2)_8](benzo\text{-}15C5)_3ClO_4 \cdot EtOH \cdot H_2O]^+$. Anal. Calcd for $C_{42}H_{74}O_{35}Cl_3Dy$: C, 35.83; H, 5.30; Found C, 36.00; H, 5.27.

Preparation of $[Tb(H_2O)_3(CH_3CN)(Bz15C5)](ClO_4)_3 \cdot (Bz\text{-}15C5) \cdot CH_3CN$ (3.4)

Bz15C5 (2 eq., 208 mg, 0.77 mmol) was added in one portion to a solution of $Tb(ClO_4)_3$(aq) (50% w/w, 1 eq., 0.232 mL, 0.38 mmol) in MeOH/MeCN (1:3, 30 mL). The solution was heated to 55°C and vigorously stirred for 3 h. After cooling to r.t., the solution was filtered through cotton wool and left to crystallize by slow evaporation. After 1 week, yellow/brown single crystals of **3.2** were isolated that were suitable for X-ray diffraction. Yield 20%. IR (cm^{-1}): 3408 (br), 2918 (w), 2877(w), 1653 (w), 1593 (m), 1254 (m), 1087 (s), 933 (s), 747 (s). UV-vis (MeOH, nm): λ_{max} = 274 (ε = 3233 L mol^{-1} cm^{-1}). ESI-MS: *m/z* = 626 $[Tb(benzo\text{-}15C5)(ClO_4)_2]^+$. Anal. cald for $C_{32}H_{68}Cl_3N_2O_{33}Tb$: C, 30.16; H, 5.38; N, 2.20 %; Found C, 29.87; H, 4.79; N, 2.59 %.

Preparation of $[Gd(H_2O)_3(CH_3CN)(Bz15C5)](ClO_4)_3 \cdot (Bz\text{-}15C5) \cdot CH_3CN$(3.5)

Bz15C5 (2 eq., 200 mg, 0.745 mmol) was added in one portion to a solution of $Gd(ClO_4)_3$(aq) (50% w/w, 1 eq., 0.25 mL, 0.372 mmol) in MeOH/MeCN (1:3, 30 mL). The solution was heated to 55°C and vigorously stirred for 3 h. After cooling to r.t., the solution was filtered through cotton wool and left to crystallize by slow evaporation. After 1 week, yellow single crystals of **3.3** suitable for X-ray diffraction were isolated. Yield 14%. IR (cm^{-1}): 3380 (br), 2924 (w), 2879 (w), 1654 (w), 1595 (w), 1255 (m), 1212 (w), 930 (s), 758 (s). UV-vis (MeOH, nm): λ_{max} = 227 (ε = 6340 L mol^{-1} cm^{-1}). ESI-MS: *m/z* =

624 $[Gd(benzo\text{-}15C5)(ClO_4)_2]^+$. Anal. cald for $C_{32}H_{58}O_{31}N_2Cl_3Gd$: C, 31.12; H, 4.77; N, 2.5; Found C, 30.53; H, 4.46; N 2.43 %.

Preparation of $[Dy(H_2O)_9](ClO_4)_3 \cdot (diBz15C5)_2 \cdot 5CH_3CN$ (3.6)

DiBz15C5 (2 eq., 200 mg, 0.632 mmol) was dissolved in a 1:3 mixture of MeOH/MeCN (5 mL) and then $Dy(ClO_4)_3$ (50% w/w, 1eq., 0.14 g, 0.316 mmol) was added and the mixture was heated to 55 °C for 12 hrs. The resulting solution was warmed up to room temperature and then filtered and allowed to slowly evaporate in the fridge which afforded light brown single crystals after one week. Yield 20%. IR(cm^{-1}): 3407 (br), 2935 (w), 1642 (m), 1501 (s), 1451 (m), 1046 (s), 931 (m), 834 (w). UV-vis ($CHCl_3$, nm): λ_{max} = 276 (ε = 18313 $L \cdot mol^{-1}cm^{-1}$). ESI-MS:*m/z* = 677 $[Dy(dibenzo\text{-}15C5)(ClO_4)_2]^+$. Anal. Calcd for $C_{36}H_{62}Cl_3DyO_{31}$: C, 34.46 H 4.58 %. Found: C, 34.37; H, 4.50 %.

3.2.2 Physical measurements

Infrared spectroscopy: Infrared (IR) spectra were measured on a Bruker Alpha FT-IR spectrometer.

UV−visible studies: UV−visible studies (UV-vis) data were collected on a Beckman Coulter DU 720 General-Purpose UV−visible spectrophotometer.

Mass spectrometry: Electrospray ionization (ESI) data were measured on a Carlo Erba/Kratos GC/MS acquisition system and processed using a SPARC workstation.

Elemental analysis: Elemental analysis (C, H, and N) data were collected by Atlantic Microlab.

X-ray crystallography: Suitable single crystals of complexes **3.3** – **3.6** were mounted on a cryoloop with paratone oil and examined on a Bruker APEX-II CCD diffractometer equipped with a CCD area detector and an Oxford Cryoflex low temperature device. Data were collected at 150 (2) K with Mo Kα radiation (λ = 0.71073 Å) using the APEX-II software.[107,108] Cell refinement and data-reduction were carried out by SAINT. An absorption correction was performed by multi-scan method implemented in SADABS.[109] The structures of the complexes were solved by direct methods (SHELXS-97)[110] and refined using SHELXL-2014 in the Bruker SHELXTL suite.[110] Hydrogen atoms were added at calculated positions and refined with a riding model. Disordered solvent was removed for all the complexes using the SQUEEZE procedure in PLATON.[111] A summary of selected structural data for complexes **3.3** – **3.6** is presented in Table 3-1.

Complex	**DyBz15C5 (3.3)**	**TbBz15C5 (3.4)**	**GdBz15C5 (3.5)**	**DydiBz15C5 (3.6)**
Chemical formula	$C_{42}H_{76}Cl_3O_{35}Dy$	$C_{32}H_{52}Cl_3N_2O_{25}Tb$	$C_{32}H_{46}Cl_3N_2O_{25}Gd$	$C_{36}H_{57}Cl_3DyO_{31}$
M_r	1409.87	1130.02	1122.31	1254.66
Crystal system, space group	Triclinic, *P*-1	Triclinic, *P*-1	Triclinic, *P*-1	Orthorhombic, Pnma
Temperature (K)	150	150	150	170
a, (Å)	12.741(3)	11.9818 (7)	11.9799 (10)	9.5112 (6)
b, (Å)	13.235 (4)	12.0126 (7)	12.0526 (10)	25.0418 (17)
c, (Å)	17.923 (4)	16.4305 (9)	16.4773 (14)	19.8782 (12)
α (°)	89.94 (1)	94.557 (3)	94.555 (4)	-
β (°)	85.741 (10)	98.911 (2)	98.724 (4)	-
γ (°)	86.594 (11)	109.013 (2)	109.323 (2)	-
V (Å^3)	3008.7 (13)	2187.4 (2)	2197.6 (3)	4734.5 (5)
Z	2	2	2	4
Radiation type	Mo *K*α	Mo *K*α	Mo *K*α	Mo *K*α
μ (mm^{-1})	1.47	1.89	1.78	1.85
Crystal size (mm)	0.29 × 0.27 × 0.23	0.2 × 0.17 × 0.05	0.2 × 0.2 × 0.1	0.48 × 0.13 × 0.13
T_{min}, T_{max}	0.571, 0.747	0.699, 0747		0.654, 0.783

No. of measured, independent and observed [$I > 2\sigma(I)$] reflections	80643, 14436, 13382	28181, 14249, 13408	31560, 7727, 7419	63495, 6035, 5294
R_{int}	0.043	0.025	0.075	0.082
$(\sin\theta/\lambda)_{max}$ (Å^{-1})	0.668	0.776	0.595	0.668
$R[F^2 > 2\sigma(F^2)]$, $wR(F^2)$, S	0.069, 0.179, 1.09	0.048, 0.125, 1.09	0.052, 0.126, 0.76	0.125, 0.270, 1.23
No. of reflections	14436	14249	7727	6035
No. of parameters	694	558	528	268
No. of restraints	22	11	3	72
$\Delta\rho_{max}$, $\Delta\rho_{min}$ (e Å^{-3})	4.51, −2.58	6.32, −5.33	2.56, −2.57	7.41, −10.72

Table 3-1 Selected crystallographic parameters for **3.3** to **3.6**.

***Ab initio* studies for DyBz complex (3.3):** Calculations were performed on **3.3** by MSc student Jeffrey Regier in the Pilkington group using the coordinates determined from single crystal X-ray diffraction without any further geometry optimizations. Two structural models were considered, the first was the full model with three hydrogen bonded Bz15C5 macrocycles and three perchlorate counter-anions (Model 1), the second model considered only the effects of the coordinating ligands (Model 2). *Ab initio* calculations of the CASSCF + RASSI/SINGLE_ANISO type were performed to evaluate the electronic structure of the Dy(III) ion in the complex using the MOLCAS 8 quantum chemistry package.[112,140,141] The complete active space approach was used where the active space was chosen to include the 9 electrons of the 7 4*f* orbitals. Relativistic basis sets from the ANORCC library were used exclusively for all calculations where two types of basis sets (long and short) were used for each model. Relativistic contractions are also taken into account through the use of the Douglas-Kroll-Hess Hamiltonian. Strong, spin-orbit coupling was included in the CASSI procedure which uses the spin-free Eigenstates of the CASSCF procedure as the elements in the state interaction determinant. In the CASSCF

procedure, 21 roots were used for the sextets and 224 roots were used for the quartets. The doublet configurations were omitted due to limited computer resources. In the state interaction procedure, all 21 roots of the sextets were used and only 80 of the 224 quartet roots were used for Model 1 long due to hardware restrictions and 128 quartet roots were used for all other models. A comparison between the results generated with sextets only and the mixing of sextets and quartets for Model 1 long, showed that the high energy quartet configurations do not affect the magnitude of the energy levels and the properties of the low energy excited states to any significant degree. The g-tensors of each of the Kramers doublets were calculated using the S =1/2 pseudo-spin formalism.

***Ab initio* studies for DydiBz15C5 complex (3.6):** MOLCAS Calculations were performed by Dr. Kuduva R. Vignesh using MOLCAS 8.0,[142] *ab initio* calculations were performed on the Dy^{III} ions using the crystal structure of DydiBz15C5 **3.6**. Relativistic effects were taken into account on the basis of the Douglas−Kroll Hamiltonian.[143] The spin-free eigen states were achieved by the Complete Active Space Self-Consistent Field (CASSCF) method.[144] The basis sets were taken from the ANORCC library for the calculations. We employed the [ANO-RCC... 8s7p5d3f2g1h.] basis set[145] for Dy(III) atoms, the [ANO-RCC...2s.] basis set for H atoms, the [ANO-RCC...3s2p1d.] basis set for O atoms. In the first step, a guessorb calculation was run using the Seward module to create the starting guess orbitals. Here, nine electrons across seven 4*f* orbitals of the Dy^{III} ion were included. Then using these guess orbitals, the active space was chosen based on the number of active electrons in the number of active orbitals and the SA-CASSCF calculations were carried out. Here, the Configuration Interaction (CI) procedure were computed

for the Dy^{III} ion and where twenty-one sextet excited states, two hundred and twenty-four quartet excited states and four hundred and eighty doublet excited states were considered in the calculations to compute the anisotropy. All the excited states corresponding to each multiplets of ions were computed in the CASSCF module. After computing these excited states, all the low-lying excited states (<50,000 cm^{-1}) were mixed using the RASSI-SO[146] module to calculate the spin-orbit coupled states. Moreover, these computed SO states were considered into the SINGLE_ANISO program[147] to compute the *g*-tensors. The *g*-tensors for the Kramers doublets of Dy(III) were computed based on the pseudospin S = ½ formalism.[147] Crystal-field (CF) parameters were extracted using the SINGLE_ANISO code, as implemented in MOLCAS 8.0. The CF parameters for complex **3.6** were analyzed for deeper insight into the mechanism of the magnetic relaxation. The corresponding crystal field Hamiltonian is given by equation 3.1 below:

$$\hat{H}_{CF} = \sum_{k=-q}^{q} \sum B_k^q \tilde{O}_k^q \qquad \textbf{Eqn. 3.1}$$

where $\boldsymbol{B_k^q}$ is the crystal field parameter, while $\boldsymbol{O_k^q}$ is the Steven's operator.

Photoluminescence spectroscopy for DyBz15C5 complex (3.3): Solid state photoluminescence studies were carried out on **3.3** in collaboration with Dr .R.A.S Ferriera and Dr. L.D. Carlos at the University of Aveiro, Portugal. Luminescence data were recorded at 300 and at 12 K using a modular double grating excitation spectrofluorimeter equipped with a TRIAX 320 emission monochromator (Fluorolog-3, Horiba Scientific) coupled to a R928 Hamamatsu photomultiplier, using a front face acquisition mode. The

excitation source was a 450 W Xe arc lamp. The emission spectra were corrected for detection and optical spectral response of the spectrofluorimeter and the excitation spectra were corrected for the spectral distribution of the lamp intensity using a photodiode reference detector. The room temperature time-resolved emission spectra and emission decay curves (10^{-6}-10^{-9} s) were recorded on a Fluorolog TCSPC spectrofluorimeter (Horiba Scientific) coupled to a TBX-04 photomultiplier tube module (950 V), 200 ns time-to-amplitude converter and 70 ns delay. The excitation source was a Horiba-Jobin-Yvon pulsed diode (NanoLED-390, peak at 390 nm, 1.2 ns pulse duration, 1 MHz repetition rate and 150 ns synchronization delay). The emission decay curves (10^{-6}-10^{-2} s) were recorded at room temperature with a Fluorolog TCSPC spectrofluorometer (Horiba Scientific) coupled to a TBX-04 photomultiplier tube module (950 V), 50 μs delay. The excitation source was a Horiba Scientific pulsed diode light source (Spectra LED-355, peak at 356 nm).

Photoluminescence spectroscopy for DydiBz complex (3.6): The photoluminescence data were recorded using a modular double grating excitation spectrofluorimeter with a TRIAX 320 emission monochromator (Fluorolog-3, Horiba Scientific) coupled to a R928 Hamamatsu photomultiplier, using a front face acquisition mode. The excitation source was a 450 W Xe arc lamp. The emission spectra were corrected for detection and optical spectral response of the spectrofluorimeter and the excitation spectra were corrected for the spectral distribution of the lamp intensity using a photodiode reference detector. The time-resolved emission spectra and emission decay curves were acquired with the same instrumentation using a pulsed Xe–Hg lamp (6 μs pulse at half width and 20–30 μs tail). The temperature was varied between 297 and 15 K using a helium-closed cycle cryostat,

a vacuum system (4×10^{-4} Pa), and an autotuning temperature controller (Lakeshore 330, Lakeshore) with a resistance heater.

3.3 Results and discussion

3.3.1 Ln(III) complexes of Bz15C5

3.3.1.1 Synthesis and structural studies

All three Ln(III) Bz15C5 complexes were prepared via the reaction of the crown ether with the perchlorate Ln(III) salt in a 1:3 methanol/acetonitrile mixture. The reaction solution was heated for three hours to 55 °C, filtered and then left to cool and slowly evaporate. After carrying out numerous trial reactions to investigate a range of different solvent and solvent combinations for these reactions, we found the aforementioned mixture of solvents afforded the most suitable single crystals for structural characterization. Suitable single crystals of **3.3** for X-ray diffraction were isolated via the slow evaporation of the reaction mixture at room temperature after two weeks. X-ray crystallographic studies reveal the complex crystallizes in the triclinic space group *P*-1 and comprises of a $[Dy(OH_2)_8]^{3+}$ cation encapsulated within a cavity formed by three benzo-15C5 macrocycles, (Figure 3.3a and b), reminiscent of the benzo-15C5 adducts of Ln(III) picrates, reported by Hong *et al*. in 1996.[148] Selected bond lengths and angles for the complex are presented in Table 5-3 in the Appendix section of the thesis. The Dy–O bond distances are in the range 2.322(4)–2.392(4) Å.

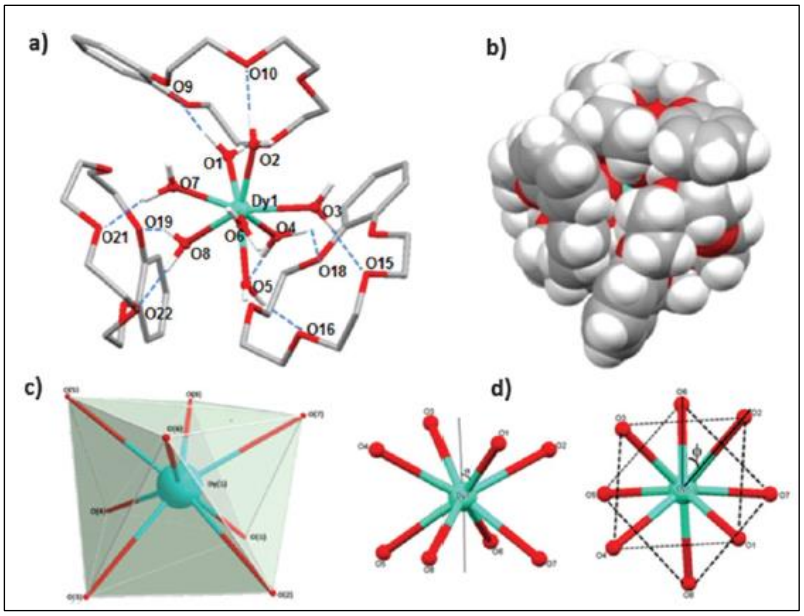

Figure 3.3 (a) Molecular structure of $[Dy(OH)_8]^{3+}(benzo\text{-}15C5)_3$ (**3.3**) showing H-bonding interactions as blue dashed lines; (b) space filling model highlighting the encapsulation of the Dy(III) ion inside the molecular cavity formed by the benzo-15C5 macrocycles. ClO_4^- counter ions and crown ether H-atoms are omitted for clarity; (c) square antiprismatic (SAP) geometry of the $[Dy(OH)_8]^{3+}$ cation; (d) the relevant angular parameters for SAP geometry: ϕ, the angle between the diagonals of the two squares or the skew angle and α, the angle between the C_4 axis and a Dy–O vector. ϕ angle should be 45° in ideal SAP while α angle 54.74°.[106]

The coordination geometry of the Dy(III) ion was investigated by continuous shape measures (CSM)[114] which reveals that the local symmetry of the *4f* cation is very close to ideal square antiprismatic, as outlined in Table 3.2 and Figure 3.4.

Polyhedron	Symmetry	Dy(III)CSM
OP-8	D_{8h}	29.80
HPY-8	C_{7v}	23.54
HBPY-8	D_{6h}	16.31
CU-8	O_h	10.87
SAPR-8	$\boldsymbol{D_{4d}}$	**0.84**
TDD-8	D_{2d}	1.28

JGBF-8	D_{2d}	14.40
JEBPY-8	D_{3h}	28.13
JBTPR-8	C_{2v}	1.88
BTPR-8	C_{2v}	1.34
JSD-8	D_{2d}	3.44
TT-8	T_d	11.56
ETBPY-8	D_{3h}	24.26

Table 3-2 Continuous shape measures (CSMs) of the 8-coordinate Dy(III) polyhedron in **3.1**. The value in red indicates the closest polyhedron according to the CSMs. Abbreviations: OP-8, Octagon; HPY-8, Heptagonal pyramid; HBPY-8, Hexagonal pyramid; CU-8, Cube; SAPR-8, Square antiprism; TDD-8, Triangular dodecahedron; JGBF-8, Johnson gyrobifastigium; JETBPY-8, Johnson elongated triangular bipyramid J14; JBTPR-8, Biaugmented trigonal prism J50; BTPR-8, Biaugmented trigonal prism; TT-8, Triakis tetrahedron; ETBPY-8, Elongated trigonal bipyramid.[106]

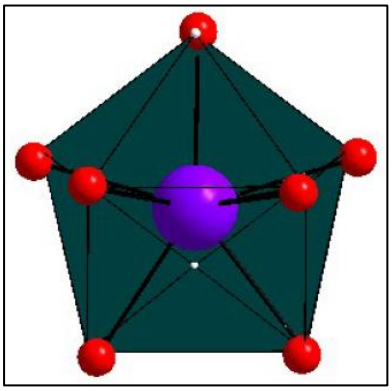

Figure 3.4 Coordination geometry of the Dy(III) cation superimposed on an idealized square antiprism (dark green) in **3.3**.[106]

In addition, detailed analysis of the molecular structure showed that the skew angle ϕ (43°) is very close to 45° for idealized D_{4d} symmetry and the average "a angle" is 58.55°, close to the calculated angle of 54.74° for an axially non-distorted antiprism (Figure 3.3 c and d).[128,149] The $[Dy(OH_2)_8]^{3+}$ complex is stabilized by H-bonding interactions between the 8 water ligands, 3 neighbouring benzo-15C5 macrocycles and the perchlorate

counterions, such that intermolecular O–H···O distances are in the range 1.71(7)–2.58(8) Å, (Figure 3.5). This encapsulation serves to magnetically isolate the hydrated cations, resulting in intermolecular Dy···Dy distances greater than 12 Å.

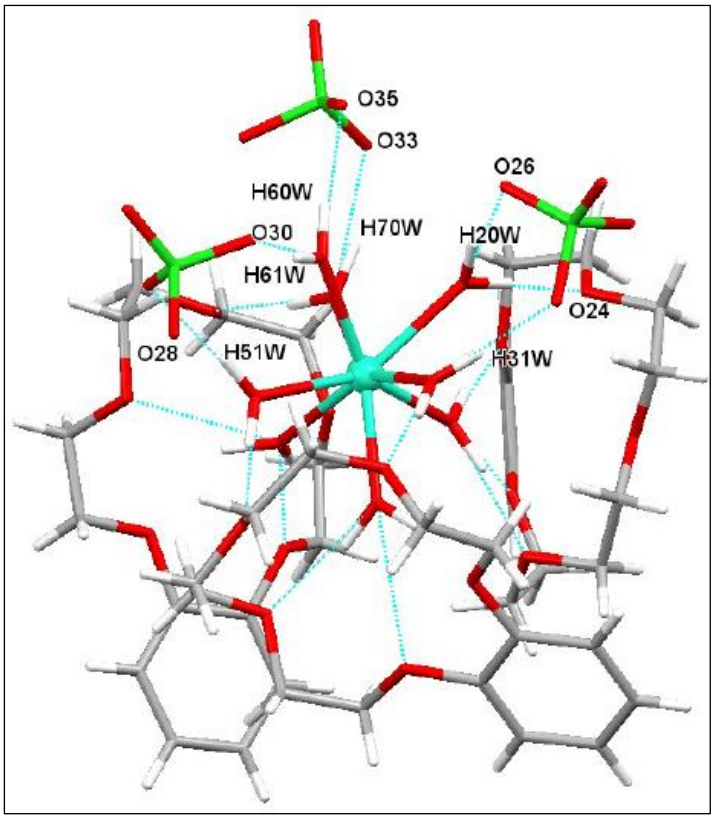

Figure 3.5 Molecular structure of $[Dy(OH_2)_8](Bz15C5)_3 \cdot (ClO_4)_3$ (**3.3**) showing H-bonding interactions to the perchlorate anions as blue dashed lines.[106]

Single crystals of the Tb and Gd complexes **3.4** and **3.5** were also characterized by X-ray diffraction studies that revealed the two complexes are isostructural, crystallizing in the triclinic space group P-1, (Table 3-1). Interestingly, instead of comprising of an encapsulated $[Ln(OH)_8]^{3+}$ ion they both have pseudo sandwich type topologies, reminiscent of the unsubstituted 15C5 complex **2.5** presented in Chapter 2. In this respect, in both complexes, the *4f* ion is directly coordinated to the oxygen atoms (O1 to O5) of

one of the crowns with three coordinated waters (O6 to O8) and an acetonitrile molecule completing their 9-coordinate geometry. As for complex **2.5**, the coordinated water molecules are H-bonded to a second Bz15C5 macrocycle, (Figure 3.6) and the intermolecular O–H···O distances are in the range 1.74(5)–1.91(6) Å for **3.4** and 1.72(8)–1.89(9) Å for **3.5**. Three perchlorate counter ions serve to charge balance the complexes. In both complexes, the coordinated benzo crown ether macrocycle has a puckered conformation with an O2-Tb-O5 angle of 83.15° in **3.4** and a comparable O4-Gd-O1 angle of 83.53° in **3.5**. The Tb-O bond lengths range from 2.33(2) to 2.52(3) Å in **3.4** and the Gd-O bond lengths range from 2.35(4) to 2.53(4) Å in **3.5**. Selected bond lengths and angles for the two complexes are presented in Table 5-4 and Table 5-5 in the Appendix section of the thesis. This change in structural topology when moving from Gd and Tb to Dy could at least in part be attributed to the size of the cations, where Gd(III) > Tb(III) > Dy(III), *vide infra*.

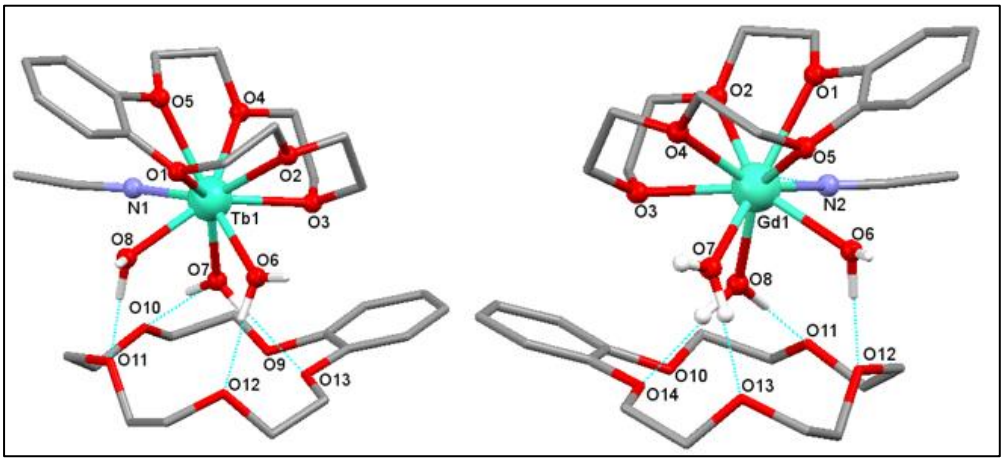

Figure 3.6 Molecular structures of **3.4** and **3.5** with the appropriate atomic labelling schemes. H-bonds to the uncoordinated Bz15C5 macrocycle are shown as blue dashed lines. For clarity lattice solvent molecules and perchlorate counter ions are omitted. Colour

code: red = O, purple = N, gray = C, white = H, green = Ln(III). H-bonding interactions are showing as blue dashed lines.

As for the Dy ion in complex **3.3**, the geometries of the *4f* ions in **3.4** and **3.5** were analyzed by continuous shape measures (CSMs)[114] and the results are presented in Table 3-3.

Polyhedron	Symmetry	Tb(III) CSM	Gd(III) CSM
EP-9	D_{9h}	36.65	36.52
OPY-9	C_{8v}	23.30	23.64
HBPY-9	D_{7h}	15.03	14.87
JTC-9	C_{3v}	15.19	14.90
JCCU-9	C_{4v}	8.86	8.60
CCU-9	C_{4v}	7.68	7.37
JCSAPR-9	C_{4v}	2.48	2.55
CSAPR-9	C_{4v}	1.62	1.63
JTCTPR-9	D_{3h}	3.62	3.82
TCTPR-9	D_{3h}	2.17	2.303
JTDIC-9	C_{3v}	11.34	11.21
HH-9	C_{2v}	10.60	10.71
MFF-9	***Cs***	**1.09**	**1.10**

Table 3-3 Continuous shape measures (CSMs) of the 9-coordinate Ln(III) coordination polyhedron in complexes Tb15C5 (**3.4**) and Gd15C5 (**3.5**). The value in red indicates the closest polyhedron according to the CSMs. Abbreviations: EP-9, Enneagon; OPY-9, Octagonal pyramid; HBPY-9, Heptagonal bipyramid; JTC-9, Johnson triangular cupola J3; JCCU-9, Capped cube J8; CCU-9, Spherical-relaxed capped cube; JCSAPR-9, Capped square antiprism; CSAPR-9, Spherical capped square antiprism; JTCTPR-9, Tricapped trigonal prism J51; TCTPR-9, Spherical tricapped trigonal prism; JTDIC-9, Tridiminished icosahedron J63; HH-9, Hula-hoop; MFF-9, muffin.

Compared to the ideal square antiprismatic geometry of the Dy(III) ion in **3.3**, the geometries of the *4f* ions in **3.4** and **3.5** are 9-coordinate and are closest to muffin polyhedra with CSMs of 1.09 and 1.10 respectively. The deviations of the coordination spheres from the idealized muffin polyhedra are shown in Figure 3.7.

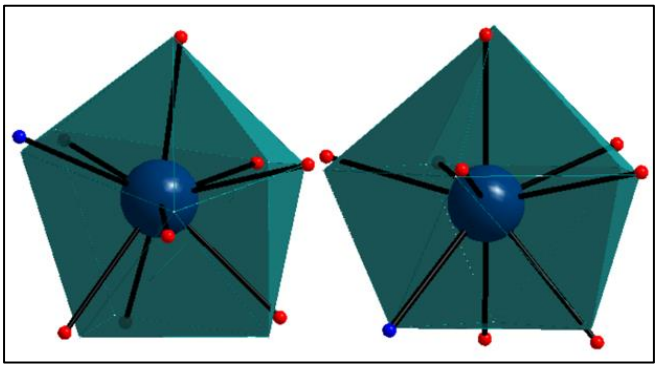

Figure 3.7 Coordination geometry of the Tb(III) ion in **3.4** (left) and the Gd(III) ion in **3.5** (right) superimposed on an idealized muffin polyhedron (dark green).

Further analysis of the X-ray crystal structures of **3.4** and **3.5** reveals that the crystal packing is stabilized by H-bonding interactions between the coordinated water molecules and the perchlorate anions, that range from 1.76–1.91 Å in **3.4** and 1.71–1.89 Å in **3.5**, (Figure 3.8). Furthermore, the shortest intermolecular Ln···Ln distances are 9.38Å for the Tb···Tb ions in **3.4** and 9.42 Å for the Gd···Gd ions in **3.5**, both of which are shorter than the shortest intermolecular Dy···Dy distances in complex **3.3**.

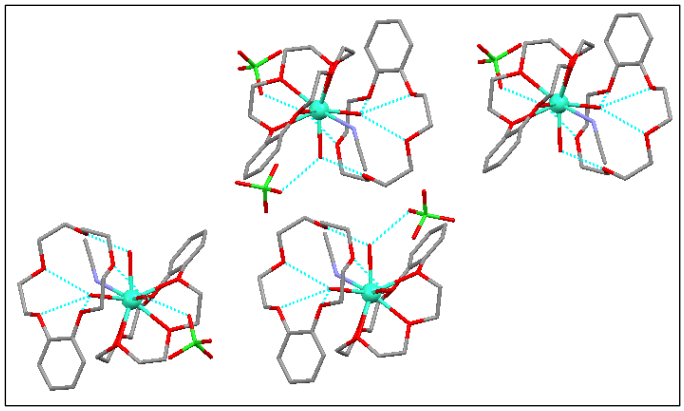

Figure 3.8 View of the crystal packing of **3.4** showing H-bonding interactions to the perchlorate anions as blue dashed lines. Colour code: red = O, blue = N, gray = C, white = H, blue/green = Tb(III).

Examining the three structures it is apparent that in all three complexes the atomic radii of the Ln(III) ion is too large to be directly coordinated in the macrocyclic cavity of the bz15C5 macrocycle that is reported to have an internal diameter that lies between 1.7 and 2.2 Å.[150] As a consequence, the *4f* ions sit out of the plane of the benzo crown ether. The difference in the structural topology of the Gd and Tb complexes *vs* the Dy analogue can most likely be attributed to the subtle differences in the ionic radii of the Ln(III) ions. In this respect, the Gd(III) ions are the largest with atomic radii of 1.107 Å for CN = 9 , followed by 1.09 Å for Tb(III) ions with CN = 9 and then the smallest, 1.027 Å for Dy (III) ions with a CN = 8.[151] In addition, theoretical calculations indicate that the interaction between the crown ether oxygen atoms and the *4f* ions decreases as the ionic radii of the *4f* ions decreases across the series,[152] which may also account as to why the smaller Dy(III) ions do not directly coordinate to the crown ether oxygen atoms, but instead it is likely energetically more preferable for them to remain fully hydrated, resulting in quite a different structural topology when compared to **3.4** and **3.5**.

3.3.1.2 Magnetic studies

Direct current susceptibility measurements (dc) were carried out on all three complexes in an applied static field of 0.1 T between 5 and 300 K. The data are shown as $\chi_M T$ *vs*. T plots in Figure 3.9. In this respect, $\chi_M T$ values of 14.14, 11.78, and 7.73 $cm^3 \cdot K \cdot mol^{-1}$ are obtained for complexes **3.3** - **3.5**, respectively, which are in a good agreement with the theoretical values of 14.17 cm^3, 11.82 and 7.88 $cm^3 \cdot K \cdot mol^{-1}$ for non-interacting Dy(III) ($^6H_{15/2}$, S = 5/2, g = 4/3), Tb(III) ($^7F_6$, S = 3, g = 3/2), and Gd(III) ($^8S_{7/2}$, S = 7/2, L = 0, g = 2) ions respectively. Examining the dc susceptibility data for the isotropic Gd(III) complex **3.5** reveals that the $\chi_M T$ product stays almost constant as the temperature is lowered ruling out the presence of any weak anti-or ferromagnetic exchange interactions, confirming that the *4f* ions in the complex are magnetically isolated.[153] For the Dy and Tb complexes, the $\chi_M T$ product remains constant until ca.100 K when it decreases due to the thermal depopulation of the excited Stark sub-levels.[66]

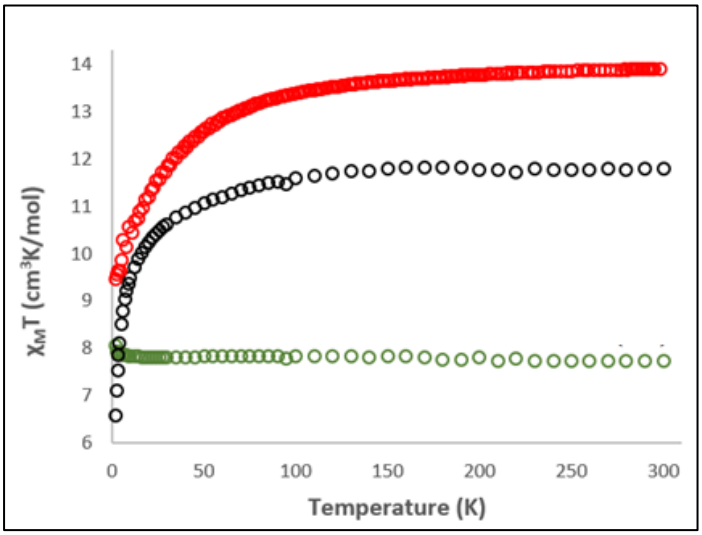

Figure 3.9 Plots of $\chi_M T$ *vs*. T shown as red, black, and green circles for complexes **3.3**-**3.5** respectively in a field of 0.1 T from 2 - 300 K.

In order to study the dynamic magnetic properties of the complexes, ac magnetic susceptibility measurements were performed on **3.3** and **3.4** in an oscillating field of 3.5 Oe in both zero and non-zero static dc fields. Measurements were carried out from 2–15 K over frequencies ranging from 50–10000 Hz. The D**y** complex **3.3** displays frequency-dependent signals in zero dc field, characteristic of an SMM however, due to quantum tunnelling of the magnetization (QTM), full maxima in the plot of χ'' *vs*. temperature were not resolved (Figure 3.10).

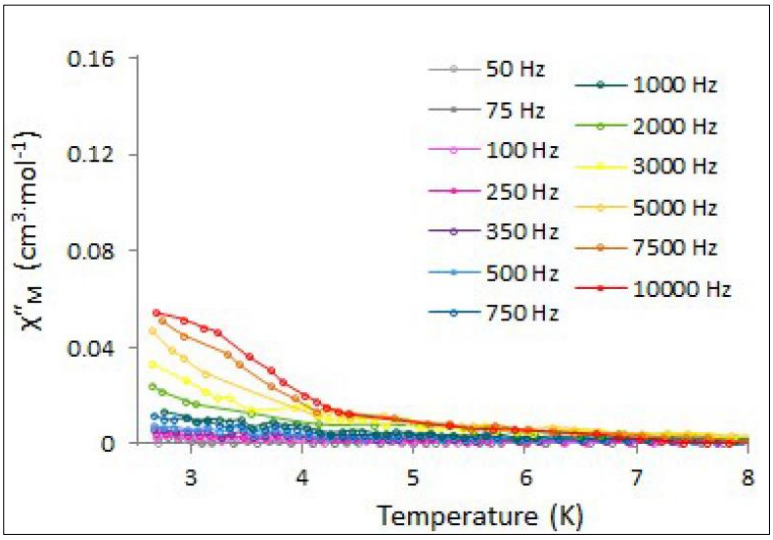

Figure 3.10 Plot of χ''_M vs temperature for **3.3** in zero dc field below 8 K, showing the frequency dependence to the susceptibility and lack of resolved maxima.[106]

Various static dc fields were then applied between 300, 800 and 1500 Oe, (Figure 3.11). When an optimized field of 800 Oe was applied to remove the degeneracy of the m_J ground states and suppress QTM, the complex displayed SMM behaviour below 15 K, with two maxima emerging at 2.5 and 6 K (Figure 3.12b and c). Both the in-phase χ' and out-of-phase χ'' components of the magnetic susceptibility show frequency dependence consistent with slow relaxation of the magnetization, Figure 3.12a and b. Furthermore, in

the low temperature region below 4.5 K, a shoulder is clearly visible in the χ'' *vs*. T plot which indicates the presence of two overlapping relaxation domains, (Figure 3.12b). In order to probe these relaxation pathways further, Cole–Cole plots were examined at different temperatures, (Figure 3.12d).

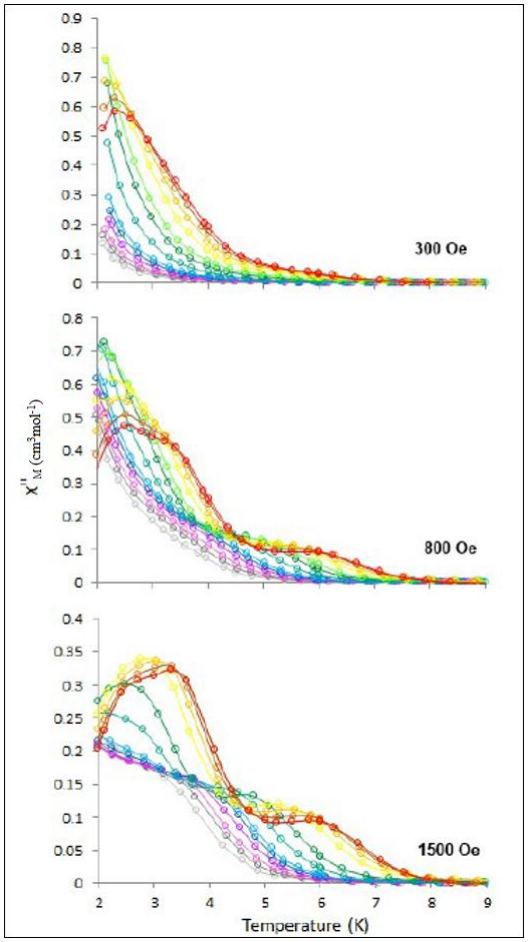

Figure 3.11 Plot of χ''_M *vs* T for **3.3** in applied dc fields of 300, 800 and 1500 Oe, below 15 K.[106]

Above 4.5 K, the semicircles are consistent with a single relaxation domain and were fit to the Cole–Cole model.[154] Below 4 K, several of the χ' *vs*. χ'' semicircles are visibly kinked indicative of two partially merged arcs, each corresponding to a distinct relaxation domain. This behaviour is reminiscent of the previously described Dy(III)15C5

pseudo-sandwich complex **2.4**,[66] and was thus modelled in a similar manner, using two combined modified Debye functions.[41]

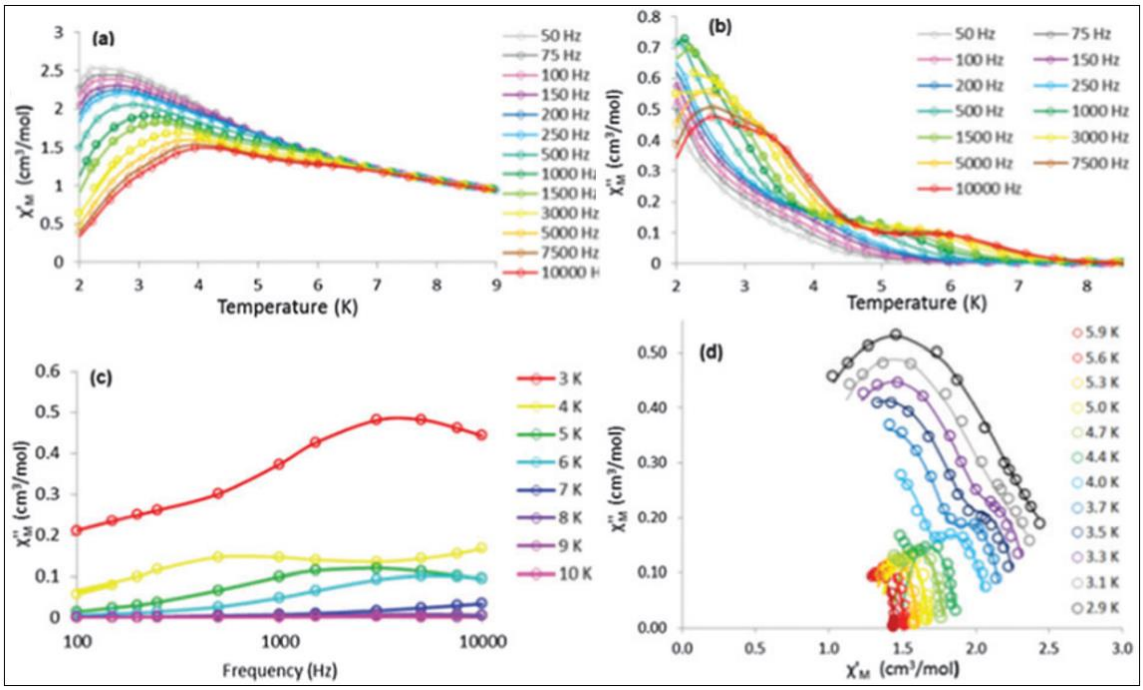

Figure 3.12 (a and b) χ'_M and χ''_M *vs*. temperature in 800 Oe applied dc field, below 10 K; (c) out-of-phase χ'' *vs*. frequency in 800 Oe applied field from 3–10 K; (d) modelled out-of-phase χ'' versus in-phase χ' plot in 800 Oe applied field with kinks in the Cole–Cole semicircles visible above 3.5 K.[106]

In the case of the Arrhenius plot, we have included only the temperature regimes which could be modelled using a one- or two-component Cole-Cole/Debye equation. We appreciate that this affords large gaps between the 0.2 to 0.25 K^{-1} points, but the data in this region could not be modelled, since this is a transition region in which the susceptibility data collected over various frequencies at each temperature point has contributions from both the low temperature domains and the single high temperature

domain. Hence, neither the one- nor the two-component equation accurately describes the observed data in this region.

The Cole-Cole model describes the ac susceptibility as:[41]

$$\chi(\omega) = \chi_S + \frac{\chi_T - \chi_S}{1 + (i\omega\tau_c)^{1-\alpha}} \qquad \textbf{Eqn. 3.2}$$

where $\omega = 2\pi f$, χ_T is the isothermal susceptibility, χ_S is the adiabatic susceptibility, τ_c is the temperature-dependent relaxation time, and α is a measure of the dispersivity of relaxation times, with $\alpha = 0$ reflecting a single Debye-like relaxation time and $\alpha = 1$ reflecting an infinitely wide dispersion of τ_c values.

Dividing Eqn. 3.2 into its in-phase and out-of-phase components gives:

$$\chi'(\omega) = \chi_S + \frac{(\chi_T - \chi_S)}{2}\left\{-\frac{\sinh[(1-\alpha)\ln(\omega\tau_c)]}{\cosh[(1-\alpha)\ln(\omega\tau_c)] + \cos\left[\frac{1}{2}(1-\alpha)\pi\right]}\right\} \qquad \textbf{Eqn. 3.3}$$

$$\chi''(\omega) = \frac{(\chi_T - \chi_S)}{2}\left\{1 - \frac{\sin\left[\frac{1}{2}(1-\alpha)\pi\right]}{\cosh[(1-\alpha)\ln(\omega\tau_c)] + \cos\left[\frac{1}{2}(1-\alpha)\pi\right]}\right\} \qquad \textbf{Eqn. 3.4}$$

In the case of complex **3.3**, the susceptibility behavior below 5 K is due to contributions from two distinct relaxation pathways. The relaxation in this temperature region can thus be described by the sum of two combined, modified Debye functions:

$$\chi(\omega) = \chi_{S1} + \frac{\chi_{T1} - \chi_{S1}}{1 + (i\omega\tau_{c1})^{1-\alpha1}} + \chi_{S2} + \frac{\chi_{T2} - \chi_{S1}}{1 + (i\omega\tau_{c2})^{1-\alpha2}} \qquad \textbf{Eqn. 3.5}$$

Dividing Eqn. 3.5 into its in-phase and out-of-phase components gives:

$$\chi'(\omega) = \chi_S + (\chi_{T1} - \chi_S)\left\{\frac{1 + (\omega\tau_{c1})^{1-\alpha_1}\sin(\pi\alpha_1/2)}{1 + (\omega\tau_{c1})^{1-\alpha_1}\sin(\pi\alpha_1/2) + (\omega\tau_{c1})^{2-2\alpha_1}}\right\} + (\chi_{T2} - \chi_S)\left\{\frac{1 + (\omega\tau_{c2})^{1-\alpha_2}\sin(\pi\alpha_2/2)}{1 + (\omega\tau_{c2})^{1-\alpha_2}\sin(\pi\alpha_2/2) + (\omega\tau_{c2})^{2-2\alpha_2}}\right\} \qquad \textbf{Eqn. 3.6}$$

$$\chi''(\omega) = (\chi_{T1} - \chi_S)\left\{\frac{1 + (\omega\tau_{c1})^{1-\alpha_1}\cos(\pi\alpha_1/2)}{1 + (\omega\tau_{c1})^{1-\alpha_1}\sin(\pi\alpha_1/2) + (\omega\tau_{c1})^{2-2\alpha_1}}\right\}$$
$$+(\chi_{T2} - \chi_S)\left\{\frac{1 + (\omega\tau_{c2})^{1-\alpha_2}\cos(\pi\alpha_2/2)}{1 + (\omega\tau_{c2})^{1-\alpha_2}\sin(\pi\alpha_2/2) + (\omega\tau_{c2})^{2-2\alpha_2}}\right\} \quad \textbf{Eqn. 3.7}$$

where $\chi_S = \chi_{S1} + \chi_{S2}$

The Arrhenius equation, relating relaxation time τ_c to temperature T, is given by:

$$\tau_c = \tau_0 e^{U_{eff}/k_B T} \quad \textbf{Eqn. 3.8}$$

where τ_0 is the tunneling rate and U_{eff} is the effective energy barrier.

As expected for an SMM, the relaxation times exhibit an exponential dependence on temperature between 2.9 and 6 K. An Arrhenius fit to the data gives three effective relaxation barriers together with their corresponding pre-exponential factors τ_0, (Figure 3.13). Interestingly, the effective energy barrier for domains B and C are both *ca.* 10 cm^{-1}, whereas for A, the second energy barrier is larger at 26 cm^{-1}. The α parameters range from 0.14 for domain A, 0.17 for domain B and 0.20 for domain C.[66,155] The temperature dependence of all three pathways indicates they contain a thermal component and cannot be assigned to pure QTM between $\pm m_J$ levels of the ground state.

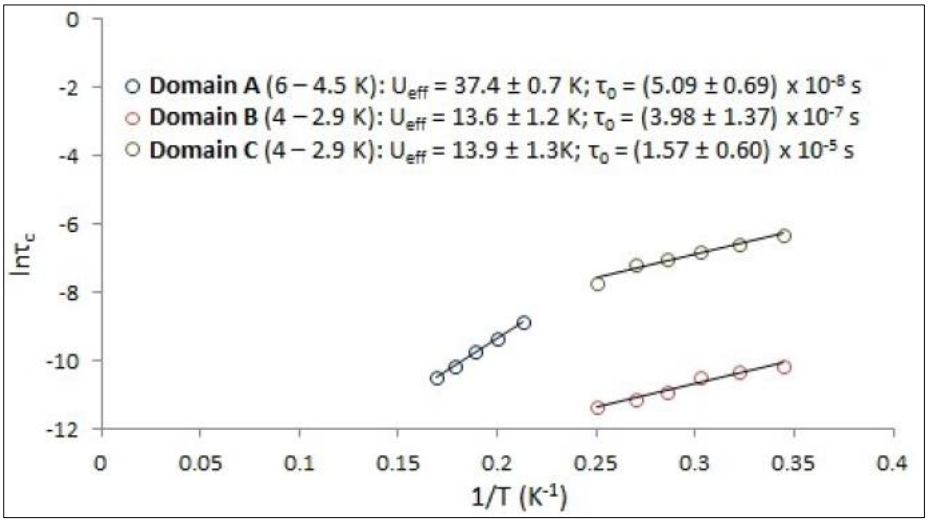

Figure 3.13 Temperature dependence of the relaxation time for **3.3** at "high" (6.0 - 4.5 K) temperature, blue circles – domain A and "low" (4.0 – 2.9 K) temperatures, red and green circles – domains B and C respectively, under a static field of 800 Oe. The solid lines represent a fit to the Arrhenius law.[106]

Unfortunately, ac studies of the Tb(III) complex did not reveal any frequency dependency to the out of phase component of the ac susceptibility and so we conclude that since Tb(III) is not a Kramers ion, then the axial crystal field of the *4f* ion was not sufficient to supress the QTM in this complex.

3.3.1.3 *Ab initio* studies

In order to further elucidate the dynamic magnetic properties of **3.3**, *ab initio* CASSCF + RASSI/SINGLE_ANISO calculations were carried out with MOLCAS 8.0.[112] Two structural models together with two basis sets (short and long) for each model were investigated (Table 5-22) The relative energies and the directionality of the main anisotropy axes of the KD in the $^6H_{15/2}$ ground state of the Dy(III) ion were evaluated for all four models as summarized in Table 5-23 and Table 5-24 in Appendix. Model 1 (long), which includes 8 coordinated water molecules, 3 H-bonded Bz15C5 macrocycles and 3 H-bonded ClO_4^- counter-ions, best describes the coordination environment of the Dy(III) ions in the complex, (Figure 3.14). Both the ground (KD1±), and first excited state Kramers doublets (KD2±) contain a significant contribution from the transverse g_{xy} parameters (Table 5-25), which is further supported by a previous calculation on a model $[Dy(OH_2)_8]^{3+}$ complex.[156] Both of these states are axial in their nature, with the axiality increased at the KD2 level. In addition, the co-parallel alignment of the KD1 and KD2 vectors should serve to suppress thermally assisted (TA) Orbach relaxation processes between the ground and first excited state KDs, (Figure 3.15a). For Model 1, the ground wavefunctions are

comprised of mainly m_J = ±15/2 and the first excited state includes a large contribution from m_J = ±13/2. However, this dramatically changes for the second excited state which includes nearly an equal contribution of all positive or negative m_J states for the respective wavefunction in the second excited state KD3±.

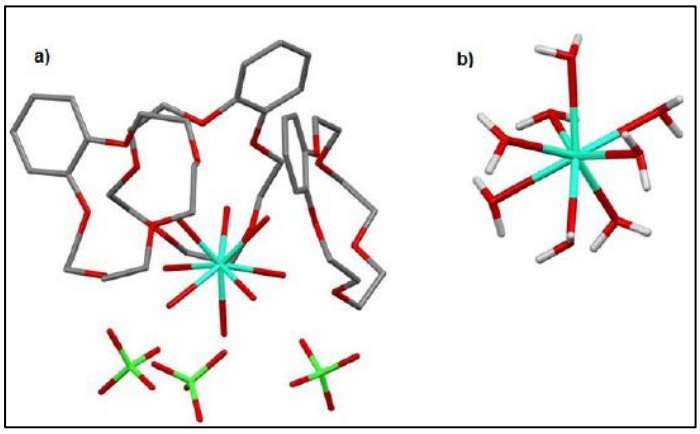

Figure 3.14 Model 1 with three hydrogen bound benzo-15C5 molecules and three perchlorate counter anions; (b) Model 2 including only the coordinating water molecules.[106]

For Model 1, an examination of the magnitude of the matrix elements between the KD2± and KD3± spin states reveals the average matrix elements between KD2(–) and KD3(+) states are very large, in comparison to the elements between KD2(–) and KD2(+) states, (Figure 3.15b). Since these elements correspond to transition moments between the two states, the *ab initio* data is therefore consistent with the presence of a dominant spin–lattice relaxation process involving the second excited state KD3±. In addition, the calculated energy gap between the ground (1±) and the first (2±) excited state is small (12.92 cm^{-1}), whereas the second (3±) excited state is well separated (43.54 cm^{-1}). These energy gaps are larger than the magnetically-derived effective anisotropy barriers since the

ab initio calculations do not take into consideration QTM, or the alteration of the Stark sub-levels in the presence of a small applied dc field.[53,66]

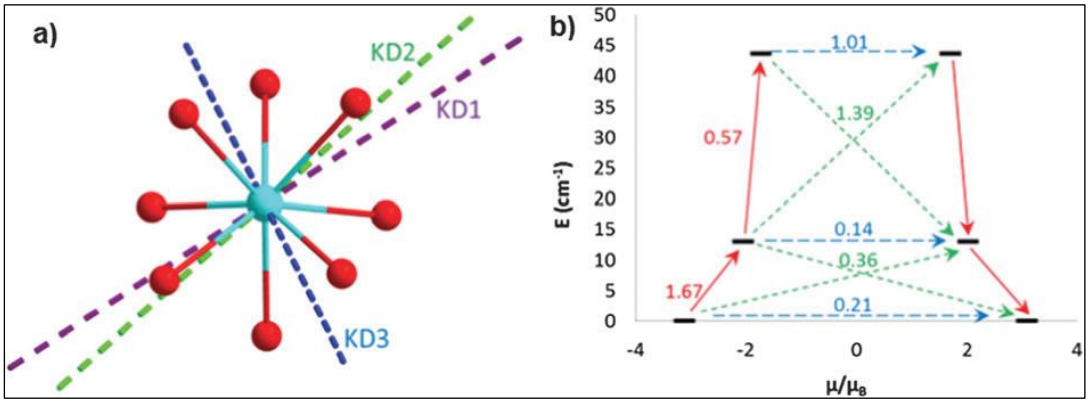

Figure 3.15 (a) View down the non-crystallographic 4-fold axis of the $[Dy(OH_2)_8]^{2+}$ cation of **3.3** showing the anisotropy axes for the three lowest Kramers doublets, the ground state (KD1), the ±1 excited state (KD2) and ±2 excited state (KD3) for Model 1 (long basis set); (b) lowest three Kramers doublets and the *ab initio* computed relaxation mechanism for Model 1 (long basis set) of DyBz(**3.3**). The thick black lines represent the Kramers doublets as a function of their magnetic moment along the main anisotropy axis. The blue dashed line corresponds to ground-state QTM, and the solid red lines to TA-QTM via the first and second excited Kramers doublets. Dashed green lines show possible Orbach processes. The values close to the arrows indicate the matrix elements of the transition magnetic moment.[106]

Interestingly, the main magnetic axes of the ground and first excited state KDs are perpendicular to the local 4-fold symmetry axis of the molecule (Figure 3.15a). This can be attributed to the orientation of the H-bonded protons of the coordinated water molecules which strongly influence the orientation of the magnetic axes, as has been reported previously for $[Na\{Dy(DOTA)(H_2O)\}]\cdot 4H_2O$.[157] Given the small first energy gap for this complex coupled with the observation of SMM behaviour in zero applied dc field, the slower relaxation process of domain C, $(1.57 \pm 0.60) \times 10^{-5}$ s in the ac data is tentatively

assigned to a predominantly QTM and the faster process of domain B $(3.98 \pm 1.37) \times 10^{-7}$ s to a thermally assisted (TA) Orbach process between KD1± and KD2±. In addition, the magnetic relaxation of domain A, $(5.09 \pm 0.69) \times 10^{-8}$ s, with the larger effective energy barrier, is assigned to a mechanism involving the second excited state KD3±, where the non-co-linearity of the axis in relation to the ground and first excited state, coupled with the significant deviation from Ising character facilitate both TA Orbach and QTM (Figure 3.15b).[157–160]

3.3.1.4 Photoluminescence studies

Given the recently demonstrated importance of photoluminescence (PL) studies for elucidating the magnetic anisotropy of Dy(III) ions,[66,105] we set out to carry out such investigations on complex **3.3**. The excitation paths for the Dy(III) ions were studied via the measurement of the excitation spectra monitored around the more intense $^4F_{9/2} \rightarrow {}^6H_{13/2}$ transition. In this respect, the emission and excitation spectra for **3.3**, acquired at 300 and 14 K reveal a broad band comprising three components at ca. 247, 275 and 281 nm associated with ligand emission, (Figure 3.16). In order to gain additional insight into the correlation between single ion magnet behaviour and luminescence properties and determine the crystal field splitting of the ground state of the Dy(III) ion in **3.3**, the low temperature (14 K) high-resolution emission spectrum in the spectral region of the $^4F_{9/2}$ - $^6H_{15/2}$ transition was determined. Figure 3.17 shows that this transition could be well-modelled by a 10-component multi-Gaussian function fit, enabling the determination of the energy gap between the KD.

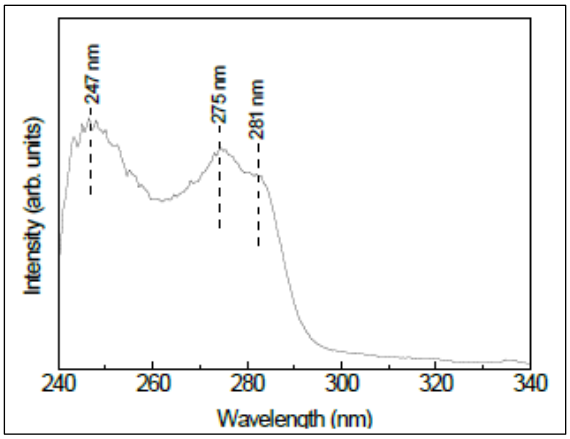

Figure 3.16 Excitation spectrum acquired at 14 K for **3.3** monitored at 440 nm.[106]

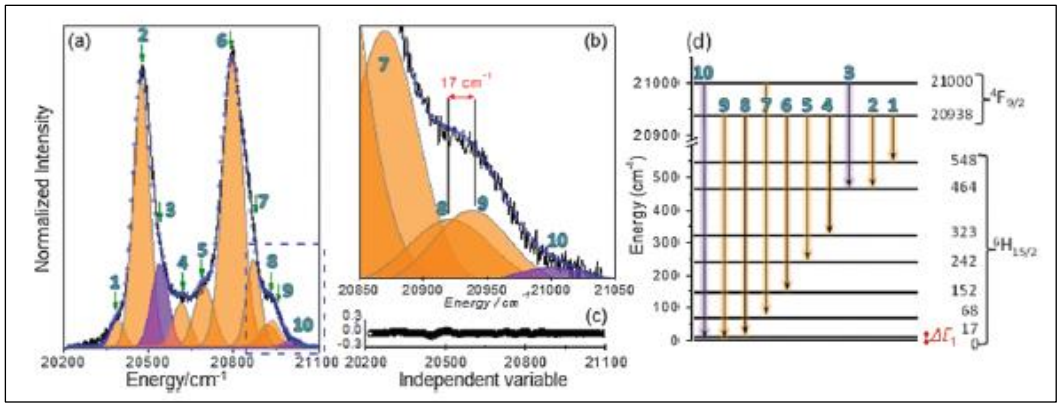

Figure 3.17 (a and b) Magnification of the $^4F_{9/2}$ - $^6H_{15/2}$ transition at 12 K and excited at 365 nm. Multi-Gaussian functions envelope fit (circles) and the components arising from the (orange shadow) first and (purple shadow) second $^4F_{9/2}$ Stark sublevels to the $^6H_{15/2}$ multiplet; (c) fit regular residual plot; (d) schematic diagram of the radiative transitions between the Stark sublevels of the $^4F_{9/2}$ and $^6H_{15/2}$ multiplets of the Dy(III) ion.[106]

In addition, a series of sharp lines arising from Dy(III) transitions occurring between the electronic levels of the $4f^5$ configuration, namely the $^6H_{15/2}$ ground level and the $^4G_{7/2}$, $^4F_{11/2}$, $^4D_{7/2,5/2}$ and $^3H_{7/2}$ excited states are also observed, Figure 3.18.

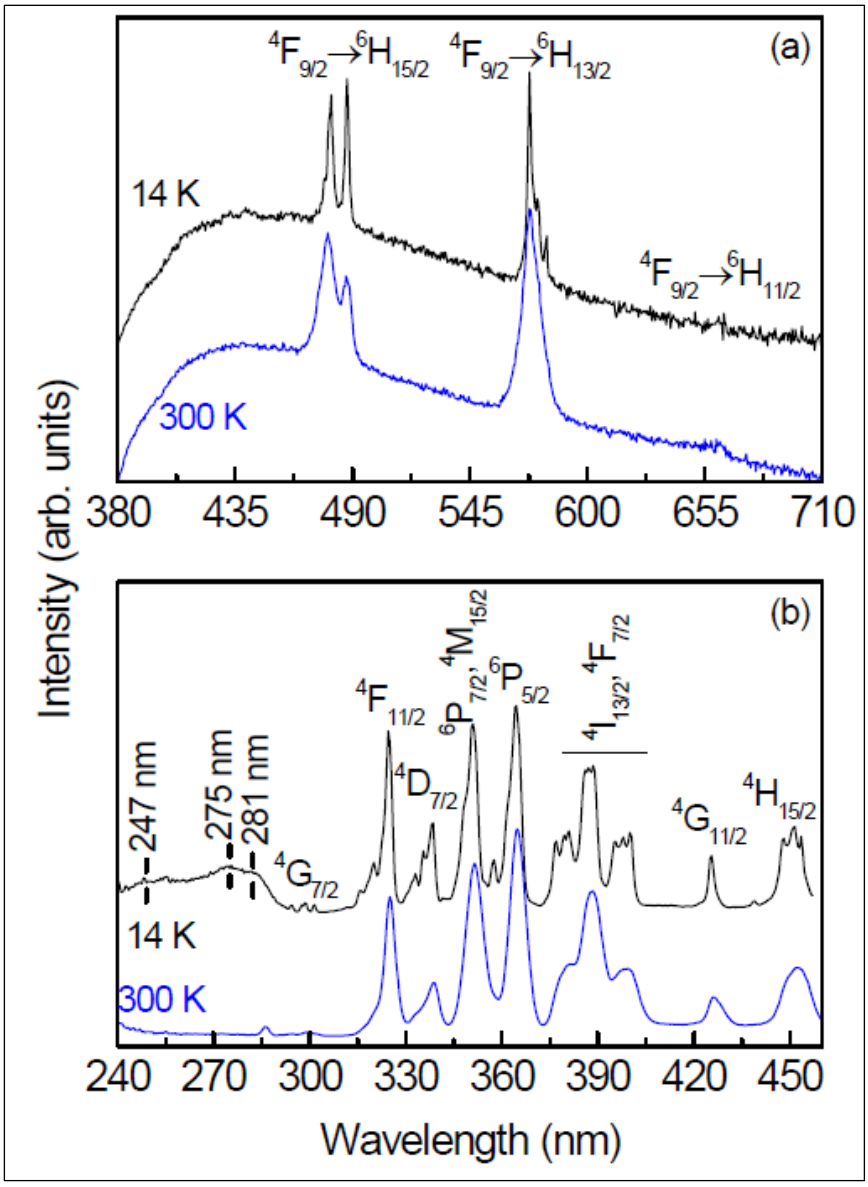

Figure 3.18 (a) Emission and (b) excitation spectra for **3.3** acquired at 300 K (blue lines) and at 14 K (black lines) for **3.3** excited at 365 nm and monitored at 574 nm respectively. In the excitation spectra the ground state ($^6H_{15/2}$) is omitted for simplicity and only the excited states are assigned.[106]

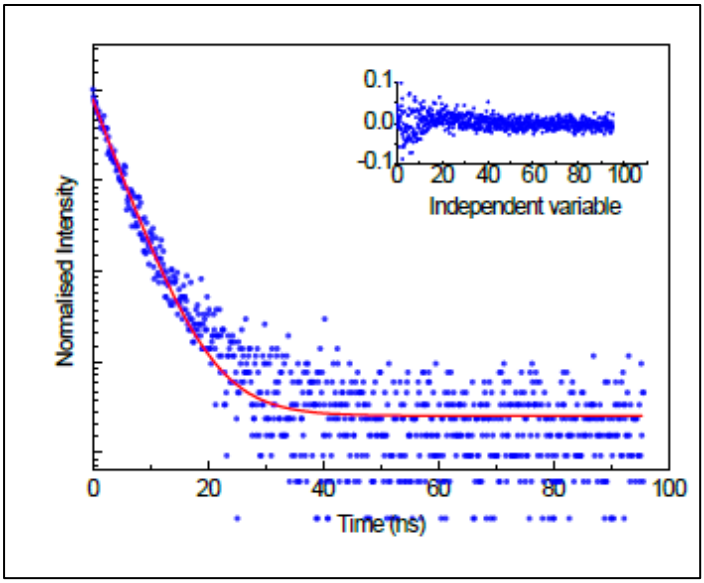

Figure 3.19 Emission decay curve (300 K) for **3.3** monitored at 577 nm and excited at 390 nm. The solid lines represent the single exponential fit. The inset shows the fit regular residual plot.[106]

Apart from a decrease in the full-width-at-half-maximum of the intra-4f^5 transitions, the emission is almost independent of the temperature. We also note that the intra-4f^5 components display lower relative intensity, so that we may readily infer that the Dy(III) excited states are mainly populated via an efficient ligand-sensitization mechanism. The room-temperature $^4F_{9/2}$ emission decay curve was monitored around the more intense transition of the Dy(III) ion ($^4F_{9/2} \rightarrow {}^6H_{13/2}$, 577 nm). The curve is well described by a single exponential function, (Figure 3.19) yielding a lifetime value of (5.75 ± 0.05) × 10^{-9} s.

The following methodology was used in order to determine the energy barrier, ΔE, based on the emission spectrum. Examining the spectrum, it is possible to discern, at least, 9 components marked with green arrows in Figure 3.17a. Taking into consideration that the Dy(III) ions have a local D_{4d} symmetry we may expect the splitting of the electronic

levels ($^4F_{9/2}$ and $^6H_{15/2}$) into the maximum number of allowed components, namely ($2J$ + 1)/2, which means that 5 and 8 components are expected for $^4F_{9/2}$ and $^6H_{15/2}$, respectively. Thus, at least, 8 Stark components are expected for the $^4F_{9/2}\rightarrow{}^6H_{15/2}$ transition if only the lower-energy Stark component of the $^4F_{9/2}$ excited state is populated, and all the transitions end at the lower-energy Stark of the ground multiplet $^6H1_{5/2}$. Since 9 components are clearly present (green arrows, Figure 3.17a), it readily points out that the second Stark component of the $^4F_{9/2}$ excited state must also be populated. This is a feasible situation, since the energy difference between that first Stark component and the second one is typically of the order of 60 cm^{-1}, as reported in the literature for several compounds.[53] Thus, at 15 ±3 K, it may be populated (up to 2 %). This rational, was behind the proposed 10-fit components. Moreover, considering transitions ending at excited Stark components of the $^6H_{15/2}$ multiplet, the energy of the Stark components of this multiplet does not match with what was reported. To locate the first and second Stark components of the $^4F_{9/2}$ level, the low wavelength region of the spectrum was inspected, so that the later component was tentatively set at 60 ±10 cm^{-1} above the clearly express transition ascribed to the 0→0 transition. Then, the 9 remaining components were fitted using a Gaussian function, whose energy was constrained to the peak position analysis based on the spectrum observation (green arrows, Figure 3.17a) taking into account the experimental uncertainty (±3 cm^{-1}); the full-width-at-half-maximum and the relative intensity was free to vary. The energy peak position and full-width-at-half maximum resulting from the fit are summarized in Table 3-4.

Assignment*	*E*	*fwhm*
10	20390.0	58.8
9	20474.0	69.6

8	20540.0	70.6
7	20615.0	70.6
6	20696.0	82.4
5	20786.1	72.4
4	20844.0	76.5
3	20921.0	76.5
2	20938.0	70.6
1	21000.0	61.0

Table 3-4 Energy peak position (E, ± 3.0 cm^{-1}) and full-width-at-half maximum (fwhm, ± 5.0 cm–1) of the $^4F_{9/2} \rightarrow {}^6H_{15/2}$ Stark components determined from the experimental emission spectrum (acquired at 12 K and excited at 365nm) best fit using a 10-component Gaussian fit. *The assignment is illustrated in Figure 3.17a.[106]

The maximum Stark splitting of the $^6H_{15/2}$ level is eight, pointing out the presence of two transitions arising from ‘‘hot’’ bands involving the first Stark component of the $^4F_{9/2}$ level. From the best fit of the data, an energy diagram of the Stark-sub-levels is presented in Figure 3.17d. From these data, the energy gap between the ground KD1± and first excited state KD2±, ΔE_1 = 17 cm^{-1}, and between KD1± and the second excited state KD3±, ΔE_2 = 68 cm^{-1}. Although the experimentally determined value of U_{eff} of domain A (26 cm^{-1}) from the ac data is smaller than the value of ΔE_2, of 44 cm^{-1} (*ab initio*) and 68 cm^{-1} (PL), these values are consistent with Orbach and/or QTM relaxation via KD3± rather than KD2± where the experimental ac data, PL data and *ab initio* calculations are all in good agreement (13.5 ± 3.5 cm^{-1}).

3.3.1.6 Conclusions and future work

To conclude, we have adopted an interdisciplinary approach towards unravelling the magnetochemistry of an emissive $[Dy(OH_2)_8]^{3+}$ complex, encapsulated within a

supramolecular cage of Bz15C5 macrocycles. The pseudo D_{4d} symmetry of the complex serves to suppress relaxation mechanisms via the ground and first excited KDs resulting in the observation of SMM behaviour. Furthermore, encapsulation results in long intermolecular Dy···Dy distances > 12 Å, analogous to magnetic dilution and is therefore a useful strategy for reducing dipolar interactions in the crystal lattice, which in turn supresses QTM. Detailed magneto-optical and theoretical studies are supportive of a dominant magnetic relaxation pathway involving the second excited state KD3± which is rare for low symmetry mononuclear Ln-SMMs, where the absence of a crystallographic axis of symmetry means the strong axial ligand field is likely the dominant factor in determining the thermal energy barrier. Interestingly, the larger size of the Gd(III) and Tb(III) ions afforded complexes with different molecular structures in the solid state, where even though the oblate Tb(III) ions were magnetically isolated, no SMM properties were observed, most likely due to the absence of an appropriate crystal field.

In light of these results we then moved forward to investigate the coordination chemistry of diBz15C5 with Dy(III).

3.3.2 Ln(III) complexes of diBz15C5

3.3.2.1 Synthesis and structural studies

Reaction of one equivalent of $Dy(ClO_4)_3$ together with two equivalents of Dibz15C5 in a 1:3 mixture of methanol and acetonitrile followed by slow evaporation of the solvent afforded suitable single crystals of $[Dy(H_2O)_9](ClO_4)_3$(diBz-15C5)$_2$ (**3.6**) for X-ray diffraction studies. Analysis of the molecular structure reveals the complex crystalizes in the orthorhombic space group Pnma, and is comprised of a $[Dy(H_2O)_9]^{3+}$ cation H-bonded to two diBz15C5 macrocycles and three perchlorate counter ions (Figure

3.2, top). A summary of selected bond lengths and angles for **3.6** are summarized in Table 5-6 in the Appendix section of this thesis.

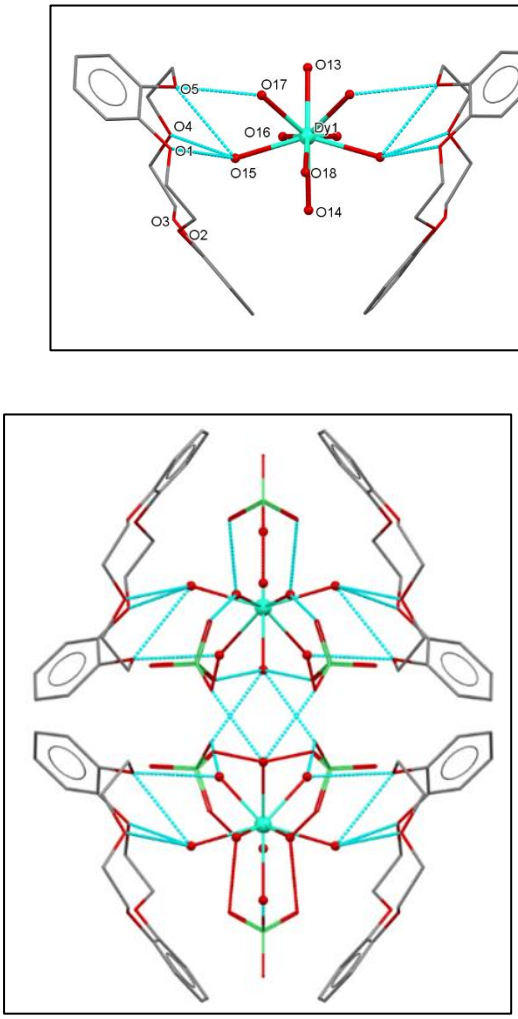

Figure 3.20 Molecular structure of **3.6** with the appropriate atomic numbering scheme. H-bonds are shown as blue dashed lines (top). Molecular structure of **3.6** highlighting intermolecular H-bonds as blue dashed lines (bottom). Colour code: red = O, gray = C, green = Cl, light green = Dy(III).

The asymmetric unit of DyDiB(**3.6**) contains one crystallographically independent dibz-15C5 macrocycle, one $[Dy(H_2O)_6]^{3+}$ unit, and two crystallographically independent perchlorate counterions. A crystallographic mirror plane runs through the Dy1 ion as well

as three coordinated water molecules (O13, O14 and O18), and Cl2 O11 and O12 of a perchlorate anion. Analysis of the coordination geometry of the Dy1 ion using continuous shape measures[161] reveals it is 9-coordinate, closest to a muffin polyhedron with a CSM of 2.36, (Figure 3.21, Table 3.5). This is in sharp contrast to the Dy(III) ion of the Bz15C5 complex **3.3**, which was very close to ideal square antiprismatic, D_{4d}.

Polyhedron	Symmetry	Dy(III) CSM
EP-9	D_{9h}	33.77
OPY-9	C_{8v}	22.74
HBPY-9	D_{7h}	13.95
JTC-9	C_{3v}	15.42
JCCU-9	C_{4v}	9.58
CCU-9	C_{4v}	7.94
JCSAPR-9	C_{4v}	4.81
CSAPR-9	C_{4v}	3.55
JTCTPR-9	D_{3h}	6.10
TCTPR-9	D_{3h}	3.97
JTDIC-9	C_{3v}	13.89
HH-9	C_{2v}	8.30
MFF-9	*Cs*	2.36

Table 3-5 Continuous shape measures (CSMs) of the 9-coordinate Dy(III) coordination polyhedron in complex **3.6**. The value in red indicates the closest polyhedron according to the CSMs. Abbreviations: EP-9, Enneagon; OPY-9, Octagonal pyramid; HBPY-9, Heptagonal bipyramid; JTC-9, Johnson triangular cupola J3; JCCU-9, Capped cube J8; CCU-9 , Spherical-relaxed capped cube; JCSAPR-9, Capped square antiprism J10; CSAPR-9, Spherical capped square antiprism; JTCTPR-9, Tricapped trigonal prism J51; TCTPR-9 , Spherical tricapped trigonal prism; JTDIC-9, Tridiminished icosahedron J63; HH-9 , Hula-hoop; MFF-9, Muffin.

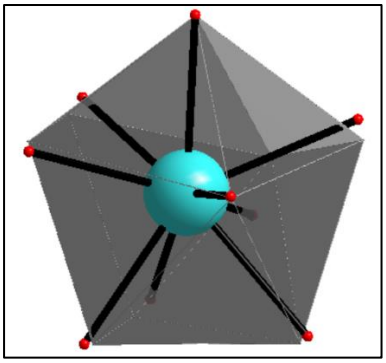

Figure 3.21 Coordination geometry of the Dy(III) cation superimposed on an idealized muffin polyhedron (grey).

The Dy-O bond lengths in **3.6** range from 2.30(2) to 2.410(18) Å and are slightly longer than those observed for the Bz15C5 complex **3.3**,[162] which is not surprising given the increase in the coordination number of the *4f* ion. Two coordinated water molecules (O15 and O17) are H-bonded to neighbouring crown ether oxygen atoms with O···O distances between 2.86(2) and 3.02(2) Å. The remaining coordinated waters are all H-bonded to neighbouring perchlorate anions with O···O distances ranging from 2.64(3) to 3.18(2) Å (Figure 3.20, bottom) The crystal packing is further stabilized by C-H···π interactions involving the π system of the benzo substituents on the crown ether ligands, with C-H···π distances of 2.70(3) - 2.94(2) Å and angles between 153 and 166°.

Interestingly, the increased size and rigidity of the diBz15C5 macrocycle *vs* Bz15C5 has completely altered the structural topology of the complex, where we now have two fully hydrated cations encircled by four dibz15C5 macrocycles with perchlorate counterions occupying the crystallographic space above and below a hydrocarbon fence, (Figure 3.22). Closer examination of the crystal packing reveals that the shortest intermolecular Dy···Dy distances are 8.370 Å, which are considerably shorter than the Dy···Dy distances (> 12 Å) that are reported for the DyBz15C5 complex, **3.3**.

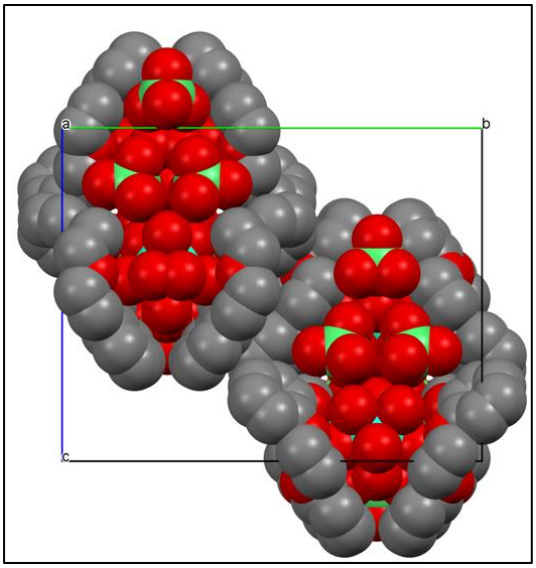

Figure 3.22 Spacefill representation of the crystal packing of **3.6** showing two the two enclosed $[Dy(H_2O)_9]^{3+}$ cations and the hydrocarbon fence around them. View down the *c*-axis; H atoms are omitted for clarity.

3.3.2.2 Magnetic studies

Variable temperature direct current (dc) magnetic susceptibility measurements were performed on crushed single crystals of **3.6** in a 1000 Oe field between 2 and 300 K range. The data are shown as a $\chi_M T$ *vs* T plot in (Figure 3.23). The experimental $\chi_M T$ value (14.15 cm^3 K mol^{-1}) at 300 K is in excellent agreement with the expected value for an isolated Dy(III) ($^6H_{15/2}$, S = 5/2, L = 5, g = 4/3) ion.[163] Upon cooling, $\chi_M T$ decreases slightly from 300 K to reach a value of 13.85 cm^3 K mol^{-1} at 100 K. Below this temperature $\chi_M T$ decreases more rapidly to a minimum value of 9.62 cm3 K mol^{-1} at 2 K. The observed steeper decrease below 100 K is once again attributed to the thermal depopulation of the excited Stark sublevels of the Dy(III) ion, rather than to the presence of intermolecular interactions.

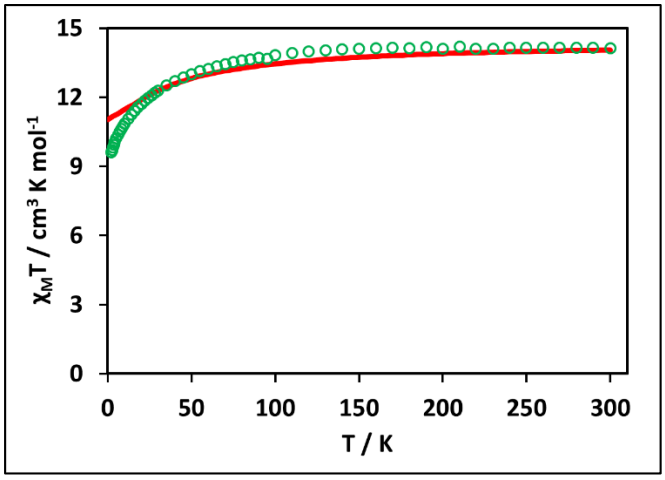

Figure 3.23 Temperature dependence of the $\chi_M T$ product for **3.6**. Solid red lines are the calculated $\chi_M T$ product from the *ab initio* studies.

In addition, the field dependence of the magnetization below 7 K was measured for **3.6** over the range of 0-7 T (Figure 3.24, left). The M *vs* H plot shows a rapid increase below 1 T followed by a slow, nearly linear increase up to 5.63 μ_B without reaching saturation (Figure 5, bottom). The lack of saturation in the magnetization of DydiBz15C5 (**3.6**), as well as the fact that the value at 7 T is considerable lower that the theoretically predicted value of 10.63 Nμ_B.[163] indicates the population of low-lying excited states. This conclusion is further supported by the reduced magnetization data, (Figure 3.24, right) where the isofield lines do not superimpose on a single master curve but slightly deviate from one another, indicating non-negligible magnetic anisotropy.

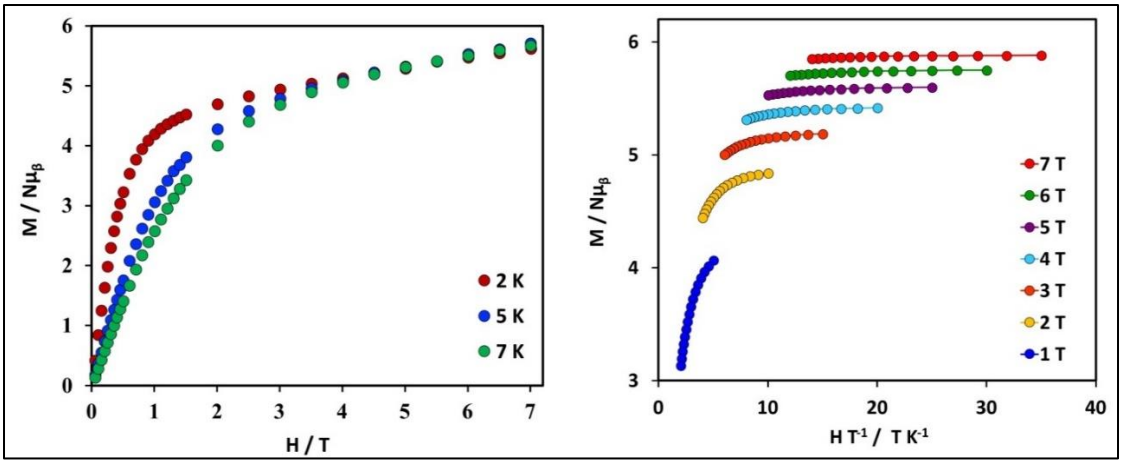

Figure 3.24 Field dependence of Magnetization (M) for **3.6** at different temperatures (left) and plot of reduced magnetization ($M/N\mu_B$) *vs.* HT^{-1} for **3.6** at applied fields of 1–7 T and in the 2–5 K temperature range (right). The solid lines are a guide for the eye.

Alternating current (ac) magnetic susceptibility measurements were also performed in order to probe the low-temperature magnetic relaxation dynamics of the complex. These studies revealed that **3.6** displays frequency-dependent out-of-phase (χ'') tails of signal below ~9 K under a zero dc static field, (Figure 3.25). The absence of peak maxima in the out-of-phase (χ'') signal in the frequency range of 1-1000 Hz from 2 to 15 K is indicative of fast magnetic relaxation due to ground state quantum tunnelling, and as previously mentioned is not uncommon for mononuclear *4f*-SMMs.[28] As previously explained, upon application of a small static dc field such QTM process can be suppressed.

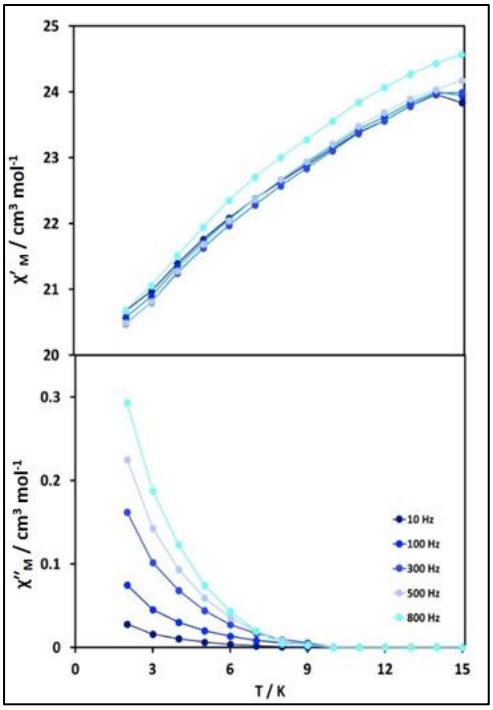

Figure 3.25 Temperature dependence of the in-phase $\chi'T$ product (top) and out-of-phase χ'' (bottom) ac susceptibility signals of DydiBz15C5 (**3.6**) in a 2 Oe field oscillating at the indicated frequencies. Solid lines are guide for the eye.

To this end, ac susceptibility measurements at various static fields (0 - 2000 Oe) were performed and the optimum applied dc field of 1000 Oe was chosen as the field at which a maximum in χ'' was visible at 5 K (Figure 3.26). Slow magnetic relaxation is therefore induced, since well-resolved peaks appear now in the χ'' *vs* frequency plot, with maxima that shift to higher frequencies as the temperature increases (Figure 3.27, left). At low temperatures (up to ~3.5 K), two relaxation processes are now observed, but at higher temperatures only one highly frequency dependent process prevails. As a result, the experimental data between 2-6.32 K were fit using a generalized Debye model to extract the τ and α parameters, considering two relaxation processes (Figure 3.27, right).

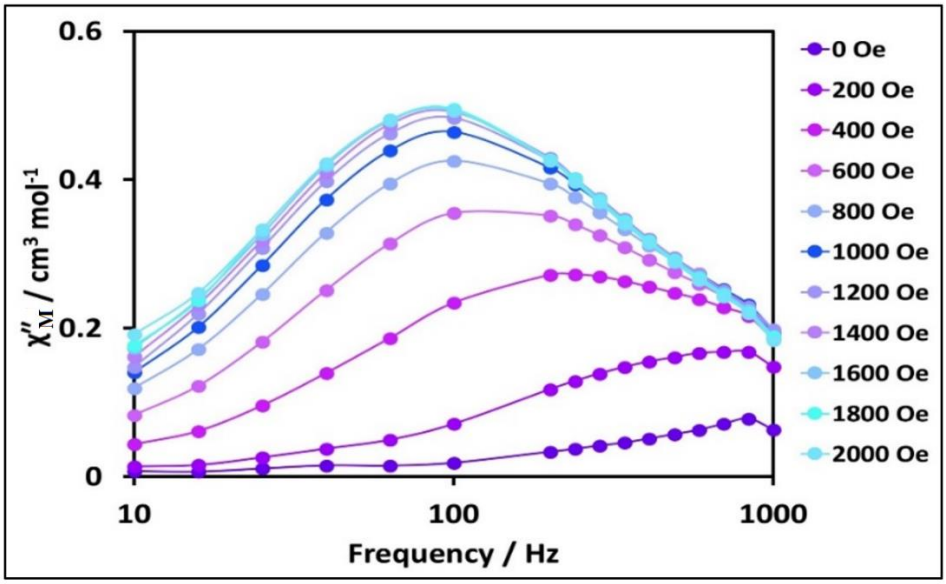

Figure 3.26 Out-of-phase susceptibility *vs* frequency plots for **3.6** in various applied dc fields at 5 K. Solid lines are guide for the eye.

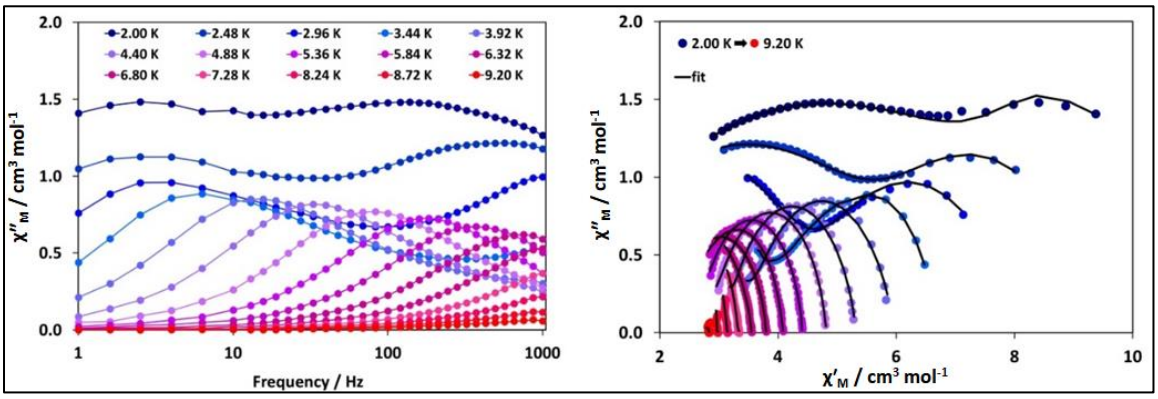

Figure 3.27 Out-phase (χ″) component of the magnetic susceptibility *vs* frequency, under 1000 Oe applied dc field (left), (solid lines are guide for the eye). Cole-Cole plot for **3.6** obtained using the ac susceptibility data under 1000 Oe applied dc field (right). The solid lines correspond to the best fit obtained with a generalized Debye model.

Unfortunately, the lack of peak maxima for the second relaxation process below 3.5 K did not allow us to further analyse the τ and α parameters for this relaxation process. Hence, we were only able to successfully model the high temperature relaxation process. In this respect the τ values obtained were used to construct a τ^{-1} *vs* T plot and the data were

analysed using least square regression based on equation **3.8** that accounts for multiple relaxation processes (Figure 3.28, right).[19,164,165]

$$\tau^{-1} = AH^4T + \frac{B_1}{1 + B_2H^2} + CT^n + \tau_0^{-1}exp\left(-\frac{U_{eff}}{k_BT}\right) \qquad \textbf{Eqn. 3.9}$$

In this equation A represents the direct process, B_1 and B_2 are QTM parameters, CT^n and, $\tau_0^{-1}\exp(-U_{eff}/k_BT)$ describe Raman, and Orbach relaxation pathways, respectively. To avoid over-parameterization, the field dependence of τ^{-1} at 5 K was initially fit based on a model (equation **3.9**), accounting for direct and tunneling relaxations and a constant to include contributions from the field independent processes (Raman and Orbach) (Figure 3.28, left).[19,164,165]

$$\tau^{-1} = AH^4T + \frac{B_1}{1 + B_2H^2} + D \qquad \textbf{Eqn. 3.10}$$

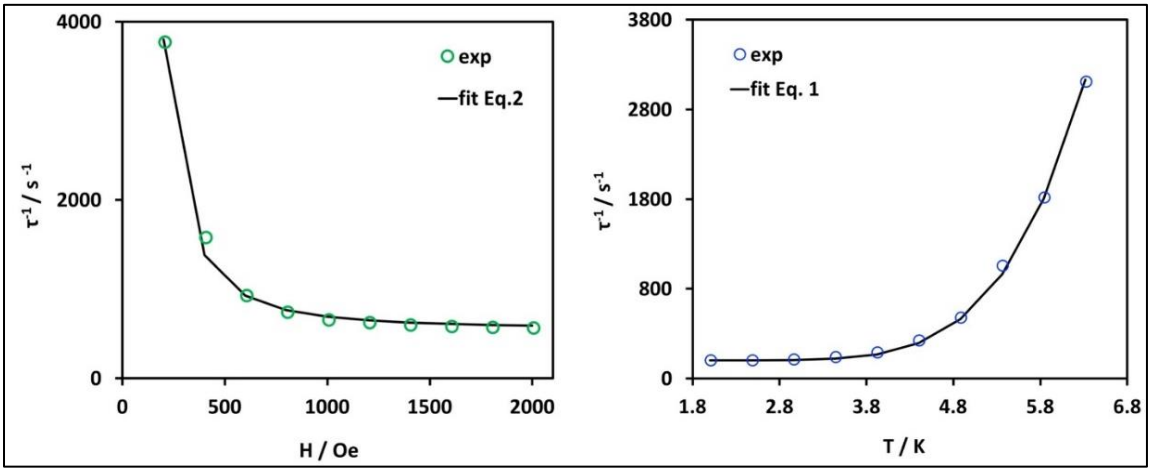

Figure 3.28 Field dependence of magnetic relaxation time τ^{-1} at 5 K (left) and temperature dependence of τ^{-1} under 1000 Oe applied filed (right). Solid lines correspond to the best fit obtained using equations 3.8 and 3.9.

The best fit was obtained for A = 1.58 x 10^{-10} s^{-1} T^{-4} K^{-1}, B_1 = 1.51 x 10^5 s^{-1} and, B_2 = 1.14 x 10^5 T^{-2}. These values are reasonable considering that above the optimum field,

τ^{-1} decreases slightly, suggesting that Raman and Orbach relaxations dominate and there are minor contributions from the direct process. The decrease of τ^{-1} with the field at low fields can be ascribed to QTM and it was successfully fit with eq. 3.9. The above parameters were then fixed in eq. 3.8 in order to model the temperature dependence of τ^{-1}. The Raman parameters obtained were n = 7.88 and, C = 4.9 x 10^{-4} s^{-1} $K^{-7.78}$. For Kramers ions, a value of n = 9 (or 5 in the presence of low-lying states) is expected, however, values between 2 and 9 are also reasonable considering the presence of both acoustic and optical phonons.[19,164,165] Finally, an effective energy barrier U_{eff} = 40.0 K and a pre-exponential factor $\tau_0 = 8.4 \times 10^{-7}$ s were extracted.

3.3.2.3 *Ab initio* studies

To examine the electronic structure and magnetic anisotropy behavior of the Dy(III) ion in complex **3.6** detailed CASSCF/RASSI/SINGLE_ANISO *ab initio* calculations were performed. Calculations reveal that the ground state Kramers doublet (KD) has negligible transverse components (g_x = 0.0034, g_y = 0.0159) and the g_z value nearly approaches the value of ~20 expected for a pure Ising m_J = 15/2 multiplet (Table 5-27). It results in a small QTM value for the ground state KD, suggesting that magnetic relaxation likely occurs through higher excited states. The larger transverse components were observed in the second excited KD when compared to the first excited KD, suggesting that as previously described for the encapsulated benzo analogue, relaxation of magnetization via the second excited KDs is mostly likely. It indicates that the magnetic anisotropy of the Dy^{III} ion is able to sufficiently block the magnetization at zero field which support the experimental observations. The eight KDs are have the energies of 0.0, 91.6, 243.3, 296.6, 336.4, 431.3, 486.0, 528.9 cm^{-1} respectively in complex **3.6,** (Table 5-27).

The *ab initio* computed magnetic susceptibility data (Figure 3.23) is in good agreement with the experimental magnetic data that gives us confidence in the computed parameters. The magnetic relaxation mechanism was constructed to extract the computed energy barrier for complex **3.6**, (Figure 3.29). The axial nature of the ground KDs leads to a small QTM value (0.003 μ_B). Moreover, the wave function analysis supports the yield of small QTM where the ground KD is mostly made up of the $m_J = \pm 15/2>$ multiplet with small contributions from the $m_J = \pm 11/2>$ multiplet. However, the enhanced transverse components of first excited KD ($g_x = 0.1157$, $g_y = 0.1254$) cause the moderate Temperature Assisted-QTM (TA-QTM) value (0.04 μ_B). The enhancement of first excited KD transverse anisotropy is further witnessed by enhanced mixed character i.e combination of $m_J = \pm 13/2 >$ and $m_J = \pm 9/2 >$ multiplets. This result stimulates relaxation via the second excited KDs to take place.[158] The crystal field parameters were calculated, (Table 5-28) to further understand the observed mechanism of magnetic relaxation.[166,167] The probability of QTM is higher when the non-axial B^k_q terms ($q \neq 0$ and $k = 2, 4$) are larger than the axial ($q = 0$ and $k = 2, 4$) terms. In complex **3.6**, the axial terms are moderately larger than the two non-axial terms, which overall leads to the presence of reasonably weaker QTM process in the ground as well as the first excited state. The large transverse components ($g_x = 0.9324$, $g_y = 1.7328$) in the second excited KDs cause fast TA-QTM (0.45 μ_B) between these KDs and allow the magnetic relaxation at 243.3 cm^{-1} (457 K). This U_{cal} value is highly overestimated compared to the experimental energy barrier of 40 K which could be due to the exclusion of intermolecular interactions in the calculation and/or the chance of a non-Orbach relaxation mechanism which could significantly reduce the experimentally determined energy barrier .[167,168]

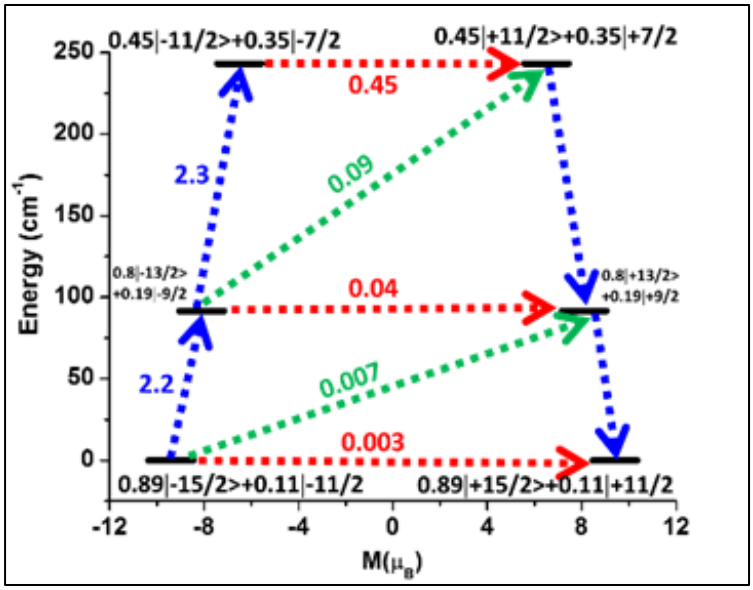

Figure 3.29 Magnetization blocking barrier for the Dy site in **3.6**. The thick black line indicates the Kramers doublets (KDs) as a function of the computed magnetic moment. The green/blue dotted arrows show the possible pathway through Orbach/Raman relaxation. The dotted red lines represent the presence of QTM/TA-QTM between the connecting pairs. The numbers provided at each arrow are the mean absolute values for the corresponding matrix element of the transition magnetic moment.

3.3.2.4 Photoluminescence studies

The thermal dependence of the emission and excitation spectra of **3.6** are shown in Figure 3.30. At room temperature, the emission spectrum is dominated by the Dy(III) transitions, namely the more intense $^4F_{9/2} \rightarrow {}^6H_{13/2}$ transition at ~573 nm overlapping a higher energy broad band in the blue spectral region arising from the organic ligands.[162] As the temperature decreases to 15 K, the relative intensity of this broad band increases being the more intense component at 15 K. Such thermal dependence suggest that the ligands-to-Dy(III) energy transfer is thermally activated yielding a relative decrease of ligand-related emission at room temperature. Comparing these data with the that acquired for complex

3.3, where the ligands-related emission is observed over the entire temperature interval (15-300 K),[162] we notice a more efficient energy transfer in the present case.

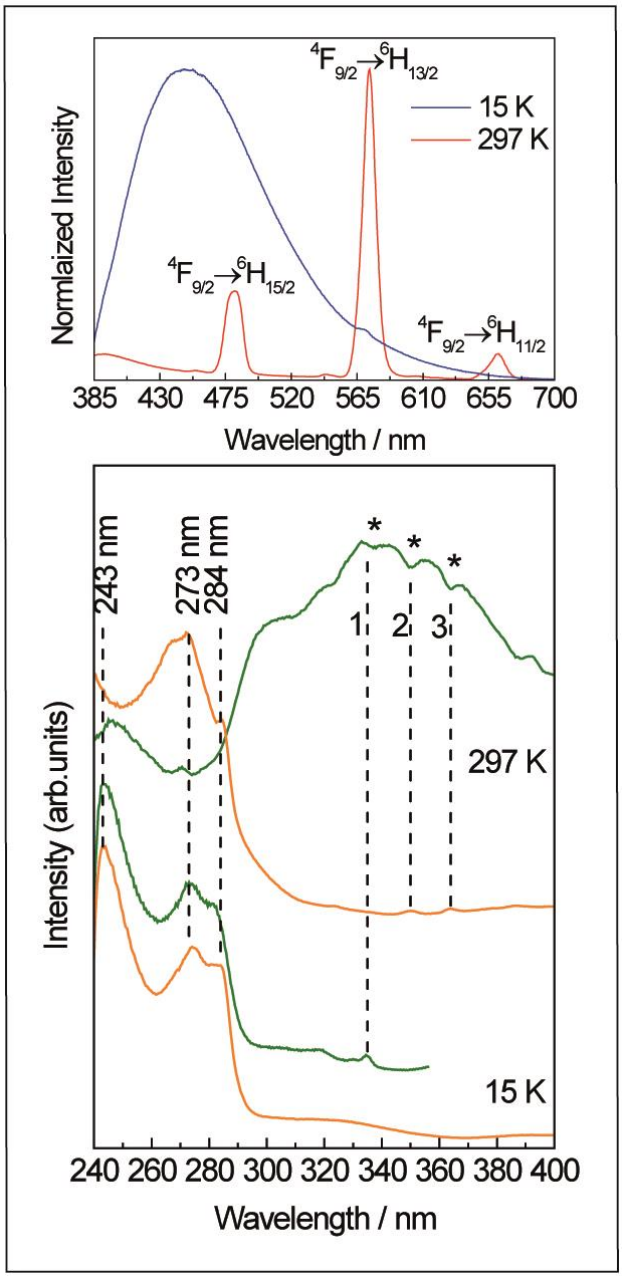

Figure 3.30 (top) Emission spectra of **3.6** acquired at 297 K and 15 K for excitation at 284 nm. (bottom) Excitation spectra of **3.6** acquired at 297 K and 15 K and monitored at (green line) 411/432 nm (orange line) and 573 nm. Self-absorptions between the $^6H_{15/2}$ level and the (1) $^4D_{7/2}$, (2) $^6P_{7/2}$, $^4M_{15/2}$ and (3) $^6P_{5/2}$ excited states.

The low temperature excitation spectrum monitored within the Dy(III) emission reveals a broad band in the UV spectral region with three components (~243, 273 and 284 nm), previously observed for complex **3.3**, ascribed to the ligands' excited states.[162] This observation is corroborated by the fact that this spectrum resembles that selectively monitored with the ligands emission at 15 K. At room temperature, a series a very low relative intensity bands ascribed to the intra-$4f^5$ transitions are also discerned in the spectrum monitored within the Dy(III) emission. Independently of the temperature, the higher relative intensity of the ligand-related bands in the spectra monitored at 573 nm points out that the Dy(III) excited state is essentially populated through sensitization, rather than by direct intra-$4f^5$ excitation, contrary to that found for complex **3.3**, where direct excitation dominates.[162] This study clearly demonstrates that local-structure of the complex favours energy transfer. We also notice that the excitation spectrum monitored within the ligands-related emission at 297 K is dominated by a high-wavelength band (300-400 nm) in which several *f-f* self-absorptions (marked with an asterisk in Figure 3.30) are discerned, indicating that part of the emitted light is absorbed by the Dy(III) ions. This band and the presence of the "inner filter affect"[169] have also been previously observed for complex **2.4,** where in both cases the Dy(III) emission is essentially excited by the ligands.[170] The ligands-related emission was further studied by time resolved spectroscopy (Figure 3.31), revealing a long-lived component with a lifetime value of the order of 10^{-3} s pointing out a triplet state. As the temperature is raised from 15 to 300 K, the lifetime value decreases in good agreement with the thermal activation of ligands-to-Dy(III) energy transfer, as discussed above.

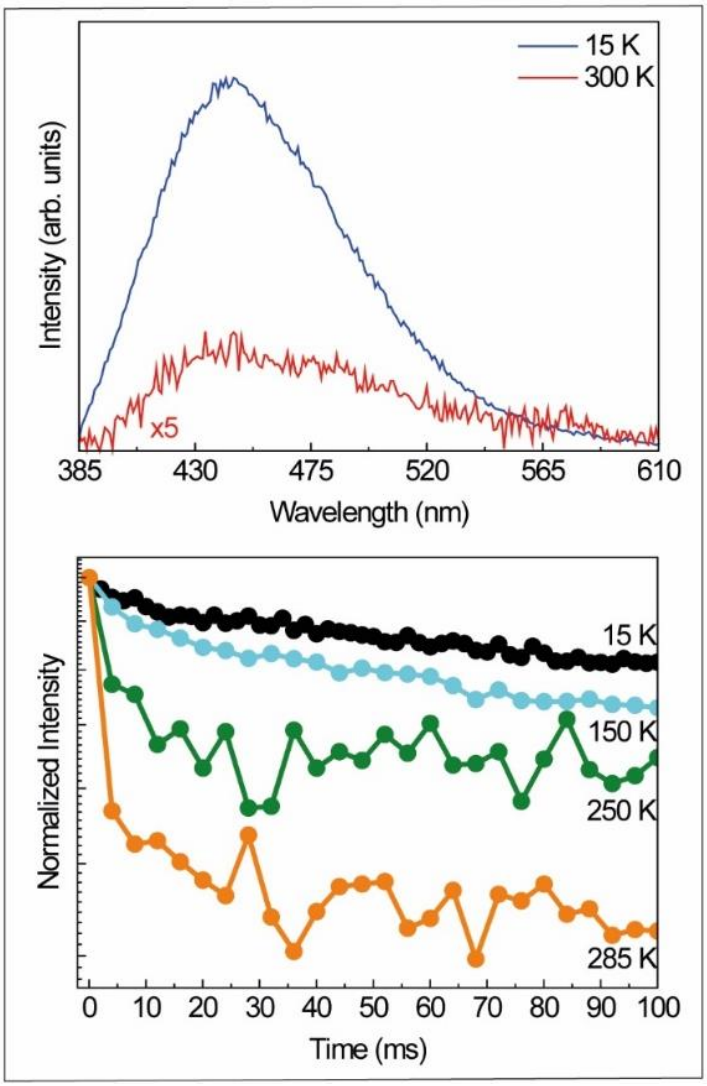

Figure 3.31 (top) Time-resolved emission spectra (starting delay = 5×10^{-5} s) excited at 284 nm and acquired at 15 K and 300 K. (bottom) Emission decay curves excited at 280 nm, monitored at 440 nm and acquired at distinct temperature values. The lines are visual guides only.

3.3.2.5 Conclusions

To conclude, when comparing the magneto-structural properties of the dibenzo complex **3.6** with the less rigid benzo system **3.3**, it is apparent that the coordination geometry of the two Dy(III) ions are quite different, i.e. 9- coordinate muffin (Cs)

geometry for **3.6**, *vs* an 8-coordinate close to D_{4d} geometry for **3.3**. Surprisingly, despite these differences the two complexes possess very similar magnetization dynamics, since both are zero field SMMs, with almost identical energy barriers namely, U_{eff} = 27 cm^{-1} for **3.3** and 28 cm^{-1} for **3.6**. Furthermore, *ab initio* studies on both complexes reveal that despite their different coordination geometries, the axiality of their ground states are almost pure Ising which means that the probability of QTM via this state is reduced which supports the experimental observations of SMM behavior in zero dc field. As for **3.3,** *ab initio* studies reveal that fast thermally assisted-QTM (TA-QTM) via the second exited KD state are also dominant for **3.6** which is evidenced by large transverse components (g_x = 0.9324, g_y = 1.7328, g_z = 12.951) and the large magnitude of the transition magnetic moment matrix element of 0.45 μB, when compared to the first excited KD. With respect to the solid-state photoluminescent studies, complex **3.6** has additional chromophores which increase its molar coefficient, where ε = 18313 L $mol^{-1}cm^{-1}$ *vs* 4700 L mol^{-1} cm^{-1} for the DyBz15C5 complex, **3.3**. This increase leads to an efficient energy transfer process from the dibenzo ligands to the excited state of the *4f* ion at room temperature, but unfortunately at low temperature this prosses is switched off and the ligand is returned to its ground state, giving rise to a broad emission that masks the *f-f* transitions. Consequently, from the solid-state photoluminescence studies, we were unable to extract the fine structure and determine the Orbach barrier for dibenzo complex, **3.6**.

4 3*d*-Heterodinuclear and 4*f*-Mononuclear Complexes of a Schiff-Base Compartmental Macrocycle

This work is unpublished to-date, the synthesis and characterization of all complexes was carried out by Ras Ali. Magnetic susceptibility data was collected by Dr. Alexandropoulus and modelled by Ras Ali in collaboration with Dr. Alexandropoulus.

4.1 Introduction

Significant attention has been paid to *4f* ions with large intrinsic magnetic anisotropy such as Dy(III) and Tb(III),[31,103,126,171] since the observation of slow relaxation of magnetization in the mononuclear $[LnPc_2]^-$ (Pc = phthalocyanine, Ln = Tb, Dy) complexes, reported by Ishikawa *et al* in 2003.[102] Over the past decade studies have shown that the incorporation of lanthanide ions particularly Dy(III) ions is an efficient strategy to obtain SMMs with large energy barriers and high blocking temperatures.[38,40] For example, the recent report of the pseudo linear complex $[(Cp^{iPr5})Dy(Cp^*)]$ $[B(C_6F_5)_4]$ (**1.7**), (Cp^{iPr5} = penta-iso-propylcyclopentadienyl, Cp* = pentamethylcyclopentadienyl),[40] with an effective energy barrier (U_{eff}) of 1541cm^{-1} and a magnetic hysteresis of 80 K, first discussed in Chapter 1, has re-energized the field of SMMs, showing that practical applications are now on the horizon. As also previously outlined, the magnetic properties of *4f* complexes depend on the interaction between the electron density of the single ion with its crystal field environment. Therefore, high performance SMMs with considerable magnetic anisotropy can now be strategically enhanced by employing the electrostatic model first introduced by Long *et al*.[30] which optimizes the ligand field environment of a complex according to whether the shape of the electron density distribution of the *4f* ion

is oblate or prolate.[172] Applying this strategy, the magnetic anisotropy of oblate Ln(III) ions such as Tb(III), Dy(III), and Ho(III) are enhanced in an axial ligand field. This includes the sandwich-type, square antiprismatic geometries of the first family of phthalocyanine (P_c) *4f*-SMMs, which minimizes the repulsion between charge clouds of the Ln(III) ions and the negative charges on the P_c ligands. In contrast, an equatorial ligand field is more suitable for those Ln(III) ions with prolate character which include Er(III), Tm(III), and Yb(III) ions.[149,171–173] Building on this theory, *ab initio* calculations were carried out in recent years suggesting that particularly large magnetic anisotropy could be achieved if an oblate *4f* ion is placed in a linear coordination environment. In this respect, coordination to one or two negatively charged donor atoms with short bond distances should provide complete overlap between the ion and ligand electron clouds that was predicted to enhance the axiality of the crystal field and afford a high energy barrier SMM where QTM are suppressed.[173] This was confirmed experimentally by the discovery of several linear Dy(III) complexes, including **1.7,** which has the highest recorded energy barrier of any SMM reported to-date.[40] However, in terms of practical applications, linear lanthanide complexes are very difficult to synthesize since due to their large ionic radii Ln(III) ions tend to prefer to form complexes with much higher coordination numbers.[137,173,174] Furthermore, most of the low-coordinated lanthanide SMM are not particularly air stable, which could also be problematic for practical applications.[32,173] One alternative strategy is to synthesise Ln(III) complexes with higher coordination geometries such as pentagonal bipyramidal, where the *4f* ion coordinates to weak field equatorial ligands but then utilize strong axial field ligands to enhance the magnetic anisotropy of oblate ions.[32,173] Following this strategy, D_{5h} symmetry has been shown to suppress QTM

and enhance the effective energy barrier, affording high-performance SMMs.[32,173–175] One of the best examples of a *4f* complex with D_{5h} geometry is [Dy(bbpen)Br] (**1.4**) (where H_2bbpen = N,N′-bis(2-hydroxybenzyl)-N,N′-bis(2-methylpyridyl)ethylenediamine) reported by Tong *et al.* The Dy(III) ion is coordinated equatorially to five weak N and two strong O^- atoms of the bbpen ligand, affording near perfect pentagonal bipyramidal geometry affording an SMM with a high energy barrier of 1025 K, Figure 1.12, Chapter 1.[32]

In previous studies the Pilkington group has employed N_5 and N_3O_2 macrocycles first developed by Nelson in the 1970's to confer pentagonal bipyramidal geometry on *3d* and *4f* ions.[74] Unfortunately, the resulting *4f* complexes were not crystalline which made magneto-structural studies difficult, so the group moved to investigating the coordination chemistry of a dual compartmental Schiff-base macrocycle that contains both an N_3O_2 Schiff base cavity and a O_3O_2 crown-like cavity. Following this strategy, three Ln(III) complexes with general formula $[Na_2Ln_2(\mathbf{L_3})_2Cl_4(MeOH)]\cdot xH_2O$, (Ln(III) = Dy (III), Tb (III), and Er(III)) were prepared and studied.[100] In all three complexes, the Na^+ cation occupies the O_3O_2 crown-like cavity, while the *4f* ion is equatorially coordinated in the N_3O_2 Schiff-base cavity together with two axial ligands, affording pentagonal bipyramidal geometry. Magneto-structural and *ab initio* studies confirm that $[Na_2Dy_2(\mathbf{L_3})_2Cl_4(MeOH)]\cdot 2H_2O$ (**4.1**) (Figure 4.1) is an SMM with an energy barrier of U_{eff} =12.6 cm^{-1}.[100]

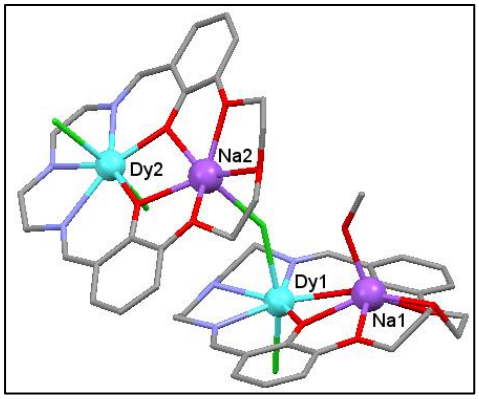

Figure 4.1 Crystal structure of $[Dy_2Na_2(L_3)_2(Cl)_4(MeOH)]\cdot 2H_2O$ (**4.1**). Colour code: gray = C, red = O, blue = N, green = Cl and aqua blue = Dy(III) ion. H atoms are omitted for clarity.[100]

Further advancing this work, the aim of this project was to study the coordination chemistry of the N_3O_2 cavity with *3d* ions and to investigate the coordination chemistry of the second O_3O_2 crown-like cavity with select *4f* metal ions. In this respect, we were particularly interested to employ the neutral O_3O_2 cavity to coordinate *4f* metal ions in the equatorial plane and then to introduce anionic ligands into the axial positions in order to enhance the axial anisotropy of the oblate Ln(III) ions.

4.2 Experimental

Preparation of Intermediate L_3'.[176]

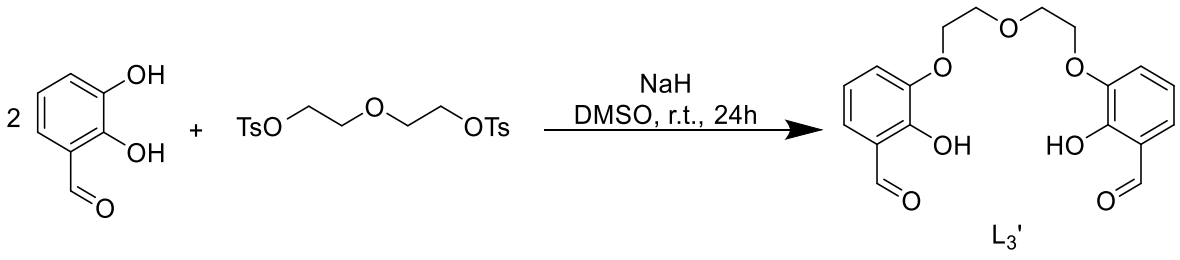

Scheme 4.1 Preparation of the L_3'.[176]

A solution of 2,3-dihydroxybenzaldehyde (1000 mg, 7 mmol) in dry DMSO (5 mL) was added dropwise over 2 h to a suspension of NaH (580 mg, 14 mmol) in dry DMSO (5 mL) under N_2 with vigorous stirring. The resulting solution was stirred for 1h after which time triethylene glycol ditosylate (1.660 mg, 3.62 mmol) was added and the resulting solution was stirred at r.t. for an additional 24 h. On completion, water (300 mL) was added and the solution was filtered, washed with chloroform (100 mL) and then dried over $MgSO_4$. Removal of the solvent afforded intermediate **L_3'** as a yellow oil in 51% yield. The spectroscopic data for the compound is in good agreement with the literature.[176]

^{1}H NMR ($CDCl_3$) δ (pmm) : 10.94 (s, 2H, OH), 9.93 (s, 2H, CHO), 7.22-7.17 (m, 4H, Ar-H), 6.95-6.90 (m, 2H, Ar-H), 4.27-4.24 (m, 4H, CH_2O), 4.00-3.97 (m, 4H, CH_2O). ^{13}C NMR ($CDCl_3$) δ (pmm) : 196.2, 152.2, 147.4, 125.2, 121.2, 120.9, 119.5, 69.9, 69.3. IR (cm^{-1}): 3566 (O-H), 2855 (C-H aldehyde), 1650 (C=O).

Preparation of ligand H_2L_3.[176]

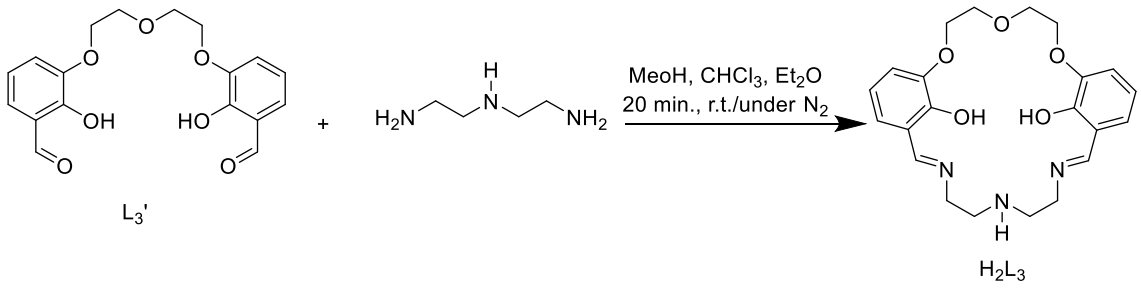

Scheme 4.2 Preparation of **H_2L_3.**[176]

To a solution of diethylenetriamine (0.28 mL, 2 mmol) in MeOH (5 mL) and Et_2O (400 mL) in a 500 mL round bottomed flask under N_2, a solution of L_3' (930 mg, 1.4 mmol) in $CHCl_3$ (3 mL) was added dropwise over a period of 30 mins. The resulting solution containing a yellow precipitate was stirred for a further 20 mins and then the solvent was

removed to afford **H_2L_3** as yellow solid in 80% yield. **H_2L_3** was then placed under vacuum for 2 h and stored under N_2. The spectroscopic data for the ligand is in good agreement with the literature.[176]

^{1}HNMR ($CDCl_3$) δ (ppm) : 8.33 (s, 2H, CHN), 6.89-6.69 (m, 6H, Ar-H), 4.21 (m, 4H, CH_2O), 4.07 (m, 4H, CH_2O), 3.97 (m, 4H, $CNCH_2$), 3.79 (m, 1H, N-H), 2.99 (m, 4H, CH_2NH). ^{13}CNMR ($CDCl_3$) δ (ppm) : 166.2 (C=N), 147.3 (Ar-OC), 144.7 (Ar-OH), 123.5 (Ar-CH_2N), 118.6 (*m*-Ar), 117.7 (*p*-Ar), 116.1 (*m*-Ar), 69.4 (C-*o*-Ar), 68.0 (CH_2O), 59.2 (C-NC), 49.8 (C-HN). IR υ (cm^{-1}): 2871 (C-H), 1634 (C=N), 1245 (C-O). ESI-MS: *m/z* = 414 $[M+H]^+$. Anal. calcd. for $C_{22}H_{27}N_3O_5 \cdot H_2O$: C 61.24, H 6.77, N 9.74 %; found C 60.91, H 6.98, N 10.74%.

Preparation of $[CuNa(L_{3b})ClCH_3OH]\cdot 6H_2O$ (4.2)

A methanolic solution (5 ml) of NaOH (38.6 mg, 0.968 mmol) was added to a chloroform solution (10 ml) of **H_2L_3** (200 mg, 0.484 mmol) and the reaction mixture was stirred for 5 mins after which time a methanolic solution (5 ml) of $CuCl_2 \cdot 2H_2O$ (83.4 mg, 0.484 mmol) was added and the resulting solution was refluxed overnight. The reaction mixture was cooled to room temperature and the solvent was removed under vacuum and the resulting solid was dissolved in MeOH (5 mL). Slow diffusion of Et_2O into this MeOH solution afforded suitable single crystals of the complex for X-ray diffraction in 32% yield. Select IR υ (cm^{-1}): 3298 (m, N-H), 2933 (s, C-H), 1627 (s, C=N), 1214 (s, C-O), 1166 (s, C-N). λ_{max} = 375 (ε =10865 $Lmol^{-1}$ cm^{-1}). ESI-MS: *m/z* 677 $[Cu_2(H_2L_3)Cl(CH_3OH)_2(H_2O)_2+H]^+$. Anal. calcd. for $C_{23}H_{28}ClCuN_3NaO_6 \cdot 6H_2O$: C 41.07, H 5.99, N 6.25%; found C 41.27, H 5.99, N 6.45%.

Preparation of [ZnNa(L_{3b})(CH_3COO)(CH_3OH)]·H_2O (4.3)

A methanolic solution (5 ml) of NaOH (38.6 mg, 0.968 mmol) was added to a chloroform solution (10 ml) of **H_2L_3** (200 mg, 0.484 mmol) that was subsequently stirred for 5 mins, after which time a methanolic solution (5 ml) of $Zn(CH_3COO)_2·2H_2O$ (106 mg, 0.484 mmol) was added. The resulting solution was then refluxed overnight. The reaction mixture was cooled to room temperature and the solvent was removed under vacuum and the resulting solid was dissolved in MeOH (5 mL). Slow diffusion of Et_2O into this solution afforded suitable single crystals of the complex for X-ray diffraction in 46% yield. Select IR υ (cm^{-1}): 3176 (m, N-H), 2919 (s, C-H), 1650 (s, C=N), 1216 (s, C-O), 1124 (m, C-N). ESI-MS: *m/z* = 273 $[Zn(H_2L_3)(CH_3OH)(H_2O)_2+2H]^{2+}$. Anal. calcd. for $C_{25}H_{32}N_3NaO_8Zn·H_2O$: C 49.31, H 5.63, N 6.90%; found C 49.04, H 5.42, N 7.25%.

Preparation of [Mn_3Na_2(L_{3b})$_2$(CH_3COO)$_4$]·4CH_3OH·H_2O (4.4)

A methanolic solution (5 ml) of NaOH (38.6 mg, 0.968 mmol) was added to a chloroform solution (10 ml) of **H_2L_3** (200 mg, 0.484 mmol), that was subsequently stirred for 5 mins after which time a methanolic solution (5 ml) of $Mn(CH_3COO)_2·6H_2O$ (118 mg, 0.484 mmol) was added. The resulting solution was then refluxed overnight. On completion, the reaction mixture was cooled to room temperature and the solvent removed under vacuum. The resulting solid was re-dissolved in MeOH (5 mL) and then slow diffusion of Et_2O at room temperature afforded brown plates suitable for X-ray diffraction in 25% yield. Select IR υ (cm^{-1}): 3307 (m, N-H), 2916 (s, C-H), 1631 (s, C=N), 1214 (s, C-O). λ_{max} = 347 (ε = 17318 $Lmol^{-1}$ cm^{-1}). ESI-MS: *m/z* = 1415 $[M]^+$. Anal. calcd. for $C_{56}H_{71}Mn_3N_6Na_2O_{23}$: C 47.65, H 5.09, N 5.97%; found C 47.65, H 5.68, N 5.60%.

Preparation of $[Dy(H_2L_3)(H_2O)_2(CH_3OH)_2]Cl_3 \cdot CH_3OH$ (4.5)

A methanolic solution (5 ml) of $DyCl_3 \cdot 6H_2O$ (90 mg, 0.241 mmol) was added to a chloroform solution (10 ml) of $\mathbf{H_2L_3}$ (100 mg, 0.241 mmol) and the resulting solution was refluxed overnight. The reaction mixture was then cooled to room temperature after which time the solvent was removed under vacuum. The resulting solid was dissolved in MeOH (5 mL) and slow diffusion of Et_2O into the resulting solution at room temperature afforded single crystals of **4.5** suitable for X-ray diffraction studies after 3 days in 40% yield. Select IR υ (cm^{-1}): 3175 (br, O-H), 2933 (m, C-H), 1650 (s, C=N), 1222 (s, C-O), 1173 (m, C-N). λ_{max} = 393 (ε = 19496 $L \cdot mol^{-1}$ cm^{-1}). ESI-MS: *m/z* = 711 $[(H_2L_3)Dy(CH_3O)_2(H_2O)_5]^+$. Anal. calcd. for $C_{25}H_{42}Cl_3DyN_3O_{10} \cdot 1.5H_2O \cdot 0.1CHCl_3$: C 35.63, H 5.29, N 4.97%; found C 35.14, H 4.79, N 5.47%.

Preparation of $[Ln(H_2L_3)(H_2O)_3(CH_3OH)]Cl_3$ where Ln = Tb (4.6), Er (4.7), Gd (4.8)

A methanolic solution (5 ml) of $LnCl_3.6H_2O$ (0.241 mmol) was added to a chloroform solution (10 ml) of $\mathbf{H_2L_3}$ (100 mg, 0.241 mmol) and the resulting solution was refluxed overnight. The reaction mixture was then cooled to room temperature and the solvent was removed under vacuum. The resulting solid was dissolved in MeOH (5 mL) and Et_2O was diffused in slowly to afford suitable single crystals of all the complexes suitable for X-ray diffraction after *ca*. 3 days.

$[Tb(H_2L_3)(H_2O)_3(CH_3OH)]Cl_3$ (4.6)

Yield = 40%; select IR υ (cm^{-1}): 3251 (br, O-H), 2933 (m, C-H), 1649 (s, C=N), 1219 (s, C-O), 1174 (m, C-N). λ_{max} = 391 (ε = 14707 $L \cdot mol^{-1}$ cm^{-1}). ESI-MS: *m/z* = 706

$[(H_2L_3)Tb(CH_3O)_2(H_2O)_4]^+$.Anal. calcd. for $C_{23}H_{37}Cl_3TbN_3O_9 \cdot 2.4H_2O$: C 34.19, H 5.21, N 5.2%; found C 34.50, H 5.45, N 4.89%.

$[Er(H_2L_3)(H_2O)_3(CH_3OH)]Cl_3$ (4.7)

Yield = 47%; select IR υ (cm^{-1}): 3176 (br, O-H), 2933 (m, C-H), 1650 (s, C=N), 1222 (s, C-O), 1175 (m, C-N). λ_{max} = 388 (ε = 11462 $Lmol^{-1}$ cm^{-1}). ESI-MS*: m/z* = 713 $[(H_2L_3)Er(CH_3O)_2(H_2O)_4]^+$.Anal. calcd. for $C_{23}H_{37}Cl_3ErN_3O_9 \cdot 1.5H_2O \cdot 2CH_3OH$: C 34.74, H 5.6, N 4.86%; found C 34.09, H 5.81, N 4.5%.

$[Gd(H_2L_3)(H_2O)_3(CH_3OH)]Cl_3$ (4.8)

Yield = 30%; select IR υ (cm^{-1}): 3275 (br, O-H), 2934 (m, C-H), 1653 (s, C=N), 1225 (s, C-O), 1174 (m, C-N). ESI-MS*: m/z* = 641 $[(H_2L_3)GdCl_2]^+$ Anal. calcd. for $C_{23}H_{37}Cl_3GdN_3O_9 \cdot 2.9H_2O \cdot 0.3CHCl_3$: C 32.72, H 5.07, N 4.9%; found C 32.41, H 5.31, N 5.21%.

4.2.1 Physical measurements

NMR spectroscopy: ^{1}H- and ^{13}C-NMR spectra were recorded at 400 MHz on a Bruker Advance III HD 400 Digital NMR spectrometer in deuterated solvents.

Infrared spectroscopy: Infrared (IR) spectra were performed on a Bruker Alpha FT-IR spectrometer.

UV−visible studies: UV−visible studies (UV-vis) data were collected on a Beckman Coulter DU 720 General-Purpose UV−visible spectrophotometer.

Mass spectrometry: Electrospray ionization (ESI) data were measured on a Carlo Erba/Kratos GC/MS acquisition system and processed using a SPARC workstation.

Samples were introduced through a direct inlet system, with tris(perflouroheptyl-S-triazine) as the internal standard.

Elemental analysis: Elemental analysis (C, H, and N) data were collected by Atlantic Microlab.

X-ray crystallography: Suitable single crystals of all complexes were mounted on a cryoloop with paratone oil and examined on a Bruker APEX-II CCD diffractometer equipped with a CCD area detector and an Oxford Cryoflex low temperature device. Data were collected at 150(2) K with Mo Kα radiation (λ = 0.71073 Å) using the APEX-II software.[107,108] Cell refinement and data-reduction were carried out by SAINT. An absorption correction was performed by multi-scan method implemented in SADABS.[109] The structures of the complexes were solved by direct methods (SHELXS-97)[110] and refined using SHELXL-2014 in the Bruker SHELXTL suite.[110] Hydrogen atoms were added at calculated positions and refined with a riding model. In all four Ln(III) complexes (**4.5** – **4.8)**, as well as the Zn(II) complex **4.3**, disordered solvent was removed using the SQUEEZE procedure in PLATON.[111] Selected crystallographic data for the complexes are presented in Table 4-1 and 4.2.

Complex No	**(4.2)**	**(4.3)**	**(4.4)**
Chemical formula	$C_{23}H_{28}ClCuN_3NaO_6$	$C_{25}H_{28}N_3NaO_9Zn.CH_4O$	$C_{52}H_{53}Mn_3N_6Na_2O_{18}\cdot4(CH_4O)\cdot H_2O$
M_r	564.46	634.91	1406.98
Crystal system	Monoclinic	Monoclinic	Monoclinic
space group	$P2_1/n$	$P2_1/n$	$P2_1/c$
Temperature (K)	150	150	150
a, (Å)	10.7172 (10)	12.2326 (12)	14.9909 (13)
b, (Å)	10.8161 (10)	9.9081 (9)	17.7499 (15)
c, (Å)	11.6505 (11)	23.140 (2)	24.681 (2)

α (°)			
β (°)	114.484 (4)	95.910 (5)	90.701 (2)
γ (°)			
V (Å^3)	1229,1 (2)	2197.6 (3)	6566.9 (10)
Z	2	4	4
Radiation type	Mo $K\alpha$	Mo $K\alpha$	Mo $K\alpha$
μ (mm^{-1})	1.06	0.95	0.66
Crystal size (mm)	0.3 × 0.05 × 0.01	0.2 × 0.2 × 0.05	0.2 × 0.2 × 0.05
T_{min}, T_{max}	0.676, 0.747	0.632, 0.745	0.584, 0.746
No. of measured, independent and observed [$I > 2\sigma(I)$] reflections	26085, 5960, 5705	47021, 10403, 9013	13962, 8180, 7374
R_{int}	0.034	0.028	0.036
(sin θ/λ)$_{max}$ (Å^{-1})	0.668	0.773	0.538
$R[F^2 > 2\sigma(F^2)]$, $wR(F^2)$, S	0.030, 0.066, 1.06	0.036, 0.116, 0.70	0.110, 0.280, 1.15
No. of reflections	5960	10403	8180
No. of parameters	318	345	816
No. of restraints	1		8
$\Delta\rho_{max}$, $\Delta\rho_{min}$ (e Å^{-3})	0.42, −0.31	1.18, −0.77	2.37, −0.68
Absolute structure parameter			0.085 (11)

Table 4-1 Selected crystallographic parameters for complexes **4.2** – **4.4**.

Complex No	(**4.5**)	(**4.6**)	(**4.7**)	(**4.8**)
Chemical formula	$C_{25}H_{42}Cl_3DyN_3O_{10}$	$C_{23}H_{37}Cl_3TbN_3O_9$	$C_{23}H_{37}Cl_3ErN_3O_9$	$C_{23}H_{37}Cl_3GdN_3O_9$
M_r	813.46	764.84	773.17	763.16
Crystal system	Orthorhombic	Orthorhombic	Orthorhombic	Orthorhombic
space group	$P2_12_12_1$	$P2_12_12_1$	$P2_12_12_1$	$P2_12_12_1$
Temperature (K)	150	150	150	150
a, (Å)	12.0592 (15)	12.1921 (14)	12.1588 (5)	12.2624(11)
b, (Å)	16.047 (2)	15.5895 (18)	15.5224 (6)	15.4198(10)
c, (Å)	19.621 (2)	19.698 (3)	19.6992 (9)	19.7420(17)
α (°)	90	90	90	90
β (°)	90	90	90	90
γ (°)	90	90	90	90

V (Å^3)	3796.9 (8)	3744.1 (8)	3717.9 (3)	3732.9(5)
Z	4	4	4	4
Radiation type	Mo Kα	Mo Kα	Mo Kα	Mo Kα
μ (mm^{-1})	2.23	2.14	2.52	2.03
Crystal size (mm)	0.15 × 0.1 × 0.05	0.15 × 0.1 × 0.05	0.15 × 0.1 × 0.05	0.25 × 0.08 × 0.06
T_{min}, T_{max}	0.456, 0.753	0.456, 0.753	0.456, 0.753	0.367, 0.765
No. of measured, independent and observed [I > 2σ(I)] reflections	39756, 11279, 10388	50216,8976, 8109	19706, 7614, 6969	12675, 6371,5097
R_{int}	0.033	0.067	0.036	0.071
$(\sin \theta/\lambda)_{max}$ (Å^{-1})	0.719	0.673	0.639	0.595
R[F^2 > 2σ(F^2)], wR(F^2), S	0.049, 0.133, 1.17	0.061, 0.157, 1.13	0.042, 0.118, 0.62	0.079, 0.242, 0.82
No. of reflections	11279	8976	7614	6371
No. of parameters	402	348	354	271
No. of restraints	8			
$\Delta\rho_{max}$, $\Delta\rho_{min}$ (e Å^{-3})	1.93,−1.66	2.19, −2.98	1.78, −1.32	1.85, −1.74
Absolute structure parameter	0.106(18)	0.21(2)	0.126(18)	0.33(4)

Table 4-2 Selected crystallographic parameters for complexes **4.5 - 4.8**.

Magnetic susceptibility measurements: dc measurements were carried out using a Quantum Design SQUID MPMS magnetometer. Temperature scans were carried out at applied fields between 0.1 – 0.2 T, from 2–300 K. Field scans were performed over the range -5 to 5 T, at temperatures between 3–5 K. Ac susceptibility measurements were performed using a Quantum Design PPMS, with an oscillating field of 3.5 Oe, over multiples frequencies between 25 and 1500 MHz. Static fields ranging from 0 to 0.5 T were applied from 2 to 15 K.

EPR measurements: The EPR spectrum of complex **4.2** was measured in the solid state at room temperature on a Bruker EMX plus EPR spectrometer running at X-band frequency (ca. 9.8 GHz)

by Dr. J.M. Rawson (U. Windsor).

4.3 Results and discussion

4.3.1 Synthesis and structural studies of select *3d* complexes of H_2L_3

Following previous work by Regier in the Pilkington group studying the coordination chemistry of the N_3O_2 pocket of **H_2L_3** with select 4*f* ions, the objectives of this project were: (i) to investigate the coordination chemistry of the ligand with select *3d* ions; (ii) to explore the coordination chemistry of the crown ether O_2O_3 pocket with *4f* ions and (iii) to determine whether or not it is possible to simultaneously coordinate metal ions in both cavities to target heterometallic *3d/4f* systems. In order to meet our first objectives, transition metal complexes were synthesised via reaction of one equivalent of **H_2L_3** together with two equivalents of NaOH in order to fully deprotonate the two OH groups of the ligand before adding the appropriate transition metal salt. This resulted first in the formation of Na_2L_3, where the Na^+ ions from the base coordinate in the deprotonated O_3O_2 cavity of the macrocycle, leaving the N_3O_2 site free for subsequent coordination to the *3d* metal ions. Following this methodology, a broad range of *3d* transition metal ions were employed, but single crystals of only the Cu, Zn, and Mn complexes could be grown for X-ray diffraction studies and are thus presented in this Chapter. After deprotonation, **H_2L_3** was treated with one equivalent of the transition metal salt and then the resulting solution was refluxed overnight, after which time the solvent was removed and the resulting product was dissolved in methanol. Subsequent diffusion of diethyl ether afforded single crystals of all three complexes that were suitable for X-ray diffraction studies. A summary of the selected structural data for the complexes is presented in Table 4-1. A summary of selected bond lengths and angles for each complex can be found in Table 5-7 - Table 5-9 the

Appendix section of this thesis. For the Cu(II) complex (**4.2**), X-ray diffraction studies reveal that its molecular structure is [CuNa(L_{3b})ClCH_3OH] and it crystallizes in the monoclinic space group $P2_1$. The Na^+ cation occupies the O_3O_2 cavity and is equatorially coordinated to three neutral crown ether oxygen atoms O2 O3 and O4, as well as two bridging phenolate anions, O1 and O5, that are also coordinated to the Cu(II) ion. The axial ligation of a MeOH completes its 6-coordinate geometry, (Figure 4.2).

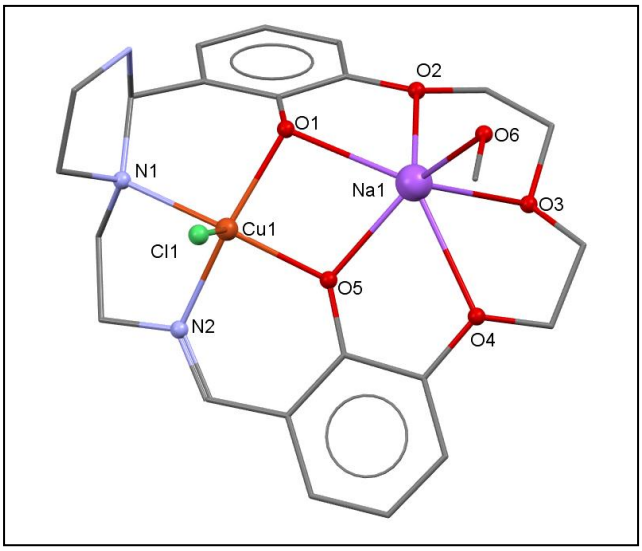

Figure 4.2 Molecular structure of [CuNa(**L_{3b}**)ClCH_3OH]H_2O (**4.2**). H-atoms and solvent molecules are omitted for clarity. Colour code: red = O, gray = C, blue = N, green = Cl, orange = Cu(II) and purple = Na(I).

Close inspection of the molecular structure of the macrocycle reveals that while in solution, nucleophilic addition of the lone pair of one of the secondary amines of the N_3O_2 cavity to the carbon atom of its adjacent imine has occurred, leading to a contraction of the N_3O_2 framework and the formation of a five-membered imidazoline ring to give the modified macrocyclic ligand, **L_{3b}**. This type of ring contraction is fairly common in the literature and has been reported previously for other Schiff-base macrocycles, particularly

when alkaline-earth metal ions are replaced by smaller *3d* ions such as Mn(II), Fe(II), Co(II), or Zn(II).[177,178] It has been proposed that this ring contraction occurs due to a mis-match between the cavity size of the macrocycle and the atomic radii of the transition metal ion which favours a reduction in the denticity of the macrocycle, rendering it a more suitable cavity size for the smaller *3d* ion.[177,179] It is also noteworthy to mention that ring contractions of this type have also has been reported for Ln(III) Schiff-base macrocycles, where the contraction tends to occur in a free cavity to better facilitate the spatial arrangement of the ligand lone pairs around the *4f* ion.[180] The Cu(II) ion is 5-coordinate where the N_2O_2 cavity of the macrocycle occupies the equatorial sites and an axial Cl^- ligand completes its square pyramidal geometry. The axial Cu1-N1 bond length of 2.089(3) Å is longer than the other equatorial Cu-N2 (1.96(3) Å), Cu1-O1 (1.98(2) Å) and Cu1-O5 (1.93 (2) Å). The coordination geometry of the Cu(II) ion was further analyzed by continuous shape measures (CSMs)[114] which reveal the coordination geometry of the Cu(II) ion is close to ideal spherical square pyramidal geometry, with a CSM of 0.62, (Table 4-3) (Figure 4.3). Furthermore, for this ion the structural parameter $\tau = 0.1$, further confirming its close to ideal square pyramidal geometry.[181] CSM also confirms that the geometry of the Na^+ cation is closest to pentagonal pyramidal, (Figure 4.3).

Polyhedron	Symmetry	Cu(II) CSM
PP-5	D_{5h}	32.56
VOC-5	C_{4v}	2.68
TBPY-5	D_{3h}	4.69
SPY-5	C_{4v}	0.62
JTBPY-5	D_{3h}	8.18

Table 4-3 Continuous shape measures (CSMs) for the 5-coordinate Cu(II) ion in **4.2**. The value in red indicates the closest polyhedron according to the CSMs. Abbreviations: PP-5, pentagon; VOC-5, vacant octahedron; TBPY-5, trigonal bipyramid; SPY-5, spherical square pyramid; JTBPY-5, Johnson trigonal bipyramid J12.

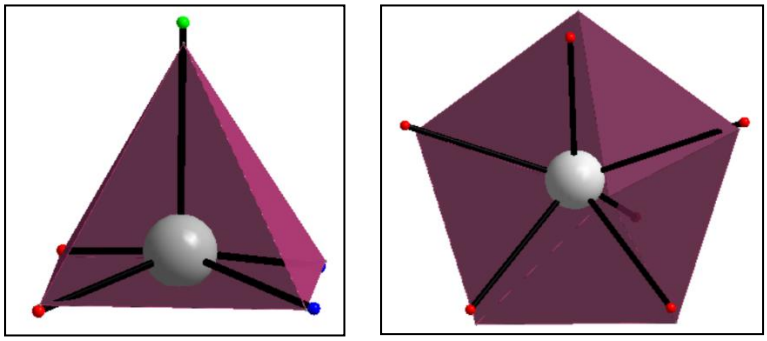

Figure 4.3 Coordination geometry of the Cu(II) cation superimposed on an idealized spherical square pyramidal polyhedron (purple) in **4.2** (left) and coordination geometry of Na(I) cation superimposed on an idealized pentagonal pyramidal polyhedron (purple) (right).

Examining the crystal packing of **4.2**, the shortest intermolecular Cu···Cu distances are 10.28(8) Å. Furthermore, we see that there is an intermolecular H-bond involving the N atom of one of the 5-membered rings of the macrocycle and the OH group of a coordinated methanol molecule, such that O(6)-H···N(3) = 2.764(3) Å, Figure 4.4.

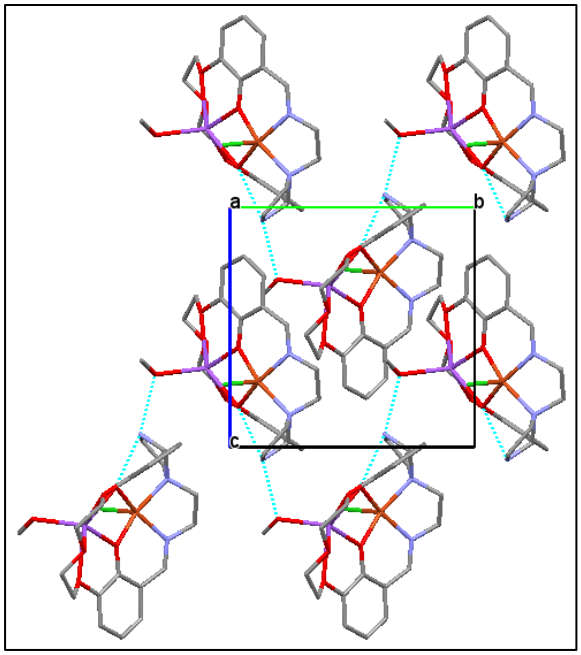

Figure 4.4 Crystal packing of **4.2**. View down the *a*-axis of the unit cell. H-bonds are shown as blue dashed lines. H atoms are omitted for clarity.

Given that the Cu(II) complex has a contracted N_3O_2 framework bearing a five-membered imidazoline ring, we subsequently set out to prepare the analogous Zn(II) complex, since if single crystals could not be obtained we could characterize the molecular structure of the complex by NMR spectroscopy. Following a similar strategy, the Zn complex was prepared by first reacting the **H_2L_3** with NaOH prior to the addition of zinc acetate. Fortunately, single crystals of **4.3** were obtained by slow diffusion of diethyl ether into the reaction mixture. X-ray diffraction studies of the complex reveal that it crystallizes in the monoclinic space group $P2_1/n$, with one independent molecule in the asymmetric unit. The complex has the molecular formula $[ZnNa(L_{3b})(CH_3COO)(CH_3OH)]$, (Figure 4.5). Select crystallographic parameters for **4.3** are summarised in Table 4-1. Select bond lengths and angles are summarized in Table 5-8 of the Appendix section of this thesis.

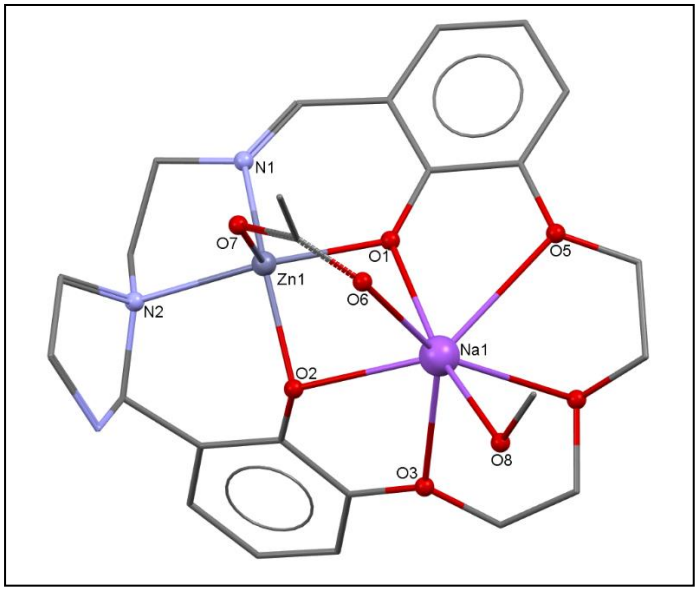

Figure 4.5 Molecular structure of [ZnNa(**L3b**)(CH_3COO)(CH_3OH)] (**4.3**). H-atoms are omitted for clarity. Colour code: red = O, light gray = C, blue = N, gray = Zn(II) and purple = Na(I).

The molecular structure of **4.3** is quite similar to the previously described Cu(II) complex however, the axially coordinated chloride ion in **4.2** is now replaced by a bridging acetate, which increases the coordination number of the Na(I) ion from 6 to 7. In this respect, the Na^+ is coordinated in the O_3O_2 cavity of the macrocycle together with acetate and MeOH ligands in the axial positions. As reported for the Cu(II) complex, the macrocycle in **4.3** also undergoes a contraction of its N_3O_2 cavity resulting in N_2O_2 coordination of the Zn(II) ion in the equatorial plane. The Zn-N distances are 2.09(12) Å and 2.25(12) Å, which are slightly longer than the Cu-N distances in **4.2**. In addition, the N3-Zn-N1 angle is 79.79(11)°, which is smaller than N2-Cu-N1 angle of 83.95(11)°. The Zn-O bonds involving the phenolate oxygens are 2.009(11) Å and 1.99(10) Å, for O1 and O5 respectively, which are slightly longer than Cu-O distances of 1.98(2) Å and 1.93(2) Å. Continuous shape measures (CSMs)[114] reveal the coordination geometry of the Zn(II)

ion is close to ideal spherical square pyramidal geometry given that $\tau = 0.04$[181] and it has a CSM of 0.26 (Table 4-4) (Figure 4.6). In contrast to the Cu(II) complex, the Na^+ ion in **4.3** is closest to a capped trigonal prismatic coordination geometry, (Figure 4.6).

Polyhedron	Symmetry	Zn(II) CSM
PP-5	D_{5h}	31.41
VOC-5	C_{4v}	2.26
TBPY-5	D_{3h}	5.05
SPY-5	C_{4v}	0.26
JTBPY-5	D_{3h}	7.39

Table 4-4 Continuous shape measures (CSMs) for the 5-coordinate Zn(II) coordination polyhedron in complex **4.3**. The value in red indicates the closest polyhedron according to the CSMs. Abbreviations: PP-5, pentagon; VOC-5, vacant octahedron; TBPY-5, trigonal bipyramid; SPY-5, spherical square pyramid; JTBPY-5, Johnson trigonal bipyramid J12.

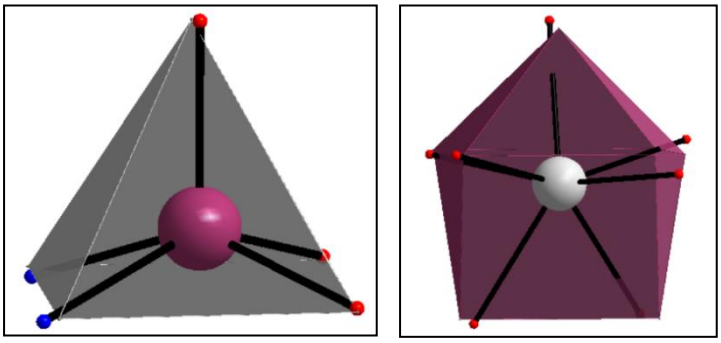

Figure 4.6 Coordination geometry of the Zn(II) cation superimposed on an idealized spherical square pyramidal polyhedron shown in grey for **4.3** (left) and coordination geometry of Na^+ cation superimposed on an idealized capped trigonal prism polyhedron shown in purple for **4.3** (right).

Further analysis of the crystal structure reveals that the shortest intermolecular Zn···Zn distances are 8.1920(7) Å. Close examination of the crystal packing of this complex reveals the molecules order in a head to tail arrangement of chains that run along the a-axis of the unit cell. Each molecule in a chain is related to its neighbour by a

crystallographic inversion centre. The structure is stabilized by intermolecular hydrogen bonding interactions from one of the oxygen atoms of a bridging acetate to the H atom of a neighbouring methanol solvent molecule (O7···O9 = 2.720(4) Å), as well as from one of the N atoms of the 5-membered ring of the macrocycle to the hydrogen atom of a coordinated methanol (O8···N3 = 2.792(3) Å), Figure 4.7.

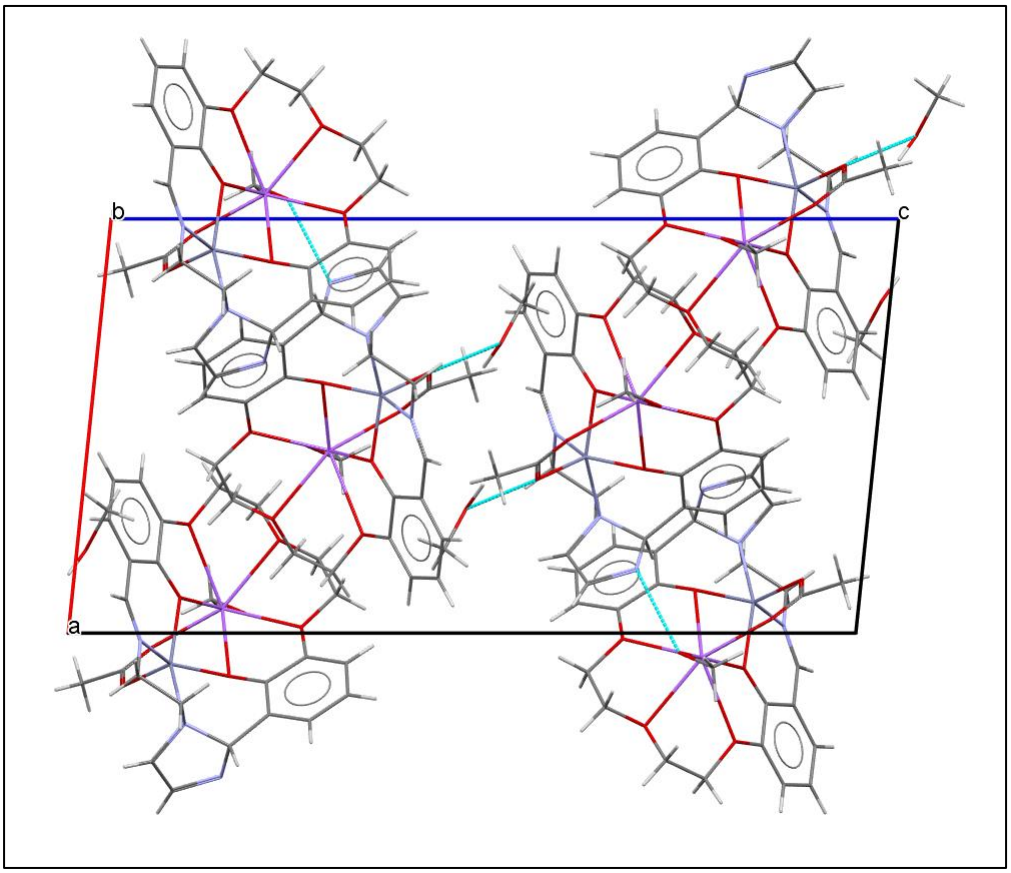

Figure 4.7 Crystal packing of **4.3**. View down the *b*-axis of the unit cell. H-bonds are shown as blue dashed lines.

The Mn complex **4.4** was prepared by reacting first **H_2L_3** with NaOH in methanol before the addition of $Mn(CH_3COO)_2 \cdot 6H_2O$ and refluxing the solution overnight. Single crystals of the complex were obtained by slow diffusion of diethyl ether into the reaction mixture. Selected crystallographic data for **4.4** is summarized in Table 4-1and bond lengths

and angles in Table 5-9. X-ray diffraction studies reveals the complex crystallizes in the monoclinic space group $P2_1/c$. The asymmetric unit comprises of a Mn_3 trimer of structural formula $[Mn_3Na_2(L_3)_2(CH_3COO)_4]\cdot 4CH_3OH\cdot H_2O$, where two crystallographically independent macrocycles are linked via a bridging $Mn(OAc)_2$ unit, Figure 4.8.

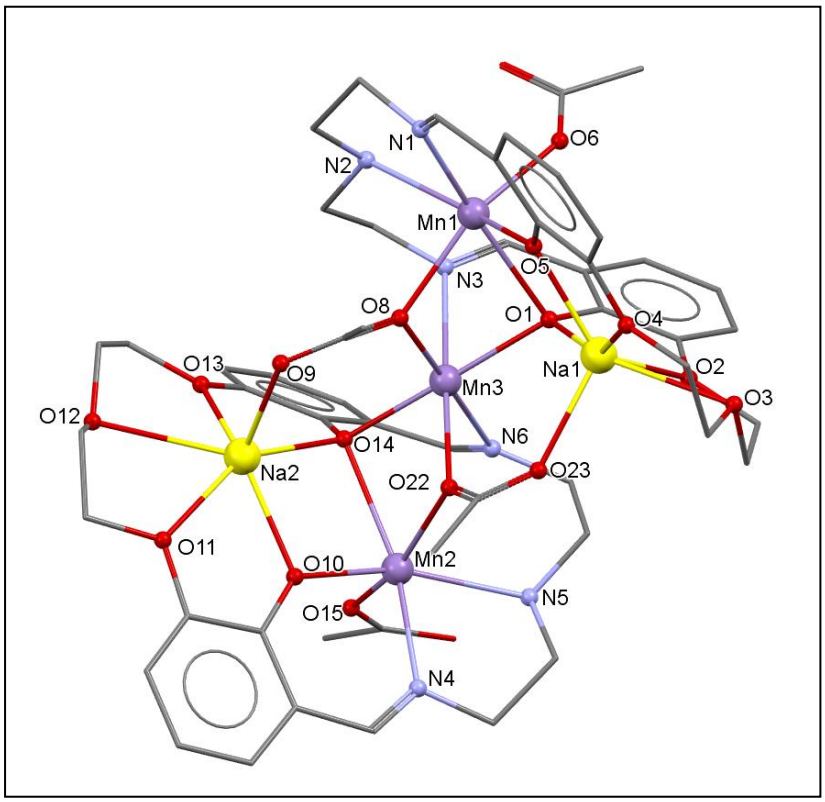

Figure 4.8 Molecular structure of $[Mn_3Na_2(L_3)_2(CH_3COO)_4]\cdot 4CH_3OH\cdot H_2O$ **(4.4)**. H-atoms and solvent molecules are omitted for clarity. Colour code: red = O, gray = C, blue = N.

Both of the macrocycles of the trimer coordinate a Mn(II) ion in the N_3O_2 pocket and a Na^+ ion in the O_3O_2 cavity. In this respect, the Mn1 and Mn2 ions are coordinated to N1, N2 and N4, N5 respectively, together with an additional two O atoms (O1, O5 and O10, O14) in the equatorial plane. Bridging and capping acetate ligands coordinate to the axial positions to complete the octahedral geometry. The third N atom of the N_3O_2 pocket

from each macrocycle (N3 and N6) is coordinated to a third Mn3 ion that bridges the two dual compartmental macrocycles within the trimer. In addition to these N atoms, the central Mn3 ions are further coordinated to phenolate anions from the two macrocycles (O5 and O10), as well O atoms of the bridging acetates (O8 and O22), completing the 6-coordinate geometry. The Mn-N distances range from 2.23(9) Å- 2.35(9) Å and the Mn-O bond lengths range from 2.07(8) Å- 2.46 (7) Å. The Mn-O-Mn angles are between 92.5(3)° and 99.5(3)°. The intramolecular Mn···Mn distances in the trimer are 3.28(2) and 3.31(2) Å for Mn1···Mn3 and Mn2···Mn3 respectively. Further analysis of the coordination geometry of the Mn(II) ions was carried out by continuous shape measures (CSMs).[114] These studies confirm that the coordination geometries of all three Mn(II) ions are octahedral, where the Mn3 ion is the least distorted with a CSM value of 1.56, when compared to values of 4.76 and 4.59 for Mn1 and Mn2 respectively, (Table 4-5 and Figure 4.9). The CSM analysis also reveals that the coordination geometry of the Na^+ ion in **4.4** is closest to pentagonal pyramidal (Figure 4.10).

Polyhedron	Symmetry	Mn1(II) CSM	Mn2(II) CSM	Mn3(II) CSM
EP-6	D_{6h}	28.77554	28.38082	23.94374
PPY-6	C_{5v}	16.63690	16.61009	25.58925
OC-6	O_h	4.76567	4.59720	1.56257
TPR-6	D_{3h}	8.04754	7.87714	15.43807
JPPY-6	C_{5v}	19.97968	20.04383	27.85041

Table 4-5 Continuous shape measures (CSMs) of the 6-coordinate Mn(II) coordination polyhedron in complex **4.4**. The value in red indicates the closest polyhedron according to the CSMs. Abbreviations: HP-6, Hexagon; PPY-6, Pentagonal pyramid; OC-6, Octahedron; TPR-6, Trigonal prism; JPPY-6; Johnson pentagonal pyramid J2.

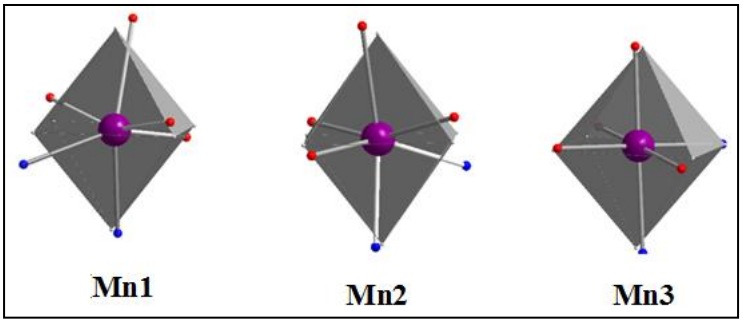

Figure 4.9 Coordination geometry of the Mn1, Mn2, and Mn3 cations in complex **4.4**, superimposed on an idealized octahedron (shown in grey).

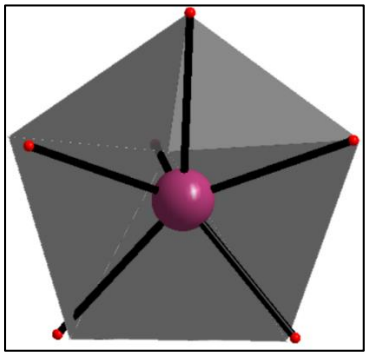

Figure 4.10 Coordination geometry of Na(I) cation superimposed on an idealized pentagonal pyramid polyhedron shown in gray for **4.4**.

A view of the crystal packing of the trimers reveals the complex adopts a butterfly-like shape, Figure 4.11. Then butterflies are organized in a head-to-tail arrangement of ribbons along the *c*-axis of the unit cell. The void space between the ribbons are occupied by solvent molecules which are involved in intramolecular hydrogen bonding interactions to neighbouring bridging acetate oxygen atoms such that O16···O18 = 2.64 (1) Å.

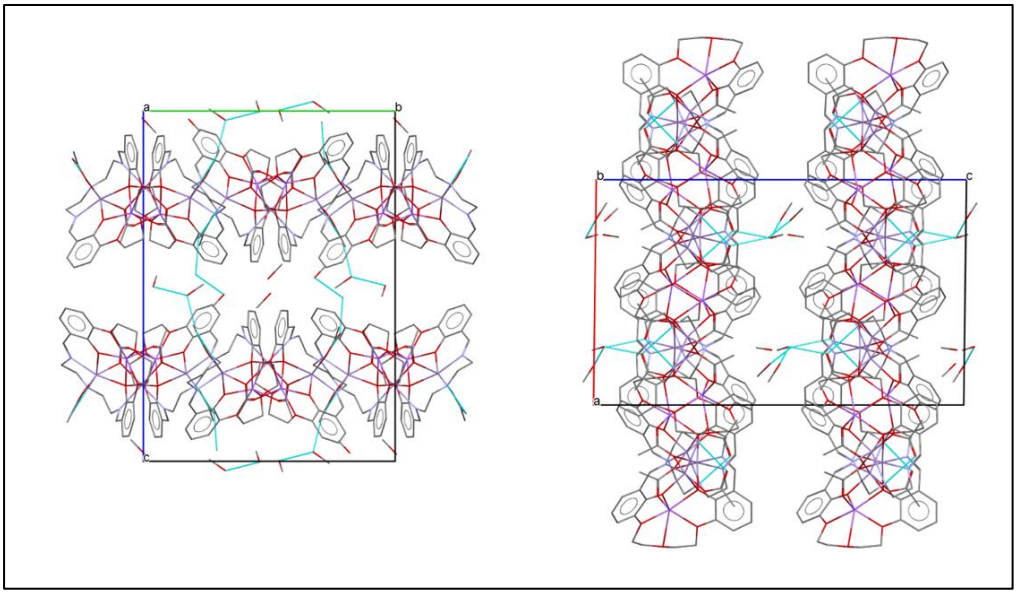

Figure 4.11 The crystal packing of the Mn_3 trimers in complex **4.4** showing H-bonding interactions as blue dashed lines. H-atoms are omitted for clarity; (left) view down the ***a***-axis of the unit cell highlighting the butterfly shaped topology; (right) view down the *b*-axis of the unit cell showing the ribbons with the solvent molecules in the void space in between the ribbons.

4.3.2 Magnetic and EPR studies

Direct current susceptibility measurements (dc) were carried out on crushed single crystals of the complexes **4.2** and **4.4** in an applied static field of 0.1 T between 2 and 300 K. The $1/\chi$ *vs* T plot for **4.2**, affords a Curie constant of 0.414 $cm^3 \cdot K \cdot mol^{-1}$ and a Weiss constant θ = -1.5 K, for g = 2.0 and *S* = ½, (Figure 4.12 left), which supports the presence of weak antiferromagnetic interactions, consistent with the long intermolecular Cu··Cu distances observed in the crystal structure. A plot of $\chi_M T$ *vs* T for **4.2** is shown in Figure 4.12 (right) and reveals that the χMT product is fairly constant until 20 K when it rapidly decreases to reach a value of 0.33 $cm^{3} \cdot K \cdot mol^{-1}$ at 2 K. The room temperature value of $\chi_M T$

of 0.406 $cm^3 \cdot K \cdot mol^{-1}$ is close to the theoretical value of 0.413 $cm^3 \cdot K \cdot mol^{-1}$ expected for an isolated Cu(II) ion (S = ½, g = 2.09).

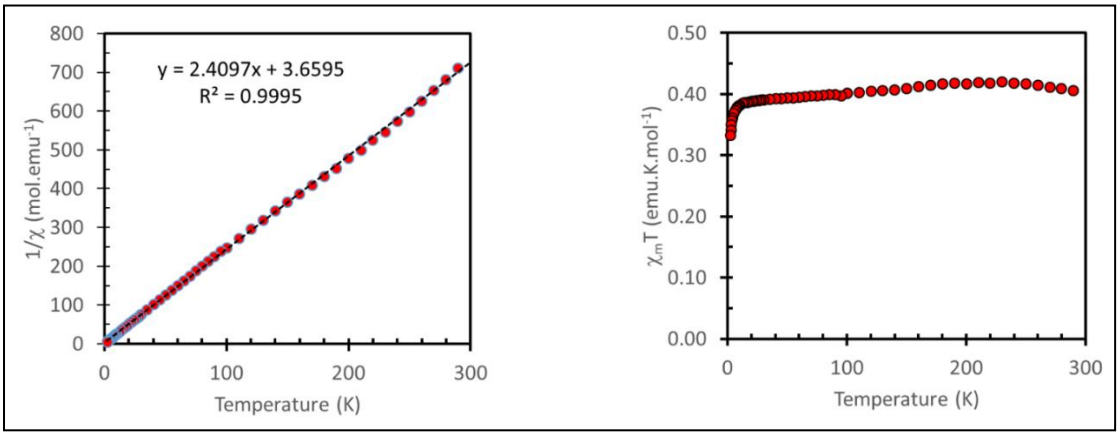

Figure 4.12 Left, plot of 1/χ *vs* T for **4.2**; the blue line is the best fit to the Curie Weiss plot for S = ½ and g = 2.0); right, plot of $\chi_M T$ *vs* T for **4.2** at 0.1 T from 2 – 300 K.

The field dependence of the magnetization for complex **4.2** was measured from 2 -7 K, between 0-7 T. A plot of M *vs* H at different temperatures together with a fit to the Brillouin function at each temperature (dashed line) is excellent for a well-isolated S = ½ spin and a g value of 2, Figure 4.21 (left)). A plot of the reduced magnetisation *vs* field **4.2** is shown in (Figure 4.21 (right), revealing that all of the plots fall onto the same curve, again supporting the presence of a well-isolated spin ground state. Furthermore, the magnetization saturates at *ca.* 1 $N\mu_B$ which again is consistent with the presence of an isolated S= ½ system.

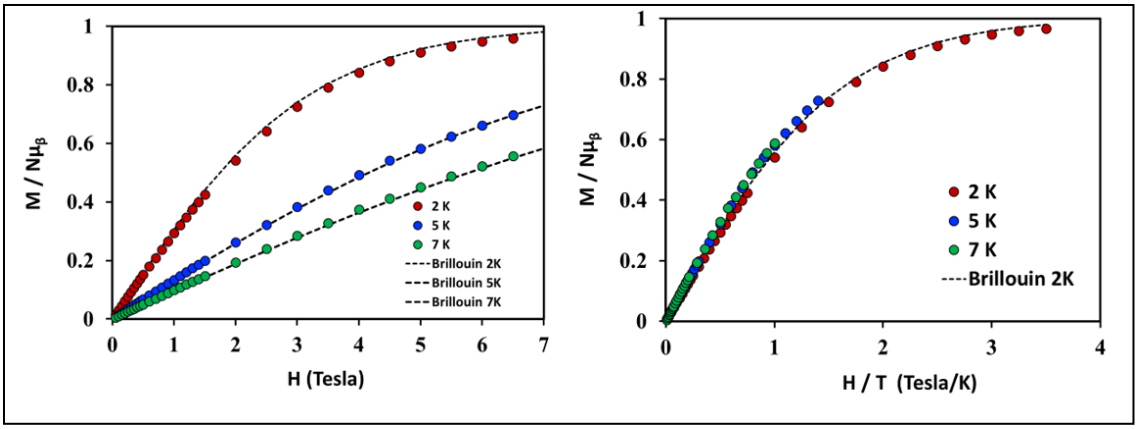

Figure 4.13 Plot of M *vs* H for **4.2** at 2, 5 and 7 K (left). The dashed lines represent a fit to the Brillouin function for g = 2 and *S* = ½. Plot of the reduced magnetization *vs* H for **4.2** (right), with a fit to the Brillouin function (dashed lines) for g = 2 and *S* = 1/2.

The EPR spectrum 0f 4.2 recorded in the solid state at room temperature, shows a broad signal centered at g = 2.089, characteristic of an S=1/2 system, further supporting the dc susceptibility data.

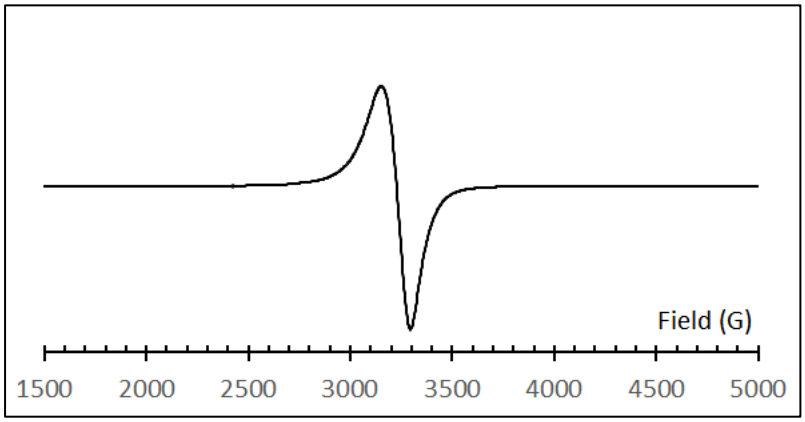

Figure 4.14 X-band EPR spectrum of complex **4.2** at room temperature.

Examining the dc susceptibility data for the Mn_3 trimer **4.4** reveals the value of the $\chi_M T$ product below 100 K decreases slightly as the temperature is lowered to reach a value

of 11.14 $cm^3 \cdot K \cdot mol^{-1}$ at 40 K and then rapidly decreases below 50 K to reach a value of 5.6 $cm^3 \cdot K \cdot mol^{-1}$ at 2 K, consistent with the presence of weak antiferromagnetic interactions, (Figure 4.15).

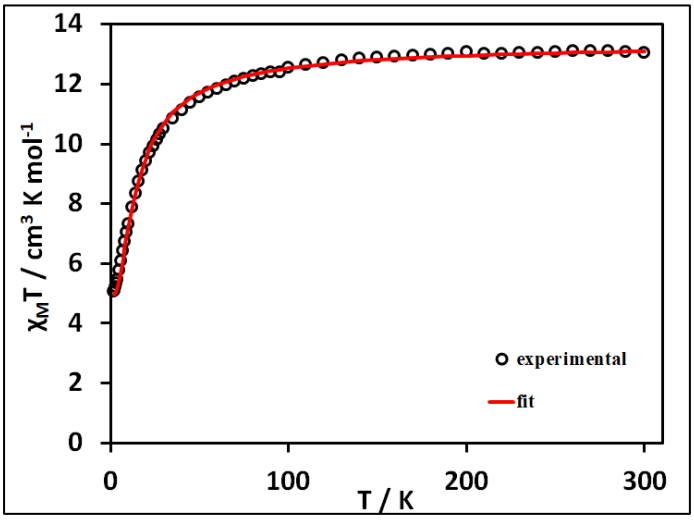

Figure 4.15 Plot of $\chi_M T$ *vs*. T for the Mn_3 trimer, **4.4** in a field of 0.1 T from 2 - 300 K. The experimental data is plotted as black circles and the magnetic fit to a 1-J model is shown as a red line.

Investigating closely the Mn···Mn distances and geometries of three Mn(II) ions in the core of the complex, we assume that due to their long distances (6.482(2) Å) the Mn1···Mn2 exchange interactions are negligible and due to their similar bond lengths and angles, we have assigned the same *J* value to the Mn1···Mn2 and Mn2···Mn3 sets of interactions as shown in Figure 4.16. The magnetic data was fit over the entire temperature range to a 1-*J* model using the PHI program,[182] applying the following Hamiltonian (Eqn. 4.11):

$$H = -2J(\hat{S}_1 \hat{S}_3 + \hat{S}_2 \hat{S}_3) \qquad \textbf{Eqn. 4.12}$$

Where *J* is the exchange interaction described above and *S* is the spin state of each of the three Mn(II) ions.

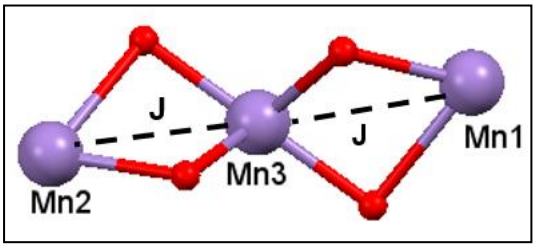

Figure 4.16 The 1*J* model used to fit the experimental dc magnetic data in PHI.

The best fit gave a *g* value = 2.02 and $J = -0.67$ cm^{-1}, which is very similar to the *J* value of –1.2 cm^{-1} for the structurally similar Mn_3 trimer **4.9,** previously reported in the chemical literature, (Figure 4.21).[183]

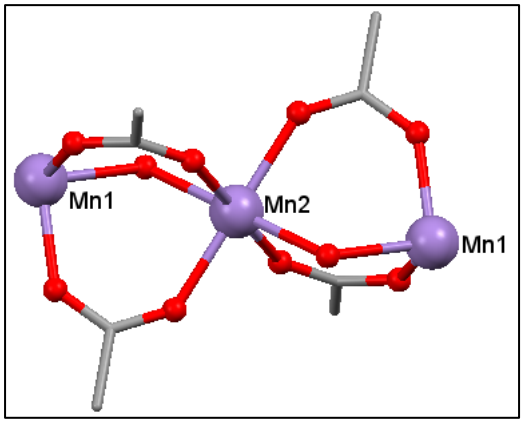

Figure 4.17 Molecular structure of the Mn_3 trimer **4.9**. H-atoms and solvent molecules are omitted for clarity. Colour code: red = O, gray = C and purple = Mn.[183]

The field dependence of the magnetization for the Mn_3 trimer at 2K shows that although it does not reach saturation, the value is approaching *S* = 15/2 that is to be expected for three well-isolated Mn(II) ions, (Figure 4.18)

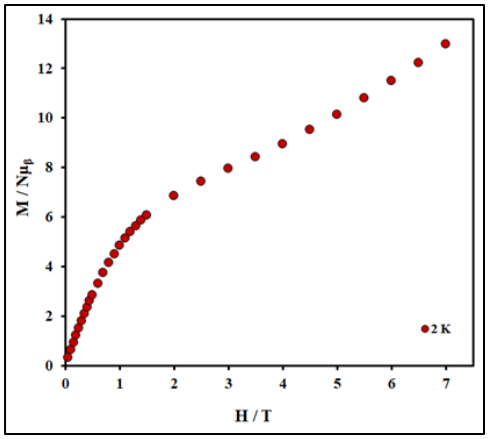

Figure 4.18 Plot of M *vs* H for complex **4.4** at 2K.

4.3.3 Synthesis and structural studies of Ln(III) complexes of H_2L_3

Our second objectives were to investigate the coordination chemistry of the O_2O_3 cavity with 4*f* ion and to study the magnetic properties of the resulting complexes. To address these goals, four complexes **4.5** - **4.8** were synthesized by reacting equal equivalents of **H_2L_3** and the appropriate Ln(III) salt in a 1:1 solvent mixture of MeOH/$CHCl_3$. On completion of the reaction the solvent was removed and the resulting solid was dissolved in the minimum amount of methanol (*ca* 5mL). Single crystals of all four complexes were obtained via the slow diffusion of Et_2O into this solution and their molecular structures were characterized by X-ray diffraction. A summary of selected bond lengths and angles for the complexes can be found in Table 5-10 - Table 5-13 of the Appendix section of the thesis. X-ray diffraction studies reveal that all four complexes crystallize in the orthorhombic space group $P2_12_12_1$, with one independent molecule in the asymmetric unit. The Dy(III) complex, **4.5** has the structural formula $[Dy(H_2L_3)(H_2O)_2(CH_3OH)_2]Cl_3 \cdot CH_3OH$, where in addition to the O_2O_3 ligands, two water and two methanol molecules complete the coordination geometry of the *4f* ion, (Figure 4.19 (left)). The other three complexes, **4.6**–**4.8** are isostructural with a general formula

$[Ln(H_2L_3)(H_2O)_3(CH_3OH)]Cl_3$, in which the O_2O_3 ligands of the macrocycle, together with one methanol and three water molecules are coordinated to the Ln(III) ion. As a representative example, the molecular structure of the Tb(III) complex is shown in (Figure 4.19 (right)).

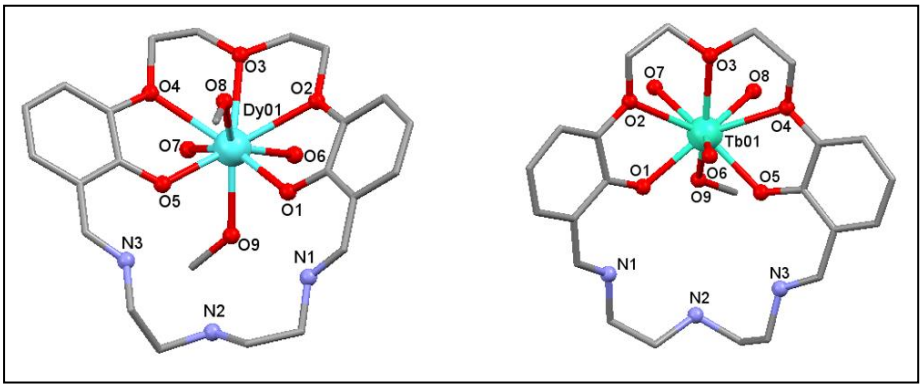

Figure 4.19 Molecular structures of complexes **4.5** and **4.6** with selected labelling. H-atoms and counterions are omitted for clarity. Colour code: red = O, purple = N, gray = C and blue/green = Ln(III) ion.

In all the four complexes, since no base was added during the reaction, the phenol OH group on the macrocycle remains protonated. This is supported by the presence of three Cl^- counter ions in the crystal lattice to balance the +3 charge of the Ln(III) ions. Furthermore, the Ln-O1 and Ln-O5 bond distances are 2.27(6) and 2.28(6) Å respectively, which are in good agreement with the Ln-O distances reported in the literature for the closely related methyl complex **4.10**, bearing a protonated phenol substituent, Figure 4.20.[84]

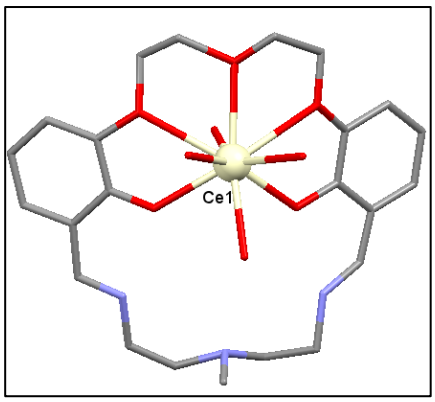

Figure 4.20 Molecular structure of Ce(III) complex (**4.10**) of the methyl analogue. H-atoms are omitted for clarity. Colour code: red = O, purple = N, gray = C. Reproduced with permission from reference.[84]

It is also noteworthy to mention an O-H str is also observed in the IR spectra of all four complexes, further supporting that the macrocycle is neutral. In all four complexes the *4f* ions coordinate to five oxygen atoms in the equatorial plane i.e. by the two phenolic O1, O5 and three ether type oxygen atoms O2, O3 & O4 from the O_2O_3 crown-like cavity of the macrocycle. An additional two water O6, O7 and two methanol ligands O8, O9 coordinate in the axial positions for the Dy(III) complex **4.5,** or three water (O6, O7 & O8) and one methanol ligand (O9) in complexes **4.6**-**4.8**, complete the coordination sphere of the *4f* ion. Interestingly, this differs from the coordination geometry of the *4f* complexes of the methyl derivative **4.10**, that have four coordinated water ligands in addition to the five equatorially coordinated O_2O_3 oxygen atoms.[84]

For complex **4.5**, the Dy-O bond lengths involving the two phenolic (O1, O5) oxygens are 2.27(6) and 2.28(6) Å respectively, which as expected are significantly shorter than that the comparable bond lengths involving the neutral ether type oxygen atoms which range from 2.47(5) to 2.56(6) Å. The Dy-O bond lengths involving the water ligands (O6, O7) are 2.39(6) and 2.41(6) Å respectively, which are very similar to the Dy-O the bond lengths of the neutral methanol molecules (O8, O9) that are 2.42(6) and 2.37(6) Å respectively. Close examination of the crystal packing of the Dy(III) complex reveals the shortest intermolecular Dy···Dy distances are 8.97(8) Å, (Figure 4.22). For complexes **4.6**-**4.8**, we observe the same trend in the Ln-O bond distances as previously described for the Dy(III) system, where the distances for the two phenolic (O1, O5) oxygen atoms are shorter, i.e. between 2.25(6) and 2.31(1) Å, when compared to the Ln-O bonds involving

the ether type oxygen atoms which range from 2.45(6) to 2.58(8) Å. In addition, the Ln-O bond lengths involving the three axial water ligands (O6 to O8) are between 2.36(6) and 2.45(1) Å, which are slightly larger than the Ln-O9 bond lengths for the axial methanol ligand which range from 2.36(6) - 2.40(1) Å. Continuous shape measures (CSMs)[114] were employed to further analyze the coordination geometries of the *4f* ions in the four complexes and assess how much they deviate from the closest matched polyhedron, and the results are shown in Figure 4.21. This study revealed that the coordination geometries of all four *4f* ions are closest to spherical capped square antiprismatic geometry with CSMs of 1.16, 1.75, 1.64, and 1.82 for complexes **4.5** - **4.8** respectively, Table 4-6.

Polyhedron	Symmetry	Dy(III) (4.5) CSM	Tb(III) (4.6) CSM	Er(III) (4.7) CSM	Gd(III) (4.8) CSM
EP-9	D_{9h}	32.34	32.45	32.66	32.36
OPY-9	C_{8v}	24.08	24.37	24.17	24.17
HBPY-9	D_{7h}	17.46	17.07	17.13	16.57
JTC-9	C_{3v}	15.24	15.42	15.30	15.58
JCCU-9	C_{4v}	8.09	7.87	7.74	7.79
CCU-9	C_{4v}	7.23	6.97	6.88	6.85
JCSAPR-9	C_{4v}	2.21	2.37	2.23	2.45
CSAPR-9	C_{4v}	1.61	1.75	1.64	1.82
JTCTPR-9	D_{3h}	1.87	1.96	1.90	2.15
TCTPR-9	D_{3h}	1.63	1.71	1.66	1.83
JTDIC-9	C_{3v}	12.93	12.68	12.74	12.32
HH-9	C_{2v}	9.33	8.95	9.01	8.52
MFF-9	Cs	1.94	2.08	1.97	2.15

Table 4-6 Continuous shape measures (CSMs) of the 9-coordinate Ln(III) coordination polyhedra in complexes **4.5-4.8**. The value in red indicates the closest polyhedron according to the CSMs. Abbreviations: EP-9, Enneagon; OPY-9, Octagonal pyramid; HBPY-9, Heptagonal bipyramid; JTC-9, Johnson triangular cupola J3; JCCU-9, Capped cube J8; CCU-9, Spherical-relaxed capped cube; JCSAPR-9, Capped square antiprism;

CSAPR-9, Spherical capped square antiprism; JTCTPR-9, Tricapped trigonal prism J51; TCTPR-9, Spherical tricapped trigonal prism; JTDIC-9, Tridiminished icosahedron J63; HH-9, Hula-hoop; MFF-9, muffin.

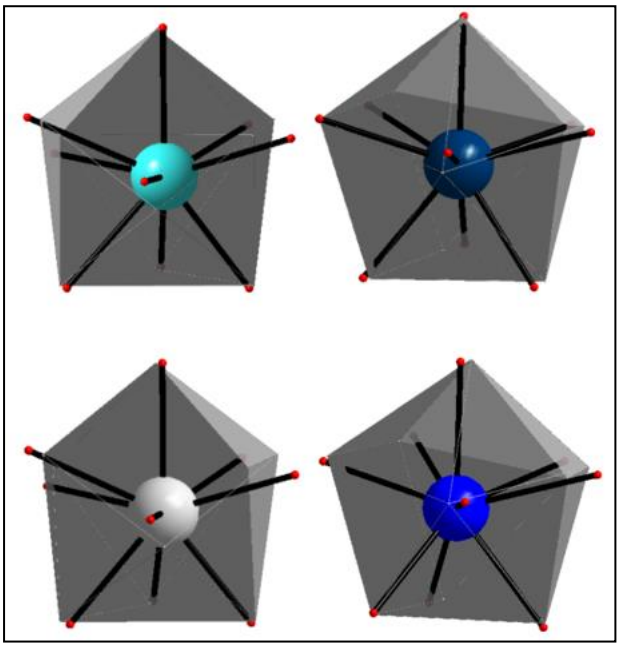

Figure 4.21 Coordination geometry of Dy(III) (top left), Tb(III) (top right), Er(III) (bottom left), and Gd(III) (bottom right) ions superimposed on an idealized spherical capped square antiprismatic polyhedra (shown in grey) for complexes **4.5**-**4.8**.

The crystal packing of **4.5** is further stabilized by O-H···Cl interactions involving the Cl^- counterions and the H atom of the axially coordinated methanol (Cl1···O8 = 3.047(7) Å), and water ligands (Cl1···O6 = 3.088(6) Å), as well as between Cl^- counterions and the MeOH solvent molecules (Cl2···O10 = 3.133(9) Å), (Figure 4.22).

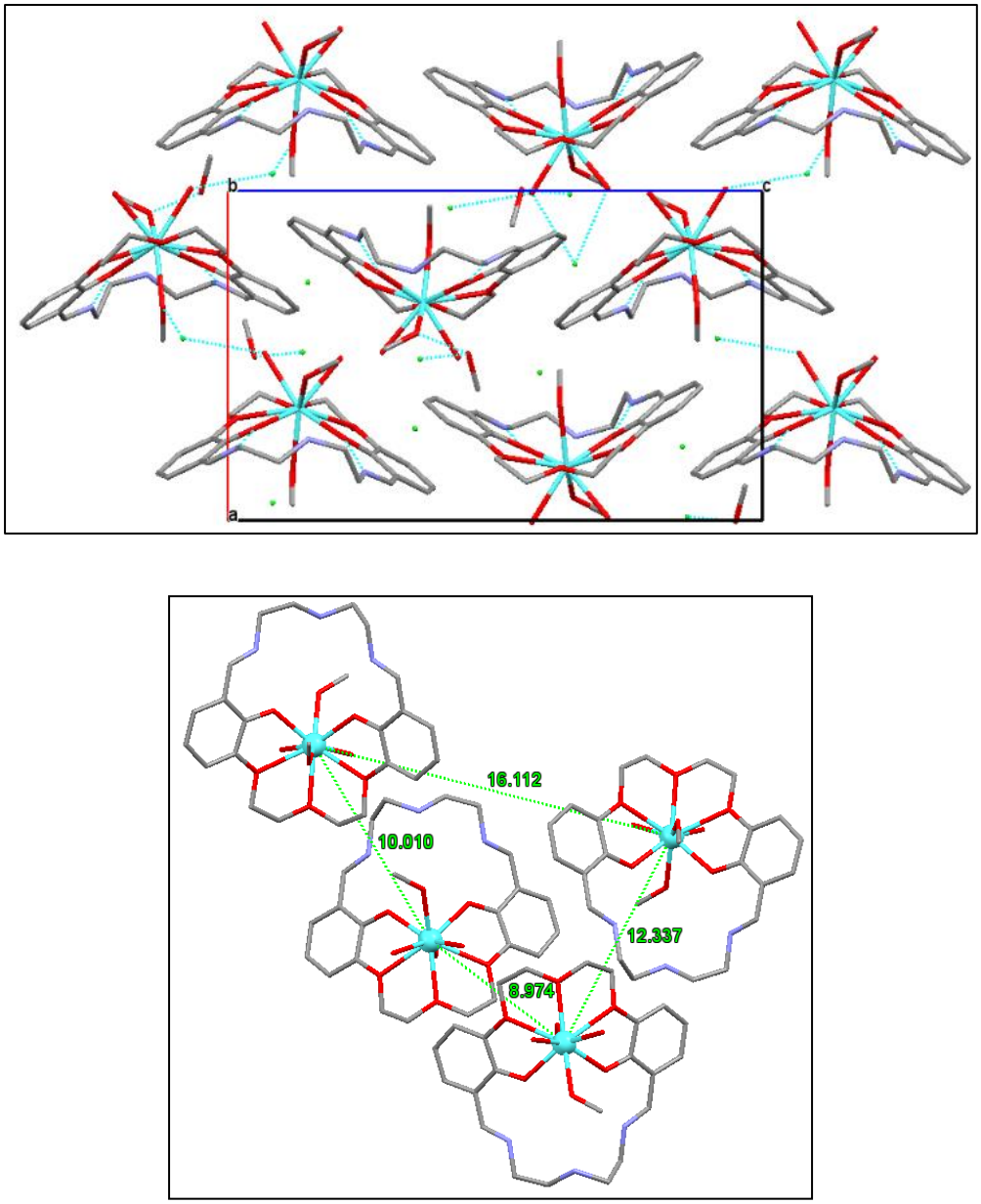

Figure 4.22 View of the crystal packing of **4.5** down the *b*-axis of the unit cell showing hydrogen bonding interactions and the shortest intermolecular Dy···Dy distances as blue (top) and green dashed lines (bottom) respectively.

The crystal packing of **4.6** also stabilized by O-H···Cl interactions that involve the Cl^- counterions and the H atom of the axially coordinated water ligands in the range Cl···O

= 3.039(8)–3.151(8) Å and hydrogen bonding interactions between the O5-H···N3 = 2.729(13) Å (Figure 4.23). The shortest intermolecular Tb···Tb distance is 8.957(9) Å

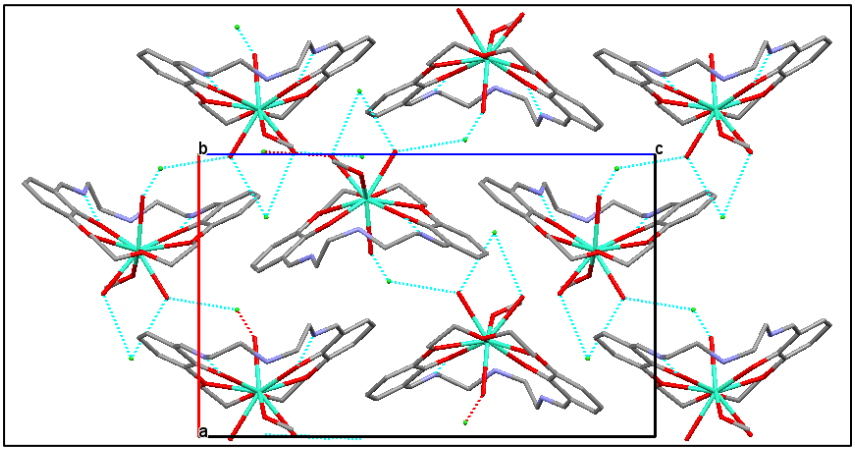

Figure 4.23 Crystal packing of **4.6**. View down the *b*-axis of the unit cell showing the H-bonds as blue dashed lines.

4.3.4 Magnetic studies

Direct current susceptibility measurements (dc) were carried out on single crystals of all four complexes in an applied static field of 0.1 T over the temperature range 5–300 K. The data are shown as $\chi_M T$ *vs*. T plots in (Figure 4.24). The room temperature $\chi_M T$ values of 14.12, 11.75, 11.08 and 7.81 $cm^3 \cdot K \cdot mol^{-1}$ are consistent with the theoretical values of 14.17, 11.82, 11.48 and 7.88 $cm^3 \cdot K \cdot mol^{-1}$ for non-interacting Dy(III) ($^6H_{15/2}$, S = 5/2, g = 4/3), Tb(III) ($^7F_6$, S = 3, g = 3/2), Er(III) ($^4I_{15/2}$, S = 3/2, g = 6/5), and Gd(III) ($^8S_{7/2}$, S = 7/2, L = 0, g = 2) ions in **4.5 - 4.8** respectively. Although as previously mentioned Gd(III) is an isotropic ion and thus not a suitable ion for the preparation of SMMs, its isotropic nature permits us to investigate the presence of any magnetic exchange interactions between the *4f* ions in these complexes. The $\chi_M T$ product of **4.8** stays almost constant as the temperature is lowered ruling out the presence of any weak anti-or ferromagnetic exchange interactions, confirming that the *4f* ions in the complex are

magnetically isolated.[153] In the anisotropic *4f* complexes **4.5 - 4.7**, the decrease in χT below 50 K is mostly attributed to the thermal depopulation of excited Stark sub-levels within the ground multiplet of the respective Ln(III) ion, which masks the presence of any weak intermolecular interactions.[66]

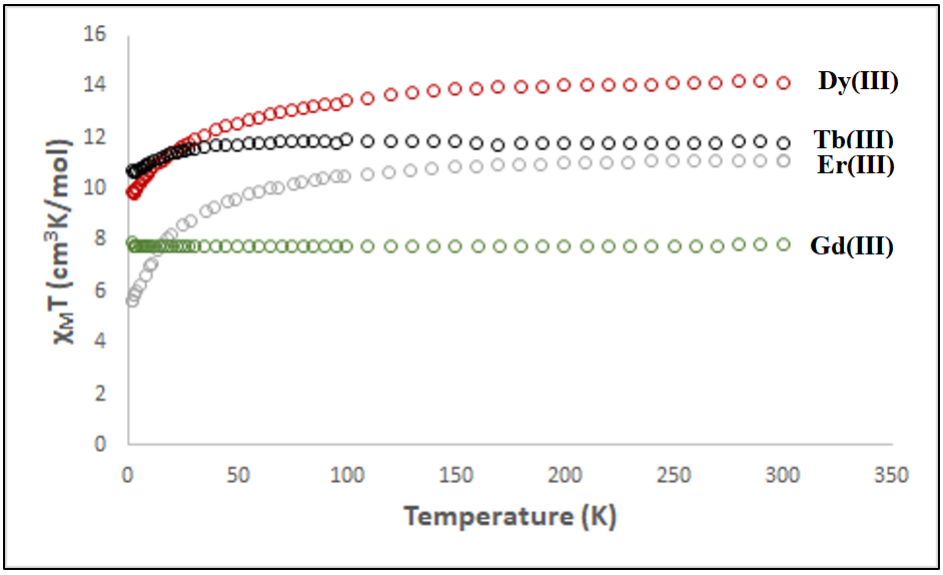

Figure 4.24 Plots of χ_MT *vs.* T shown as red, black, grey and green circles for complexes **4.5 - 4.8** respectively in a field of 0.1 T from 2 - 300 K.

The field dependence of the magnetization measurements were measured for the Dy and Tb complexes between 2 and 7 K over the range of 0-7 T (Figure 4.25). The *M vs. H* plots show a rapid increase below 1 T, followed by a slow linear increase without reaching saturation. The magnetization at the highest field and lowest temperature reaches values of 6.01and 6.05 $N\mu_B$ for **4.5** and **4.6** respectively, which is lower then the theoretical saturation values of 10.65 and 9.72 $N\mu_B$ for Dy(III) and Tb(III) ions, indicating the presence of populated, low-lying excited states.

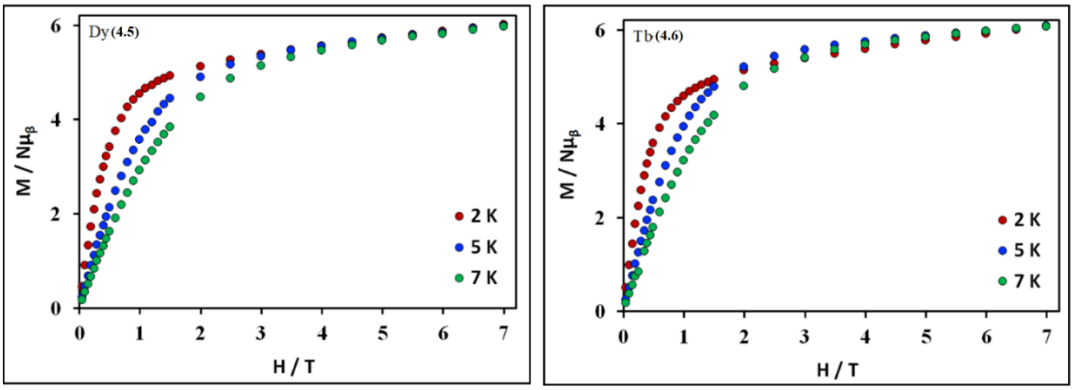

Figure 4.25 Field dependence of the magnetization, i.e. plots of M *vs* T for complexes (**4.5**, left) and (**4.6,** right).

In order to probe the presence of slow relaxation of magnetization for complexes **4.5** to **4.7,** ac magnetic susceptibility measurements were performed in a frequency range of 1-1000 Hz from 2 to 15 K, under a zero static dc field. Under these conditions only complex **4.5** displayed frequency-dependent out-of-phase (χ'') tails below ~9 K, indicating the presence of slow relaxation of the magnetisation, characteristic of an SMM, (Figure 4.26). Unfortunately, in this case, the peak maxima for the out-of-phase (χ'') signal were not observed, due to the presence of QTM. In the next series of magnetic studies, the quantum tunnelling which suppressed via the application of a small static dc field to remove the degeneracy of M_J states.

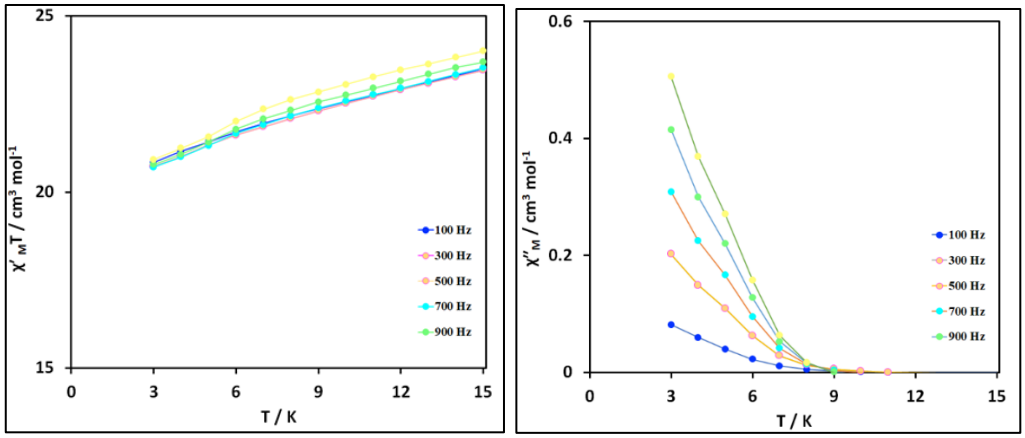

Figure 4.26 Temperature dependence of the in-phase χ′T (left) and out-of-phase χ″ (right) component of the ac susceptibility for the Dy(III) complex **4.5** in a 2 Oe field, oscillating at the indicated frequencies. Solid lines are guide for the eye.

In order to determine the optimum dc field, ac susceptibility measurements were first performed in static fields ranging from 0 to 2000 Oe. From this data, the 400 Oe field was chosen as the optimum field, since the most obvious maximum in χ″ is visible at 2 K, (Figure 4.27).

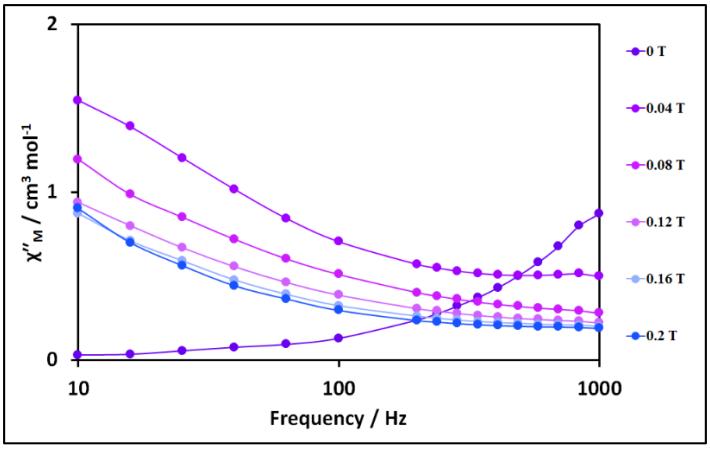

Figure 4.27 Out-of-phase susceptibility for complex **4.5** in various applied dc fields at 2 K. Solid lines are guide for the eye.

As expected, ac susceptibility measurements in the presence of a small applied static dc field show both in phase χ' (Figure 4.28, left) and out of phase χ'' (Figure 4.28, right) frequency dependent signals, consistent with the slow relaxation of magnetization of an SMM. In the χ'' data, there are obvious maxima up to 3 K that shift to higher frequencies as the temperature is increased, Figure 4.28.

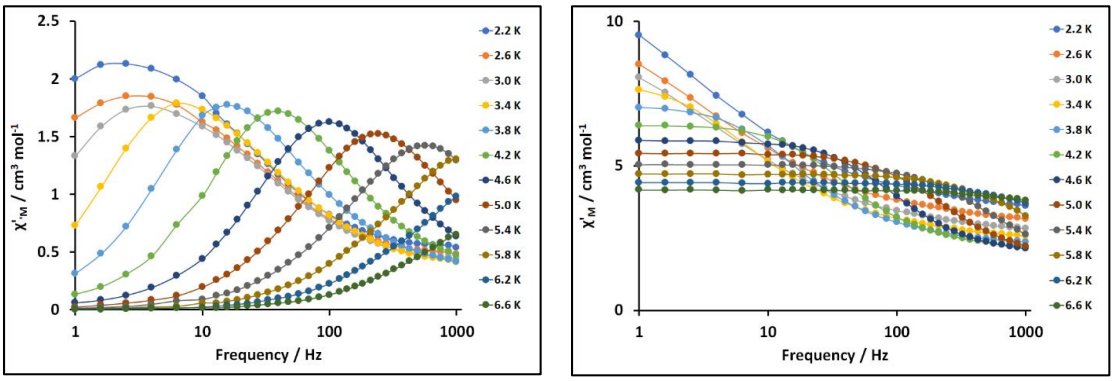

Figure 4.28 In phase χ' (left) and out-phase (χ'') (right) components of the magnetic susceptibility *vs*. frequency for complex **4.5** under a 400 Oe applied dc field. Solid lines are guide for the eye.

The experimental data between 2-6 K were used to construct the Cole-Cole plot as shown in (Figure 4.29), and subsequently fitted into Debye equation to extract the relaxation rate τ and the α parameter. The values for α were in the range 0.20-0.51, suggesting the presence of multiple relaxation processes, most likely due to the presence of both QTM and thermally assisted relaxation pathways. The temperature dependent relaxation times, τ_c obtained from the above fitting were plot against 1/T to give the Arrhenius plot shown in (Figure 4.28). The data in the high-temperature regime, corresponds to the thermally activated relaxation and was therefore analyzed by the Arrhenius equation $\ln \tau = \ln \tau_0 + U_{eff}/k_B T$, where k_B is the Boltzmann constant and τ_0 is the

pre-exponential factor to afford an effective energy barrier U_{eff} = 62.03 K (43 cm^{-1}) and a relaxation rate (or pre-exponential factor) $\tau_0 = 2.47 \times 10^{-9}$ s.

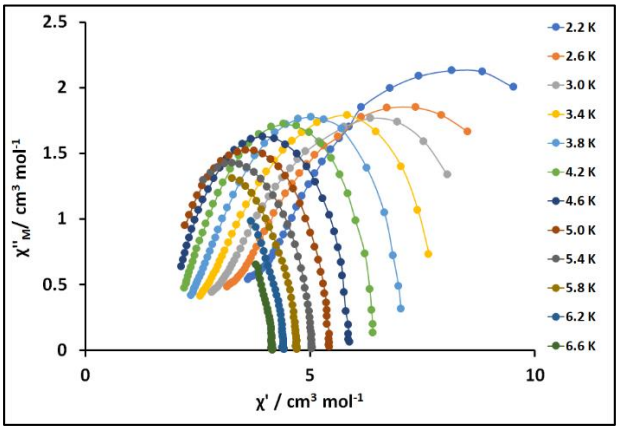

Figure 4.29 Cole-Cole plot for complex **4.5** obtained from the ac susceptibility data collected under a 400 Oe applied dc field. The solid lines correspond to the best fit obtained using a generalized Debye model.

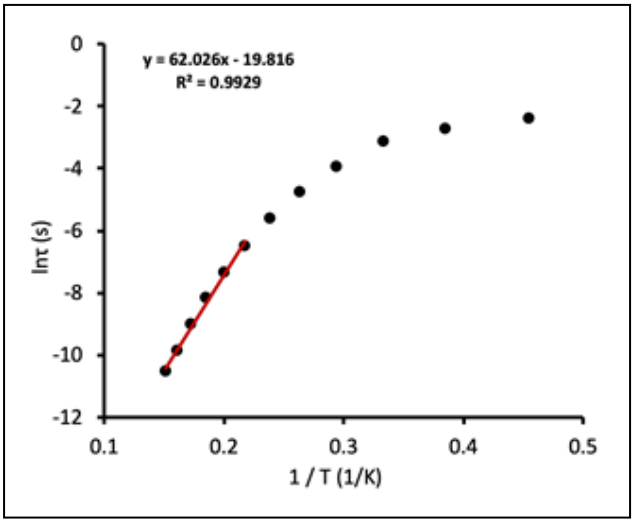

Figure 4.30 Arrhenius plot for the Dy(III) complex **4.5** under a 400 Oe applied dc field. The red line corresponds to the fit of the high-temperature magnetic data.

As previously mentioned, ac susceptibility studies of the Tb(III) and Er(III) complexes reveal no frequency-dependence in both zero or applied static dc fields and hence we can conclude that these complexes are not SMMs. In this respect, ac data for the

Tb complex **4.6** is shown in (Figure 4.11). This is fairly common for Tb(III) complexes since as a non-Kramers ion, Tb(III) exhibits ground state doublets only when its ligands have the appropriate axially elongated crystal field symmetry. For the Er(III) complex, in contrast to Dy and Tb, the *4f* ion is prolate in its electronic density distribution and thus requires the presence of strong equatorial field ligands which is not provided by the O_2O_3 set of the macrocycle.

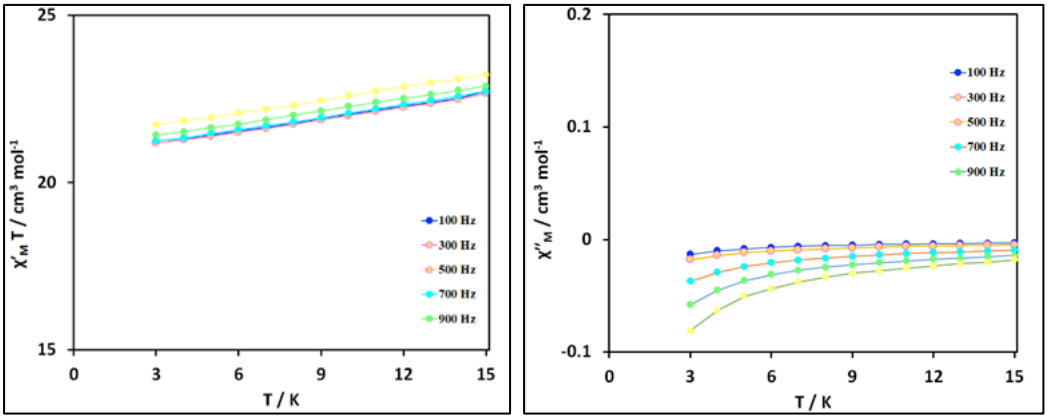

Figure 4.31 χ' *vs.* T (left) and χ'' *vs.* T (right) plots for the Tb(III) complex **4.6** in zero dc field.

Comparing the magnetic properties of complexes **4.1** and **4.5** where the Dy(III) ions are equatorially coordinated by the N_3O_2 and O_2O_3 sets in the macrocyclic cavity respectively, it is apparent that the effective energy barrier U_{eff} of **4.5** is larger by approximately 43 cm^{-1}, (Table 4.7).[100] This may in part be due to the weaker equatorial field exerted by the O_3O_2 binding pocket, since in contrast to the N_3O_2 site which contains two deprotonated phenolate anions, the oxygen donors in complex **4.5** are all neutral. The neutral donor set most likely reduces the electrostatic repulsion between the equatorial ligands and the electronic cloud of the oblate Dy(III) ion which enhances its axial

anisotropy and better isolates the first excited state Kramers doublets. Furthermore, it is also worth noting that in complex **4.5** the Dy(III) ion has a 9-coordinate square antiprismatic geometry, while in **4.1** it has a 7-coordinate, pentagonal bipyramidal geometry which will also contribute to differences in the dynamics of the magnetization. This study serves to highlight how subtle modifications to the coordination sphere of a *4f* ion can brings about significant changes to the symmetry and in turn the crystal field of a coordination complexes, which although synthetically challenging to optimize can nevertheless be successfully tuned and modified to suppress QTM and increase the energy barriers of SMMs.

Complex	**Coordination geometry of *4f* ion**	**U_{eff} (cm^{-1})**	**τ_0 (s)**	**SMM behavior**
$[Na_2Dy_2(L_3)_2Cl_4(MeOH)]2H_2O$ (**4.1**)	pentagonal bipyramidal	12.6	2.91×10^{-7}	Field induced
$[Dy(H_2L_3)(H_2O)_2(CH_3OH)_2]Cl_3 \cdot CH_3OH$ (**4.5**)	capped square antiprismatic	43	2.47×10^{-9}	Zero field

Table 4-7 Summary of the coordination geometries and SMM properties of complexes **4.1** and **4.5**.

4.4 3*d*-4*f* Heterodinuclear complexes of a dual compartmental macrocycle

One of the methods proven successfully to suppress QTM and enhance SMM behavior is to introduce a second paramagnetic *3d* center which can act as a small magnetic moment to perturb and remove the degeneracy of the m_J states in the *4f* ion.[184] Furthermore, coordination of a second diamagnetic ion such as Zn(II) has also been shown to be effective in increasing the energy gap between the ground and first excited state of Dy(III) ions.[185] Thus, the preparation of 3*d*/4*f* -heterodinuclear complexes was attempted.[184] These attempts first involved using the *4f i*ons Dy(III) and Tb(III), together with the diamagnetic

Zn(II) ion. In order to accomplish this, we first prepared the *4f* complexes **4.5** and **4.6**, and then attempted to introduce the *3d* ion into the Schiff-base N_3O_2 cavity via the addition of methanol solution of $ZnCl_2$ in the presence of Et_3N base.[83] The reaction was first heated for half an hour after, which time the solvent was removed by filtration. The resulting product was dissolved in MeOH and then Et_2O was diffused slowly into the resulting solution, but unfortunately no single crystals were obtained. The resulting solid was then subsequently characterized by IR and CHN elemental analysis, which fit for just the *4f* complexes **4.5** and **4.6**, confirming that no Zn(II) ions were coordinated in that second, N_3O_2 cavity. We subsequently attempted to change the reaction conditions by heating the reaction to reflux and systematically varying the Zn(II) salts employed, the base, solvent(s) and crystallization method, but no heterometallic *3d/4f* complexes could be isolated. In addition to Zn(II) we also attempted coordination with paramagnetic 3*d* ion which included Mn(II), Cu(II) and Ni(II), but again as with the Zn(II) system, no *3d/4f* complexes could be isolated.

4.5 Conclusions and future work

To conclude, in this chapter we have investigated the coordination chemistry of the N_3O_2 cavity of the dual compartmental macrocycle **H_2L_3** with select *3d* transition metal ions. In the presence of NaOH, this strategy afforded a magnetically interesting Mn_3 trimer, together with Cu(II) and Zn(II) complexes, where the Schiff-base macrocyclic framework is contracted, affording a 5-membered imidazoline ring. In the absence of base, we exploited the coordination chemistry of the O_3O_2 cavity of the macrocycle together with select *4f* ions. Following this strategy, the Dy(III) complex **4.5** was isolated which undergoes slow relaxation of magnetisation under a 400 Oe static applied dc field, with an effective energy barrier U_{eff} = 62.03 K and $\tau_0 = 2.47 \times 10^{-9}$ s. In contrast, the Tb(III) and

Er(III) complexes displayed no such SMM properties, most likely due to the lack of an appropriate crystal field which resulted in fast QTM. Future work will involve the preparation of Dy(III) mononuclear complexes with Dy(III) ions in the (O_3O_2) cavity and then introducing charged anions into the axial positions in order to enhance the magnetic anisotropy of the oblate *4f* ion. Although attempts to prepare heterometallic *3d/4f* complexes have been unsuccessful to-date, future work could involve modifying the cavity size of the macrocycle to better optimise it for coordination to *3d* ions.

5 Appendices

5.1 Crystallographic data

Table 5-1 Selected bond lengths (Å) and angles (°) for Dy15C5 complex (**2.5**).

Bond	Length (Å)	Bond	Length (Å)
Dy1—O1	2.412 (4)	Dy2—O13	2.343 (4)
Dy1—O2	2.404 (4)	Dy2—O14	2.441 (3)
Dy1—O4	2.329 (4)	Dy2—O16	2.438 (4)
Dy1—O5	2.414 (4)	Dy2—O17	2.434 (3)
Dy1—O7	2.480 (4)	Dy2—O19	2.453 (4)
Dy1—O8	2.445 (4)	Dy2—O20	2.419 (4)
Dy1—O10	2.392 (3)	Dy2—O22	2.391 (3)
Dy1—O11	2.397 (4)	Dy2—O23	2.378 (3)
Dy1—O12	2.369 (4)	Dy2—O24	2.353 (4)
Bond	**Angle (°)**	**Bond**	**Angle (°)**
O4—Dy1—O12	130.23 (16)	O13—Dy2—O24	129.13 (14)
O4—Dy1—O10	88.2 (2)	O13—Dy2—O23	85.06 (17)
O12—Dy1—O10	72.31 (14)	O24—Dy2—O23	72.23 (13)
O4—Dy1—O11	85.2 (2)	O13—Dy2—O22	84.89 (17)
O12—Dy1—O11	87.84 (15)	O24—Dy2—O22	90.14 (13)
O10—Dy1—O11	147.29 (13)	O23—Dy2—O22	146.77 (12)
O4—Dy1—O2	141.47 (19)	O13—Dy2—O20	78.59 (15)
O12—Dy1—O2	78.92 (13)	O24—Dy2—O20	150.26 (14)
O10—Dy1—O2	128.49 (13)	O23—Dy2—O20	127.48 (13)
O11—Dy1—O2	69.62 (13)	O22—Dy2—O20	81.06 (13)
O4—Dy1—O1	142.38 (18)	O13—Dy2—O17	143.06 (17)
O12—Dy1—O1	77.97 (16)	O24—Dy2—O17	78.10 (13)
O10—Dy1—O1	76.90 (14)	O23—Dy2—O17	130.87 (12)
O11—Dy1—O1	124.98 (14)	O22—Dy2—O17	68.83 (13)
O2—Dy1—O1	55.58 (13)	O20—Dy2—O17	72.22 (13)
O4—Dy1—O5	52.93 (15)	O13—Dy2—O16	144.87 (16)
O12—Dy1—O5	77.74 (16)	O24—Dy2—O16	76.17 (14)
O10—Dy1—O5	76.1 (2)	O23—Dy2—O16	80.70 (13)
O11—Dy1—O5	74.4 (2)	O22—Dy2—O16	123.07 (13)
O2—Dy1—O5	137.43 (18)	O20—Dy2—O16	84.95 (14)
O1—Dy1—O5	148.0 (2)	O17—Dy2—O16	54.35 (13)

O4—Dy1—O8	75.70 (17)	O13—Dy2—O14	52.59 (12)
O12—Dy1—O8	150.57 (14)	O24—Dy2—O14	77.33 (13)
O10—Dy1—O8	128.90 (13)	O23—Dy2—O14	74.49 (13)
O11—Dy1—O8	80.15 (14)	O22—Dy2—O14	74.25 (13)
O2—Dy1—O8	71.73 (14)	O20—Dy2—O14	126.21 (13)
O1—Dy1—O8	87.05 (16)	O17—Dy2—O14	135.11 (13)
O5—Dy1—O8	123.54 (18)	O16—Dy2—O14	148.08 (13)
O4—Dy1—O7	72.42 (17)	O13—Dy2—O19	74.97 (15)
O12—Dy1—O7	138.75 (15)	O24—Dy2—O19	134.68 (14)
O10—Dy1—O7	75.19 (14)	O23—Dy2—O19	73.09 (13)
O11—Dy1—O7	132.04 (14)	O22—Dy2—O19	133.70 (13)
O2—Dy1—O7	102.99 (15)	O20—Dy2—O19	54.54 (12)
O1—Dy1—O7	70.42 (16)	O17—Dy2—O19	104.44 (13)
O5—Dy1—O7	117.98 (17)	O16—Dy2—O19	70.21 (14)
O8—Dy1—O7	53.75 (13)	O14—Dy2—O19	119.54 (13)

Table 5-2 Selected bond lengths (Å) and angles (°) for Tb15C5 complex (**2.6**).

Bond	**Length (Å)**	**Bond**	**Length (Å)**
Tb1-O1	2.500 (10)	Tb1-O8	2.445 (12)
Tb1-O2	2.457 (10)	Tb1-O10	2.326 (10)
Tb1-O4	2.464 (12)	Tb1-O11	2.318 (9)
Tb1-O6	2.441 (12)	Tb1-O12	2.353 (17)
Tb1-O7	2.5261 (12)		
Bond	**Angle (°)**	**Bond**	**Angle (°)**
O1-Tb1-O2	51.9 (3)	O4-Tb1-O10	70.4 (4)
O1-Tb1-O4	105.4 (4)	O4-Tb1-O11	128.3 (4)
O1-Tb1-O6	72.9 (4)	O4-Tb1-O12	75.2 (5)
O1-Tb1-O7	114.2 (4)	O6-Tb1-O7	149.7 (4)
O1-Tb1-O8	72.7 (4)	O6-Tb1-O8	145.6 (4)
O1-Tb1-O10	132.2 (3)	O6-Tb1-O10	122.9 (4)
O1-Tb1-O11	72.8 (3)	O6Tb1-O11	79.5 (4)
O1-Tb1-O12	140.3 (4)	O6-Tb1-O12	77.4 (5)
O2-Tb1-O4	75.4 (4)	O7Tb1-O8	51.0 (4)
O2-Tb1-O6	86.2 (4)	O7-Tb1-O10	75.6 (4)
O2-Tb1-O7	122.1 (4)	O7-Tb1-O11	75.2 (3)
O2-Tb1-O8	73.7 (4)	O7-Tb1-O12	80.6 (5)
O2-Tb1-O10	82.4 (3)	O8-Tb1-O10	82.4 (4)

O2-Tb1-O11	124.7 (3)	O8-Tb1-O12	131.6 (5)
O2-Tb1-O12	150.6 (5)	O10-Tb1-O11	148.1 (3)
O4-Tb1-O6	52.6 (4)	O10-Tb1-O12	86.3 (4)
O4-Tb1-O7	139.1 (4)	O11-Tb1-O12	76.4 (4)
O4-Tb1-O8	140.9 (4)		

Table 5-3 Selected bond lengths and angles for DyBz15C5 complex (**3.3**).

Bond	**Length (Å)**	**Bond**	**Length (Å)**
Dy1—O1	2.321 (4)	Dy1—O4	2.378 (4)
Dy1—O7	2.333 (4)	Dy1—O8	2.388 (5)
Dy1—O3	2.362 (5)	Dy1—O2	2.392 (4)
Dy1—O5	2.364 (4)	Dy1—O6	2.404 (4)
Bond	**Angle (°)**	**Bond**	**Angle (°)**
O1—Dy1—O7	81.65 (16)	O4—Dy1—O8	74.79 (16)
O1—Dy1—O3	103.17 (17)	O1—Dy1—O2	74.73 (15)
O7—Dy1—O3	144.70 (16)	O7—Dy1—O2	74.35 (16)
O1—Dy1—O5	146.80 (16)	O3—Dy1—O2	73.39 (15)
O7—Dy1—O5	109.43 (17)	O5—Dy1—O2	137.92 (16)
O3—Dy1—O5	85.79 (17)	O4—Dy1—O2	126.99 (15)
O1—Dy1—O4	77.13 (16)	O8—Dy1—O2	140.57 (16)
O7—Dy1—O4	142.95 (16)	O1—Dy1—O6	142.81 (16)
O3—Dy1—O4	70.59 (16)	O7—Dy1—O6	75.81 (17)
O5—Dy1—O4	75.95 (15)	O3—Dy1—O6	80.43 (19)
O1—Dy1—O8	80.55 (16)	O5—Dy1—O6	69.77 (17)
O7—Dy1—O8	72.01 (16)	O4—Dy1—O6	136.26 (16)
O3—Dy1—O8	143.18 (16)	O8—Dy1—O6	118.71 (18)
O5—Dy1—O8	73.92 (17)	O2—Dy1—O6	70.94 (16)

Table 5-4 Selected bond lengths and angles for TbBz15C5 complex (**3.4**).

Bond	**Length (Å)**	**Bond**	**Length (Å)**
Tb1—O7	2.332 (2)	Tb1—O3	2.464 (2)
Tb1—O8	2.353 (2)	Tb1—O5	2.512 (2)
Tb1—O6	2.356 (3)	Tb1—O1	2.514 (3)
Tb1—N1	2.435 (5)	Tb1—O4	2.520 (3)
Tb1—O2	2.449 (3)		
Bond	**Angle (°)**	**Bond**	**Angle (°)**

O7—Tb1—O8	78.42 (9)	N1—Tb1—O5	73.16 (14)
O7—Tb1—O6	73.61 (9)	O2—Tb1—O5	83.15 (9)
O8—Tb1—O6	77.82 (10)	O3—Tb1—O5	119.71 (8)
O7—Tb1—N1	71.26 (14)	O7—Tb1—O1	141.76 (9)
O8—Tb1—N1	72.90 (15)	O8—Tb1—O1	69.34 (9)
O6—Tb1—N1	137.79 (13)	O6—Tb1—O1	79.84 (9)
O7—Tb1—O2	128.52 (8)	N1—Tb1—O1	115.88 (15)
O8—Tb1—O2	127.25 (10)	O2—Tb1—O1	64.07 (8)
O6—Tb1—O2	71.09 (9)	O3—Tb1—O1	129.06 (9)
N1—Tb1—O2	150.98 (14)	O5—Tb1—O1	61.91 (9)
O7—Tb1—O3	70.45 (8)	O7—Tb1—O4	101.29 (9)
O8—Tb1—O3	144.02 (9)	O8—Tb1—O4	142.55 (9)
O6—Tb1—O3	76.49 (9)	O6—Tb1—O4	138.67 (9)
N1—Tb1—O3	111.95 (16)	N1—Tb1—O4	71.74 (14)
O2—Tb1—O3	65.75 (9)	O2—Tb1—O4	82.56 (9)
O7—Tb1—O5	144.04 (9)	O3—Tb1—O4	63.64 (8)
O8—Tb1—O5	96.07 (9)	O5—Tb1—O4	62.06 (8)
O6—Tb1—O5	140.56 (9)	O1—Tb1—O4	116.76 (8)

Table 5-5 Selected bond lengths and angles for the GdBz15C5 complex (**3.5**).

Bond	**Length (Å)**	**Bond**	**Length (Å)**
Gd1—O8	2.357 (4)	Gd1—O3	2.474 (4)
Gd1—O6	2.371 (4)	Gd1—O5	2.516 (4)
Gd1—O7	2.373 (4)	Gd1—O2	2.535 (4)
Gd1—N2	2.411 (4)	Gd1—O1	2.538 (4)
Gd1—O4	2.474 (4)		
Bond	**Angle (°)**	**Bond**	**Angle (°)**
O8—Gd1—O6	79.37 (14)	N2—Gd1—O5	117.11 (15)
O8—Gd1—O7	73.63 (14)	O4—Gd1—O5	63.79 (13)
O6—Gd1—O7	77.97 (15)	O3—Gd1—O5	128.76 (14)
O8—Gd1—N2	70.63 (15)	O8—Gd1—O2	101.28 (14)
O6—Gd1—N2	73.59 (15)	O6—Gd1—O2	142.07 (14)
O7—Gd1—N2	137.51 (15)	O7—Gd1—O2	139.17 (14)
O8—Gd1—O4	127.92 (14)	N2—Gd1—O2	71.11 (15)
O6—Gd1—O4	126.83 (14)	O4—Gd1—O2	82.97 (14)
O7—Gd1—O4	70.75 (14)	O3—Gd1—O2	63.62 (14)
N2—Gd1—O4	151.44 (15)	O5—Gd1—O2	116.11 (14)

O8—Gd1—O3	70.36 (14)	O8—Gd1—O1	144.19 (14)
O6—Gd1—O3	145.01 (14)	O6—Gd1—O1	95.43 (14)
O7—Gd1—O3	77.01 (14)	O7—Gd1—O1	140.42 (14)
N2—Gd1—O3	110.77 (15)	N2—Gd1—O1	73.91 (15)
O4—Gd1—O3	65.54 (14)	O4—Gd1—O1	83.53 (14)
O8—Gd1—O5	142.44 (14)	O3—Gd1—O1	119.37 (14)
O6—Gd1—O5	69.27 (14)	O5—Gd1—O1	61.58 (13)
O7—Gd1—O5	79.92 (14)	O2—Gd1—O1	61.79 (13)

Table 5-6 Selected bond lengths and angles for the DydiBz15C5 complex (**3.6**).

Bond	**Length (Å)**	**Bond**	**Length (Å)**
Dy1—O13	2.30 (2)	Dy1—O15i	2.386 (16)
Dy1—O17i	2.331 (13)	Dy1—O14	2.40 (2)
Dy1—O17	2.331 (13)	Dy1—O16i	2.410 (18)
Dy1—O18	2.356 (19)	Dy1—O16	2.410 (18)
Dy1—O15	2.386 (16)		
Bond	**Angle (°)**	**Bond**	**Angle (°)**
O13—Dy1—O17i	71.2 (7)	O13—Dy1—O14	145.8 (10)
O13—Dy1—O17	71.2 (7)	O17i—Dy1—O14	132.8 (6)
O17i—Dy1—O17	73.1 (9)	O17—Dy1—O14	132.9 (6)
O13—Dy1—O18	139.3 (9)	O18—Dy1—O14	74.9 (8)
O17i—Dy1—O18	76.4 (5)	O15—Dy1—O14	73.6 (3)
O17—Dy1—O18	76.4 (5)	O15i—Dy1—O14	73.6 (3)
O13—Dy1—O15	104.7 (4)	O13—Dy1—O16i	71.1 (8)
O17i—Dy1—O15	138.5 (6)	O17i—Dy1—O16i	109.4 (5)
O17—Dy1—O15	66.8 (6)	O17—Dy1—O16i	138.8 (6)
O18—Dy1—O15	83.9 (5)	O18—Dy1—O16i	144.8 (5)
O13—Dy1—O15i	104.7 (4)	O15—Dy1—O16i	107.8 (6)
O17i—Dy1—O15i	66.8 (6)	O15i—Dy1—O16i	68.2 (6)
O17—Dy1—O15i	138.5 (6)	O14—Dy1—O16i	76.9 (7)
O18—Dy1—O15i	83.9 (5)	O13—Dy1—O16	71.1 (8)
O15—Dy1—O15i	146.9 (7)	O17i—Dy1—O16	138.8 (6)

Table 5-7 Selected bond lengths and angles for the Cu complex (**4.2**).

Bond	Length (Å)	Bond	Length (Å)
Cu1—O5	1.933 (2)	Cu1—N1	2.089 (3)
Cu1—N2	1.969 (3)	Cu1—Cl1	2.4667 (8)
Cu1—O1	1.985 (2)		
Bond	**Angle (°)**	**Bond**	**Angle (°)**
O5—Cu1—N2	89.62 (10)	O1—Cu1—Cl1	104.08 (6)
O5—Cu1—O1	86.13 (8)	N1—Cu1—Cl1	100.39 (7)
N2—Cu1—O1	155.93 (9)	O5—Cu1—Na1	40.34 (6)
O5—Cu1—N1	162.28 (10)	N2—Cu1—Na1	128.51 (8)
N2—Cu1—N1	83.95 (11)	O1—Cu1—Na1	46.50 (6)
O1—Cu1—N1	93.04 (9)	N1—Cu1—Na1	138.73 (8)
O5—Cu1—Cl1	96.97 (7)	Cl1—Cu1—Na1	97.99 (3)
N2—Cu1—Cl1	99.94 (8)		

Table 5-8 Selected bond lengths and angles for the Zn complex (**4.3**).

Bond	Length (Å)	Bond	Length (Å)
Zn1—O8	1.9924 (10)	Zn1—N3	2.0920 (12)
Zn1—O5	1.9933 (10)	Zn1—N1	2.2544 (12)
Zn1—O1	2.0090 (11)		
Bond	**Angle (°)**	**Bond**	**Angle (°)**
O8—Zn1—O5	104.95 (4)	O1—Zn1—N1	148.13 (5)
O8—Zn1—O1	106.83 (5)	N3—Zn1—N1	79.79 (5)
O5—Zn1—O1	87.86 (4)	O8—Zn1—Na1	93.67 (3)
O8—Zn1—N3	109.70 (5)	O5—Zn1—Na1	49.23 (3)
O5—Zn1—N3	145.23 (4)	O1—Zn1—Na1	44.77 (3)
O1—Zn1—N3	84.91 (5)	N3—Zn1—Na1	129.29 (4)
O8—Zn1—N1	104.62 (4)	N1—Zn1—Na1	137.80 (3)
O5—Zn1—N1	89.01 (4)		

Table 5-9 Selected bond lengths and angles for the Mn_3 complex (**4.4**).

Bond	Length (Å)	Bond	Length (Å)
Mn1—Na1	3.402 (4)	Mn3—O1	2.145 (7)
Mn1—N1	2.236 (9)	Mn3—O8	2.172 (7)
Mn1—N2	2.358 (9)	Mn3—O14	2.130 (7)
Mn1—O1	2.454 (7)	Mn3—O22	2.205 (7)

Mn1—O5	2.073 (7)	Na1—O1	2.325 (8)
Mn1—O6	2.076 (8)	Na1—O2	2.311 (8)
Mn1—O8	2.188 (7)	Na1—O3	2.594 (9)
Mn2—Na2	3.427 (4)	Na1—O4	2.326 (9)
Mn2—N4	2.252 (9)	Na1—O5	2.274 (8)
Mn2—N5	2.358 (9)	Na1—O23	2.229 (9)
Mn2—O10	2.104 (7)	Na1—C48	3.103 (12)
Mn2—O14	2.464 (7)	Na2—O9	2.224 (9)
Mn2—O15	2.090 (8)	Na2—O10	2.252 (8)
Mn2—O22	2.187 (7)	Na2—O11	2.340 (8)
Mn3—N3	2.347 (9)	Na2—O12	2.632 (8)
Mn3—N6	2.337 (9)		
Bond	**Angle (°)**	**Bond**	**Angle (°)**
N1—Mn1—Na1	121.0 (3)	O8—Mn1—N2	83.7 (3)
N1—Mn1—N2	75.8 (3)	O8—Mn1—O1	73.5 (2)
N1—Mn1—O1	164.1 (3)	N4—Mn2—Na2	121.0 (3)
N2—Mn1—Na1	156.9 (2)	N4—Mn2—N5	75.4 (3)
N2—Mn1—O1	119.4 (3)	N4—Mn2—O14	164.0 (3)
O1—Mn1—Na1	43.11 (18)	N5—Mn2—Na2	156.4 (2)
O5—Mn1—Na1	40.7 (2)	N5—Mn2—O14	119.6 (3)
O5—Mn1—N1	80.8 (3)	O10—Mn2—Na2	39.7 (2)
O5—Mn1—N2	153.9 (3)	O10—Mn2—N4	81.8 (3)
O5—Mn1—O1	83.4 (3)	O10—Mn2—N5	154.1 (3)
O5—Mn1—O6	96.4 (3)	O10—Mn2—O14	82.3 (3)
O5—Mn1—O8	91.9 (3)	O10—Mn2—O22	91.1 (3)
O6—Mn1—Na1	95.2 (2)	O14—Mn2—Na2	42.91 (17)
O6—Mn1—N1	98.1 (3)	O15—Mn2—Na2	97.7 (2)
O6—Mn1—N2	98.0 (3)	O15—Mn2—N4	96.6 (3)
O6—Mn1—O1	84.9 (3)	O15—Mn2—N5	96.8 (3)
O6—Mn1—O8	155.8 (3)	O15—Mn2—O10	98.0 (3)
O8—Mn1—Na1	76.60 (19)	O15—Mn2—O14	87.5 (3)
O8—Mn1—N1	105.6 (3)	O15—Mn2—O22	157.6 (3)
O22—Mn2—Na2	76.51 (19)	O8—Mn3—N3	91.9 (3)
O22—Mn2—N4	104.9 (3)	O8—Mn3—N6	178.9 (3)
N4—Mn2—Na2	121.0 (3)	O8—Mn3—O22	88.6 (3)
O22—Mn2—N5	83.0 (3)	O14—Mn3—N3	101.0 (3)
O22—Mn2—O14	73.5 (2)	O14—Mn3—N6	76.8 (3)
N6—Mn3—N3	88.0 (3)	O14—Mn3—O1	176.3 (3)

O1—Mn3—N3	76.1 (3)	O14—Mn3—O8	102.1 (3)
O1—Mn3—N6	100.7 (3)	O14—Mn3—O22	80.1 (2)
O1—Mn3—O8	80.4 (3)	O22—Mn3—N3	178.6 (3)
O1—Mn3—O22	102.8 (3)	O22—Mn3—N6	91.5 (3)

Table 5-10 Selected bond lengths and angles for the Dy complex (**4.5**).

Bond	**Length (Å)**	**Bond**	**Length (Å)**
Dy01—O1	2.276 (6)	Dy01—O8	2.425 (6)
Dy01—O5	2.289 (6)	Dy01—O3	2.471 (6)
Dy01—O9	2.376 (6)	Dy01—O4	2.557 (6)
Dy01—O6	2.390 (5)	Dy01—O2	2.562 (6)
Dy01—O7	2.413 (6)		
Bond	**Angle (°)**	**Bond**	**Angle (°)**
O1—Dy01—O5	92.1 (2)	O7—Dy01—O4	66.8 (2)
O1—Dy01—O9	70.9 (2)	O8—Dy01—O4	70.7 (2)
O5—Dy01—O9	73.1 (2)	O3—Dy01—O4	62.16 (19)
O1—Dy01—O6	87.1 (2)	O1—Dy01—O2	64.7 (2)
O5—Dy01—O6	145.9 (2)	O5—Dy01—O2	141.74 (19)
O9—Dy01—O6	74.4 (2)	O9—Dy01—O2	121.12 (19)
O1—Dy01—O7	143.2 (2)	O6—Dy01—O2	66.85 (19)
O5—Dy01—O7	90.3 (2)	O7—Dy01—O2	126.8 (2)
O9—Dy01—O7	74.8 (2)	O8—Dy01—O2	70.2 (2)
O6—Dy01—O7	71.2 (2)	O3—Dy01—O2	61.16 (18)
O1—Dy01—O8	78.5 (2)	O4—Dy01—O2	117.3 (2)
O5—Dy01—O8	75.8 (2)	O6—Dy01—O8	136.9 (2)
O9—Dy01—O8	134.8 (2)	O7—Dy01—O8	137.3 (2)
O1—Dy01—O3	124.72 (19)	C20—O3—Dy01	117.0 (5)
O5—Dy01—O3	124.9 (2)	C21—O3—Dy01	117.2 (5)
O9—Dy01—O3	151.1 (2)	C17—O4—Dy01	116.0 (5)
O6—Dy01—O3	81.8 (2)	C19—O4—Dy01	121.0 (5)
O7—Dy01—O3	82.2 (2)	C18—O5—Dy01	125.5 (5)
O8—Dy01—O3	74.1 (2)	Dy01—O5—H51	117.2
O1—Dy01—O4	144.9 (2)	Dy01—O6—H61	118 (5)
O5—Dy01—O4	64.8 (2)	Dy01—O6—H62	135 (5)
O9—Dy01—O4	121.3 (2)	Dy01—O7—H71	124 (5)
O6—Dy01—O4	127.1 (2)	Dy01—O7—H72	126 (5)
C1—O1—Dy01	124.2 (5)	C23—O8—Dy01	129.7 (6)

Dy01—O1—H1	117.9	C24—O9—Dy01	131.7 (5)
C2—O2—Dy01	114.6 (5)	C24—O9—H91	128 (7)
C22—O2—Dy01	123.4 (5)	Dy01—O9—H91	100 (7)
C20—O3—C21	116.4 (7)		

Table 5-11 Selected bond lengths and angles for the Tb complex (**4.6**).

Bond	**Length (Å)**	**Bond**	**Length (Å)**
Tb01—O5	2.262 (8)	Tb01—O8	2.422 (7)
Tb01—O1	2.279 (7)	Tb01—O3	2.495 (7)
Tb01—O9	2.389 (7)	Tb01—O4	2.565 (8)
Tb01—O7	2.394 (7)	Tb01—O2	2.579 (7)
Tb01—O6	2.418 (7)		
Bond	**Angle (°)**	**Bond**	**Angle (°)**
O5—Tb01—O1	93.1 (3)	O7—Tb01—O3	81.7 (3)
O5—Tb01—O9	73.1 (3)	O6—Tb01—O3	75.5 (2)
O1—Tb01—O9	70.5 (2)	O8—Tb01—O3	82.2 (2)
O5—Tb01—O7	145.6 (3)	O5—Tb01—O4	64.6 (3)
O1—Tb01—O7	87.3 (3)	O1—Tb01—O4	146.1 (3)
O9—Tb01—O7	74.7 (3)	O9—Tb01—O4	121.2 (3)
O5—Tb01—O6	74.3 (3)	O7—Tb01—O4	125.7 (3)
O1—Tb01—O6	78.5 (3)	O6—Tb01—O4	71.2 (3)
O9—Tb01—O6	133.0 (2)	O8—Tb01—O4	66.5 (3)
O7—Tb01—O6	138.8 (3)	O3—Tb01—O4	61.9 (2)
O5—Tb01—O8	90.0 (3)	O5—Tb01—O2	142.1 (2)
O1—Tb01—O8	142.7 (3)	O1—Tb01—O2	64.6 (3)
O9—Tb01—O8	75.0 (3)	O9—Tb01—O2	121.3 (3)
O7—Tb01—O8	70.1 (3)	O7—Tb01—O2	67.6 (2)
O6—Tb01—O8	137.6 (3)	O6—Tb01—O2	71.4 (3)
O5—Tb01—O3	124.4 (2)	O8—Tb01—O2	126.6 (2)
O1—Tb01—O3	124.7 (2)	O3—Tb01—O2	61.0 (2)
O9—Tb01—O3	151.5 (2)	O4—Tb01—O2	117.2 (3)

Table 5-12 Selected bond lengths and angles for the Er complex (**4.7**).

Bond	Length (Å)	Bond	Length (Å)
Er1—O1	2.256 (6)	Er1—O7	2.381 (7)
Er1—O5	2.276 (7)	Er1—O3	2.458 (6)
Er1—O9	2.364 (6)	Er1—O2	2.547 (6)
Er1—O8	2.365 (6)	Er1—O4	2.552 (7)
Er1—O6	2.373 (6)		
Bond	**Angle (°)**	**Bond**	**Angle (°)**
O1—Er1—O5	92.6 (2)	O8—Er1—O3	76.2 (2)
O1—Er1—O9	69.9 (2)	O6—Er1—O3	81.5 (3)
O5—Er1—O9	73.1 (2)	O7—Er1—O3	81.6 (2)
O1—Er1—O8	78.7 (2)	O1—Er1—O2	65.0 (2)
O5—Er1—O8	74.5 (2)	O5—Er1—O2	142.1 (2)
O9—Er1—O8	133.1 (2)	O9—Er1—O2	121.0 (2)
O1—Er1—O6	86.1 (2)	O8—Er1—O2	71.4 (2)
O5—Er1—O6	145.9 (3)	O6—Er1—O2	66.6 (2)
O9—Er1—O6	74.6 (2)	O7—Er1—O2	126.2 (2)
O8—Er1—O6	137.9 (2)	O3—Er1—O2	61.3 (2)
O1—Er1—O7	141.9 (2)	O1—Er1—O4	147.0 (2)
O5—Er1—O7	90.6 (3)	O5—Er1—O4	64.9 (2)
O9—Er1—O7	74.9 (2)	O9—Er1—O4	120.6 (2)
O8—Er1—O7	138.2 (2)	O8—Er1—O4	72.3 (2)
O6—Er1—O7	70.8 (2)	O6—Er1—O4	126.2 (2)
O1—Er1—O3	125.5 (2)	O7—Er1—O4	66.0 (2)
O5—Er1—O3	125.0 (2)	O3—Er1—O4	62.3 (2)
O9—Er1—O3	150.7 (2)	O2—Er1—O4	118.0 (2)

Table 5-13 Selected bond lengths and angles for the Gd complex (**4.8**).

Bond	Length (Å)	Bond	Length (Å)
Gd01—O5	2.300 (13)	Gd01—O7	2.451 (13)
Gd01—O1	2.306 (13)	Gd01—O3	2.477 (14)
Gd01—O9	2.396 (14)	Gd01—O4	2.578 (12)
Gd01—O8	2.429 (14)	Gd01—O2	2.578 (15)
Gd01—O6	2.436 (12)		
Bond	**Angle (°)**	**Bond**	**Angle (°)**
O5—Gd01—O1	94.6 (5)	O8—Gd01—O3	77.0 (5)

O5—Gd01—O9	70.0 (5)	O6—Gd01—O3	83.0 (5)
O1—Gd01—O9	73.7 (5)	O7—Gd01—O3	81.4 (5)
O5—Gd01—O8	78.4 (5)	O5—Gd01—O4	63.5 (5)
O1—Gd01—O8	72.9 (5)	O1—Gd01—O4	142.3 (4)
O9—Gd01—O8	131.3 (5)	O9—Gd01—O4	120.2 (5)
O5—Gd01—O6	84.8 (5)	O8—Gd01—O4	72.8 (5)
O1—Gd01—O6	145.6 (5)	O6—Gd01—O4	66.8 (4)
O9—Gd01—O6	73.8 (6)	O7—Gd01—O4	125.7 (5)
O8—Gd01—O6	139.6 (5)	O3—Gd01—O4	61.8 (5)
O5—Gd01—O7	142.3 (5)	O5—Gd01—O2	147.4 (5)
O1—Gd01—O7	90.7 (5)	O1—Gd01—O2	64.2 (5)
O9—Gd01—O7	75.8 (5)	O9—Gd01—O2	121.5 (5)
O8—Gd01—O7	138.3 (5)	O8—Gd01—O2	72.0 (5)
O6—Gd01—O7	70.4 (4)	O6—Gd01—O2	126.9 (5)
O5—Gd01—O3	124.4 (5)	O7—Gd01—O2	66.4 (5)
O1—Gd01—O3	123.6 (5)	O3—Gd01—O2	61.6 (4)
O9—Gd01—O3	151.7 (5)	O4—Gd01—O2	118.0 (5)

5.2 Computational details

Table 5-14 Long (B_1) and short (B_2) basis sets used for the calculations of the Dy and Tb complexes **2.5** and **2.6**.

Basis Set 1 (B1)	Basis Set 2 (B2)
Ln.ANO-RCC-VQZP	Ln.ANO-RCC-VDZP
O.ANO-RCC-VTZP (coordinated)	O.ANO-RCC-VDZP (coordinated)
O.ANO-RCC-VDZP	O.ANO-RCC-VDZP
N.ANO-RCC-VTZP (coordinated)	N.ANO-RCC-VDZP (coordinated)
N.ANO-RCC-VDZP	N.ANO-RCC-VDZP
Lu.ANO-RCC-VQZP	Lu.ANO-RCC-VDZP
Cl.ANO-RCC-VDZP	Cl.ANO-RCC-VDZP
C.ANO-RCC-VDZP	C.ANO-RCC-MB
H.ANO-RCC-VDZP	H.ANO-RCC-MB

Table 5-15 Energies of the eight Kramers doublets within the $^6H_{15/2}$ multiplet for the two Dy(III) ions in complex (**2.5**).

Basis Set	B1	B2	B1	B2	B1	B2	B1	B2
Model	1	1	2	2	1	1	2	2
KD	Dy1	Dy1	Dy1	Dy1	Dy2	Dy2	Dy2	Dy2
1	0.000	0.000	0.000	0.000	0.000	0.000	0.000	0.000
2	21.442	47.457	68.628	82.740	30.676	85.786	87.219	101.595
3	58.452	90.358	126.465	142.551	56.850	116.367	152.990	160.988
4	82.734	128.599	203.846	216.416	85.727	170.183	207.521	219.352
5	116.830	149.633	240.823	237.190	122.264	200.315	250.297	252.820
6	142.992	176.990	259.022	254.906	156.264	216.513	281.146	283.810
7	171.438	205.507	276.086	271.944	185.508	242.625	313.727	313.187
8	222.416	235.175	381.835	394.126	257.141	278.068	375.420	404.680

Table 5-16 Energies of the 13 singlet states within the $^7F_6$ multiplet for the Tb(III) ion of complex (**2.6**).

Basis Set	B1	B2	B1	B2
Model	1	1	2	2
SO-State				
1	0.00	0.00	0.00	0.00
2	0.49	0.37	0.38	0.59
3	37.32	39.18	85.49	81.25
4	39.21	40.56	88.39	84.20
5	105.75	95.57	135.41	118.07
6	108.38	97.95	148.86	132.79
7	164.69	141.24	154.80	146.92
8	189.69	160.44	193.89	185.98
9	222.16	185.37	213.69	203.65
10	277.63	215.74	263.29	240.15
11	287.44	224.21	272.42	247.75
12	455.49	375.20	324.01	293.19
13	456.20	375.50	325.88	294.37

Table 5-17 g-Tensors for the eight Kramers doublets within the $^{6}H1_{5/2}$ multiplet for the two Dy(III) ions of complex (**2.5**).

Basis Set	B1	B2	B1	B2	B1	B2	B1	B2
Model	1	1	2	2	1	1	2	2
KD	Dy1	Dy1	Dy1	Dy1	Dy2	Dy2	Dy2	Dy2
1	1.093	0.230	0.147	0.117	0.878	0.095	0.069	0.057
	2.504	0.411	0.396	0.254	1.741	0.170	0.135	0.098
	16.360	18.408	18.814	18.943	17.494	19.231	19.224	19.230
2	0.121	2.497	0.906	1.010	2.597	1.916	0.633	0.802
	3.551	4.372	1.066	1.486	2.878	4.533	0.788	1.313
	13.183	13.185	15.999	15.479	12.391	13.086	16.916	16.115
3	1.015	1.353	0.239	0.443	0.194	9.576	0.553	0.248
	4.548	5.038	1.772	1.911	3.203	6.927	2.467	2.309
	11.609	9.817	14.028	12.997	9.779	0.212	14.595	13.980
4	0.720	0.053	0.991	2.633	3.606	3.750	4.443	4.465
	1.365	4.001	2.126	3.176	4.799	4.687	5.193	6.069
	17.167	11.829	11.217	9.699	6.655	7.675	9.706	9.722
5	7.815	8.434	7.284	8.585	0.440	0.632	7.877	3.874
	5.488	4.473	5.197	5.780	2.627	4.361	6.789	4.861
	0.405	0.385	0.168	0.315	11.391	11.896	2.003	8.841
6	0.255	0.139	1.836	0.090	10.616	1.462	3.508	9.535
	5.980	2.328	2.660	1.283	6.424	4.466	4.588	7.229
	11.816	12.501	12.298	10.408	0.702	8.354	11.686	3.903
7	3.048	8.131	0.408	10.254	1.482	1.476	0.804	0.437
	4.266	5.509	2.250	5.581	4.222	3.924	1.566	1.087
	11.673	2.211	13.246	0.803	12.610	11.288	17.275	17.799
8	0.549	1.737	0.009	0.010	0.213	0.285	0.007	0.039
	1.312	4.454	0.072	0.080	0.626	2.953	0.133	0.181
	17.594	13.458	19.362	19.425	18.555	16.091	19.322	19.450

Table 5-18 Energies of the Eight Kramers Doublets (KDs) in the $^6H_{15/2}$ Multiplet for the Dy1 and Dy2 Ions in (**2.5**).

KD	E (cm^{-1})	g_x	g_y	g_z	angle (deg)
Dy1					
1	1 0.000	1.093	2.504	16.360	0.000
2	21.442	3.551	3.551	13.183	129.637
3	58.452	4.548	4.548	11.609	57.182
4	82.734	1.365	1.365	17.167	42.533
5	116.830	5.488	5.488	0.405	90.396
6	142.992	5.980	5.980	11.816	37.416
7	171.438	4.266	4.266	11.673	83.543
8	222.416	1.312	1.312	17.594	86.211
Dy2					
1	0.000	0.878	1.741	17.494	0.000
2	30.676	2.597	2.878	12.391	91.763
3	56.850	0.194	3.203	9.779	78.655
4	85.727	3.606	4.799	6.655	67.594
5	122.264	0.440	2.627	11.391	40.468
6	156.264	10.616	6.424	0.702	106.811
7	185.508	1.482	4.222	12.610	96.588
8	257.141	0.213	0.626	18.555	109.126

Figure 5.1 Plots of the stationary states within the $^6H_{15/2}$ multiplet of Dy1 in (**2.5**) using the different structural models and basis sets. The possible magnetic relaxation pathways which utilize the first two Kramers doublets are shown as arrows, such that, red corresponds to thermal transitions, blue for spin-lattice relaxation pathways and black for

QTM pathways. Stationary states are plotted as energy against ⟨μ⟩, the average magnetic moment.

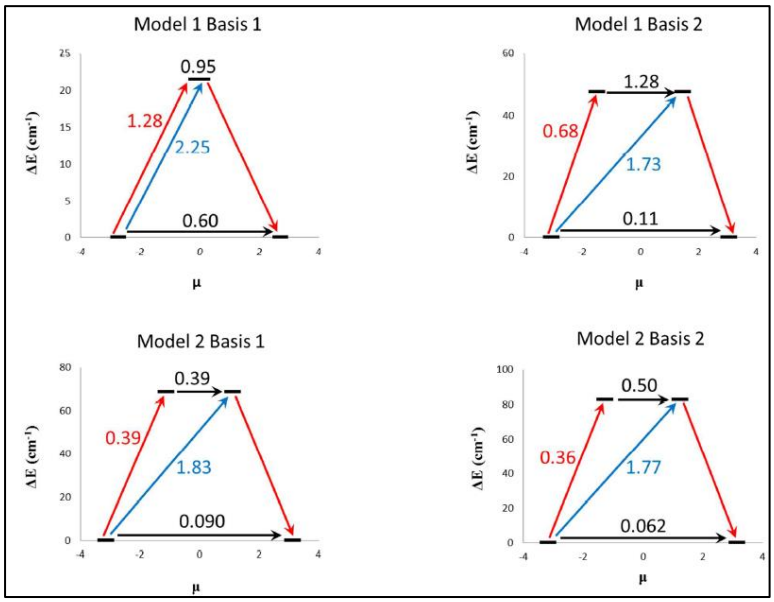

Figure 5.2 Plots of the stationary states within the $^{6}H_{15/2}$ multiplet of Dy2 in (**2.5**) using the different structural models and basis sets. The possible magnetic relaxation pathways which utilize the first two Kramers doublets are shown as arrows, such that, red corresponds to thermal transitions, blue for spin-lattice relaxation pathways and black for QTM pathways. Stationary states are plotted as energy against ⟨μ⟩, the average magnetic moment.

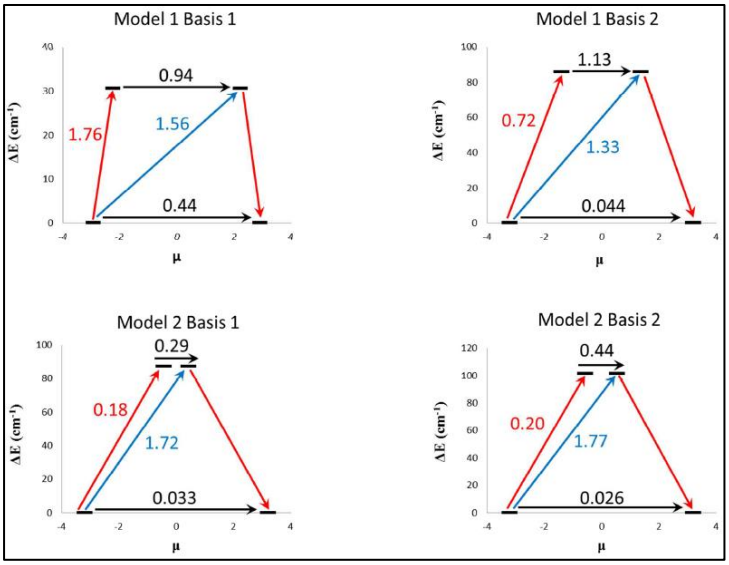

Figure 5.3 Plots of the stationary states within the $^7F_6$ multiplet of Tb(III) in (**2.6**) using the different structural models and basis sets. The possible magnetic relaxation pathways which utilize the first two Kramers doublets are shown as arrows, such that, red corresponds to thermal transitions, blue for spin-lattice relaxation pathways and black for the tunnel splitting. Stationary states are plotted as energy against ⟨μ⟩, the average magnetic moment.

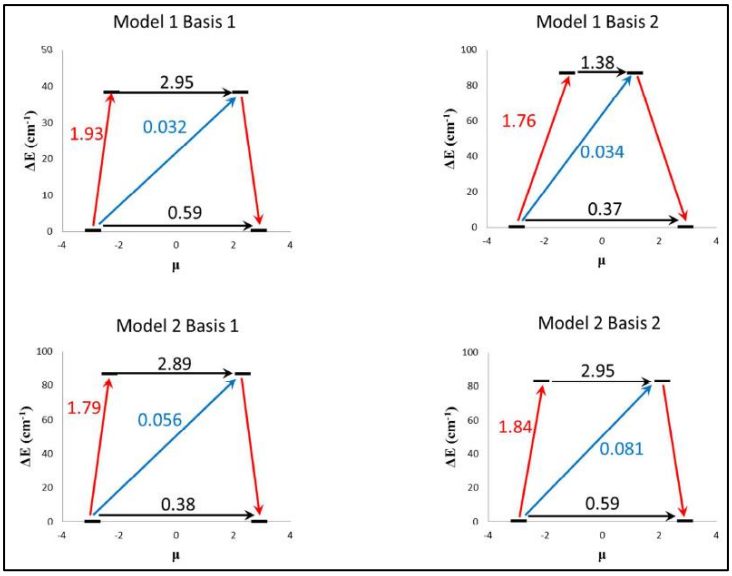

Table 5-19 Crystal field parameters for the Dy1 ion of complex (**2.5**) using the CASSCF/RASSI wavefunctions.

k	Q	B_q^k	B_q^k	B_q^k	B_q^k
		Model 1 (B1)	**Model 1 (B2)**	**Model 2 (B1)**	**Model 2 (B2)**
2	-2	-3.63E-01	2.76E-01	1.41E-01	1.01E-01
	-1	-5.81E-01	-6.55E-01	-1.03E+00	-5.46E-01
	0	-1.96E-01	-4.13E-01	-1.07E+00	-1.09E+00
	1	8.09E-01	2.71E-01	3.56E-02	-2.09E-02
	2	-2.69E-02	9.61E-02	2.14E+00	2.04E+00
4	-4	2.13E-03	6.47E-03	-7.13E-03	-5.82E-03
	-3	-5.81E-03	-3.16E-02	1.44E-02	1.09E-02
	-2	2.49E-04	3.13E-03	1.63E-04	3.64E-04
	-1	1.50E-02	4.88E-03	6.23E-03	1.20E-03
	0	-1.86E-03	-2.60E-03	-2.73E-03	-2.65E-03
	1	-1.51E-03	3.73E-03	3.57E-03	3.77E-03
	2	1.88E-04	-4.31E-04	2.64E-03	2.69E-03
	3	3.77E-02	1.02E-02	-3.03E-02	-2.88E-02
	4	-6.66E-03	-1.31E-03	-9.84E-04	3.10E-03
6	-6	1.73E-05	-2.98E-04	-1.13E-04	-9.21E-06
	-5	-3.74E-04	4.42E-04	-5.90E-04	-6.26E-04
	-4	-2.61E-05	-8.16E-06	1.18E-05	3.82E-05
	-3	2.63E-05	8.84E-06	1.19E-04	1.64E-04
	-2	2.26E-04	2.11E-04	7.73E-05	1.06E-04
	-1	2.64E-04	2.40E-04	2.52E-04	2.80E-04
	0	5.02E-06	-1.74E-05	-9.23E-06	-1.67E-05
	1	-1.25E-04	-1.89E-04	-1.30E-05	-2.73E-05
	2	-1.01E-04	-7.34E-05	2.17E-04	2.06E-04
	3	-3.47E-05	-1.89E-04	1.96E-04	1.43E-04
	4	-7.45E-05	-6.31E-05	1.06E-04	6.45E-05
	5	-5.68E-04	-3.93E-04	-1.88E-04	1.21E-05
	6	2.19E-04	-4.56E-05	2.19E-04	3.05E-04

Table 5-20 Crystal field parameters for the Dy2 ion of complex (**2.5**) using the CASSCF/RASSI wavefunctions.

k	Q	B_q^k	B_q^k	B_q^k	B_q^k
		Model 1 (B1)	**Model 1 (B2)**	**Model 2 (B1)**	**Model 2 (B2)**
2	-2	5.51E-01	3.79E-02	-1.52E-01	-5.76E-01
	-1	-2.68E-01	-1.63E-01	-1.34E+00	-5.84E-01
	0	-3.19E-01	-7.61E-01	-1.26E+00	-1.31E+00
	1	2.23E+00	-1.61E+00	-1.38E+00	-1.45E+00
	2	4.99E-01	4.82E-01	1.76E+00	1.71E+00
4	-4	-5.62E-03	-2.23E-03	4.62E-03	-8.51E-04
	-3	2.59E-02	-1.92E-02	1.08E-02	-1.31E-03
	-2	-4.52E-03	-3.55E-03	-2.50E-04	-1.69E-03
	-1	1.63E-03	-9.78E-04	4.95E-03	7.99E-04
	0	-2.45E-03	-2.45E-03	-2.39E-03	-2.20E-03
	1	-5.19E-03	2.52E-04	1.18E-03	6.18E-04
	2	-4.94E-04	2.67E-03	3.36E-03	3.18E-03
	3	8.90E-03	2.26E-02	2.47E-02	2.63E-02
	4	1.98E-05	3.49E-03	1.34E-03	4.25E-03
6	-6	1.46E-04	2.10E-05	-6.81E-05	-2.65E-04
	-5	-8.10E-05	2.05E-04	-3.63E-04	-1.36E-04
	-4	1.27E-04	-1.32E-05	-8.14E-05	-7.49E-05
	-3	1.62E-04	1.19E-04	2.10E-04	2.33E-04
	-2	-3.39E-05	-1.33E-04	-1.11E-04	-1.67E-04
	-1	-1.76E-05	1.83E-04	2.99E-04	2.86E-04
	0	-2.31E-05	-3.40E-05	-1.92E-05	-2.48E-05
	1	-3.26E-04	2.37E-04	1.05E-04	1.62E-04
	2	-1.23E-04	-2.95E-05	1.44E-04	1.10E-04
	3	-2.30E-04	2.23E-04	-1.30E-04	-4.63E-06
	4	-4.53E-05	-8.65E-05	7.72E-05	-2.09E-05
	5	-1.78E-04	-1.76E-04	-9.74E-05	-3.84E-04
	6	1.43E-04	-2.59E-04	1.86E-04	3.73E-07

Table 5-21 Crystal field parameters for the Tb(III) ion of complex (**2.6**) using the CASSCF/RASSI wavefunctions.

k	Q	B_q^k	B_q^k	B_q^k	B_q^k
		Model 1 (B1)	**Model 1 (B2)**	**Model 2 (B1)**	**Model 2 (B2)**
2	-2	-7.82E-01	-2.13E+00	2.13E-01	1.45E+00
	-1	7.34E-01	-1.88E+00	2.66E+00	2.09E+00
	0	-3.09E+00	-2.33E+00	-2.03E+00	-1.82E+00
	1	1.76E+00	2.61E+00	-9.06E-02	-3.52E-01
	2	3.56E+00	-1.85E+00	1.61E+00	9.40E-01
4	-4	2.23E-02	2.50E-02	-1.88E-02	2.60E-03
	-3	4.20E-02	-3.31E-02	1.50E-01	6.63E-02
	-2	-1.03E-02	-1.39E-03	-2.08E-02	-8.80E-03
	-1	-1.92E-02	1.81E-02	-2.06E-02	-1.40E-02
	0	5.38E-03	3.83E-04	-4.70E-03	-4.52E-03
	1	-3.11E-02	-3.67E-02	-1.38E-02	-1.02E-02
	2	-2.71E-03	2.23E-03	2.83E-03	1.55E-02
	3	-1.55E-02	-1.11E-02	-3.22E-02	-1.14E-01
	4	3.28E-02	-3.13E-02	1.18E-02	2.39E-02
6	-6	3.00E-04	1.32E-04	1.60E-05	4.19E-05
	-5	5.98E-04	4.38E-04	7.88E-04	7.66E-04
	-4	-1.57E-04	6.50E-05	-8.61E-06	-2.61E-04
	-3	-3.40E-04	1.62E-04	3.75E-04	2.23E-04
	-2	-6.29E-05	2.01E-04	1.56E-04	1.65E-04
	-1	2.70E-04	8.69E-05	-1.13E-04	-1.04E-04
	0	8.35E-06	3.59E-05	1.30E-05	8.15E-06
	1	2.96E-04	1.16E-04	1.15E-04	1.56E-04
	2	-8.28E-05	-2.07E-05	2.41E-05	-4.09E-05
	3	-3.35E-04	3.78E-04	-1.30E-04	-3.82E-04
	4	2.93E-05	-4.27E-05	-3.43E-04	-1.46E-04
	5	1.02E-04	-1.12E-05	5.25E-04	-7.13E-04
	6	3.33E-04	3.74E-04	2.62E-05	9.44E-06

Table 5-22 (left) long basis sets and (right) short basis sets used for each structural model for the DyBz15C5 complex (**3.3**).

Long Basis Sets		Short Basis Sets	
Dy	ANO-RCC-VQZP	Dy	ANO-RCC-VDZP
O_{coord}	ANO-RCC-VTZP	O	ANO-RCC-VDZP
O	ANO-RCC-VDZP	H	ANO-RCC-VDZP
Cl	ANO-RCC-VTZP		
C	ANO-RCC-VDZP		
H	ANO-RCC-VQZP		

Table 5-23 Energies of the eight Kramers doublets (KD) in the $^6H_{15/2}$ multiplet for the DyBz15C5 complex (**3.3**).

KD	Model 1 short (cm^{-1})	Model 1 Long (cm^{-1})	Model 2 Short (cm^{-1})	Model 2 long (cm^{-1})
1	0.00	0.00	0	0.00
2	19.31	15.54	15.54	34.51
3	72.07	43.54	45.47	37.45
4	92.18	65.69	78.57	64.80
5	137.97	114.95	123.39	109.42
6	157.57	127.57	139.81	124.99
7	184.63	146.25	163.99	153.90
8	569.53	520.81	519.62	493.81

Table 5-24 Difference between the main magnetic axes of the eight Kramers doublets in the $^6H_{15/2}$ multiplet for the DyBz15C5 complex (**3.3**).

KD	Model 1 short (°)	Model 1 Long (°)	Model 2 Short (°)	Model 2 long (°)
1	0.00	0.00	0	0.00
2	25.55	12.92	17.53	24.86
3	20.49	117.63	119.57	78.96 90.55
4	41.36	56.60	44.49	59.73
5	37.58	49.52	17.35	41.36
6	22.19	55.67	103.09	48.09
7	114.26	118.19	113.71	77.99
8	8.46	13.22	102.7	96.14

Table 5-25 g-tensors of the eight Kramers doublets (KD) of the $^6H_{15/2}$ multiplet for the DyBz15C5 complex (**3.3**).

KDs		Model 1 Short	Model 1 Long	Model 2 Short	Model 2 Long
1	g_x	0.15230	0.34925	0.25181	0.17539
	g_y	023688	1.04049	0.54358	0.60276
	g_z	19.47789	18.40045	19.30460	18.7044
2	g_x	0.27928	0.05088	0.20732	0.51926
	g_y	0.47063	0.51400	1.07942	0.92606
	g_z	17.37565	17.43218	16.47758	17.93311
3	g_x	1.81422	1.91173	2.67007	2.96932
	g_y	3.90371	3.26142	4.25130	4.45079
	g_z	12.97951	13.54675	13.50178	13.69288
4	g_x	1.72513	9.38593	8.71331	0.94389
	g_y	4.95520	6.28668	7.12959	5.49821
	g_z	9.25547	2.66812	0.16044	10.26467
5	g_x	2.01703	1.62801	0.80271	1.77971
	g_y	3.59845	2.49449	4.91717	2.81536
	g_z	12.98379	8.57434	10.985669	12.70925
6	g_x	0.50607	9.93759	9.19074	0.83293
	g_y	1.49166	6.33552	5.93763	0.93475
	g_z	17.90282	1.43966	0.81720	11.16628
7	g_x	1.32591	2.13506	1.14921	1.06758
	g_y	1.92365	6.45724	4.53106	2.65314
	g_z	15.81185	11.51571	15.51931	17.53194
8	g_x	0.00077	0.00110	0.00000	0.00171
	g_y	0.00173	0.00214	0.00000	0.00297
	g_z	19.86937	19.95836	19.86328	19.85986

Figure 5.4 Main magnetic axes and relaxation pathways for Model 1 (short basis set) for DyBz complex (**3.3**).

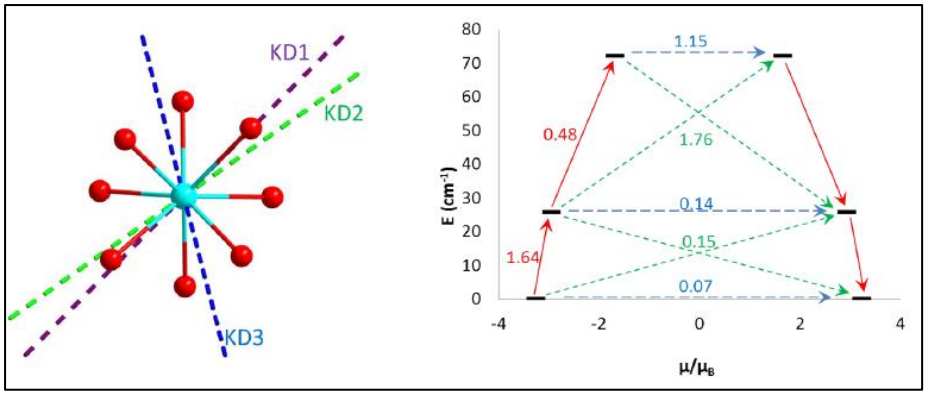

Figure 5.5 Main magnetic axes and relaxation pathways for Model 1 (long basis set) for DyBz complex (**3.3**).

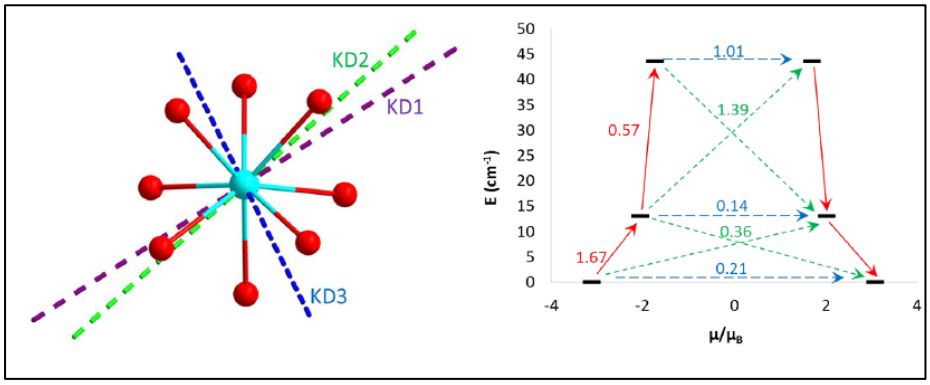

Figure 5.6 Main magnetic axes and relaxation pathways for Model 2 (short basis set) for the DyBz15C5 complex (**3.3**).

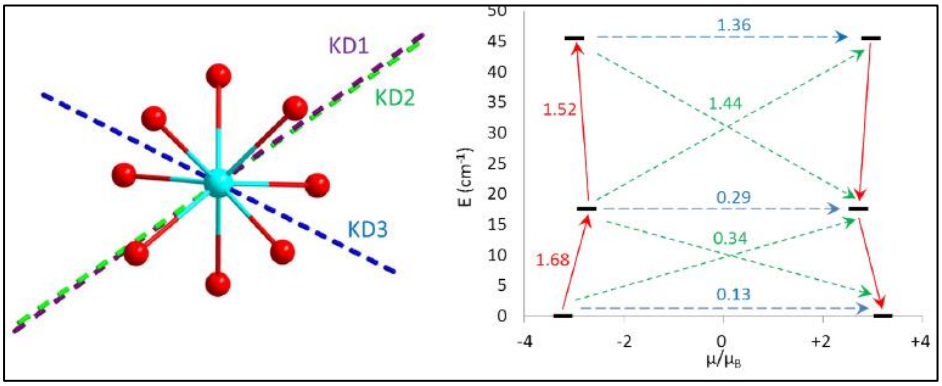

Figure 5.7 Main magnetic axes and relaxation pathways for Model 2 (long basis set) for the DyBz15C5 complex (**3.3**).

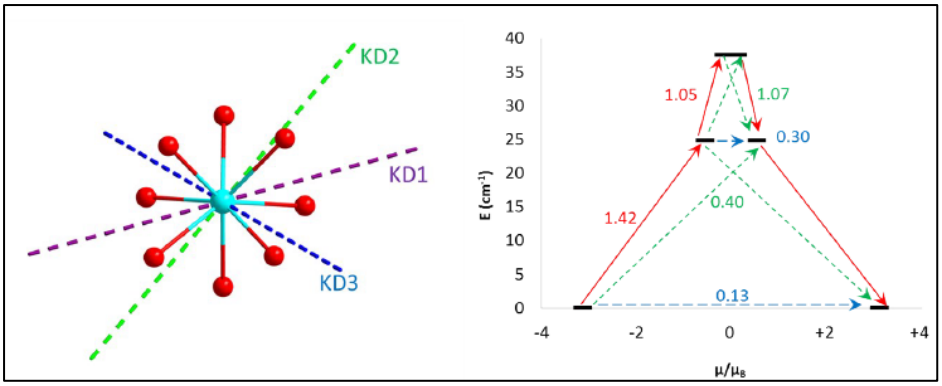

Table 5-26 Computed crystal field parameters for the four models of the complex using the CASSCF/RASSI wavefunctions for the DyBz15C5 complex (**3.3**).

k	q	B^k_q Model 1 Short	B^k_q Model 1 Long	B^k_q Model 2 Short	B^k_q Model 2 Long
2	-2	2.3877136	2.5264830	2.3173897	2.5234365
	-1	0.5573864	-0.5581149	0.3509611	-0.6506982
	0	-1.6866326	-1.4416573	-1.5404061	-1.4488759
	1	0.0791404	-0.3372874	0.4425036	-0.3536646
	2	1.4970987	-0.1195828	-0.3083320	-0.2936741
4	-4	0.0421639	0.0042569	0.0042211	-0.0015332
	-3	-0.0098588	-0.0298887	-0.0104997	-0.0300936
	-2	-0.0186180	-0.0183344	-0.0206006	-0.0182073
	-1	0.0007881	0.0055049	-0.0011925	0.0065336
	0	0.0016525	0.0017039	0.0018043	0.0017416
	1	0.0041007	0.0109261	0.0069731	0.0114432
	2	-0.0082744	0.0052295	0.0040592	0.0066066
	3	-0.0085059	0.0116407	-0.0107233	0.0160401
	4	-0.0056692	-0.0427308	-0.0408991	-0.0435595
6	-6	0.0001560	-0.0002909	-0.0003262	-0.0003116
	-5	-0.0001786	0.0001596	0.0000586	0.0002205
	-4	-0.0001527	0.0000219	0.0000296	0.0000413
	-3	0.0000233	0.0001072	0.0000314	0.0000973
	-2	0.0001739	0.0001780	0.0002290	0.0001822

	-1	-0.0001119	-0.0000344	-0.0000405	-0.0000441
	0	-0.0000003	0.0000022	0.0000009	0.0000021
	1	-0.0000557	-0.0001688	-0.0000719	-0.0001840
	2	0.0001306	-0.0000005	0.0000137	-0.0000138
	3	0.0000540	-0.0001879	-0.0000755	-0.0002217
	4	0.0000748	0.0001449	0.0001852	0.0001471
	5	0.0001246	0.0002325	-0.0000131	0.0002207
	6	-0.0002692	-0.0000605	-0.0000499	-0.0000006

Table 5-27 *Ab Initio* computed eight low-lying Kramers doublet energies (cm^{-1}) and g-tensors of each Kramers doublets in DydiBz15C5 complex (**3.6**).

KDs	Energy (cm^{-1})	g_x, g_y and g_z	KDs
1	0.0	g_x	0.0034
		g_y	0.0159
		g_z	19.7814
2	91.6	g_x	0.1157
		g_y	0.1254
		g_z	16.1927
3	243.3	g_x	0.9324
		g_y	1.7328
		g_z	12.9516
4	296.6	g_x	3.7997
		g_y	5.6717
		g_z	10.9222
5	336.4	g_x	0.5674
		g_y	2.5734
		g_z	10.8538
6	431.3	g_x	1.1532
		g_y	1.7290
		g_z	14.4363
7	486.0	g_x	0.1629
		g_y	0.2482
		g_z	18.4689
8	528.9	g_x	0.0418
		g_y	0.1731
		g_z	18.2868

Table 5-28 SINGLE_ANISO computed crystal field parameters for DydiBz complex (**3.6**). The major components in the Table are in bold. B_k^q is the crystal field parameter and O_k^q is the extended Stevens operator. The quantization axis is chosen to be the main magnetic axis of the ground pseudo-Doublet.

k	q	B_k^q
2	-2	**2.16**
	-1	-0.03
	0	**-2.37**
	1	0.19
	2	**1.83**
4	-4	0.002
	-3	-0.001
	-2	0.02
	-1	0.001
	0	-0.002
	1	-0.0005
	2	0.02
	3	-0.003
	4	-0.003

6 References

1 B. Sieklucka and D. Pinkowicz, *Molecular Magnetic Materials: Concepts and Applications*, Weinheim, Germany : Wiley-VCH, 2017.

2 W. Brostow and H. E. H. Lobland, *Materials: Introduction and Applications*, John Wiley & Sons, 2016.

3 O. Kahn, *Molecular magnetism*, VCH, New York, NY, 1993.

4 J. S. Miller and A. J. Epstein, *Angew. Chem. Int. Ed. Engl.*, 1994, **33**, 385–415.

5 J. M. D. Coey, *Magnetism and magnetic materials*, Cambridge University Press, 2010.

6 R. L. Carlin, *Magnetochemistry*, Springer Science & Business Media, 2012.

7 G. W. Gokel and L. Barbour, *Comprehensive Supramolecular Chemistry II*, Elsevier, 2017.

8 J. S. Miller, *Chem. Soc. Rev.*, 2011, **40**, 3266–3296.

9 S. Blundell, *Magnetism in condensed matter*, Oxford University press, 2001.

10 J. A. Maurer, *PhD thesis: I. Structure-Function Analysis of the Mechanosensitive Channel of Large Conductance. II. Design of Novel Magnetic Materials using Crystal Engineering*, California Institute of Technology, 2003.

11 E. Stares, *PhD thesis: Novel Magnetic Materials Based on Macrocyclic Ligands: Towards High Relaxivity Contrast Agents and Mononuclear Single-Molecule Magnets*, Brock University, 2015.

12 J. S. Miller, *Mater. Today*, 2014, **17**, 224–235.

13 J. Yakhmi, *Bull. Mater. Sci.*, 2009, **32**, 217–225.

14 J. S. Miller, *Pramana*, 2006, **67**, 1–16.

15 H. L. C. Feltham and S. Brooker, *Coord. Chem. Rev.*, 2014, **276**, 1–33.

16 D. Gatteschi, R. Sessoli and J. Villain, *Molecular Nanomagnets*, Oxford University press, 2006.

17 R. Bagai and G. Christou, *Chem. Soc. Rev.*, 2009, **38**, 1011–1026.

18 S. T. Liddle and J. van Slageren, *Chem. Soc. Rev.*, 2015, **44**, 6655–6669.

19 J. M. Zadrozny, M. Atanasov, A. M. Bryan, C.-Y. Lin, B. D. Rekken, P. P. Power, F. Neese and J. R. Long, *Chem. Sci.*, 2012, **4**, 125–138.

20 Y. Peidong, *The Chemistry Of Nanostructured Materials*, World Scientific, 2003.

21 S. Gao and M. Affronte, *Molecular nanomagnets and related phenomena*, Berlin: Springer, 2015.

22 R. Sessoll, D. Gatteschi, A. Caneschi and M. Novak, *NATURE*, 1993, **365**, 141–143.

23 T. Lis, *Acta Crystallogr. B*, 1980, **36**, 2042–2046.

24 S. Brooker and J. A. Kitchen, *Dalton Trans.*, 2009, **48**, 7331–7340.

25 I. Oyarzabal, J. Ruiz, J. M. Seco, M. Evangelisti, A. Camón, E. Ruiz, D. Aravena and E. Colacio, *Chem. – Eur. J.*, 2014, **20**, 14262–14269.

26 M. H. V. Werts, *Sci. Prog.*, 2005, **88**, 101–131.

27 K. Binnemans, *Coord. Chem. Rev.*, 2015, **295**, 1–45.

28 D. N. Woodruff, R. E. P. Winpenny and R. A. Layfield, *Chem. Rev.*, 2013, **113**, 5110–5148.

29 F. Liu, D. S. Krylov, L. Spree, S. M. Avdoshenko, N. A. Samoylova, M. Rosenkranz, A. Kostanyan, T. Greber, A. U. B. Wolter, B. Büchner and A. A. Popov, *Nat. Commun.*, 2017, **8**, 16098.

30 J. D. Rinehart and J. R. Long, *Chem. Sci.*, 2011, **2**, 2078–2085.

31 J. Lu, M. Guo and J. Tang, *Chem. – Asian J.*, 2017, **12**, 2772–2779.

32 J. Liu, Y.-C. Chen, J.-L. Liu, V. Vieru, L. Ungur, J.-H. Jia, L. F. Chibotaru, Y. Lan, W. Wernsdorfer, S. Gao, X.-M. Chen and M.-L. Tong, *J. Am. Chem. Soc.*, 2016, **138**, 5441–5450.

33 Y.-S. Ding, N. F. Chilton, R. E. P. Winpenny and Y.-Z. Zheng, *Angew. Chem. Int. Ed.*, 2016, **55**, 16071–16074.

34 C. J. Milios, A. Vinslava, W. Wernsdorfer, S. Moggach, S. Parsons, S. P. Perlepes, G. Christou and E. K. Brechin, *J. Am. Chem. Soc.*, 2007, **129**, 2754–2755.

35 J. D. Rinehart, M. Fang, W. J. Evans and J. R. Long, *J. Am. Chem. Soc.*, 2011, **133**, 14236–14239.

36 Y.-C. Chen, J.-L. Liu, L. Ungur, J. Liu, Q.-W. Li, L.-F. Wang, Z.-P. Ni, L. F. Chibotaru, X.-M. Chen and M.-L. Tong, *J. Am. Chem. Soc.*, 2016, **138**, 2829–2837.

37 S. K. Gupta, T. Rajeshkumar, G. Rajaraman and R. Murugavel, *Chem. Sci.*, 2016, **7**, 5181–5191.

38 F.-S. Guo, B. M. Day, Y.-C. Chen, M.-L. Tong, A. Mansikkamäki and R. A. Layfield, *Angew. Chem. Int. Ed.*, 2017, **56**, 11445–11449.

39 C. A. P. Goodwin, F. Ortu, D. Reta, N. F. Chilton and D. P. Mills, *Nature*, 2017, **548**, 439–442.

40 F.-S. Guo, B. M. Day, Y.-C. Chen, M.-L. Tong, A. Mansikkamäki and R. A. Layfield, *Science*, 2018, **362**, 1400–1403.

41 Y.-N. Guo, G.-F. Xu, Y. Guo and J. Tang, *Dalton Trans.*, 2011, **40**, 9953–9963.

42 K. N. Shinde, S. J. Dhoble, H. C. Swart and K. Park, in *Phosphate Phosphors for Solid-State Lighting*, Springer Berlin Heidelberg, Berlin, Heidelberg, 2012.

43 J. W. Jr and A. Springsteen, *Applied Spectroscopy: A Compact Reference for Practitioners*, Academic Press, 1998.

44 M. F. Belian, G. F. de Sá, S. Alves and A. Galembeck, *J. Lumin.*, 2011, **131**, 856–860.

45 A. D'Aléo, F. Pointillart, L. Ouahab, C. Andraud and O. Maury, *Coord. Chem. Rev.*, 2012, **256**, 1604–1620.

46 M. L. Cable, D. J. Levine, J. P. Kirby, H. B. Gray and A. Ponce, in *Advances in Inorganic Chemistry*, eds. R. van Eldik and G. Stochel, Academic Press, 2011.

47 A. Døssing, *Eur. J. Inorg. Chem.*, 2005, **2005**, 1425–1434.

48 D. M. Arias-Rotondo and J. K. McCusker, *Chem. Soc. Rev.*, 2016, **45**, 5803–5820.

49 J.-C. G. Bünzli and C. Piguet, *Chem. Soc. Rev.*, 2005, **34**, 1048–1077.

50 X. Wang, L. Zhang, J. Yang, F. Liu, F. Dai, R. Wang and D. Sun, *J. Mater. Chem. A*, 2015, **3**, 12777–12785.

51 J. Long, Y. Guari, R. A. S. Ferreira, L. D. Carlos and J. Larionova, *Coord. Chem. Rev.*, 2018, **363**, 57–70.

52 Y. Bi, X.-T. Wang, W. Liao, X. Wang, R. Deng, H. Zhang and S. Gao, *Inorg. Chem.*, 2009, **48**, 11743–11747.

53 G. Cucinotta, M. Perfetti, J. Luzon, M. Etienne, P.-E. Car, A. Caneschi, G. Calvez, K. Bernot and R. Sessoli, *Angew. Chem. Int. Ed.*, 2012, **51**, 1606–1610.

54 J. Long, R. Vallat, R. A. S. Ferreira, L. D. Carlos, F. A. A. Paz, Y. Guari and J. Larionova, *Chem. Commun.*, 2012, **48**, 9974–9976.

55 C. J. Pedersen, *Angew. Chem. Int. Ed. Engl.*, 1988, **27**, 1021–1027.

56 K. Ariga and T. Kunitake, *Supramolecular Chemistry — Fundamentals and Applications*, Springer-Verlag, Berlin/Heidelberg, 2006.

57 Y. Liu, B.-H. Han and Y.-T. Chen, *Coord. Chem. Rev.*, 2000, **200**, 53–73.

58 G. W. Gokel and M. M. Daschbach, *Coord. Chem. Rev.*, 2008, **252**, 886–902.

59 S. Sasaki and K. Koga, *Chem. Pharm. Bull. (Tokyo)*, 1989, **37**, 912–919.

60 D. Landini, A. Maia, F. Montanari and F. M. Pirisi, *J. Chem. Soc. Perkin Trans. 2*, 1980, **2**, 46–51.

61 Y. Uemura, T. N. Murakami and N. Koumura, *J. Phys. Chem. C*, 2014, **118**, 16749–16759.

62 M. C. F. C. Felinto, C. S. Tomiyama, H. F. Brito, E. E. S. Teotonio and O. L. Malta, *J. Solid State Chem.*, 2003, **171**, 189–194.

63 K. M. N. de Souza, H. J. Batista, M. F. Belian, W. E. Silva and J. A. B. da Silva, *J. Lumin.*, 2016, **170**, 571–587.

64 M. F. Belian, R. O. Freire, A. Galembeck, G. F. de Sá, R. F. de Farias and S. Alves, *J. Lumin.*, 2010, **130**, 1946–1951.

65 P. Starynowicz, *Polyhedron*, 2003, **22**, 337–345.

66 E. L. Gavey, M. A. Hareri, J. Regier, L. D. Carlos, R. A. S. Ferreira, F. S. Razavi, J. M. Rawson and M. Pilkington, *J. Mater. Chem. C*, 2015, **3**, 7738–7747.

67 L. Chen, J. Wang, J.-M. Wei, W. Wernsdorfer, X.-T. Chen, Y.-Q. Zhang, Y. Song and Z.-L. Xue, *J. Am. Chem. Soc.*, 2014, **136**, 12213–12216.

68 S. Petrosyants, Z. Dobrokhotova, A. Ilyukhin, N. Efimov, Y. Mikhlina and V. Novotortsev, *Inorganica Chim. Acta*, 2015, **434**, 41–50.

69 Y.-S. Ding, T. Han, Y.-Q. Hu, M. Xu, S. Yang and Y.-Z. Zheng, *Inorg. Chem. Front.*, 2016, **3**, 798–807.

70 H. Wada, S. Ooka, T. Yamamura and T. Kajiwara, *Inorg. Chem.*, 2017, **56**, 147–155.

71 E. Rousset, M. Piccardo, M.-E. Boulon, R. W. Gable, A. Soncini, L. Sorace and C. Boskovic, *Chem. - Eur. J.*, 2018, **24**, 14768–14785.

72 L. Maxwell, M. Amoza and E. Ruiz, *Inorg. Chem.*, 2018, **57**, 13225–13234.

73 W. A. Zoubi, *J. Coord. Chem.*, 2013, **66**, 2264–2289.

74 E. L. Gavey and M. Pilkington, *Coord. Chem. Rev.*, 2015, **296**, 125–152.

75 Chemistry, The Madura College, / Madurai Kamaraj University, India, Dr. A. Xavier and N. Srividhya, *IOSR J. Appl. Chem.*, 2014, **7**, 06–15.

76 X. Liu, C. Manzur, N. Novoa, S. Celedón, D. Carrillo and J.-R. Hamon, *Coord. Chem. Rev.*, 2018, **357**, 144–172.

77 J. Xie, J. Xie, S. Shen, S. Shen, R. Chen, R. Chen, J. Xu, J. Xu, K. Dong, K. Dong, J. Huang, J. Huang, Q. Lu, Q. Lu, W. Zhu, W. Zhu, T. Ma, T. Ma, L. Jia, L. Jia, H. Cai, H. Cai, T. Zhu and T. Zhu, *Oncol. Lett.*, 2017, **13**, 4413–4419.

78 J. A. McCleverty and T. J. Meyer, *Comprehensive Coordination Chemistry II: From Biology to Nanotechnology*, Newnes, 2003.

79 P. Guerriero, S. Tarnburini and P. A. Vigato, *Coord. Chem. Rev.*, 1995, **139**, 17–243.

80 P. A. Vigato, V. Peruzzo and S. Tamburini, *Coord. Chem. Rev.*, 2012, **256**, 953–1114.

81 P. A. Vigato and S. Tamburini, *Coord. Chem. Rev.*, 2004, **248**, 1717–2128.

82 P. A. Vigato, S. Tamburini and L. Bertolo, *Coord. Chem. Rev.*, 2007, **251**, 1311–1492.

83 A. Caneschi, L. Sorace, U. Casellato, P. Tomasin and P. A. Vigato, *Eur. J. Inorg. Chem.*, 2004, **2004**, 3887–3900.

84 U. Casellato, S. Tamburini, P. Tomasin, P. A. Vigato, S. Aime and M. Botta, *Inorg. Chem.*, 1999, **38**, 2906–2916.

85 S. Tamburini, S. Sitran, V. Peruzzo and P. A. Vigato, *Eur. J. Inorg. Chem.*, 2009, **2009**, 155–167.

86 U. Casellato, S. Tamburini, P. Tomasin and P. A. Vigato, *Inorganica Chim. Acta*, 1997, **262**, 117–121.

87 M. Botta, U. Casellato, C. Scalco, S. Tamburini, P. Tomasin, P. A. Vigato, S. Aime and A. Barge, *Chem. – Eur. J.*, 2002, **8**, 3917–3926.

88 H. L. C. Feltham, R. Clérac, A. K. Powell and S. Brooker, *Inorg. Chem.*, 2011, **50**, 4232–4234.

89 M. Andruh, *Dalton Trans.*, 2015, **44**, 16633–16653.

90 P.-H. Lin, T. J. Burchell, R. Clérac and M. Murugesu, *Angew. Chem.*, 2008, **120**, 8980–8983.

91 P.-H. Lin, T. J. Burchell, L. Ungur, L. F. Chibotaru, W. Wernsdorfer and M. Murugesu, *Angew. Chem. Int. Ed.*, 2009, **48**, 9489–9492.

92 J. Goura, J. Brambleby, C. V. Topping, P. A. Goddard, R. S. Narayanan, A. Kumar Bar and V. Chandrasekhar, *Dalton Trans.*, 2016, **45**, 9235–9249.

93 J. Long, F. Habib, P.-H. Lin, I. Korobkov, G. Enright, L. Ungur, W. Wernsdorfer, L. F. Chibotaru and M. Murugesu, *J. Am. Chem. Soc.*, 2011, **133**, 5319–5328.

94 F. Habib, P.-H. Lin, J. Long, I. Korobkov, W. Wernsdorfer and M. Murugesu, *J. Am. Chem. Soc.*, 2011, **133**, 8830–8833.

95 F. Habib, G. Brunet, V. Vieru, I. Korobkov, L. F. Chibotaru and M. Murugesu, *J. Am. Chem. Soc.*, 2013, **135**, 13242–13245.

96 Q. Wang, S. Venneri, N. Zarrabi, H. Wang, C. Desplanches, J.-F. Létard, T. Seda and M. Pilkington, *Dalton Trans.*, 2015, **44**, 6711–6714.

97 E.L. Gavey and M. Pilkington, U.S. Provisional Patent Application No. 62/174,752 filed on June 12, 2015, 51.

98 E. L. Gavey and M. Pilkington, *Polyhedron*, 2016, **108**, 122–130.

99 M. G. B. Drew, A. H. bin Othman, S. G. McFall, P. D. A. Mcllroy and S. Martin Nelson, *J. Chem. Soc. Dalton Trans.*, 1977, **12**, 1173–1180.

100 J. Regier, *MSc thesis: Ligand Design for Metal-Organic Frameworks and Single-Molecule Magnets*, Brock University, 2016.

101 C. J. Pedersen, *J. Am. Chem. Soc.*, 1967, **89**, 7017–7036.

102 M. C. F. C. Felinto, C. S. Tomiyama, H. F. Brito, E. E. S. Teotonio and O. L. Malta, *J. Solid State Chem.*, 2003, **171**, 189–194.

103 N. Ishikawa, M. Sugita, T. Ishikawa, S. Koshihara and Y. Kaizu, *J. Am. Chem. Soc.*, 2003, **125**, 8694–8695.

104 J. Long, J. Rouquette, J.-M. Thibaud, R. A. S. Ferreira, L. D. Carlos, B. Donnadieu, V. Vieru, L. F. Chibotaru, L. Konczewicz, J. Haines, Y. Guari and J. Larionova, *Angew. Chem. Int. Ed.*, 2015, **54**, 2236–2240.

105 J. P. Costes, S. Titos-Padilla, I. Oyarzabal, T. Gupta, C. Duhayon, G. Rajaraman and E. Colacio, *Inorg. Chem.*, 2016, **55**, 4428–4440.

106 M. A. Hareri, E. L. Gavey, J. Regier, Z. R. Ali, L. D. Carlos, R. a. S. Ferreira and M. Pilkington, *Chem. Commun.*, 2016, **52**, 11335–11338.

107 G. M. SHELDRICK, *Program for Empirical Absorption Correction of Area Detector Data. SADABS*, 1996.

108 Bruker, *Bruker AXS Inc Madison Wis. USA 2007*.

109 G. M. Sheldrick, *Univ. Gött. Ger.*

110 G. M. Sheldrick, *Acta Crystallogr. A*, 2008, **64**, 112–122.

111 A. L. Spek, *Acta Crystallogr. Sect. C Struct. Chem.*, 2015, **71**, 9–18.

112 F. Aquilante, L. D. Vico, N. Ferré, G. Ghigo, P.-åke Malmqvist, P. Neogrády, T. B. Pedersen, M. Pitoňák, M. Reiher, B. O. Roos, L. Serrano-Andrés, M. Urban, V. Veryazov and R. Lindh, *J. Comput. Chem.*, 2010, **31**, 224–247.

113 M. Al Hareri, Z. Ras Ali, J. Regier, E. L. Gavey, L. D. Carlos, R. A. S. Ferreira and M. Pilkington, *Inorg. Chem.*, 2017, **56**, 7344–7353.

114 H. Zabrodsky, S. Peleg and D. Avnir, *J. Am. Chem. Soc.*, 1992, **114**, 7843–7851.

115 S. Hazra, J. Titiš, D. Valigura, R. Boča and S. Mohanta, *Dalton Trans.*, 2016, **45**, 7510–7520.

116 M. J. Heras Ojea, V. A. Milway, G. Velmurugan, L. H. Thomas, S. J. Coles, C. Wilson, W. Wernsdorfer, G. Rajaraman and M. Murrie, *Chem. – Eur. J.*, 2016, **22**, 12839–12848.

117 L. van Pieterson, M. F. Reid, R. T. Wegh, S. Soverna and A. Meijerink, *Phys. Rev. B*, 2002, **65**, 045113.

118 E. Mamontova, J. Long, R. A. S. Ferreira, A. M. P. Botas, D. Luneau, Y. Guari, L. D. Carlos and J. Larionova, *Magnetochemistry*, 2016, **2**, 2–11.

119 K. Yamashita, R. Miyazaki, Y. Kataoka, T. Nakanishi, Y. Hasegawa, M. Nakano, T. Yamamura and T. Kajiwara, *Dalton Trans.*, 2013, **42**, 1987–1990.

120 F. Pointillart, B. L. Guennic, S. Golhen, O. Cador, O. Maury and L. Ouahab, *Chem. Commun.*, 2012, **49**, 615–617.

121 S. Shintoyo, K. Murakami, T. Fujinami, N. Matsumoto, N. Mochida, T. Ishida, Y. Sunatsuki, M. Watanabe, M. Tsuchimoto, J. Mrozinski, C. Coletti and N. Re, *Inorg. Chem.*, 2014, **53**, 10359–10369.

122 M. Ren, S.-S. Bao, R. A. S. Ferreira, L.-M. Zheng and L. D. Carlos, *Chem. Commun.*, 2014, **50**, 7621–7624.

123 Y. Rechkemmer, J. E. Fischer, R. Marx, M. Dörfel, P. Neugebauer, S. Horvath, M. Gysler, T. Brock-Nannestad, W. Frey, M. F. Reid and J. van Slageren, *J. Am. Chem. Soc.*, 2015, **137**, 13114–13120.

124 M. Gregson, N. F. Chilton, A.-M. Ariciu, F. Tuna, I. F. Crowe, W. Lewis, A. J. Blake, D. Collison, E. J. L. McInnes, R. E. P. Winpenny and S. T. Liddle, *Chem. Sci.*, 2016, **7**, 155–165.

125 Y. Bi, C. Chen, Y.-F. Zhao, Y.-Q. Zhang, S.-D. Jiang, B.-W. Wang, J.-B. Han, J.-L. Sun, Z.-Q. Bian, Z.-M. Wang and S. Gao, *Chem. Sci.*, 2016, **7**, 5020–5031.

126 R. A. Layfield and M. Murugesu, *Lanthanides and Actinides in Molecular Magnetism*, John Wiley & Sons, 2015.

127 E. L. Gavey, Y. Beldjoudi, J. M. Rawson, T. C. Stamatatos and M. Pilkington, *Chem. Commun.*, 2014, **50**, 3741–3743.

128 L. Sorace, C. Benelli and D. Gatteschi, *Chem. Soc. Rev.*, 2011, **40**, 3092–3104.

129 J.-L. Liu, Y.-C. Chen, Y.-Z. Zheng, W.-Q. Lin, L. Ungur, W. Wernsdorfer, L. F. Chibotaru and M.-L. Tong, *Chem. Sci.*, 2013, **4**, 3310–3316.

130 N. Ishikawa, M. Sugita and W. Wernsdorfer, *Angew. Chem. Int. Ed.*, 2005, **44**, 2931–2935.

131 S.-D. Jiang, B.-W. Wang, H.-L. Sun, Z.-M. Wang and S. Gao, *J. Am. Chem. Soc.*, 2011, **133**, 4730–4733.

132 S.-D. Jiang, S.-S. Liu, L.-N. Zhou, B.-W. Wang, Z.-M. Wang and S. Gao, *Inorg. Chem.*, 2012, **51**, 3079–3087.

133 M. Jeletic, P.-H. Lin, J. J. Le Roy, I. Korobkov, S. I. Gorelsky and M. Murugesu, *J. Am. Chem. Soc.*, 2011, **133**, 19286–19289.

134 K. R. Meihaus and J. R. Long, *J. Am. Chem. Soc.*, 2013, **135**, 17952–17957.

135 L. Ungur, J. J. Le Roy, I. Korobkov, M. Murugesu and L. F. Chibotaru, *Angew. Chem.*, 2014, **126**, 4502–4506.

136 S. K. Gupta, T. Rajeshkumar, G. Rajaraman and R. Murugavel, *Chem. Sci.*, 2016, **7**, 5181–5191.

137 V. R. Sastri, J. R. Perumareddi, V. R. Rao, G. V. S. Rayudu and J.-C. G. Bünzli, *Modern Aspects of Rare Earths and their Complexes*, Elsevier, 2003.

138 P. Starynowicz and K. Bukietyńska, *Eur. J. Inorg. Chem.*, 2002, **2002**, 1835–1838.

139 F. L. Sousa, F. A. Almeida Paz, P. C. R. Soares-Santos, A. M. V. Cavaleiro, H. I. S. Nogueira, J. Klinowski and T. Trindade, *J. Mol. Struct.*, 2004, **689**, 61–67.

140 V. Veryazov, P.-O. Widmark, L. Serrano-Andrés, R. Lindh and B. O. Roos, *Int. J. Quantum Chem.*, 2004, **100**, 626–635.

141 G. Karlström, R. Lindh, P.-Å. Malmqvist, B. O. Roos, U. Ryde, V. Veryazov, P.-O. Widmark, M. Cossi, B. Schimmelpfennig, P. Neogrady and L. Seijo, *Comput. Mater. Sci.*, 2003, **28**, 222–239.

142 F. Aquilante, J. Autschbach, R. K. Carlson, L. F. Chibotaru, M. G. Delcey, L. D. Vico, I. F. Galván, N. Ferré, L. M. Frutos, L. Gagliardi, M. Garavelli, A. Giussani, C. E.

Hoyer, G. L. Manni, H. Lischka, D. Ma, P. Å. Malmqvist, T. Müller, A. Nenov, M. Olivucci, T. B. Pedersen, D. Peng, F. Plasser, B. Pritchard, M. Reiher, I. Rivalta, I. Schapiro, J. Segarra-Martí, M. Stenrup, D. G. Truhlar, L. Ungur, A. Valentini, S. Vancoillie, V. Veryazov, V. P. Vysotskiy, O. Weingart, F. Zapata and R. Lindh, *J. Comput. Chem.*, 2016, **37**, 506–541.

143 B. A. Heß, C. M. Marian, U. Wahlgren and O. Gropen, *Chem. Phys. Lett.*, 1996, **251**, 365–371.

144 B. O. Roos and P.-Å. Malmqvist, *Phys. Chem. Chem. Phys.*, 2004, **6**, 2919–2927.

145 B. O. Roos, R. Lindh, P.-Å. Malmqvist, V. Veryazov, P.-O. Widmark and A. C. Borin, *J. Phys. Chem. A*, 2008, **112**, 11431–11435.

146 P. Å. Malmqvist, B. O. Roos and B. Schimmelpfennig, *Chem. Phys. Lett.*, 2002, **357**, 230–240.

147 L. F. Chibotaru and L. Ungur, *J. Chem. Phys.*, 2012, **137**, 064112.

148 Z.-X. Zhou, W.-C. Zheng, Y.-Z. Li, Z.-H. Mao, Z.-H. Zhou and Z. Hong, *Polyhedron*, 1996, **15**, 3519–3525.

149 J. Tang and P. Zhang, *Lanthanide single molecule magnets*, Springer, Heidelberg, 2015.

150 S. Maleknia and J. Brodbelt, *J. Am. Chem. Soc.*, 1993, **115**, 2837–2843.

151 R. D. Rogers, L. K. Kurihara and E. J. Voss, *Inorg. Chem.*, 1987, **26**, 2360–2365.

152 A. Roca-Sabio, M. Mato-Iglesias, D. Esteban-Gómez, A. de Blas, T. Rodríguez-Blas and C. Platas-Iglesias, *Dalton Trans.*, 2010, **40**, 384–392.

153 K. Bernot, *Molecular Magnetism of Lanthanides Complexes and Networks*, MDPI, 2018.

154 R. H. Cole, *J. Chem. Phys.*, 1941, **9**, 251–257.

155 I. Oyarzabal, J. Ruiz, E. Ruiz, D. Aravena, J. M. Seco and E. Colacio, *Chem. Commun.*, 2015, **51**, 12353–12356.

156 S. K. Singh, T. Gupta and G. Rajaraman, *Inorg. Chem.*, 2014, **53**, 10835–10845.

157 R. J. Blagg, L. Ungur, F. Tuna, J. Speak, P. Comar, D. Collison, W. Wernsdorfer, E. J. L. McInnes, L. F. Chibotaru and R. E. P. Winpenny, *Nat. Chem.*, 2013, **5**, 673–678.

158 T. Pugh, F. Tuna, L. Ungur, D. Collison, E. J. L. McInnes, L. F. Chibotaru and R. A. Layfield, *Nat. Commun.*, 2015, **6**, 1–8.

159 X.-C. Huang, V. Vieru, L. F. Chibotaru, W. Wernsdorfer, S.-D. Jiang and X.-Y. Wang, *Chem. Commun.*, 2015, **51**, 10373–10376.

160 E. Lucaccini, M. Briganti, M. Perfetti, L. Vendier, J.-P. Costes, F. Totti, R. Sessoli and L. Sorace, *Chem. – Eur. J.*, 2016, **22**, 5552–5562.

161 H. Zabrodsky, S. Peleg and D. Avnir, *J. Am. Chem. Soc.*, 1992, **114**, 7843–7851.

162 M. A. Hareri, E. L. Gavey, J. Regier, Z. R. Ali, L. D. Carlos, R. a. S. Ferreira and M. Pilkington, *Chem. Commun.*, 2016, **52**, 11335–11338.

163 C. Benelli and D. Gatteschi, *Chem. Rev.*, 2002, **102**, 2369–2388.

164 V. V. Novikov, A. A. Pavlov, Y. V. Nelyubina, M.-E. Boulon, O. A. Varzatskii, Y. Z. Voloshin and R. E. P. Winpenny, *J. Am. Chem. Soc.*, 2015, **137**, 9792–9795.

165 Y.-Z. Zhang, S. Gómez-Coca, A. J. Brown, M. R. Saber, X. Zhang and K. R. Dunbar, *Chem. Sci.*, 2016, **7**, 6519–6527.

166 K. R. Vignesh, D. I. Alexandropoulos, B. S. Dolinar and K. R. Dunbar, *Dalton Trans.*, 2019, **48**, 2872–2876.

167 K. R. Vignesh, S. K. Langley, K. S. Murray and G. Rajaraman, *Inorg. Chem.*, 2017, **56**, 2518–2532.

168 D. I. Alexandropoulos, K. A. Schulte, K. R. Vignesh and K. R. Dunbar, *Chem. Commun.*, 2018, **54**, 10136–10139.

169 M. C. Gonçalves, N. J. O. Silva, V. de Zea Bermudez, R. A. Sá Ferreira, L. D. Carlos, K. Dahmouche, C. V. Santilli, D. Ostrovskii, I. C. Correia Vilela and A. F. Craievich, *J. Phys. Chem. B*, 2005, **109**, 20093–20104.

170 E. L. Gavey, M. A. Hareri, J. Regier, L. D. Carlos, R. A. S. Ferreira, F. S. Razavi, J. M. Rawson and M. Pilkington, *J. Mater. Chem. C*, 2015, **3**, 7738–7747.

171 P. Martı´n-Ramos and M. Silva, *Lanthanide-Based Multifunctional Materials: From OLEDs to SIMs*, Elsevier, 2018.

172 R. A. Layfield, *Organometallics*, 2014, **33**, 1084–1099.

173 S. G. McAdams, A.-M. Ariciu, A. K. Kostopoulos, J. P. S. Walsh and F. Tuna, *Coord. Chem. Rev.*, 2017, **346**, 216–239.

174 Z. Zhu, M. Guo, X.-L. Li and J. Tang, *Coord. Chem. Rev.*, 2019, **378**, 350–364.

175 Y.-C. Chen, J.-L. Liu, W. Wernsdorfer, D. Liu, L. F. Chibotaru, M. Chen and M.-L. Tong, *Angew. Chem. Int. Ed.*, 2017, **56**, 4996–5000.

176 N. Brianese, U. Casellato, S. Tamburini, P. Tomasin and P. A. Vigato, *Inorganica Chim. Acta*, 1999, **293**, 178–194.

177 M. G. B. Drew, J. Nelson and S. M. Nelson, *Dalton Trans.*, 1981, 1678–1684.

178 J. de O. Cabral, M. F. Cabral, M. G. B. Drew, F. S. Esho and S. M. Nelson, *J. Chem. Soc. Chem. Commun.*, 1982, 1068–1069.

179 S. M. Nelson, F. S. Esho, M. G. B. Drew and P. Bird, *J. Chem. Soc. Chem. Commun.*, 1979, 1035–1037.

180 P. Guerriero, U. Casellato, S. Tamburini, P. A. Vigato and R. Graziani, *Inorganica Chim. Acta*, 1987, **129**, 127–138.

181 A. W. Addison, T. N. Rao, J. Reedijk, J. van Rijn and G. C. Verschoor, *J. Chem. Soc. Dalton Trans.*, 1984, 1349–1356.

182 N. F. Chilton, R. P. Anderson, L. D. Turner, A. Soncini and K. S. Murray, *J. Comput. Chem.*, 2013, **34**, 1164–1175.

183 M. Kloskowski, D. Pursche, R.-D. Hoffmann, R. Pöttgen, M. Läge, A. Hammerschmidt, T. Glaser and B. Krebs, *Z. Für Anorg. Allg. Chem.*, 2007, **633**, 106–112.

184 A. Upadhyay, C. Das, S. Vaidya, S. K. Singh, T. Gupta, R. Mondol, S. K. Langley, K. S. Murray, G. Rajaraman and M. Shanmugam, *Chem. – Eur. J.*, 2017, **23**, 4903–4916.

185 N. Ahmed, C. Das, S. Vaidya, S. K. Langley, K. S. Murray and M. Shanmugam, *Chem. – Eur. J.*, 2014, **20**, 14235–14239.